





THESIS

This is to certify that the  
dissertation entitled  
CHARGED PARTICLE CORRELATIONS FROM  
INTERMEDIATE ENERGY NUCLEAR REACTIONS

presented by

Daniel Alan Cebra

has been accepted towards fulfillment  
of the requirements for

Ph.D. degree in Physics and  
Astronomy

*Samy D. Westfall*  
Major professor

Date June 21, 1990

**LIBRARY**  
**Michigan State**  
**University**

PLACE IN RETURN BOX to remove this checkout from your record.  
TO AVOID FINES return on or before date due.

DATE DUE	DATE DUE	DATE DUE
_____	_____	_____
_____	_____	_____
_____	_____	_____
_____	_____	_____
_____	_____	_____
_____	_____	_____
_____	_____	_____

MSU is An Affirmative Action/Equal Opportunity Institution

c:\circ\deldue.pn3-p.1

CHARGED-PARTICLE CORRELATIONS  
FROM INTERMEDIATE ENERGY  
NUCLEAR REACTIONS

By

Daniel Alan Cebra

A DISSERTATION

Submitted to  
Michigan State University  
in partial fulfillment of the requirements  
for the Degree of

DOCTOR OF PHILOSOPHY

Department of Physics and Astronomy

1990

645-3156

## ABSTRACT

# CHARGED PARTICLE CORRELATIONS FROM INTERMEDIATE ENERGY NUCLEAR COLLISIONS

by

Daniel Alan Cebra

Charged particle correlations have been used to analyze experimental data with the purpose of determining the answers to questions concerning the bulk properties of nuclear matter. A two-particle analysis has been performed on a set of 500 MeV p+Ag and p+Be data. In this analysis questions were studied concerning the density and the temperature of the interaction region reached during nuclear collisions. The radii that are extracted vary between 2.0 and 12.0 Fm depending on which particle pair is considered. The temperatures that are extracted vary between 3.0 and 5.0 MeV. These results are not significantly different from those of similar studies using heavy-ion projectiles to probe nuclear systems.

A multi-particle analysis has been performed on a set of data from the system Ar+V at a range of energies from 35 to 85 MeV/nucleon. These data were analyzed in an effort to determine at what energy the multi-fragmentation reaction channel is opened. This channel is expected to become the dominant reaction mechanism at energies which are sufficient to allow the system to expand into a region of mechanical instability. The event shape is used to determine whether a sequential decay or a simultaneous multi-fragmentation is the dominant disassembly mechanism at a given incident energy. A clear signature of the multi-fragmentation mechanism is observed at and above bombarding energies of 45 MeV/nucleon.

## ACKNOWLEDGEMENTS

My advisor, Dr. Gary Westfall, deserves a great deal of recognition for his constant support through my long and sometimes reckless graduate career. He has served in a variety of roles for me. He has been an excellent mentor who has constantly provided me with accurate advice and direction, he has been a tireless colleague who was always willing to work to the point of exhaustion to get the experiments going when things were rough; he has been an upbeat teammate who would not give up even when the softball team was down 21 to 5, and he has been a genuine friend.

I have received substantial support from the Nuclear Science Division at the Cyclotron laboratory. I am deeply indebted to those who served as associate director of nuclear science during my years at the lab (Drs Austin, Crawley, and Gelbke). The research assistantships, which were continued even while I was not in the best of standing, enabled me to concentrate on experimental physics. In addition, the support that I received for outside experiments and for conferences broadened my experiences and made me feel like a member of the international physics community.

Drs Westfall, Crawley, Benenson, and Kashy demonstrated a tremendous patience with me during my period of misadventures with the comprehensive exams. Without their assistance and encouragement I would have surely left Michigan State.

A great deal of credit should go to the laboratory staff without whom most of the experiments described in this work would not have been possible. The NSCL has, without doubt, the best working atmosphere of any laboratory within which I have worked.

I have enjoyed working in the  $4\pi$  research group. The team that has been assembled for the construction and utilization of this experimental device is extremely



cohesive and talented. The weekly group meetings were essential for co-ordinating the efforts of the 10 to 20 persons who were actively working on the project at a given time. It has taken a great deal of effort to build and operate this device, but I feel that there has been a tremendous reward. I find the results that are currently being generated to be extremely interesting. Of course, I had chosen to come to MSU because I had wanted to do this type of physics, so it is natural for me to be fascinated with these results. I made a decision in my fourth year not to finish my dissertation on the two particle studies but to stay and see the  $4\pi$  through to operation. It has certainly been worth staying.

I would like to thank Lawrence and Lori Heilbronn, whose friendship throughout the years have made my sojourn in the midwest much more pleasurable.

And finally, I would like to deeply thank my wife, Karen. Her steady impatience with my lack of progress through my graduate program served as a constant reminder of the ultimate goals.



# Contents

<b>LIST OF TABLES</b>	<b>x</b>
-----------------------	----------

<b>LIST OF FIGURES</b>	<b>xi</b>
------------------------	-----------

<b>I Introduction</b>	<b>1</b>
-----------------------	----------

A The Equation of State of Nuclear Matter . . . . .	1
---	---

B Phases and Phase Transitions . . . . .	2
--	---

C Reaction Trajectories . . . . .	4
-----------------------------------	---

D Statistical Properties of Nuclei: The Question of Temperature . . . . .	6
---	---

E The Density of Nuclear Matter . . . . .	7
---	---

F The Transition from Sequential Decay to Multi-fragmentation . . . . .	7
---	---

G Organization of the Thesis . . . . .	8
--	---

<b>II Two Particle Correlations from 500 p+Ag and p+Be</b>	<b>10</b>
--	-----------

A Introduction and Experimental Justification . . . . .	10
---	----

1 Background . . . . .	10
------------------------	----

2 The Fireball Model . . . . .	11
--------------------------------	----

3 Gamma Emitting States . . . . .	13
-----------------------------------	----

4	Two-particle Correlations Review . . . . .	18
5	Experimental Goals . . . . .	21
B	Description of the Experiment . . . . .	23
C	Extraction of Source Sizes . . . . .	24
1	Basic Method . . . . .	24
2	Source Sizes from p+Ag . . . . .	26
3	Source Sizes from p+Be . . . . .	33
4	The Effect of Energy Cuts on the Extracted Source Radii . . . . .	42
5	Summary of Extracted Source Sizes . . . . .	44
D	Extraction of Nuclear Temperatures . . . . .	45
1	Basic Method . . . . .	45
2	Backgrounds for Independent Emission . . . . .	46
3	Efficiency Calculations . . . . .	48
4	Populations of Particle Unstable States . . . . .	49
5	The Nuclear Temperature . . . . .	53
E	Conclusions . . . . .	57
<b>III The Search for Multi-Fragmentation</b>		<b>60</b>
A	Introduction . . . . .	60
B	Theoretical Studies . . . . .	64
1	Statistical Multi-fragmentation . . . . .	64
2	Transition-State Multi-fragmentation . . . . .	65

3	Geometrical Multi-fragmentation . . . . .	73
C	Experimental Studies . . . . .	74
D	Conclusions . . . . .	87
<b>IV</b>	<b>Multi-Particle Correlations</b>	<b>90</b>
A	Introduction to Multi-particle Observables . . . . .	90
B	Experimental Details . . . . .	92
1	Exp 87008A . . . . .	93
2	Exp 87008B . . . . .	93
3	Exp 88012 . . . . .	94
C	Event Characterization . . . . .	94
D	Event Shape Analysis . . . . .	96
E	Events Shape Distributions as a Function of Incident Energy . . . . .	104
F	Comparison to Published Models . . . . .	108
1	First Order Observables . . . . .	108
2	GEMINI . . . . .	111
3	López . . . . .	111
G	Other Effects That May Induce an Observed Elongation . . . . .	113
1	Finite Multiplicity Effect . . . . .	115
2	Rotational Distortions . . . . .	117
3	Collective Elongations . . . . .	118
H	The Sequential Simulation . . . . .	120

I	The Simultaneous Simulation . . . . .	125
1	Randomized Directions, Energy and Momentum Conserved . . . . .	132
2	Randomized Directions, Multiplicity Constrained . . . . .	133
3	Coulomb Trajectories . . . . .	134
J	Determination of the Reaction Mechanism . . . . .	135
K	Conclusions . . . . .	147
<b>V</b>	<b>Conclusions</b>	<b>149</b>
	<b>APPENDICES</b>	<b>152</b>
<b>A</b>	<b>Technical Descriptions of the Detectors Systems</b>	<b>152</b>
A	The 4-by-4 Close Packing Array . . . . .	152
B	The Multi-Wire Proportional Chamber . . . . .	153
C	The Multiplicity Array Detectors . . . . .	157
D	The MSU $4\pi$ Array . . . . .	157
<b>B</b>	<b>The Light Response of Plastic Scintillator</b>	<b>161</b>
A	Scintillation Theory . . . . .	161
B	The Calibration Experiments . . . . .	164
1	The Detectors . . . . .	164
2	Elastic Scattering . . . . .	165
3	Degraded Calibration Beams . . . . .	168
4	Fragmentation Beams . . . . .	172

C	The Light Responses of the Scintillators . . . . .	173
1	Response Function of the Slow Scintillator . . . . .	173
2	Response Function of the Fast Scintillator . . . . .	178
D	Conclusions . . . . .	183
<b>C</b>	<b>Phoswich Analysis Routines</b>	<b>184</b>
	<b>LIST OF REFERENCES</b>	<b>194</b>

# List of Tables

II.1	A summary of the source radii extracted from the 500 MeV p+Ag and p+Be systems. The results are compared to an earlier study of 35 MeV/nucleon N+Ag [Fox88]. . . . .	45
II.2	A list of all of the particle unstable states that could be studied with this detector system. . . . .	47
II.3	The temperatures extracted from this study. . . . .	57
IV.1	The mid-rapidity charge gates for the various impact parameter bins for the various systems that were studied. . . . .	98
IV.2	The average values for the sphericity and coplanarity parameters from the analysis of central collisions from the system $^{40}\text{Ar} + ^{51}\text{V}$ at six different beam energies. . . . .	104
IV.3	The input parameters for the simulation for the six beam energies that were studied. The simulation attempted to reproduce central events from the reaction $^{40}\text{Ar} + ^{51}\text{V}$ . . . . .	132
A.1	Characteristics of the fast and slow scintillation material. . . . .	153
B.1	A listing of the specifications of each of the four types of phoswich detector that were employed in the studies of the light response. . . .	165
B.2	The thicknesses of the aluminum degraders that were used in the calibration of the phoswich detectors and the energy deposited in each scintillator . . . . .	168
B.3	The energies of the observed fragment species during the fragmentation runs. . . . .	174

Li

I.

I.

I.

II

# List of Figures

I.1	A diagram of the predicted phases of nuclear matter in Pressure-Density space [Bond85a]. . . . .	3
I.2	A schematic diagram of the stages of a nuclear reaction and the subsequent decay of the highly excited system. . . . .	5
I.3	EOS of nuclear matter. The solid line is an isentrope. The shaded region on the left is the spinodal region. The shaded region on the right corresponds to initial conditions that will lead to breakup after expansion. . . . .	6
II.1	A schematic diagram of the the reaction $^{14}\text{N} + ^{98}\text{Ag}$ assuming the fireball ball. . . . .	12
II.2	The effective temperature extracted from a study of the populations of gamma emitting states [Morr84]. . . . .	15
II.3	The expected ratios between states as a function of temperature. . . . .	17
II.4	A schematic diagram of the reaction $p + ^{98}\text{Ag}$ . The hashed area represents the thermalized region. . . . .	22
II.5	The diagram of the experimental setup for the study of two-particle correlations from $p+\text{Ag}$ and $p+\text{Be}$ . . . . .	25
II.6	The correlation function for proton-proton pairs from the 500 MeV $p+\text{Ag}$ system. . . . .	27
II.7	The correlation function for proton-deuteron pairs from the 500 MeV $p+\text{Ag}$ system. . . . .	30
II.8	The correlation function for proton-alpha pairs from the 500 MeV $p+\text{Ag}$ system. . . . .	31
II.9	The correlation function for deuteron-deuteron pairs from the 500 MeV $p+\text{Ag}$ system. . . . .	32
II.10	The correlation function for deuteron-alpha pairs from the 500 MeV $p+\text{Ag}$ system. . . . .	34
II.11	The correlation function for triton-triton pairs from the 500 MeV $p+\text{Ag}$ system. . . . .	35
II.12	The correlation function for proton-proton pairs from the 500 MeV $p+\text{Be}$ system. . . . .	36
II.13	The correlation function for proton-deuteron pairs from the 500 MeV $p+\text{Be}$ system. . . . .	37

II.14	The correlation function for proton-alpha pairs from the 500 MeV p+Be system. . . . .	38
II.15	The correlation function for deuteron-deuteron pairs from the 500 MeV p+Be system. . . . .	39
II.16	The correlation function for deuteron-alpha pairs from the 500 MeV p+Be system. . . . .	40
II.17	The correlation function for triton-triton pairs from the 500 MeV p+Be system. . . . .	41
II.18	The correlation functions for a variety of particle pairs from the 500 MeV p+Ag system. The diamonds correspond to events selected on high total energy for the two particles of the pair, while the crosses are data selected on low total energy. . . . .	43
II.19	The detection efficiency of the MWPC . . . . .	49
II.20	The relative detection efficiency for four different particle pairs. The peak efficiency has been normalized to unity for each pair. . . . .	50
II.21	The relative momentum spectrum for proton-triton pairs (squares) and an estimate of the independent background (dashed line). The lower portion displays the counts above background (squares) and fits to the individual peaks (dotted and solid lines). . . . .	52
II.22	The relative momentum spectrum for deuteron-triton pairs (squares) and an estimate of the independent background (dashed line). The lower portion displays the counts above background (squares) and fits to the individual peaks (dotted and solid lines). . . . .	54
II.23	The relative momentum spectrum for deuteron- $\alpha$ pairs (squares) and an estimate of the independent background (dashed line). The lower portion displays the counts above background (squares) and fits to the individual peaks (dotted and solid lines). . . . .	55
II.24	The relative momentum spectrum for triton- $\alpha$ pairs (squares) and an estimate of the independent background (dashed line). The lower portion displays the counts above background (squares) and fits to the individual peaks (solid lines). . . . .	56
III.1	The measured mass yields from the reaction p+Xe. The energies of the proton beam varied from 80 to 350 GeV. The exponent of the solid curve is fit to the data. This analysis was inspired by the Fisher droplet model which predicts $d\sigma/dA \propto A^{-\tau}$ [Finn82]. . . . .	63
III.2	Predictions of a statistical multi-fragmentation model. The mean multiplicity and its dispersion as a function of the excitation energy are shown [Bond85b]. . . . .	66
III.3	The average temperature T as a function of the excitation energy $E^*/A_0$ . The onset of fragmentation occurs when the energy fluctuations are large enough to break internal bonds (crack formation). The dashed line illustrates the temperature of a free nucleon gas [Bond85b]. . . . .	67
III.4	Predictions from a micro-canonical statistical multi-fragmentation model. The relative probabilities of evaporation (E, solid), fission (F, dashed), and cracking (C, dot-dash) like events for $^{131}\text{Xe}$ are shown [Gros87]. . . . .	68

III

III.5	The excitation energy as a function of the internal temperature calculated from a statistical multi-fragmentation [Gros87]. . . . .	69
III.6	The partial widths $\Gamma_N$ for the breakup of $^{120}\text{Sn}$ into $N$ fragments with mass numbers $A > 10$ as a function of the excitation energy of the source. The curves are labeled by the value of $N$ [Lópe89b]. . . .	71
III.7	Fragment velocity correlation functions for (a) all fragments (b) charged fragments only and (c) heavy fragments ( $A > 4$ ) only. $A=150$ , $Z=62$ , and $E^*=5$ MeV/nucleon [Lópe89a]. . . . .	72
III.8	Superposition of 200 events in the sphericity-coplanarity plane for $A=150$ , $Z=62$ , and $E^*=5$ MeV/nucleon [Lópe89a]. . . . .	73
III.9	The observed IMF ( $Z > 2$ ) multiplicity distributions from 200 MeV/nucleon Au+Au. The five curves represent five participant charge multiplicity bins [Doss87, Harr87]. . . . .	75
III.10	Inclusive production cross-sections as a function of the fragment charge from the reaction Nb+Be at 11.4, 14.7, and 18.0 MeV/nucleon [Wozn88, Char88b]. . . . .	77
III.11A	plot of the charge observed in the first detector against the charge observed in the second detector. The upper right corner shows a spectrum of $Z_1 + Z_2$ [Bowm87]. . . . .	78
III.12A	plot of $Z_1$ against $Z_2$ , where $Z_1$ and $Z_2$ are the charges of the two heaviest fragments produced by a microcanonical multi-fragmentation simulation of the decay of $^{146}\text{Nd}^*$ [Gros88]. . . . .	79
III.13	Relative velocity distributions between IMFs. The solid dots are the experimental data with statistical errors [Klot89], the dashed line is the prediction from a sequential decay code, and the solid curve is the calculation from a simultaneous multi-fragmentation [Gros89]. . . .	80
III.14	Calculations for two systems ( $^{18}\text{O} + ^{197}\text{Au}$ , and $\alpha + ^{197}\text{Au}$ ). The left side shows the effective mass ( $A_{eff}$ ) of the compound system as a function of the original excitation energy; the right side displays the centroid of the relative velocity distribution [Poch89b]. . . . .	81
III.15A	plot of the average IMF multiplicity as a function of excitation energy for various beams on silver (top) and gold (bottom) targets [Trau89].	82
III.16	The relative velocity correlation functions from 84 MeV/nucleon $^{18}\text{O}$ on $^{197}\text{Au}$ (top) and $^{nat}\text{Ag}$ (bottom). The three curves are calculations from a sequential decay code with an adjustable decay time scale [Trau89].	84
III.17	The relative angles (left) and relative velocities (right) between pairs of IMFs from the reaction Ne + Au at 60 MeV/nucleon. The particles are ranked from heaviest to lightest [Boug89b]. . . . .	85
III.18	Shape analysis for data from the reaction 43 MeV/nucleon Kr + Au, Ag, and Th. The $ND$ value represents the number of IMFs detected [Boug89a]. . . . .	86
III.19	Shape analysis plots for the breakup of $^{16}\text{O}$ into four $\alpha$ s (c). For comparison, the predictions from a multi-fragmentation (a) and a sequential decay (b) are shown [Poul89]. . . . .	88

IV.1	The mid-rapidity charge as a function of the known impact parameter. Both the total charge and the quantity that passed the filtering requirements are displayed [Ogil89a]. . . . .	97
IV.2	The relative contributions that different impact parameters make to each of the bins [Ogil89a]. . . . .	97
IV.3	Illustration of a typical event. a) The lengths of the vectors corresponds to the velocity of the particles in the laboratory reference frame. b) The same event transformed to the center-of-mass reference frame. . .	99
IV.4	A display of which areas of the S-C space correspond to which spheroidal shapes. . . . .	102
IV.5	The average sphericity parameter extracted from a set of 70 MeV/nucleon La+La data as a function of the velocity with which the data were transformed. . . . .	103
IV.6	A contour plot of the event shape distribution gated on central events from the system 35 MeV/nucleon $^{40}\text{Ar} + ^{51}\text{V}$ . . . . .	105
IV.7	A contour plot of the event shape distribution gated on central events from the system 45 MeV/nucleon $^{40}\text{Ar} + ^{51}\text{V}$ . . . . .	105
IV.8	A contour plot of the event shape distribution gated on central events from the system 55 MeV/nucleon $^{40}\text{Ar} + ^{51}\text{V}$ . . . . .	106
IV.9	A contour plot of the event shape distribution gated on central events from the system 65 MeV/nucleon $^{40}\text{Ar} + ^{51}\text{V}$ . . . . .	106
IV.10A	contour plot of the event shape distribution gated on central events from the system 75 MeV/nucleon $^{40}\text{Ar} + ^{51}\text{V}$ . . . . .	107
IV.11A	contour plot of the event shape distribution gated on central events from the system 85 MeV/nucleon $^{40}\text{Ar} + ^{51}\text{V}$ . . . . .	107
IV.12	The first order observables for the system $^{40}\text{Ar} + ^{51}\text{V}$ at 35 meV/nucleon. a) The identified multiplicity, b) the total multiplicity, c) the mass distribution, d) the charge distribution, e) the proton kinetic energy spectrum, and f) the helium kinetic energy spectrum. . . . .	110
IV.13	The results of the GEMINI simulation (circles) compared to the experimental data (crosses). . . . .	112
IV.14	The results of López's simulation (circles) compared to the experimental data (crosses). . . . .	114
IV.15	The trajectory of the S and C centroids as a function of multiplicity. .	116
IV.16	The trajectories of the S and C centroids as a function of multiplicity for emission from a rotating source. . . . .	119
IV.17	An expanded view of the trajectories from the rotational simulations in the region of the multiplicities that are measured for the experimental data. . . . .	119
IV.18	An overview of the relative magnitudes of the various effects that induce elongations. . . . .	121
IV.19	The results of the sequential simulation (circles) compared to the first order observables from the experimental data for the system Ar+V at 35 MeV/nucleon (crosses) . . . . .	126

IV

A

IV.20	The results of the sequential simulation (circles) compared to the first order observables from the experimental data for the system Ar+V at 45 MeV/nucleon (crosses) . . . . .	127
IV.21	The results of the sequential simulation (circles) compared to the first order observables from the experimental data for the system Ar+V at 55 MeV/nucleon (crosses) . . . . .	128
IV.22	The results of the sequential simulation (circles) compared to the first order observables from the experimental data for the system Ar+V at 65 MeV/nucleon (crosses) . . . . .	129
IV.23	The results of the sequential simulation (circles) compared to the first order observables from the experimental data for the system Ar+V at 75 MeV/nucleon (crosses) . . . . .	130
IV.24	The results of the sequential simulation (circles) compared to the first order observables from the experimental data for the system Ar+V at 85 MeV/nucleon (crosses) . . . . .	131
IV.25	A scatter plot showing the sphericity and coplanarity values for 100 events generated from the sequential simulation (crosses) and for 100 events from the simultaneous simulation (circles). . . . .	136
IV.26	Distributions of the relative velocity and angle between any two particles from central events from the reaction 100 MeV/nucleon Ar+V. .	137
IV.27	A comparison of the predicted event shape distributions from the a) sequential and c) simultaneous simulations to that measured for the b) experimental data for the reaction Ar+V at 35 MeV/nucleon. . . . .	138
IV.28	A comparison of the predicted event shape distributions from the a) sequential and c) simultaneous simulations to that measured for the b) experimental data for the reaction Ar+V at 45 MeV/nucleon. . . . .	139
IV.29	A comparison of the predicted event shape distributions from the a) sequential and c) simultaneous simulations to that measured for the b) experimental data for the reaction Ar+V at 55 MeV/nucleon. . . . .	140
IV.30	A comparison of the predicted event shape distributions from the a) sequential and c) simultaneous simulations to that measured for the b) experimental data for the reaction Ar+V at 65 MeV/nucleon. . . . .	141
IV.31	A comparison of the predicted event shape distributions from the a) sequential and c) simultaneous simulations to that measured for the b) experimental data for the reaction Ar+V at 75 MeV/nucleon. . . . .	142
IV.32	A comparison of the predicted event shape distributions from the a) sequential and c) simultaneous simulations to that measured for the b) experimental data for the reaction Ar+V at 85 MeV/nucleon. . . . .	143
IV.33	The trajectories of the sphericity and coplanarity centroids as the beam energy is increased from 35 to 85 MeV/nucleon. . . . .	145
IV.34	$S_{Average}$ and $C_{Average}$ for the two simulations and for the experimental data at each of the six beam energies. . . . .	146
IV.35	A plot of $S_{Average}$ as a function of the incident energy for the two simulations and for the experimental data. . . . .	146
A.1	A side view of four of the detectors. . . . .	154

A.2	Perspective view of the 4-by-4 array stacked for installation behind the MWPC. . . . .	154
A.3	Scatter plots of the X and Y positions determined by the MWPC when in coincidence with phoswichs 1-16 . . . . .	156
A.4	A schematic diagram of the MSU $4\pi$ Array. . . . .	158
A.5	A schematic diagram of a single module of the $4\pi$ Array. . . . .	159
B.1	The experimental configuration for a calibration of the response to protons and deuterons. . . . .	166
B.2	A scatter plot of the magnitude of the signal from the slow scintillator against the calculated energy of the recoil proton from the reaction $p[p,p]p$ . . . . .	167
B.3	A scatter plot of the magnitude of the signal from the slow scintillator against the recoil proton energy. . . . .	169
B.4	The centroids of the light distribution were determined for each recoil energy. a) displays the proton response function, and b) displays the deuteron response function. The solid curves correspond to fits to the experimental calibration data. . . . .	170
B.5	The light response as a function of energy for the slow scintillator for deuterons and $\alpha$ particles. . . . .	171
B.6	A scatter plot displaying the raw data from a fragmentation calibration run. These data are from a single detector and a single rigidity setting. Several different isotopic species are simultaneously produced for each element. . . . .	175
B.7	This figure displays the light response of the slow scintillator as a function of energy for several different particle types. These data are from the fragmentation run in the 60 inch chamber using type I detectors. . . . .	176
B.8	This figure displays the light response of the slow scintillator as a function of energy for several different particle types. These data are from the fragmentation run using the S320 spectrometer and 6 type III detectors. . . . .	176
B.9	This figure displays the light response of the slow scintillator as a function of energy for several different particle types. These data are from a fragmentation run at GANIL [Gont90]. . . . .	177
B.10	An illustration of the ionization density as a function of depth in scintillation material for a 100 MeV deuteron (solid line) and a 25 MeV deuteron (dotted line). . . . .	179
B.11	A compilation of the data from the various calibration runs. This figure displays the light response of the fast scintillator as a function of energy for several different particle types. . . . .	181
B.12	A calibration of the $\Delta E$ scintillator for energy near the punch-in region. . . . .	182
C.1	The electronics diagram for the analysis of signals from the phoswich detectors used in the MSU $4\pi$ Array. . . . .	185

C.2	An idealized phoswich signal for a charged particle incident on a detector with a fast plastic front scintillator and a slow plastic stopping scintillator. . . . .	187
C.3	A scatter plot of the signal in the fast gate versus the signal in the slow gate. The data are from a $4\pi$ phoswich at $23^\circ$ , the reaction is 35 MeV/nucleon Ar+V. . . . .	188
C.4	$\Delta L-L$ plots for 16 phoswichs. The gains are set for $\alpha$ s. The data are from the reaction 500 MeV p+Ag. . . . .	190
C.5	A summation of $\Delta L-L$ spectra from the same 16 phoswichs displayed in the previous figure. . . . .	192
C.6	The predicted particle bands (dotted) and the particle identification gates (solid). . . . .	193

C

I

A

In

bot

dis

sys

wh

lar

iso

sur

as

ph

cle

the

ert

# Chapter I

## Introduction

### A The Equation of State of Nuclear Matter

In 1881, van der Waals demonstrated that a system containing particles that exhibit both a weak attraction and a strong short range repulsion will contain at least two discrete phases. This was demonstrated in the study of the equation of state of systems of molecules. The equation of state used by van der Waals was:

$$P = \frac{RT}{v - b} - \frac{a}{v^2} \quad (\text{I.1})$$

where  $P$  is the pressure,  $R$  is the gas constant,  $T$  is the temperature,  $v$  is the molar volume, and  $a$  and  $b$  are constants. For temperatures below a critical value, isotherms on a Pressure-Volume (P-V) diagram are multivalued with respect to pressure. A Maxwell-Gibbs construct can be used to explain this area on the diagram as a metastable region in which there is a coexistence of both the liquid and the gas phases.

The force between nucleons is similar in nature to the intermolecular forces. Nucleons exhibit an attractive force and a short-range hard-core repulsion. Estimates of the nuclear equation of state suggest that the matter should exhibit the same properties and phase transitions as a van der Waals system [Lamb78, Dani79, Barr80,

Fre

of t

wh

tha

def

con

On

var

**B**

Usi

dis

var

a li

reg

pha

be

me

pha

liq

as

exp

ma

[Frei81, Schu82, Curt83, Bert83, Jaqa83, Bond85a]. Using a Skryme parameterization of the nuclear force, one can determine an equation of state for nuclear matter (EOS):

$$P = 2 \frac{\sigma + 2 T}{\sigma + 1} \frac{1}{v} - \frac{\sigma + 2}{\sigma} \frac{1}{v^2} + \frac{2}{\sigma(\sigma + 1)} \frac{1}{v^{\sigma+2}} \quad (\text{I.2})$$

where  $P$ ,  $T$ , and  $v$  are the pressure, temperature, and volume, and  $\sigma$  is a parameter that controls the value of the compressibility ( $\kappa$ ) [Jaqa83]. The compressibility is defined as the density ( $n$ ) times the partial of pressure ( $P$ ) with respect to density at constant entropy ( $S$ ) [Bert83]

$$\kappa = n \left. \frac{\partial P}{\partial n} \right|_S. \quad (\text{I.3})$$

One observes from Equations I.1 and I.2 that the nuclear EOS is similar in form to van der Waals EOS.

## B Phases and Phase Transitions

Using an EOS, one can construct a phase diagram for nuclear matter. Figure I.1 displays an example of such a diagram [Bond85a]. This diagram resembles that of a van der Waals system. Isotherms for temperatures below a critical value pass from a liquid phase at high densities into a region of coexistence marked by the hashed region on the figure. The portion of the total volume occupied by the liquid and gas phases is determined by the condition that the chemical potentials of the two phases be equal, which corresponds to the Maxwell-Gibbs construct. As one first enters the metastable region from the liquid region, the majority of the volume is in the liquid phase. The gas phase contribution is represented by bubbles contained within the liquid volume. The proportion of the matter that is in the gaseous phase will increase as the density is reduced. As the gas phase contribution increases, the bubbles will expand and proliferate. A point of critical opalescence will be reached when the majority of the volume is filled by matter in the gaseous phase. At this point, instead

of p  
con

Fig  
spa

of i  
dys

pre  
(La

all  
der

ten  
If t

liqu  
mi  
flu

If gaseous bubbles contained within a volume that is mostly liquid, the system will consist of droplets of liquid matter contained within a mostly gaseous volume.

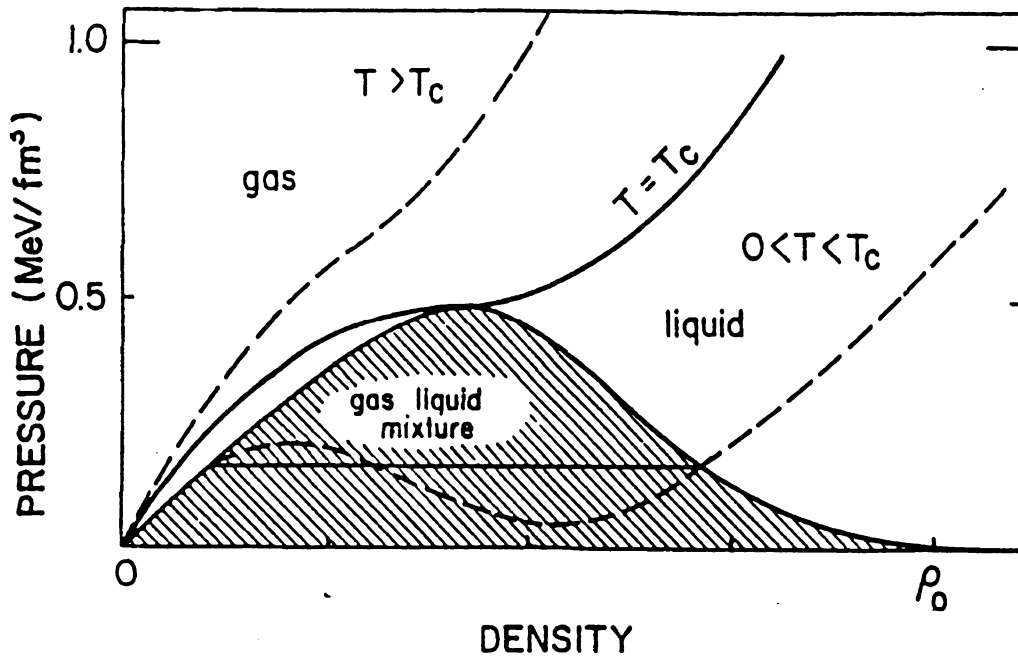


Figure I.1: A diagram of the predicted phases of nuclear matter in Pressure-Density space [Bond85a].

A phase transition is expected to occur if a homogeneous system enters a region of mechanical instability. The requirements for stability are a positive heat capacity (thermodynamic stability), a positive compressibility (mechanical stability), and a positive pressure [Barr80]. A negative pressure can not be excluded for any physical reasons [Bond85a]. For the EOS suggested for nuclear matter, the heat capacity is positive for all temperatures. The compressibility, however, is negative at low temperatures and low densities. In this mechanical instability region (spinodal region) a homogeneous system is unstable against fluctuation growth [Bert83, Peth87, Heis88, Sura89, Boal89]. If these density fluctuations are able to grow, the system will separate into distinct liquid and vapor components. The magnitude of the fluctuation growth will be determined by the duration of time spent in the spinodal region and the growth rate of the fluctuations [Heis88]. The growth rate of the fluctuations is related to the velocity of

sou

C

A r

Th

of t

tar

gen

nuc

ma

to

rea

pat

the

The

unt

this

corr

will

indi

the

whe

The

sound in nuclear matter and hence to the EOS [Sura89].

## C Reaction Trajectories

A nuclear reaction should proceed through several stages as diagrammed in Figure I.2. These stages can be characterized by their thermodynamic properties. The first stage of the reaction occurs from the point of initial contact between the projectile and the target. During this phase, the interaction region is compressed and heated. Entropy is generated during the course of this compression as the kinetic energy of the projectile nucleus is converted into internal excitation energy of the system. The second stage is marked by the expansion of the thermalized region. This expansion stage is expected to be isentropic [Curt83]. If the system has sufficient energy, it will fragment upon reaching a freeze-out density, which is defined as the density for which the mean free path of a nucleon is equal to the size of the thermalized region. During this stage of the interaction, the system will disassemble into an array of excited nuclear fragments. These newly formed fragments will continue to de-excite in the post-interaction phase until they have dissipated all of their internal energy.

Figure I.3 displays an alternate EOS diagram for nuclear matter [Bert83]. On this figure one can follow the trajectory of a reaction (dashed line). The solid line corresponds to the  $S = 0$  unperturbed state. The initial compression of the system will generate entropy which will place the excited system above the  $S = 0$  line as indicated in the figure (dashed line). The relationship between the energy put into the system and the density should be [Bert83]

$$E = a(n - n_0)^2 \quad (\text{I.4})$$

where  $a$  is the binding energy,  $n$  is the density, and  $n_0$  is the normal nuclear density. The system will follow the trajectory suggested by the dashed line on Figure I.3.

Pr

Co  
Th

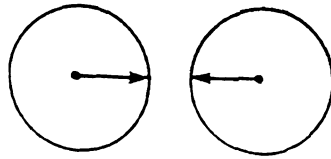
Ex

Fr

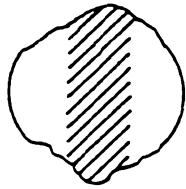
Sec  
of

Figur  
deacy

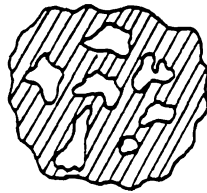
Pre-Reaction



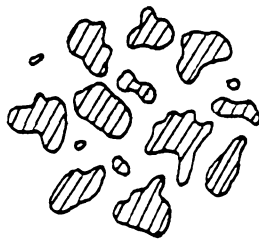
Compression/  
Thermalization



Expansion



Fragmentation



Secondary Decay  
of Excited Fragments

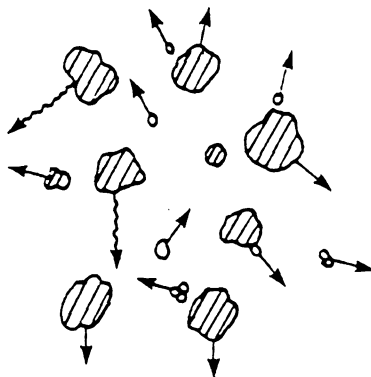


Figure I.2: A schematic diagram of the stages of a nuclear reaction and the subsequent decay of the highly excited system.

Follow  
The i  
was s  
spino

Figur  
on th  
initia  
the tr

D

In the  
statis  
produ  
this p  
time  
inter  
equili

Following the initial compression of the system, it will then expand along an isentrope. The isentropes follow the same form of the  $S = 0$  line. If the initial excitation energy is sufficient to place the system in the overstressed region, it will expand into the spinodal zone.

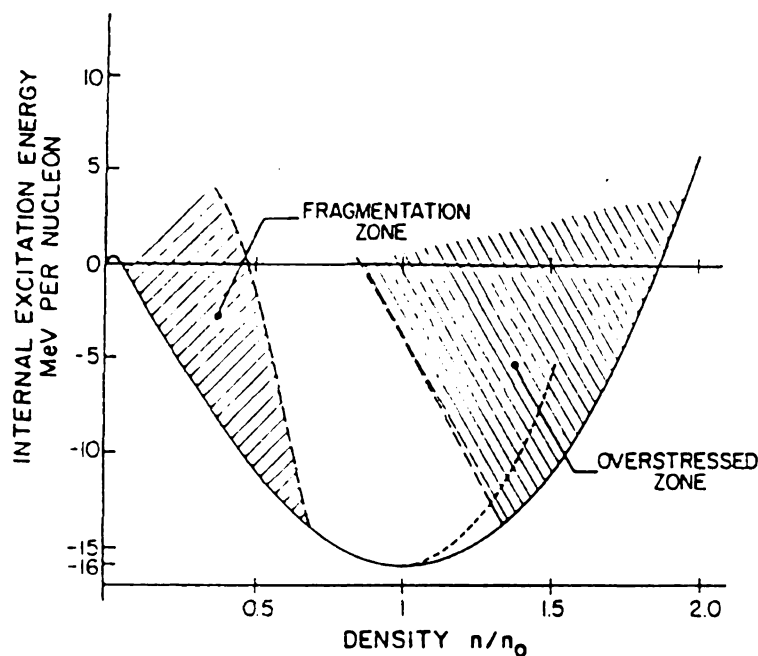


Figure I.3: EOS of nuclear matter. The solid line is an isentrope. The shaded region on the left is the spinodal region. The shaded region on the right corresponds to initial conditions that will lead to breakup after expansion. The dashed line suggests the trajectory of the compression stage of a reaction [Bert83].

## Statistical Properties of Nuclei: The Question of Temperature

In the previous discussion of phases of nuclear matter it has been tacitly assumed that statistical concepts can be applied to nuclear systems. However, nuclear interactions produce systems that contain fewer than 500 particles (the experiments described in this particular work consider systems of approximately 100 nucleons). The relaxation time of these nuclear systems is of the same order of magnitude as the duration of the interaction. Therefore, the simplifying assumptions of infinite matter and thermal equilibrium can not necessarily be applied. One method of probing the statistical

nat

du

me

**E**

Du

sho

sta

em

exp

sev

be

frag

esti

sou

**F**

At

em

con

safe

is i

will

hea

nature of thermalized nuclear systems is to study the apparent temperatures formed during the course of an interaction. If a true equilibrium has been achieved, all methods of measuring the temperature should yield similar values.

## E The Density of Nuclear Matter

During the course of a nuclear reaction, the temperature and density of the system should vary. One expects that the hottest and most dense period will be at the initial stages of the reaction. As the system equilibrates, it will expand and cool through emission of energetic particles. At some point during this expansion, a *freeze-out* is expected. At this point the expansion will cease, and the system will contract into several droplets or fragments. The kinetic energy dissipated in the reaction shall be converted into potential energy which manifests itself as a set of less well bound fragments. This freeze-out process is expected to occur at a specific density. An estimate of this density can be made by determining the dimensions and mass of the source of fragments.

## F The Transition from Sequential Decay to Multi-fragmentation

At low excitation energies, a heated nuclear system is able to de-excite through the emission of gamma rays. The time-scale for electro-magnetic interaction is large compared to the nuclear time-scale, and for these emissions the nuclear system can safely be assumed to have reached a thermal equilibrium. As the excitation energy is increased, channels open for the emission of neutrons and protons. These decays will be favored over the gamma emitting channels due to their shorter lifetimes. For heavy nuclei fission channels may also be open. For these energies the assumption of

th  
Fo  
lo  
Th  
br  
is  
is  
en  
Fo  
co  
G  
Th  
de  
de  
ter  
th  
we  
ha  
de  
pa  
sp  
als  
of  
de

thermal equilibrium still holds. This form of de-excitation is analogous to evaporation. For higher excitation energies this slow equilibrium process of nucleon emission is no longer sufficiently rapid to dissipate the excitation energy of the expanding system. The system reaches a region of mechanical instability. The internal energy is expended breaking nuclear bonds within the nucleus itself. This form of rapid de-excitation is known as *simultaneous multi-fragmentation*. It is a disassembly mechanism that is qualitatively different than the thermal emission of particles. For even higher energies, the internal temperature of the system should rise above a critical value. For such systems the distinction between the differing phases is lost. The system will completely vaporize.

## G Organization of the Thesis

This thesis addresses the main issues raised in the introduction. Specifically, do nuclear systems attain a thermal equilibrium during the course of a reaction, at what density does the nuclear freeze-out occur, and can nuclear matter be understood in terms of phases? The first question is addressed in chapter II through a study of the temperatures attained during the course of nuclear interactions. Temperatures were measured through a study of the distribution of excited states of fragments that had been emitted from the decaying systems. The excited state distribution was determined through the measurement of the correlation functions of light-charged particles. The correlation functions contain peaks at the relative energies that correspond to the particle unstable excited states of heavier nuclei. The second question is also addressed in chapter II. The same set of data is analyzed to determine the sizes of the sources that emit light fragments. From estimates of the source sizes one can determine the freeze-out density.

T

locat

addr

while

a glo

cours

the c

a hot

evide

sugg

to a

T

chap

the b

Thes

sent

first

detai

analy

raw c

The question of whether a multi-fragment reaction mechanism exists and the location of the transition point where it becomes the dominant form of decay is addressed in chapters III and IV. Chapter III reviews efforts by other research groups while chapter IV details the results of a study performed at MSU. This study employs a global event shape analysis to search for evidence of decays that occur early in the course of the reaction. The existence of such decays suggests a large time scale for the disassembly process which indicates that the decaying nuclear system behaves as a hot compressible liquid drop as modeled by Baym et al. [Baym71]. A failure to find evidence of early decays that dissipate large amounts of excitation energy is taken to suggest that the reaction occurs simultaneously, which indicates that the transition to a rapid decay mechanism has taken place.

The final chapter of the thesis reiterates the major conclusions reached within chapters II and IV. The technical details of the experimental detection systems and the basic procedures employed to analyze the raw data are detailed in the appendices. These sections address points which are crucial to this analysis, but would not be essential to another experimenter doing similar studies with a different apparatus. The first appendix describes the physical features of the detectors; the second appendix details how the energy calibrations were determined; and the third outlines the basic analysis procedures that were employed to extract the particle identification from the raw data.

# Chapter II

## Two Particle Correlations from 500 p+Ag and p+Be

### A Introduction and Experimental Justification

#### 1 Background

Intermediate energy heavy-ion collisions create short lived nuclear systems which contain a finite number of particles. These systems are sufficiently ephemeral that one can reasonably question whether it is possible to consider equilibrium quantities such as temperature, density, entropy, or pressure. Simple models of nuclear reactions at these energies predict that the incident energy of the projectile will be converted into center of mass motion and excitation energy of the fused system. The system will thermalize, expand, and decay. The disassembly of the system is considered to be a process which can be described as *freeze-out*. Whether this freeze-out occurs at a characteristic density or temperature is currently an open question. Attempts to measure the nuclear temperature and density at freeze-out can lead to a better understanding of nuclear matter.

The  
estat  
the i  
rang  
is th  
a sch  
port  
The  
and t  
the t  
to co  
veloc

Th  
sourc  
It is u  
sectio  
spectr  
emissi  
velocit  
of a g  
the Co  
param  
sourc  
peratu

## 2 The Fireball Model

The *fireball model* is a simple model for nuclear collisions [West76], which assumes the establishment of a thermal equilibrium. It has been applied successfully to describe the inclusive cross-sections of fragments emitted from nuclear collisions in the energy range from 20 to 200 MeV/nucleon [Jaca83]. The primary consideration of this model is the geometry of the system for a given nuclear reaction. Figure II.1 provides a schematic view of the evolution of a reaction as considered in this model. The portion of the projectile that overlaps with the target is considered to form a fireball. The velocity of this fireball can be determined from the incident energy of the beam and the relative weights of the projectile and target contributions. The portions of the target and the projectile that did not overlap during the reaction are considered to continue in their original trajectories relatively unchanged by the collision. Their velocities are slightly modified, and some heating occurs.

This model has been applied to experimental data through the use of moving source fits. This has become a standard technique in the analysis of inclusive data. It is used for the extraction of source velocities, temperatures, and production cross-sections [Jaca83, Jaca87, Wada89]. Typically, one considers the detected fragment spectra to be formed by the superposition of three Maxwellians that correspond to emission from three distinct thermal sources. These sources each have a characteristic velocity and temperature. The emission is assumed to be isotropic in the rest frame of a given source. The energy spectrum is a Maxwellian; the peak corresponds to the Coulomb repulsion between the source and the emitted fragment, and the slope parameter is supposed to correspond to the temperature of the source. The three sources correspond to the projectile remnant (velocity approximately  $V_{beam}$ , low temperature), the interaction region (velocity approximately  $V_{beam}/2$ , high temperature),

PP

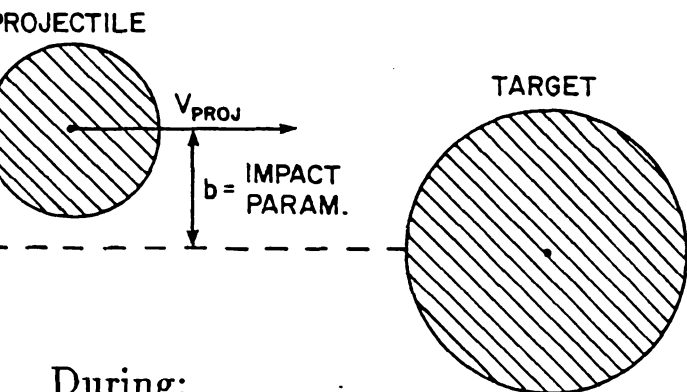


Fig

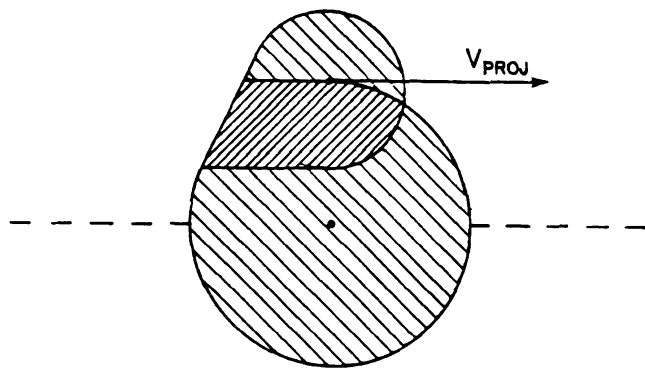
ball

## Heavy-Ion Induced Reactions

Before:



During:



After:

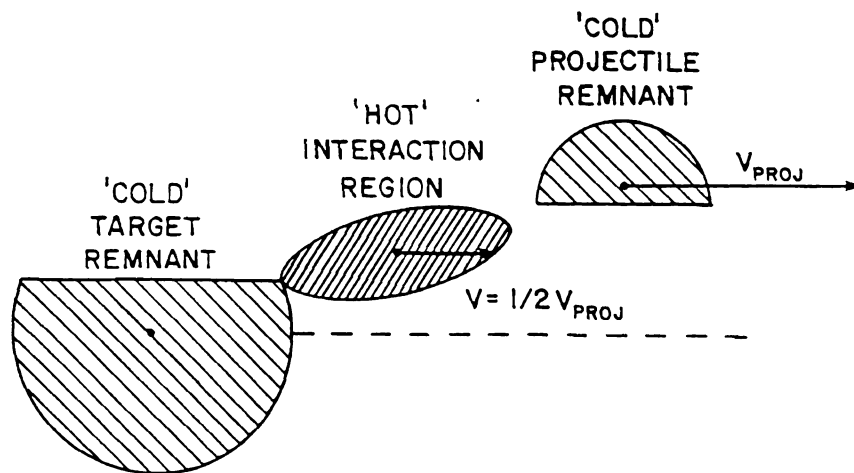


Figure II.1: A schematic diagram of the the reaction  $^{14}\text{N} + ^{98}\text{Ag}$  assuming the fireball model.

at

T

ex

tu

T

a

**3**

B

pr

be

dis

of

po

sim

If

are

the

pop

wit

nu

effi

(Li

tem

and the target remnant (almost at rest in the laboratory frame, low temperature). The slope parameters of the intermediate velocity source which are extracted from experimental data using these moving source fits are considered to be the temperatures of the thermalized regions. The slope parameters scale with incident energy. Therefore this observable seems to have the basic features that one would expect of a nuclear temperature.

### 3 Gamma Emitting States

**Basic Theory:** An alternate method of measuring the nuclear temperature was proposed by Morrissey [Morr84]. This method assumes that an equilibration has been established by the time of fragment production. Therefore, the excited state distributions of fragments produced from a thermal source should be representative of the temperature of the source.

In order to extract an estimate of the nuclear temperature, one may measure the population distribution of a set of excited states for a given fragment type. The simplest cases are those for which there are only a small number of low lying states. If one assumes that all of the fragments that are emitted from the thermal source are either in the ground state or in one of these low lying gamma emitting states, then a measure of the total number of fragments of a given type will yield the total population of all states, while a measure of the gamma rays detected in coincidence with these fragments will indicate the populations of various excited states of the nucleus. One corrects the raw measures of the gamma populations for the absolute efficiency of the detection system. For a nucleus with a single low-lying gamma state ( $\text{Li}^7$  or  $\text{Be}^7$  for example), one can use the Boltzmann two level formula to extract the temperature. The ratio between the population of the excited state and the ground

s

Y

s

t

T

M

P

C

t

fr

F

p

m

b

gi

co

to

M

87

be

pe

co

[L

state is given by:

$$\frac{n_{ex.}}{n_{g.s.}} = \frac{2j_{ex.} + 1}{2j_{g.s.} + 1} e^{-\Delta E/T_{eff}} \quad (II.1)$$

where  $n_{ex.}$  is the population of the excited state,  $n_{g.s.}$  is the population of the ground state,  $j_{ex.}$  and  $j_{g.s.}$  are the spins of the two states,  $\Delta E$  is the relative energy between the states, and  $T_{eff}$  is the effective temperature.

**Temperature Measurements:** A series of experiments was performed at the N.S.C.L. at MSU by Morrissey et al. [Morr84, Morr85, Morr86, Bloc86]. These experiments employed silicon telescopes to detect isotopes of lithium and beryllium. Gamma rays were detected with an array of NaI and bismuth-germanate scintillators. Gamma events were only recorded when in coincidence with a detected charged fragment. The temperatures that were extracted from these studies are displayed in Figure II.2. All of these temperatures are less than 1 MeV. For comparison, the slope parameters of the kinetic energy distributions for the lithium and beryllium fragments yielded temperature estimates of 15 MeV. There is clearly a large discrepancy between these two methods of estimating the nuclear temperature.

This method of determining temperatures was checked at low bombarding energies [Morr86, Lee90a, Lee90b] where nuclear reactions are known to proceed through compound nucleus formation. The compound system is assumed to be long-lived and to reach a state of equilibrium prior to de-excitation through fragment evaporation. Morrissey et al. studied the system  $^{14}N + ^{12}C$  for a range of incident energies from 87.5 to 350 MeV [Morr86]. The temperatures extracted for bombarding energies below 112 MeV using the populations of gamma emitting states agreed with the expected compound nucleus temperature. Above 112 MeV, the temperatures remained constant at 0.5 MeV. Lee et al. studied  $^{40}Ar + ^{12}C$  at 8, 10, and 12 MeV/nucleon [Lee90a, Lee90b]. Their results showed that the populations of excited states reflected



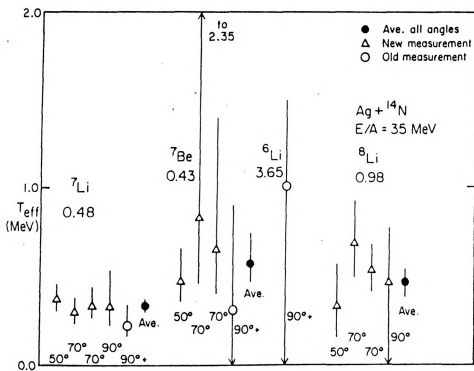


Figure II.2: The effective temperature extracted from a study of the populations of gamma emitting states [Morr84].

the temperature expected from the compound nucleus and were consistent with the temperature determined from the slope parameter of the kinetic energy distributions.

**Corrections for Sequential Feeding:** At intermediate energies, the temperatures that were extracted using the populations of the gamma-emitting states were completely different from those extracted from the slope parameters of the kinetic energy spectra [Morr84, Morr85, Bloc86]. This discrepancy was very troubling and several explanations were proposed [Boal84, Hahn87, Frie88]. The most widely accepted of these explanations was the suggestion that population distributions that were measured corresponded to final state distributions and not to the distributions that had been established at the time of nuclear freeze-out [Morr84, Poch85a]. The primordial distribution that had been established at the time of freeze-out contained highly excited fragments. For high temperature systems, many of these fragments would be in particle unstable states which would decay prior to detection. It is these decays of the highly excited resonances that distort the estimates of the nuclear temperature. When these resonances break apart, they preferentially feed the ground states of the lighter nuclei [Hahn87]. This causes the experimenter to overestimate the ground state population with respect to that of the gamma emitting excited states, and thus yields a low estimate for the temperature. Theoretical calculations for the effect that this sequential feeding would have upon the temperature measurements were performed using a quantum statistical model [Stöc83, Hahn87]. Figure II.3 displays the magnitude of this effect on the excited state ratios that had been used for the extraction of temperature. It is evident that for temperatures above 2 MeV the ratios of these gamma emitting states will not yield accurate measurements of the temperature. Hahn and Stöcker's reanalysis of the earlier data yielded temperature estimates from 4 to 8 MeV. This temperature range corresponds to the range of val-

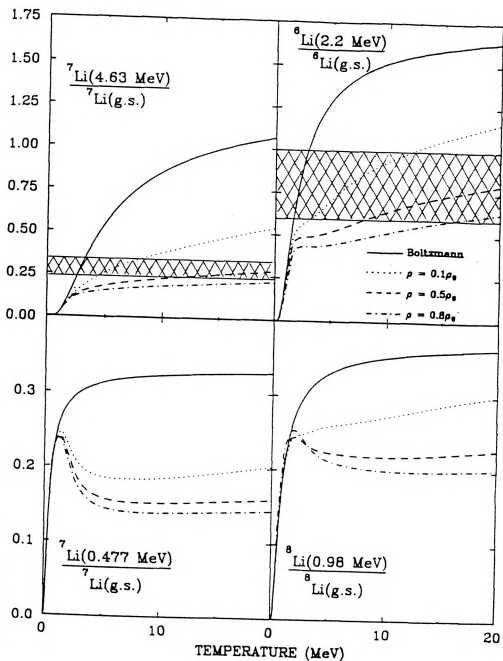


Figure II.3: The expected ratios between states as a function of temperature. In this model, the initial population of a state is given by its chemical potential, statistical weight, and the temperature. The calculation includes 40 stable and 500 unstable nuclear levels (up to mass 20). The excited states that had been populated in the initial phase then decay following the known branching ratios. The solid line corresponds to ratios predicted using the simple two level formula. The dotted, dashed, and dash-dot lines include sequential decay effects for three possible freeze-out densities. The shaded region indicates the experimentally observed ratios [Hahn87].

es for which the prediction assuming a  $0.1 \rho_0$  freeze-out density (dotted line) agrees with the experimental measurement (hashed region).

A study by Xu et al. increased the total number of gamma states used for the estimate of nuclear temperature [Xu86, Xu89]. The results were corrected for the feeding using the quantum statistical model of Stöcker. The effective temperature estimated from this study was 3-4 MeV, which was still well below the 15 MeV that was measured for the slope parameter of the kinetic energy distributions.

#### 4 Two-particle Correlations Review

A partial solution to the problem of feeding from higher states could be found by measuring the populations of the particle unstable states. These states are less susceptible to distortions because they are less likely to be populated by decays from heavier fragments. As a system decays, excitation energy is converted into kinetic energy and into mass (lighter fragments are less well bound). Thus a decay cascade will preferentially feed the lowest states of the daughter nuclei. The unstable state populations were studied through the detection of both decay particles at small relative momentum. This also had the added advantage that it allowed the experimenter to study the size of the emitting source.

##### The Nuclear Temperature

Measurements of the temperature were carried out using the populations of particle unstable states by several experimenters [Poch85a, Chit86, Chen87d, Bloc87, Galo87, Fox88, Sain88, Naya89]. These experiments studied asymmetric heavy-ion induced reactions and covered a range of beam energies from 35 to 94 MeV/nucleon. The earliest studies focused on the states accessible through detection of light charged particles (p, d, t,  $\alpha$ ) and found temperatures of around 5 MeV for the systems 35

MeV/nucleon N+Ag [Chit86, Chen87a, Chen87c, Chen87d, Fox88], 60 MeV/nucleon Ar+Au [Poch85a, Poch85c, Sain88], and 94 MeV/nucleon O+Au [Chen87d]. This work was complemented by a series of experiments using a technique for studying neutron emitting excited states [Deák87]. These experiments measured temperatures of 3 MeV for the 35 MeV/nucleon N+Ag system [Bloc87, Bloc88], and 1 MeV for the N+Ho system [Kiss87, Galo87]. Nayak et al. extended these to charged-particle studies to heavier fragments. However, the extracted temperatures remained in the 4 to 5 MeV range [Naya89].

Attempts to understand the extracted temperatures had little success. Chen et al. found no dependence of the temperature on the impact parameter as measured by the fission fragment folding angle [Chen87a]. Fox et al. found no dependence on the emission angle [Fox88]. Saint-Laurent et al. found no dependence on either the charged-particle multiplicity or the energy of the detected fragments [Sain88]. However, Deák et al. did find that the population distributions did depend on the energy of the detected particles [Deák89]. In their study, the ratio of fragments emitted in the excited state dropped as a function of the total energy of the measured particles, which indicates a lower temperature. With the exception of the last result, the measured temperatures seemed to be a constant of nature.

### The Sizes of Nuclear Systems

Hanbury-Brown and Twiss introduced a method for measuring the radii of distant stars through the use of photon-photon correlations [Hanb54]. This correlation technique was adapted to the physics of particles by Goldhaber [Gold60]. However, the method of Goldhaber had to be extended to the case of multiple particle emission, which is common in heavy-ion reactions. Kopylov and Podgoretskii proposed a definition for the correlation function that resolved the problems of multiple particle

emission [Kopy74]:

$$C(\mathbf{p}_1, \mathbf{p}_2) = \frac{1}{\sigma} \frac{\partial^6 \sigma}{\partial \mathbf{p}_1 \partial \mathbf{p}_2} / \frac{1}{\sigma} \frac{\partial^3 \sigma}{\partial \mathbf{p}_1} \frac{1}{\sigma} \frac{\partial^3 \sigma}{\partial \mathbf{p}_2} \quad (\text{II.2})$$

where  $\mathbf{p}_1$  and  $\mathbf{p}_2$  were the momenta of the two detected particles,  $\sigma$  was the total production cross-section for that type of particle,  $\partial^6 \sigma / \partial \mathbf{p}_1 \partial \mathbf{p}_2$  is the double differential cross-section for the production of two particles with momenta  $\mathbf{p}_1$  and  $\mathbf{p}_2$ , and  $\partial^3 \sigma / \partial \mathbf{p}_1$  and  $\partial^3 \sigma / \partial \mathbf{p}_2$  are the inclusive differential cross-sections of the production of a particle with momentum  $\mathbf{p}_1$  or  $\mathbf{p}_2$  respectively. This correlation function is then compared to predictions which assume emission from a source of a given size.

Several studies have been performed to measure the source radius and to determine on what it depends [Clit85, Poch86a, Kyan86, Poch87, Chen87a, Fox88, Sain88, DeYo89]. Many of these studies have also been used to address the question of nuclear temperature. Therefore, the systematic studies concerning source size focus on the same variables as the studies of temperature. The extracted radii have been explored as a function of energy of the detected particle pair [Poch86a, Chen87, Poch87], as a function of detection angle [Fox88], and as a function of associated charged particle multiplicity [Kyan86]. The source radii were found to decrease with total energy of the detected particle pair. This was presented as evidence that the collision initially formed a small *hot spot*. The first particles that were emitted from the collision would have come from this small region of space. As the system equilibrated and the remaining portion of the system was thermalized, the temperature of the source region dropped. Therefore, one expected the low energy region of the distribution to be dominated by the final stage of the reaction (a large, equilibrated source), while the high energy tails should come primarily from the initial stage (a small, hot spot) [Poch86a, Chen87, Poch87]. The detection angle was expected to influence whether the detected particle spectra were dominated by decays of the projectile, of the target, or of the interaction zone. Within the uncertainties of the measurements,



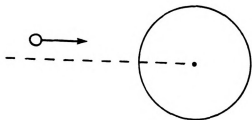
evidence was found to suggest that the extracted radii depended on the detection angle [Fox88]. The associated charged particle multiplicity is considered to be a measure of the impact parameter of an event. It was expected that the most central events should display the largest source radii, because these events created the largest interaction regions. This expectation was confirmed by Kyanowski et al. [Kyan86].

## Experimental Goals

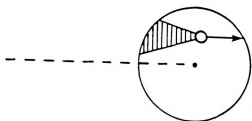
It is possible that the dynamics of the heavy-ion induced reaction had clouded the picture. The spectator regions of the target and the projectile should contribute to the observed fragments (refer to Figure II.1). The remnants should be cold, possibly giving a depressed estimate of the temperature of the interaction region. In addition, the impact parameter could not be measured, therefore the relative sizes of the target remnant, interaction region, and projectile remnant were not well defined. Therefore an experiment was proposed to study proton induced reactions, because reaction dynamics are less complicated. Figure II.4 displays a schematic diagram of a proton induced reaction. The systems chosen for study were 500 MeV p+Ag and 490 MeV N+Be. The p+Ag study complemented the 35 MeV/nucleon N+Ag studies that had been performed at MSU. The total energy of the nitrogen projectile (490 MeV) is almost equal to that of the proton (500 MeV), and the target nucleus was the same. Therefore, the target can potentially receive the same input excitation energy, however, the manner in which this energy is delivered to the system is different. The reaction dynamics should be less complicated in the proton induced case, because the projectile remnant (proton) would not be an additional source of energetic fragments. An intermediate velocity source would essentially be contiguous with the target remnant. The proton is expected to undergo several nucleon-nucleon interactions as it passes through the target nucleus. This will create a thermalized zone within the

### Proton Induced Reactions

Before:



During:



After:

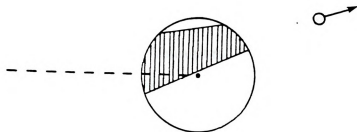


Fig. 11.4: A schematic diagram of the reaction  $p + {}^{98}\text{Ag}$ . The hashed area represents the thermalized region.

target as opposed to an independent thermalized source which has been proposed for the heavy-ion induced reactions. It was felt that the p+Ag study would provide a less complicated system, which would help resolve the questions that had been raised by the N+Ag studies.

The p+Be system would be even less complicated than the p+Ag system. As compared with the p+Ag system, the projectile would not complicate the emission spectra. For the Be system, however, the target remnant would be even simpler. One would not expect to have a large bulk of spectator matter in a system that contained only 10 nucleons. The small size of the system also reduces the effect that feeding from higher states will have upon the final fragment distributions. Additionally, the assumption of equilibrium seems absurd for a system with so few nucleons. One does not expect multiple interactions as the incident proton passes through the bulk of the target material, instead only a single collision is likely.

## Description of the Experiment

The experiment was performed in the Proton Hall of the Tri-University Meson Facility (TRIUMF), which is located in Vancouver, British Columbia. This laboratory contains a large room temperature cyclotron that accelerates  $H^-$  beams up to 500 MeV. The beam can be stripped within the cyclotron to create a proton beam, which is then extracted and focused down the beamlines in the Proton Hall. Alternatively, the beam can be stopped in a production target in order to create secondary meson beams, which are focused to experimental areas in the Meson Hall. This latter use of the beam is the primary function of the facility; the experimental proton program is run parasitically off of the meson program.

The detection apparatus was set up in the Simon Fraser University (SFU) 60"



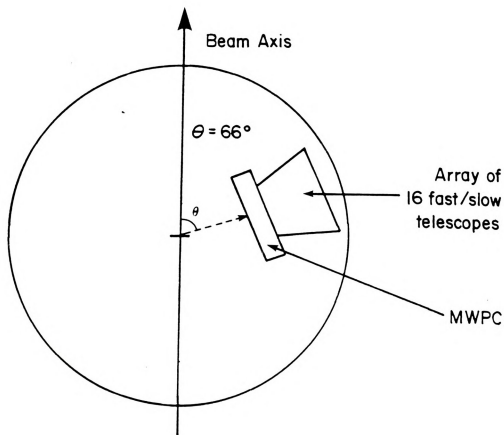
tering chamber. This chamber is located close to the cyclotron, and the vault walls between the accelerator and the experimental vault are thin by TRIUMF standards. The thin vault walls resulted in a high radiation background which did have an effect on the performance of the detection apparatus in this experiment. Beams of 504, 300 and 200 MeV protons were extracted. These beams were incident on targets of Ag, CH<sub>2</sub>, and CD<sub>2</sub>. The 300 and 200 MeV beams and the CH<sub>2</sub> and CD<sub>2</sub> targets were used exclusively for detector calibration.

The detector apparatus consisted of a close-packed array of phoswich detectors which was placed immediately behind a multi-wire proportional chamber (MWPC). The phoswichs provided particle identification and energy determination for light nuclear fragments while the MWPC provided information on the emission angles. Details concerning the dimensions, performance, and calibration of these detectors (phoswichs and MWPC) are given in the appendices. The central angle of the array was chosen to be 60°. A diagram of the experimental configuration is given in Figure II.5

## Extraction of Source Sizes

### Basic Method

For every pair of light particles (p, d, t, <sup>4</sup>He), a correlation function was generated. The correlation function was constructed by dividing the relative momentum spectrum for a given pair of light particles by a spectrum generated from random particle pairs. These random events were created by analyzing particles from different realizations. This method of generating the divisor for the correlation function calculation is superior to using the measured singles distributions (equation II.2) because it precludes the biases implicit in the requirement that two particles are detected in



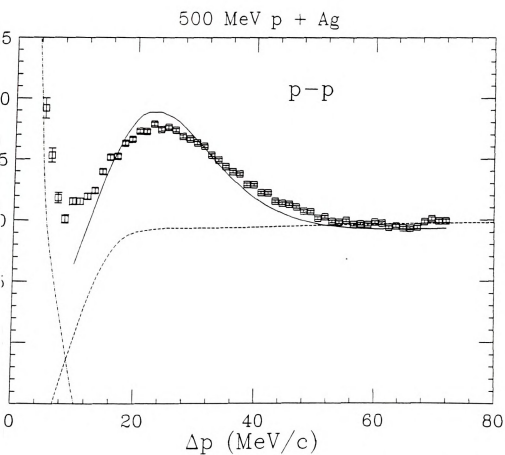
5: The diagram of the experimental setup for the study of two-particle correlations from p+Ag and p+Be.

idence in the detector array. For this analysis, 40 random pairs were generated for each real event. This minimized the contribution to the statistical error related to the random spectrum.

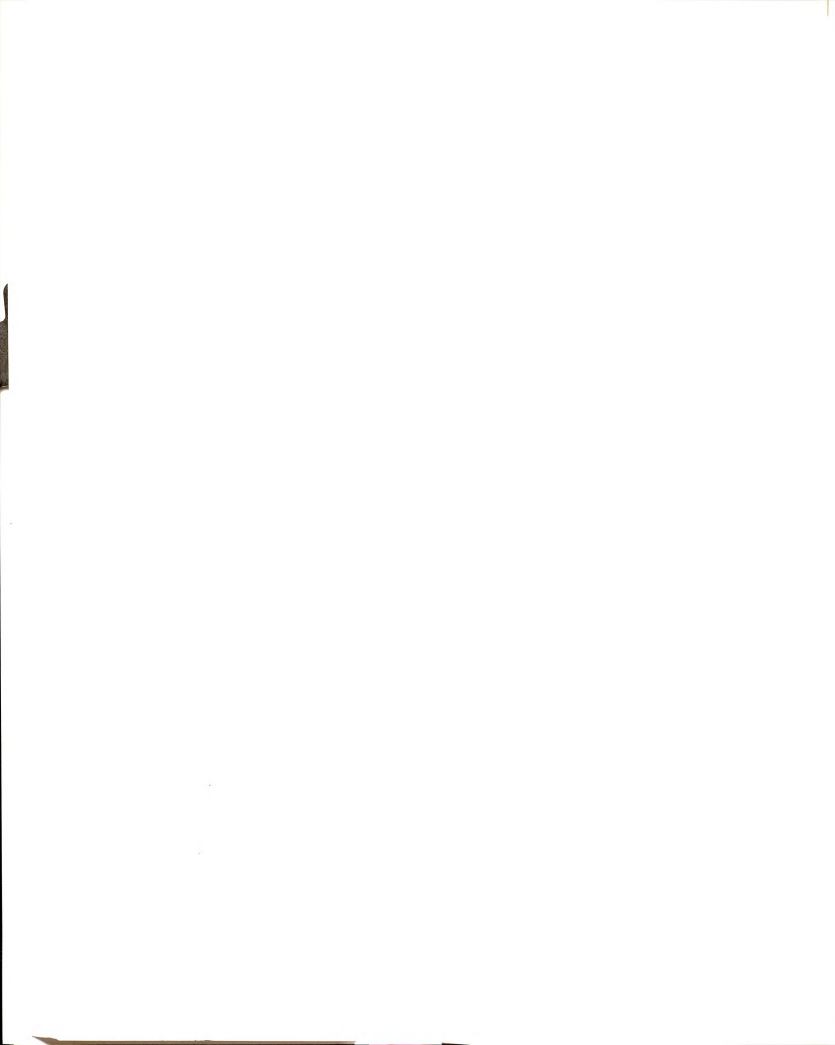
The extraction of source size was done by comparing the experimental correlation functions to predictions which were generated by a model that considered independent emission from a source region that is parameterized as a Gaussian in space and time. The source acts as an ensemble of independent emitters rather than as a single excited state [Boal86]. This model calculated the partial waves using both Coulomb and nuclear potentials. The nuclear phase shift data for a given particle pair were analyzed using a Woods-Saxon potential. The charge is assumed to be distributed uniformly within a sphere of a given radius. In this manner, expected correlation functions could be calculated for an arbitrary source radius. These predictions were compared to the experimental measurements of the correlation function. The estimated source radius was taken as the calculated correlation function that reproduced the experimental data.

## Source Sizes from $p+Ag$

**Proton-Proton:** The pair that was detected most frequently was proton-proton, therefore it is appropriate that this be the first correlation function discussed. Figure 6 displays the correlation function  $(R(\Delta P) + 1)$  for the  $p-p$  pair from the 500 MeV  $p+Ag$  system. In this analysis, a value of the correlation function equal to unity corresponds to uncorrelated emission. Values below unity represent anti-correlations, and values above unity are enhancements. One expects that the correlation function will drop to zero at small relative momentum, because two charged particles emitted close together in phase space will exhibit a strong repulsion due to the Coulomb interaction. The data presented in this work unfortunately demonstrate a sharp peak



The correlation function for proton-proton pairs from the 500 MeV p+Ag



relative momentum. This is due to a slight misalignment of the detector array. Allowed single particles to scatter between neighboring phoswich detectors, thus giving a genuine coincidence. An effort has been made to estimate this contamination (the dotdash line on Figure II.6). A Gaussian was fit to the contamination peak. The centroid was constrained to be at zero relative momentum and the width was determined by the precision of the detection apparatus. At large relative momentum, the correlation function is fixed at unity. A normalization constant is determined for each pair to ensure that the correlation function approaches unity. There should be no correlated or anti-correlated emission at large relative momentum because the nuclear fragments should be too widely separated in phase space to interact. At  $20 \text{ MeV}/c$ , there is a broad peak in the correlation function. This peak can be interpreted as an attractive  $s$ -wave nuclear interaction, or alternatively as the decay of  $^2\text{He}$ . The dashed curve represents the Coulomb contribution to the expected correlation function if one assumes emission from a source of radius  $9.0 \text{ Fm}$  [Boal86]. The solid curve includes the nuclear interactions and corresponds to emission from a source of radius  $11.8 \text{ Fm}$ , which was the radius for which the model best fits the experimental data.

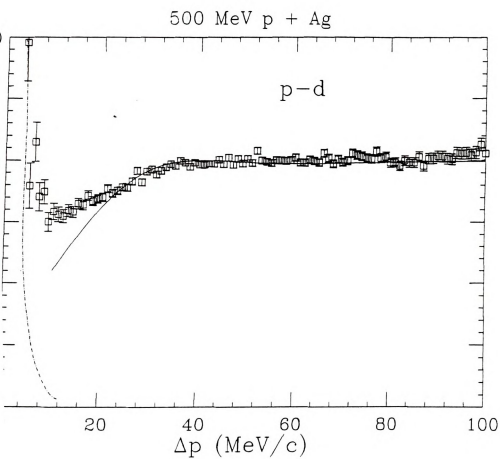
**p-Deuteron:** The proton-deuteron correlation does not contain any nuclear interactions. There is only the Coulomb repulsion that results in an anti-correlation at low relative momentum. Figure II.7 displays this correlation function. The dotdash line is an estimate of the contamination, and the solid curve is a prediction for emission from a source of radius  $11.8 \text{ Fm}$ . It has been suggested that the p-d correlation is the best for extracting a reliable estimate of the source size [Poch86b]. This is because the proton and the deuteron have different charge-to-mass ratios. This results in each particle receiving a different acceleration in the Coulomb field of the

target residue. The result of this distortion is an overestimate of the source

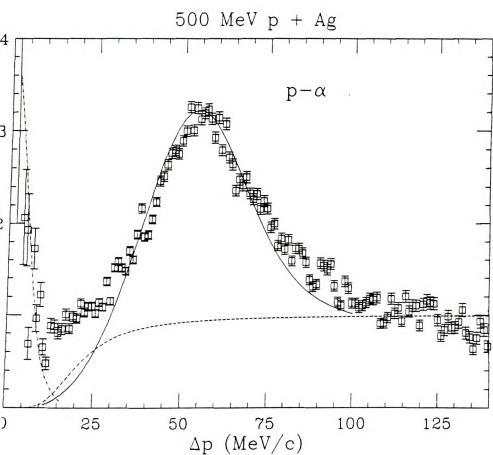
**n-Alpha:** The ground state of  ${}^5\text{Li}$  is not stable with respect to proton emission. Therefore there is a strong nuclear resonance in the p- $\alpha$  correlation function. Figure II.8 displays this correlation function. The nuclear resonance appears as a prominent peak at  $\Delta p$  of 55 MeV/c. The contamination is estimated by the dot-dash line, the Coulomb background is displayed for emission from a 9.0 Fm source (dotted line), and the predicted correlation based on a calculation that includes that interaction is shown by the solid line for emission from a 1.8 Fm source. Note that the predicted curves fail to account for the experimental data in the region  $\Delta p > 25$  MeV/c. There is an excess in the experimental correlation function. This 'peak' has been demonstrated to be associated with the partial detection of the  ${}^9\text{B}$  decay  ${}^9\text{B} \rightarrow p + \alpha + \alpha$  [Poch85b].

**n-Deuteron:** The deuteron-deuteron correlation function contains no evidence of nuclear resonances because excited states of  ${}^4\text{He}$  are stable with respect to deuteron emission. Therefore there is only the contribution related to the Coulomb correlation of independently emitted deuterons. Figure II.9 displays the measured correlation function, the estimate of the contamination (dot-dash line), and the prediction assuming emission from a 9.4 Fm source. Chitwood et al. noted that the correlation function could not be associated with the decay of unstable resonances because the extracted radius was substantially larger than that estimated for the  ${}^9\text{B}$  decay [Chit85].

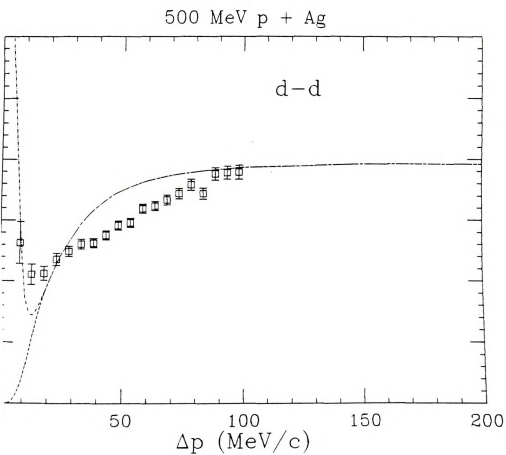
**n-Alpha:** The deuteron-alpha correlation contains several peaks that are associated with particle unstable states of  ${}^6\text{Li}$ . Figure II.10 displays this correlation



The correlation function for proton-deuteron pairs from the 500 MeV



The correlation function for proton-alpha pairs from the 500 MeV p+Ag



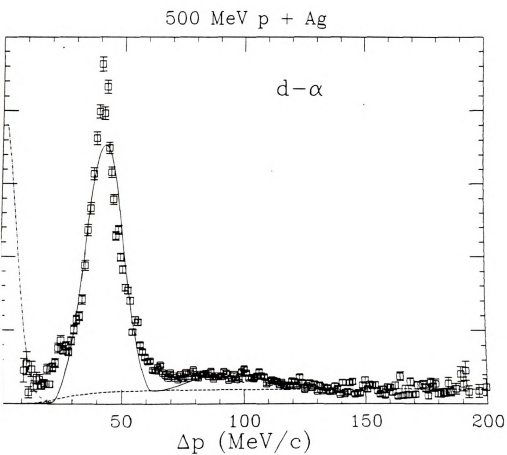
The correlation function for deuteron-deuteron pairs from the 500 MeV p + Ag reaction.

Also displayed are an estimate of the contamination (dot-dash curve), assuming only Coulomb interactions (dashed curve, 9.0 Fm source radius), prediction including nuclear interactions (solid line, 2.0 Fm source size). The peak at 42 MeV/c corresponds to the 2.186 MeV state of  ${}^6\text{Li}$ , while the broad peak at 90 MeV/c corresponds to two unresolved states, one at 4.31 MeV and one at 5.65 MeV.

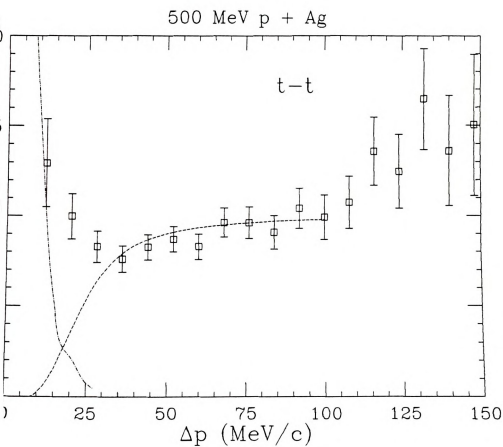
**Triton:** The triton-triton pair has no measurable nuclear resonances. As with p-p and d-d, the correlation function (Figure II.11) displays only the valley at zero relative momentum which is due to the Coulomb interaction. The prediction is shown for a 11 Fm source radius (dashed line).

### Source Sizes from p+Be

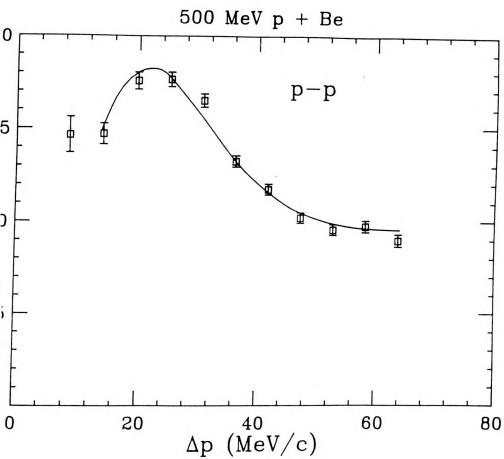
The p+Be reaction should create a system whose dimensions are smaller than that of the p+Ag reaction because there should be fewer nucleons involved. Therefore, the source radii extracted from the p+Be data should be different from those discussed above. Figures II.12 to II.17 display the correlation functions that were extracted from the p+Be data for the same six particle pairs that have been discussed for the p+Ag system. The basic features are similar to the p+Ag case for all of the pairs considered. For all six plots, the solid line corresponds to the calculation from a source of a given radius. The radii for which the calculation best fits the data are: 3.3 Fm for the p-p case, 12.2 Fm for the p-d case, 1.6 Fm for the p- $\alpha$  case, 1.9 Fm for the d-d case, 1.9 Fm for the d- $\alpha$  case, and 10 Fm for the t-t case.



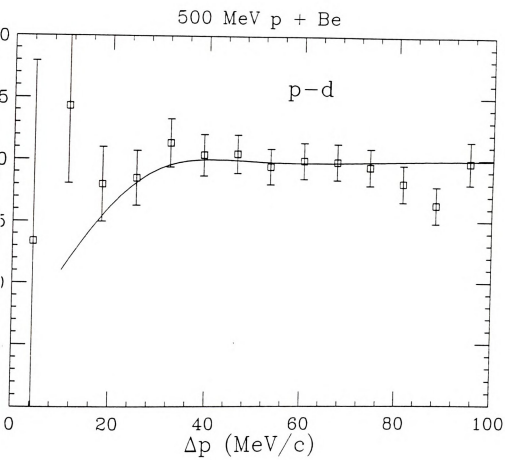
The correlation function for deuteron-alpha pairs from the 500 MeV p + Ag reaction.



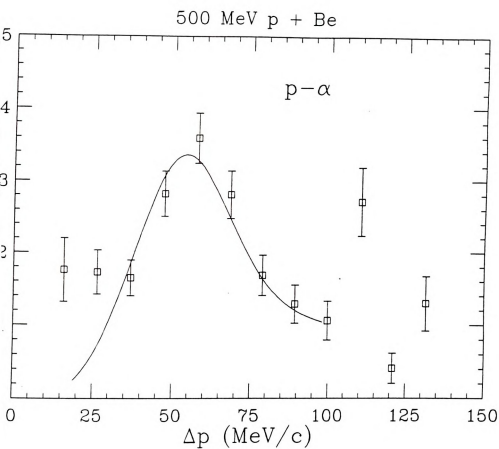
The correlation function for triton-triton pairs from the 500 MeV p+Ag



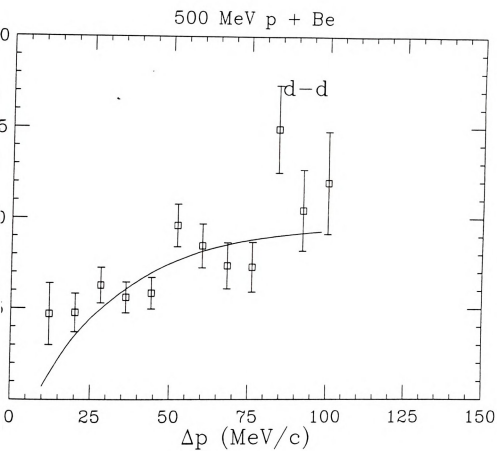
2: The correlation function for proton-proton pairs from the 500 MeV p + Be reaction.



: The correlation function for proton-deuteron pairs from the 500 MeV n.



: The correlation function for proton-alpha pairs from the 500 MeV p+Be



: The correlation function for deuteron-deuteron pairs from the 500 MeV p + Be reaction.

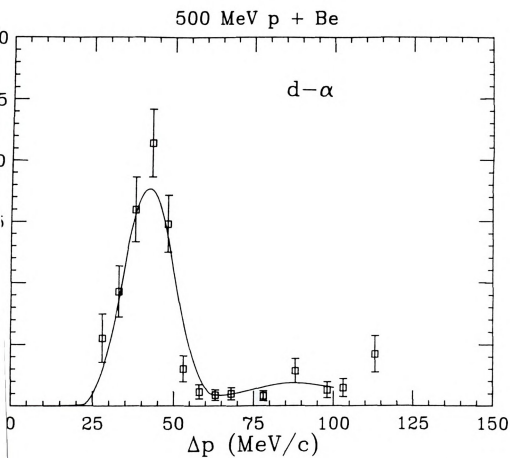
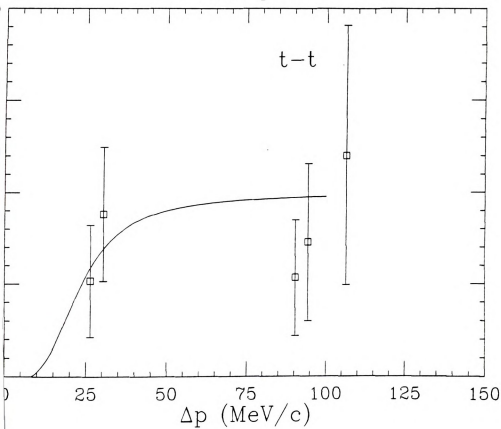


Fig. 3: The correlation function for deuteron-alpha pairs from the 500 MeV p + Be reaction.



500 MeV p + Be

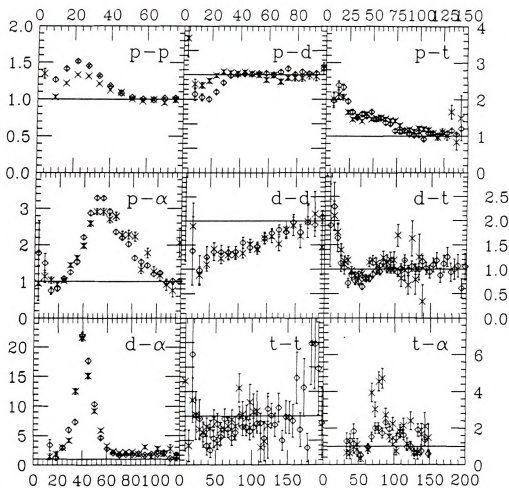


The correlation function for triton-triton pairs from the 500 MeV p+Be

## The Effect of Energy Cuts on the Extracted Source Radii

been proposed that by placing cuts on the total energy of the two particles in one can select upon the class of events [Poch86a, Chit86]. It is argued that the energy pairs should come predominantly from the hottest reactions. Evidence is presented that suggests that the source radius extracted from higher energy pairs is smaller than that extracted from low energy pairs [Poch86a, Chit86, Chen87]. It has been put forth to suggest that thermal equilibrium has not been established in these reactions.

Correlation functions for the  $p+Ag$  system have been analyzed in this manner in an effort to confirm these results. High and low total energy gates were set for each pair type. Figure II.18 displays several different particle pairs each with this total energy gate. The data from the high energy gate are represented by diamonds on each plot, while the data for the low energy portion of the pair are represented by the crosses. There is no significant difference between the high and low energy data for any pair except  $p-p$  and  $p-d$ . For the  $p-p$  pair, the high energy data (diamonds) show a stronger correlation than the low energy data (crosses). Since  $p-p$  is a pair which contains a nuclear resonance, a large value of the correlation function corresponds to a small source radius. For the  $p-d$  pair, the high energy data show a stronger anti-correlation near zero relative momentum. Since  $p-d$  has no nuclear resonances, the size of the source is related to the magnitude of the anti-correlation. A larger valley corresponds to a smaller source. Thus both the  $p-p$  and  $p-d$  pairs suggest a smaller source size for the high energy selection. For the other pairs, the data for the high and low energies are indistinguishable. This suggests that protons and deuterons are emitted early during the course of the reaction. They may be emitted from the hot dense interaction region that



18: The correlation functions for a variety of particle pairs from the 500 MeV fem. The diamonds correspond to events selected on high total energy for particles of the pair, while the crosses are data selected on low total energy.

created at the start of the event. This may be considered as emission prior to thermalization of the entire system. The more complex particles, on the other hand, show no influence of total energy on source size. This may indicate that they are all emitted at the final stage of the reaction, after complete equilibration of the source.

## Summary of Extracted Source Sizes

The source sizes that were extracted are summarized in Table II.1. In addition, results from an experiment performed earlier with the same detection system are presented for the 35 MeV/nucleon N+Ag system [Fox88]. The most striking feature of this data is the wide range of values extracted. The pairs that contain resonant states (p-p, p- $\alpha$ , and d- $\alpha$ ) all exhibit extremely small source radii for both the p+Ag and the p+Be system. The pairs which contain no resonances (p-d, d-d, t-t) all yield large estimates for the source radius. These radii range from 9 to 12 Fm. This suggests that the pairs that contain nuclear resonances do not accurately measure the size of the thermalized system. Instead these pairs are dominated by the decay of the emitted fragments. The radius measured for these pairs is the radius of the parent fragment and not the radius of the system that emitted that fragment. A simple estimate of a nuclear radius is given by:

$$R = 1.12A^{1/3} \quad (\text{II.3})$$

where  $A$  is the mass of the nucleus. Using this equation, one notes that the nuclear radius for  ${}^5\text{Li}$  is 1.9 Fm which compares remarkably well with the radius values extracted from the p- $\alpha$  pair. The nuclear radius for  ${}^6\text{Li}$  is 2.0 Fm, which agrees with the values extracted from the d- $\alpha$  pair. The p-p pair does not compare well with an estimate for a mass 2 nucleus, but one does not expect  ${}^2\text{He}$  to be well-bound.

The freeze-out density can be estimated from the measured source radius from the pairs without resonances. These pairs are not influenced by the decays of particles

Table II.1: A summary of the source radii extracted from the 500 MeV p+Ag and p+Be systems. The results are compared to an earlier study of 35 MeV/nucleon N+Ag [Fox88].

Pair	500 MeV p+Ag	500 meV p+Be	35 MeV/nucleon N+Ag
p-p	$4.0 \pm 0.5$	$3.3 \pm 1.1$	4.3-4.8
p-d	$11.8 \pm 1.6$	$12.2 \pm 2.6$	
p- $\alpha$	$1.8 \pm 1.2$	$1.6 \pm 1.8$	
d-d	$9.4 \pm 2.1$	$9 \pm 5$	6.7-8.8
d- $\alpha$	$2.0 \pm 1.1$	$1.9 \pm 1.2$	4.9-5.2
t-t	$11 \pm 8$	$10 \pm 6$	

emitted in highly excited states and therefore give a truer estimate of the size of the nuclear source. For the case of 500 MeV p+Ag, the source radius, as estimated from the p-d, d-d, and t-t pairs, ranges from 9 to 12 Fm. The radius of a silver nucleus at rest is 5.2 Fm. If one assumes that the thermalized system contains the same number of nucleons as the target, one estimates the freeze-out density to range from 0.19 to 0.08  $\rho_0$ , where  $\rho_0$  is normal nuclear density. Of these three estimates of the source size, the values from the d-d correlation function is the most reliable. The p-d pair will lead to an overestimate of the source radius due to the unequal acceleration of the two particles in the Coulomb field of the emitting source [Poch86b], and the uncertainty on the t-t measurement is extremely large due to the low counting rate. Therefore, the best estimate of the freeze out density can be attained using the radius value extracted from the d-d pair, which yields  $\rho_{freezeout} = 0.17^{+0.17}_{-0.08}\rho_0$ .

## D Extraction of Nuclear Temperatures

### 1 Basic Method

The populations of particle unstable excited states are studied through the detection of the two daughter fragments that are associated with the breakup of the resonance.

These nuclear resonance states can be observed as peaks in the relative energy spectrum for a given pair of light particles. By measuring the counts above background in these peaks and correcting for detection efficiency one can determine the excited state populations and then extract the effective temperature.

The various states that can be studied with this detector apparatus are listed in Table II.2. For this analysis however, we will consider only pairs that contain multiple breakup channels for a given parent fragment. This allows one to study the extracted temperature between two states for which the detection biases are the same. To make comparisons between the populations of particle unstable states (detected with the array) and the ground state populations (measured using silicon telescopes) requires many corrections to ensure that no experimental biases affect the final result. Additionally, comparisons between particle-unstable states and stable states are complicated by differential feeding. Considering only the highly excited particle-unstable states facilitates the analysis and reduces potential systematic errors because the same detection system with the same experimental biases has been used to measure all states. A measurement of the ground state would require only a single particle to be detected by the array. The requirement of only a single hit may sample a different class of events than the multiple hit requirement necessary to study unstable resonances.

## **2 Backgrounds for Independent Emission**

The relative momentum spectra contain events that are associated with the decay of unstable resonances as well as events that are random coincidences between two particles which were independently emitted from the same thermalized system. The random background must be subtracted from the spectra in order to get estimates of the contribution associated with the decay of particle unstable excited states. An

Table II.2: A list of all of the particle unstable states that could be studied with this detector system.

Pair	Parent	Energy MeV	$J^\pi$	$\Delta p$ MeV/c	Reference
p-p	$^2\text{He}$			22	
p-d	$^3\text{He}$				
p-t	$^4\text{He}$	20.1	$0^+$	20.47	[Fiar73]
p-t	$^4\text{He}$	21.1	$0^-$	42.62	[Fiar73]
p-t	$^4\text{He}$	22.1	$2^-$	56.69	[Fiar73]
$p\text{-}^3\text{He}$	$^4\text{Li}$	24.5	$2^-$	81.04	[Fiar73]
$p\text{-}^4\text{He}$	$^5\text{Li}$	g.s.	$3/2^-$	54.18	[Ajze88]
$p\text{-}^4\text{He}$	$^5\text{Li}$	16.66	$3/2^+$	166.6	[Ajze88]
$p\text{-}^4\text{He}$	$^5\text{Li}$	18	$(1/2^+)$	172.6	[Ajze88]
$p\text{-}^4\text{He}$	$^5\text{Li}$	20.0	$(3/2, 5/2)^+$	181	[Ajze88]
d-d	$^4\text{He}$	26.4	$2^-$	69.6	[Fiar73]
d-t	$^5\text{He}$	16.76	$3/2^+$	11.58	[Ajze88]
d-t	$^5\text{He}$	19.8	$(3/2, 5/2)^+$	83.25	[Ajze88]
$d\text{-}^3\text{He}$	$^5\text{Li}$	16.66	$3/2^+$	24	[Ajze88]
$d\text{-}^4\text{He}$	$^6\text{Li}$	2.186	$3^+$	42.05	[Ajze88]
$d\text{-}^4\text{He}$	$^6\text{Li}$	4.31	$2^+$	83.99	[Ajze88]
$d\text{-}^4\text{He}$	$^6\text{Li}$	5.65	$1^+$	98.43	[Ajze88]
t-t	$^6\text{He}$	13.6		60.3	[Ajze88]
$t\text{-}^3\text{He}$	$^6\text{Li}$	21.0	$2^-$	120.6	[Ajze88]
$t\text{-}^3\text{He}$	$^6\text{Li}$	21.5	$0^-$	126.2	[Ajze88]
$t\text{-}^3\text{He}$	$^6\text{Li}$	25	$4^-$	160	[Ajze88]
$t\text{-}^3\text{He}$	$^6\text{Li}$	26.6	$3^-$	175	[Ajze88]
$t\text{-}^4\text{He}$	$^7\text{Li}$	4.630	$7/2^-$	83.06	[Ajze88]
$t\text{-}^4\text{He}$	$^7\text{Li}$	6.68	$5/2^-$	116.0	[Ajze88]
$t\text{-}^4\text{He}$	$^7\text{Li}$	7.456	$5/2^-$	126.2	[Ajze88]
$t\text{-}^4\text{He}$	$^7\text{Li}$	9.67	$7/2^-$	151.6	[Ajze88]
$^3\text{He}\text{-}^3\text{He}$	$^6\text{Be}$	23	$4^-$	179	[Ajze88]
$^3\text{He}\text{-}^3\text{He}$	$^6\text{Be}$	26	$2^-$	201	[Ajze88]
$^3\text{He}\text{-}^3\text{He}$	$^6\text{Be}$	27	$3^-$	208	[Ajze88]
$^3\text{He}\text{-}^4\text{He}$	$^7\text{Be}$	4.57	$7/2^-$	97.6	[Ajze88]
$^3\text{He}\text{-}^4\text{He}$	$^7\text{Be}$	6.73	$5/2^-$	128.2	[Ajze88]
$^3\text{He}\text{-}^4\text{He}$	$^7\text{Be}$	9.27	$7/2^-$	157	[Ajze88]
$^3\text{He}\text{-}^4\text{He}$	$^7\text{Be}$	9.9	$3/2^-$	163	[Ajze88]
$^3\text{He}\text{-}^4\text{He}$	$^7\text{Be}$	11.01	$3/2^-$	173	[Ajze88]
$^4\text{He}\text{-}^4\text{He}$	$^8\text{Be}$	g.s.	$0^+$	18.5	[Ajze88]
$^4\text{He}\text{-}^4\text{He}$	$^8\text{Be}$	2.94	$2^+$	106.3	[Ajze88]
$^4\text{He}\text{-}^4\text{He}$	$^8\text{Be}$	11.4	$4^+$	207	[Ajze88]

estimate of this independent background was made using the Koonin model [Koon77] from which the *Coulomb only* correlation function predictions were generated. The source radius used for these estimates of the independent background was 9.0 Fm. This value came from the d-d correlation. There is some reason to believe that the p-d correlation may yield a slight overestimate of the source size [Poch86b], and the uncertainty on the t-t measurement was extremely large. The value extracted from the d-d correlation was therefore deemed to be the most reliable.

### 3 Efficiency Calculations

The efficiency of the detector array varies as a function of the breakup channel and the relative momentum between the daughters. This efficiency function must be calculated before the yields of the particle unstable states can be determined. In general, the efficiency function is zero at small relative momentum, because in this case the two decay products will both be focused into the same phoswich element. The efficiency is also small for high relative momentum, because in this case the opening angle between the two fragments will be larger than the acceptance of the detector array. The efficiency of the detection system used in these experiments was optimized for relative momenta between 20 MeV/c and 100 MeV/c which corresponds to the locations of the most important resonances.

In addition to the geometric efficiency, the detection efficiency must also be considered. For the phoswich detectors this was not a problem. The efficiency of the MWPC, however, drops as a function of energy for p, d, and t. Figure II.19 displays the detection efficiency of the MWPC as a function of particle type and energy.

The overall efficiency functions were determined using a Monte Carlo program. The inputs to the program included the detector geometry, the detection efficiency of the MWPC, and the kinetic energy spectrum of the parent particle. The program

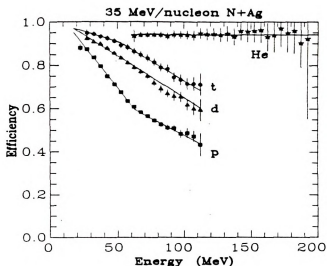


Figure II.19: The detection efficiency of the MWPC

assumed that the excited state distribution was independent of the kinetic energy of the emitted fragment. A simulation was run in which parent particles were directed at random locations on the array. The fragments decayed in flight with a given separation energy. An evaluation was then made to determine whether both of the daughter particles would have been detected and properly identified. Events were considered failures if: either of the two particles failed to hit an element of the array, both daughters hit the same phoswich element, the MWPC efficiency excluded either fragments, or a fragment hit an edge between two detectors. The efficiency was the ratio of successful detections to total events. Figure II.20 displays the overall efficiency function for the p-t, d-t, d- $\alpha$ , and the t- $\alpha$  pairs.

#### 4 Populations of Particle Unstable States

An unstable nuclear resonance will decay through particle emission. These will cause emission lines with relatively discrete values in the relative momentum spectra. The width of these peaks are broadened by the experimental detection resolution. The resolution is affected by uncertainties in both energy and emission angle which causes

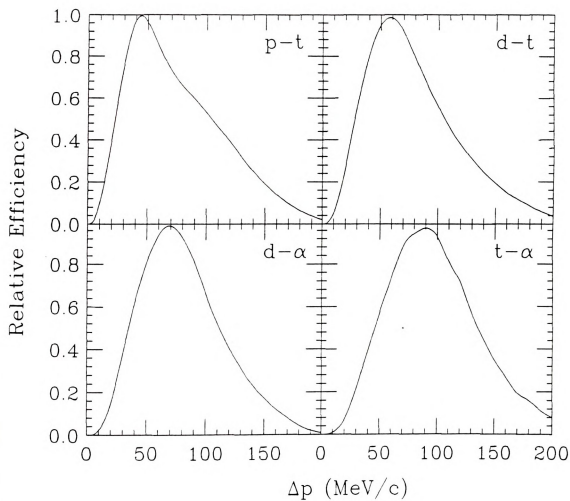


Figure 11.20: The relative detection efficiency for four different particle pairs. The peak efficiency has been normalized to unity for each pair.

the peak width to increase. An estimate of the background independent emission is subtracted from the measured relative momentum spectrum. Peaks are fitted to the remaining resonant decay contribution, and a correction is made for detector efficiency as a function of relative momentum. One then has an estimate of the relative population for various particle unstable excited states from which an effective temperature can be extracted using equation II.1.

**Proton-Triton:** The method for determining the relative populations of states is illustrated in Figure II.21. The top portion of the figure displays the relative momentum spectrum for p-t pairs. The estimated independent contribution is also displayed. The portion above this background can be associated with the contribution from the decay of unstable states of  ${}^4\text{He}$ . The lower portion of the figure displays only the counts above background. Three gaussians are fit to the distribution. These three gaussians represent the first three excited states of  ${}^4\text{He}$ : the 20.1 MeV state, the 21.1 MeV state, and the 22.1 MeV state. The centroids of the gaussians were constrained by the energy of the states. The widths were determined by the detector resolution and in a few cases by the known width of the state (only for a few very broad states). The fitting routine varied only the relative heights of the various peaks. The dotted curves in the lower part of the figure display the contributions from the individual gaussians, while the solid curve is the sum of all three. For this pair, the extracted temperature is  $5.6 \pm 1$  MeV. The uncertainty is estimated from the fitting routine and does not consider possible systematic errors.

**Deuteron-Triton:** The d-t pair contains peaks associated with the decays of  ${}^5\text{He}$  from the 16.76 and 19.8 MeV states. The upper portion of Figure II.22 displays the relative momentum spectrum and an estimate of the independent background.

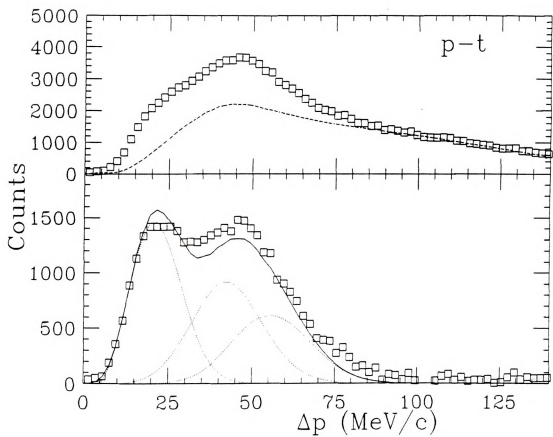


Figure II.21: The relative momentum spectrum for proton-triton pairs (squares) and an estimate of the independent background (dashed line). The lower portion displays the counts above background (squares) and fits to the individual peaks (dotted and solid lines).

The lower portion of the figure displays the counts above background and fits to the excited states of  ${}^6\text{He}$ . The temperature extracted from the ratio of these two peaks is  $4.8 \pm 1$  MeV.

**Deuteron-Alpha:** The d- $\alpha$  spectrum contains peaks associated with the 2.186, 4.31, and 5.65 MeV states of  ${}^6\text{Li}$ . The lowest peak appears well above the background in the upper portion of Figure II.23. The two higher energy states are broad and are not resolved as individual peaks with this detection system. The temperature extracted from the ratio of these states is  $3.5 \pm 1$  MeV.

**Triton-Alpha:** There are four states which contribute to the t- $\alpha$  relative momentum spectrum. The 4.63, 6.68 (which is quite broad), 7.46, and 9.67 MeV states. The analysis of this state is further complicated because there are relatively poor statistics for this particle pair as can be seen in Figure II.24. The relative heights of the highest three peaks are not well defined. The extracted temperature is  $3 \pm 2$  MeV.

## 5 The Nuclear Temperature

A summary of the temperatures extracted in this study is contained in Table II.3. The errors quoted correspond to the uncertainty in fitting the populations of the individual states above the estimated background. Therefore, it is essentially a statistical error and should not be considered an estimate of the potential systematic error. This analysis is susceptible to substantial systematic errors. The main effect that would introduce a systematic error is the manner in which the independent background is estimated. The background affects the relative heights of the peaks and therefore affects the resulting temperatures. A smaller source size would have resulted in a different background and, therefore, a lower temperature. Additionally, had the nuclear

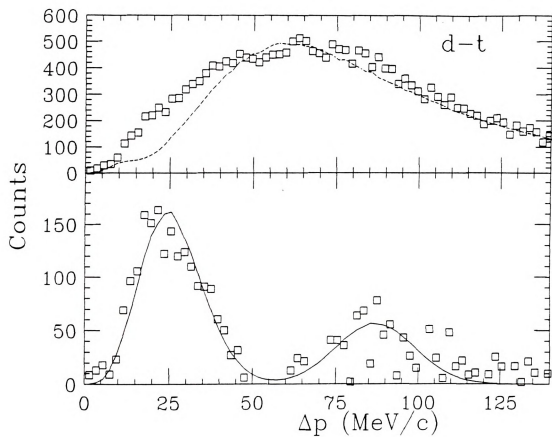


Figure II.22: The relative momentum spectrum for deuteron-triton pairs (squares) and an estimate of the independent background (dashed line). The lower portion displays the counts above background (squares) and fits to the individual peaks (dotted and solid lines).

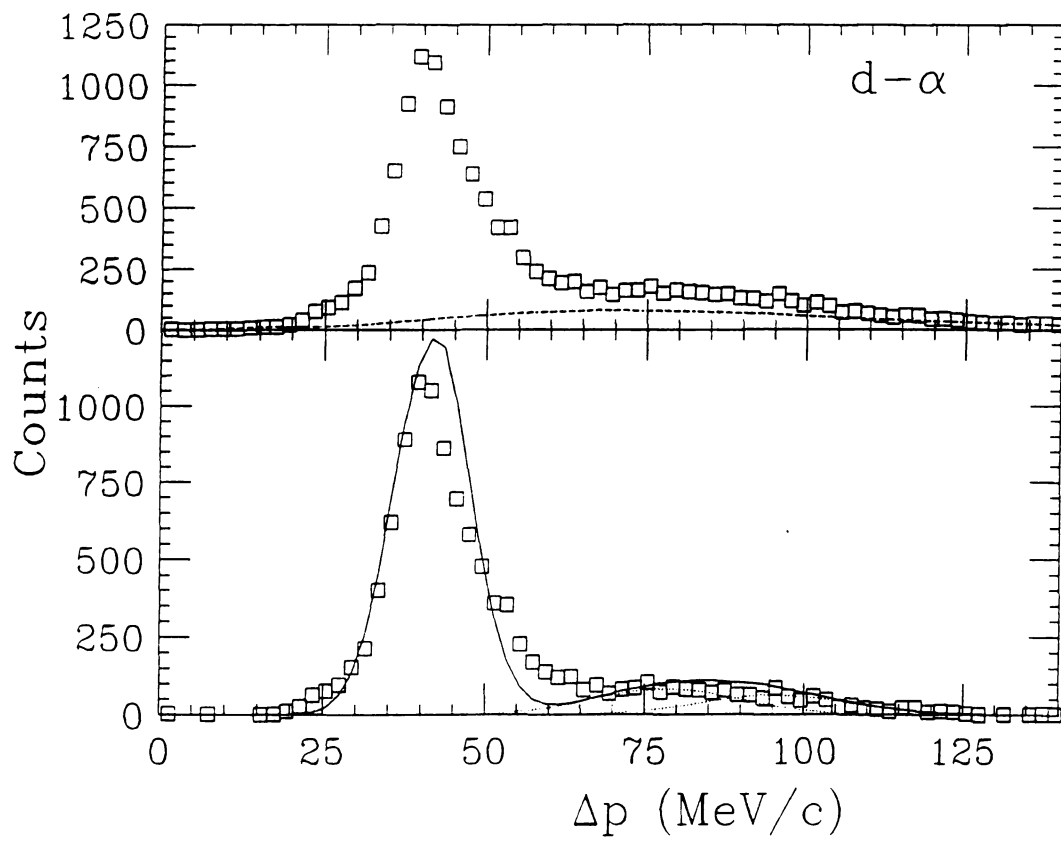


Figure II.23: The relative momentum spectrum for deuteron- $\alpha$  pairs (squares) and an estimate of the independent background (dashed line). The lower portion displays the counts above background (squares) and fits to the individual peaks (dotted and solid lines).

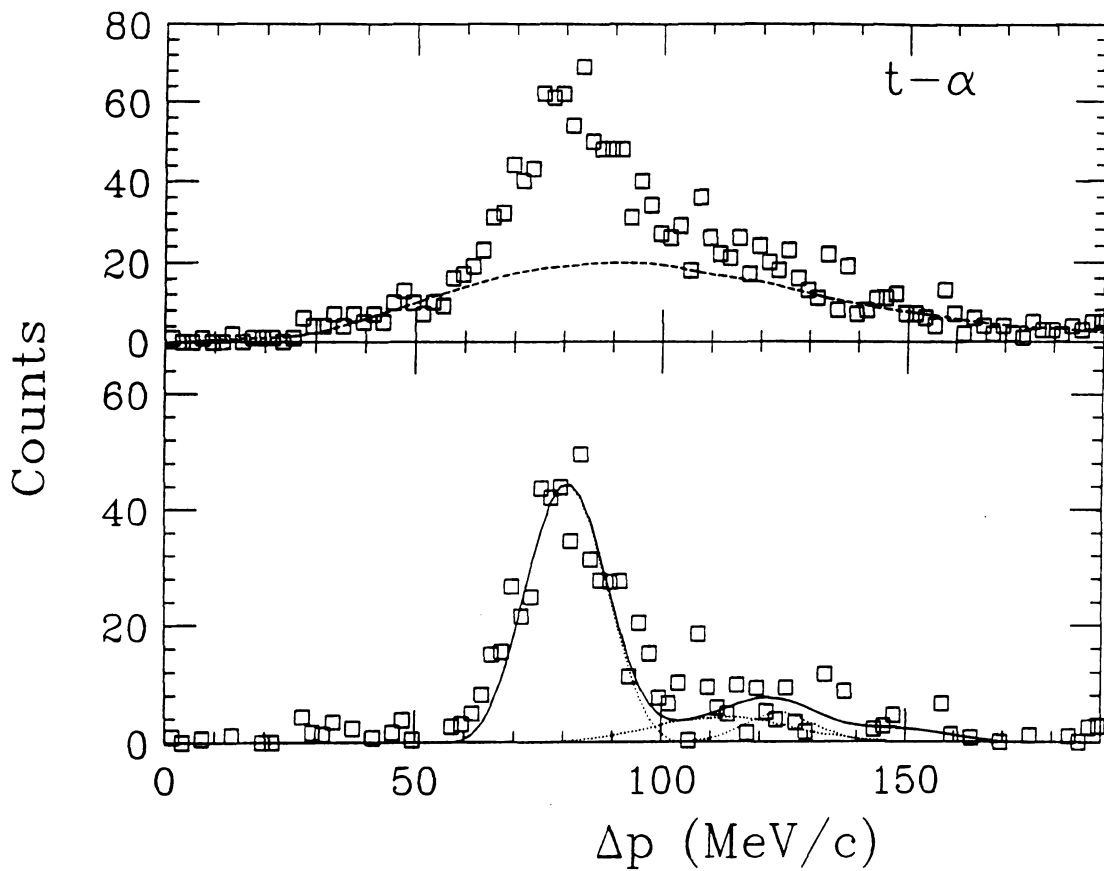


Figure II.24: The relative momentum spectrum for triton- $\alpha$  pairs (squares) and an estimate of the independent background (dashed line). The lower portion displays the counts above background (squares) and fits to the individual peaks (solid lines).

Table II.3: The temperatures extracted from this study.

System	Pair	Temperature (MeV)
500 MeV p+Ag	p-t	$5.6 \pm 1.0$
500 MeV p+Ag	d-t	$4.8 \pm 1.0$
500 MeV p+Ag	d- $\alpha$	$3.5 \pm 1.0$
500 MeV p+Ag	t- $\alpha$	$3 \pm 2$
500 MeV p+Be	d- $\alpha$	< 4

contribution to the independent background been included, a different temperature would have been extracted. Errors are also introduced by the estimates of the branching ratios for given excited states. Several states are open to neutron emission as well as particle emission, and an accurate estimate of the branching ratios must be used.

The average temperature extracted in this study is about 4 MeV. This value can be compared to the slope parameters of the kinetic energy spectra. These spectra were measured in an earlier experiment by Green and Korteling [Gree80]. The values derived from that study were from 15 to 20 MeV depending on the specific fragment species. As with the heavy-ion induced reactions, the temperature extracted from the excited state populations was substantially lower than that suggested by the kinetic energy spectra.

## E Conclusions

It is evident from the data presented in this chapter that the determination of the dimensions of the source of energetic fragments is not a straight-forward task. The effective source for fragments of a given type is not the same as that for a differing pair. One might expect the lighter pairs to come from predominately smaller sources, because fewer nucleons are required to form such pairs. This is not observed, instead the evidence from the 500 MeV p+Ag study suggests that only states that do not

contain nuclear resonances can be used for estimates of the size of the thermalized source. The pairs that contain resonances are dominated by the decays of these fragments which masks the contribution from the independent emission from the thermalized source. From pairs with nuclear resonances one learns mostly about the size of the parent nuclear fragment and not about the thermalized source. The pairs without resonances all yield high values for the source radius. This is taken to be an unbiased estimate of the size of the source.

It has been tacitly assumed in the introduction to this work that the nuclear freeze-out took place at a specific nuclear density. One of the goals of this work was to measure the source size, from which the density could then be estimated. The data presented in this thesis suggest a freeze-out density of  $0.17_{-0.08}^{+0.17}\rho_0$ , which is derived from the d-d correlation function. A major weaknesses of this method is that it assumes simultaneous emission from a static surface. However, the system is expanding prior to fragment formation at freeze-out. If the system had just enough energy to reach freeze-out, then the fragments would be emitted from a region that had reached the limits of its expansion. However, if the system had excess energy, it could still be expanding radially at the time of fragment formation. This would distort the perceived source radius, because the emitted fragments should also contain a radial momentum component. The temporal extent of the source can not be separated from the spatial extent using this method of analysis. Thus, the extracted source radius will be an overestimate for any system with a non-negligible life time.

As it turns out, the data can also be understood in terms of a specific *temperature* for freeze-out. This casts further doubt on the concept of a well-defined freeze-out density. The extracted temperature from the 500 MeV p+Ag study is  $4 \pm 1$  MeV. This value agrees with the temperature estimates from several heavy-ion induced reactions [Poch85c, Chen87, Bloc87, Fox88]. As with the heavy-ion studies, the tem-

perature extracted from the distributions of excited states is not in agreement with that suggested by the slope parameters of the fragment kinetic energy spectra. The excited state populations are providing information about the final stages of the reaction (fragmentation and final-state interactions), while the fragment spectra seem to be established at an earlier stage. The temperatures extracted using kinetic energy spectra are dominated by the data that make up the high energy tail. Thus, the portion of the spectrum that contains the fewest counts will have the greatest effect on the extracted slope parameter. These high energy particles may be emitted at the earliest/hottest stages of the reaction. The temperature measured using the populations of states weights particles of all energies equally, and is therefore dominated by the data from the low end of the kinetic energy spectrum, which contains the largest number of counts. Thus the temperature extracted using the populations of states is dominated by the stage of the reaction in which the largest number of fragments is formed. Additionally, if the freeze-out occurs while the system is still undergoing an expansion, the energy spectra would not agree with the chemical temperatures. The thermal models assume emission is from an equilibrated source.

A comparison of this work to the heavy-ion induced studies suggests that the major features previously observed are still present and are therefore not artifacts of the reaction dynamics. The source size analysis is clearer in the p+Ag study suggesting that the thermalized region which is formed is more well defined than that created during a heavy-ion induced reaction. The temperature estimates agree with the earlier studies.

## Chapter III

# The Search for Multi-Fragmentation

### A Introduction

Multi-fragmentation is the simultaneous disassembly of a hot nuclear system into several intermediate mass fragments (IMFs). It is a disassembly mechanism that has been proposed to occur when the excitation energy of a nuclear system is sufficient to allow the system to expand into a region of mechanical instability. Theoretical studies have suggested that at excitation energies around 4 MeV/nucleon this mechanism should become the dominant decay process [Bond85a, Bond85b, Gros86]. At lower excitation energies, the de-excitation of a nucleus is accurately described by the Weisskopf model [Blat79]. This model considers the formation of a compound nucleus and its subsequent statistical decay through emission of protons, neutrons, and alpha particles. For heavy nuclei ( $A \geq 100$ ) a binary fission is also a possible de-excitation mechanism. The multi-fragmentation models propose that for nuclei with large amounts of excitation energy, the slow disassembly process depicted by the Weisskopf model is insufficient to cool the rapidly expanding system. The fluctuations in temperature and density grow fast enough ( $\approx 10$  Fm/c) to tear the nucleus apart. (Refer to Figure I.2 for a schematic diagram of the a reaction and subsequent

decay of the highly excited nuclear system.) Cracks are formed as nuclear bonds are broken within the nucleus. These cracks expand to form bubbles. At this point, the nucleus contains regions of high and low density. The high density regions condense to form droplets which mutually repel one another due to the Coulomb force. This proposed disassembly process represents a completely different sort of de-excitation than the sequential emission that is observed at lower energies.

For this work, multi-fragmentation shall refer exclusively to the simultaneous disassembly of a thermalized nuclear system into several intermediate mass fragments (IMFs, defined as fragments with  $A \geq 4$ ). Multi-fragment emission, on the other hand, will be used to indicate an observed emission of multiple IMFs without reference to the mechanism of decay. Observation of multi-fragment emission therefore is not sufficient evidence to conclude a multi-fragmentation process is present. Specifically, modifications of the Weisskopf model have extended the theory to allow decay by emission of all species of particles. This change allows a sequential binary decay model to produce events with multiple IMFs. A signature for identification of multi-fragmentation will require sensitivity to the time scale of the disassembly process.

There is a great deal of interest in the multi-fragmentation process because it is a rapid disassembly process and can thus yield information about the early stages of nuclear reactions. Identification of its existence and determination of its characteristics will allow one to study features of the equation of state of nuclear matter. The maximum amount of internal excitation energy that a nucleus can support is indicated by the onset energy of the multi-fragmentation decay process. This onset energy will vary as a function of the compressibility of nuclear matter ( $\kappa$ ), because the growth rate of the density fluctuations depends upon  $\kappa$ . The onset will occur at a lower energy for a stiff EOS ( $\kappa = 380$  MeV) than for a soft EOS ( $\kappa = 200$  MeV) [Sura89].

The first experimental evidence for the existence of a multi-fragmentation decay mechanism was presented by a group from Purdue. The data were IMF production cross-sections from the reaction  $p + \text{Xe}$  at 80 to 350 GeV. The data that were presented are displayed in Figure III.1 [Finn82]. The mass yields are fit by a power law,  $d\sigma/dA \propto A^{-2.64}$ . A multi-fragmentation process was suggested, even though the results were for single particle inclusive data, because the simple models available at the time could not account for the observed shape of the mass yield spectrum. The Weisskopf model allowed for decay through emission of protons, neutrons, and alphas, but not IMFs. Total disassociation of the constituent nucleons would have left only free neutrons and protons. It was suggested that a nucleon vapor had been formed. This vapor then coalesced into droplets or IMFs. The Fisher droplet model [Fish67] for a vapor predicts a mass distribution of the form  $d\sigma/dA \propto A^{-\tau}$  where  $\tau$  is the critical exponent.  $\tau$  values between 2.0 and 3.0 are consistent with the concept of nuclear vapor formation and subsequent particle condensation. This droplet model is a 3-dimensional percolation model that was developed as a simple way to understand vapor formation. The model considers interactions only between particles (or lattice sites) that are contained within the same cluster or droplet. Interactions between droplets are assumed to be negligible. The critical point is marked by the appearance of large clusters and is manifested as a critical opalescence in macroscopic systems. The phase transitions that are produced by the Fisher droplet model are instructive for the study of nuclear phase transitions, however, since the interactions between particles in nuclear matter are not the same as the simple interactions used in percolation models, there is no guarantee that the phase transitions will have the same cluster properties [Stau79]. These data prompted many theoretical and experimental studies focusing on the multi-fragmentation process and phase-transitions in nuclear matter.

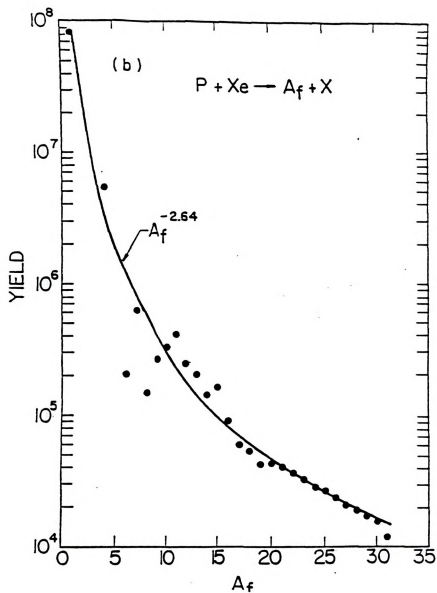


Figure III.1: The measured mass yields from the reaction  $p+Xe$ . The energies of the proton beam varied from 80 to 350 GeV. The exponent of the solid curve is fit to the data. This analysis was inspired by the Fisher droplet model which predicts  $d\sigma/dA \propto A^{-\tau}$  [Finn82].

There are three main types of models that have been employed to study multi-fragmentation. The categories are *Statistical*, *Transition-State*, and *Geometrical*. The different approaches yield similar results and are capable of reproducing the basic multi-fragment emission observables. In general, the models described below predict that multi-fragmentation becomes the dominant decay mode for thermalized systems with greater than 4 MeV/nucleon excitation energy.

## B Theoretical Studies

### 1 Statistical Multi-fragmentation

The statistical models for multi-fragmentation have three major assumptions. First, the different phase space states are all given the same weight. Second, one characterizes a given configuration with a total weight which is the summation of the weights of all of the phase space states that lead to that configuration. Lastly, it is assumed that the system is in thermodynamic equilibrium at the time of the breakup. Within the statistical studies, there is a further grouping based upon the type of ensembles used to evaluate the results. The simplest approach is a grand canonical ensemble which allows both particle number and energy to fluctuate (open system). This approach is advocated by Mekjian because of its simplicity [DeAn89]. The Copenhagen group uses a canonical approach allowing only thermal fluctuations (closed but not isolated) [Bond85a, Bond85b]. The Berlin group prefers to use a micro-canonical ensemble which conserves mass, charge, and energy explicitly (closed and isolated) [Gros86, Zhan87, Gros87]. In order to keep the calculations manageable, they employ a Metropolis sampling [Metr53] which is an intelligent method of getting a good sample of the representative states of a complex system.

Predictions from Bondorf's calculations are displayed in Figures III.2 and III.3.

These figures show the average IMF multiplicity and average temperature as a function of the internal excitation energy of the nucleus. This model predicts that at 3 MeV/nucleon the onset of multi-fragmentation occurs. That excitation energy corresponds to a temperature a little above 5 MeV. Bondorf's model predicts that the energy fluctuations will be large enough at this point to start the formation of cracks within the nucleus. These cracks represent the breaking of internal nuclear bonds. This cracking then leads to multi-fragment emission, which is why the average multiplicity starts to rise at 3 MeV/nucleon. The temperature levels off after crack formation, because at this point the system has entered the region of the liquid-gas co-existence as depicted in Figure I.1. As the system traverses this region, the temperature remains constant until the excitation energy is great enough to vaporize completely the entire system. Beyond that point, the temperature curve follows the free nucleon gas prediction.

The micro-canonical models of the Berlin group make similar predictions as those of the Copenhagen group. The relative probabilities for three different decay processes are displayed in Figure III.4 [Gros87]. There are two noticeable transitions. At  $E^* = 400$  MeV (3.0 MeV/nucleon) there is a marked decrease in the evaporation yield complemented by an increase in the fission yield. At  $E^* = 650$  MeV (5.0 MeV/nucleon), the cracking mode becomes the dominant decay process. These two transitions can also be seen in plots of the temperature against the excitation energy as in Figure III.5. The temperature levels off at 3 MeV for the evaporation/fission transition, and at 5 MeV for the cracking transition.

## 2 Transition-State Multi-fragmentation

The transition-state approach to multi-fragmentation is an extension of Bohr and Wheeler's relative potential model for nuclear fission [Bohr39]. Bohr and Wheeler's

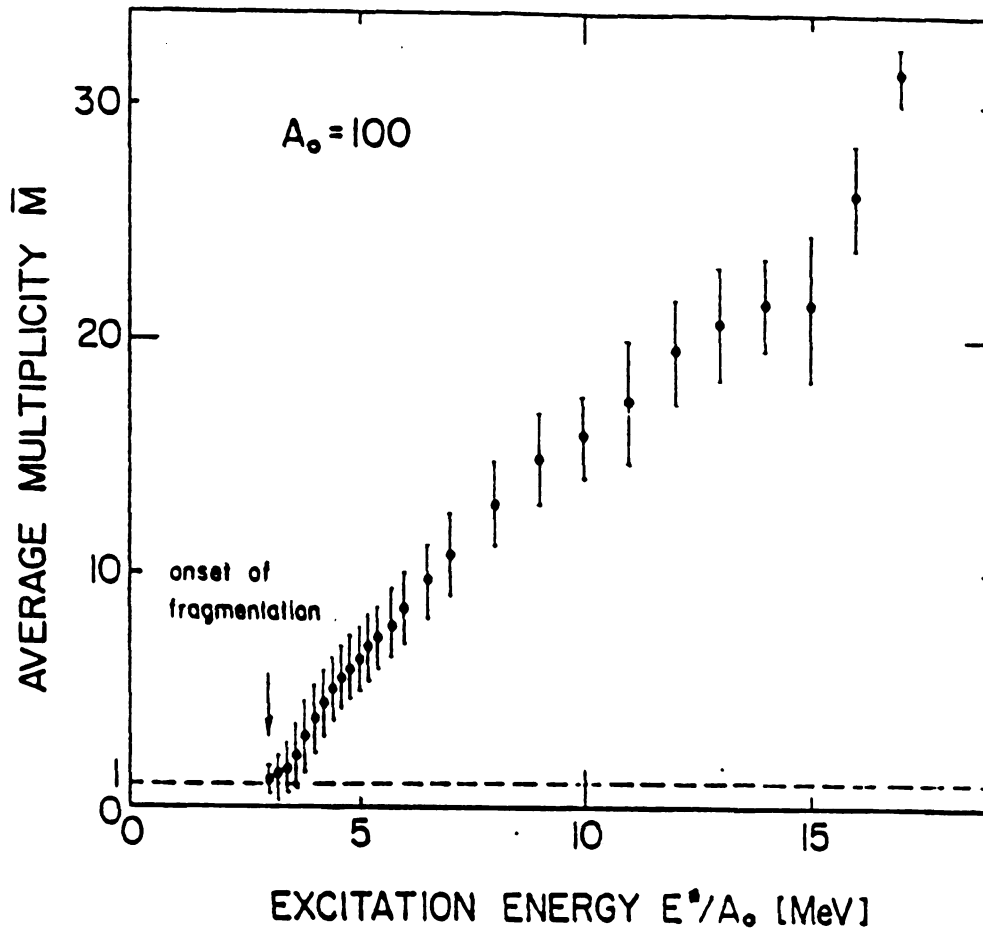


Figure III.2: Predictions of a statistical multi-fragmentation model. The mean multiplicity and its dispersion as a function of the excitation energy are shown [Bond85b].

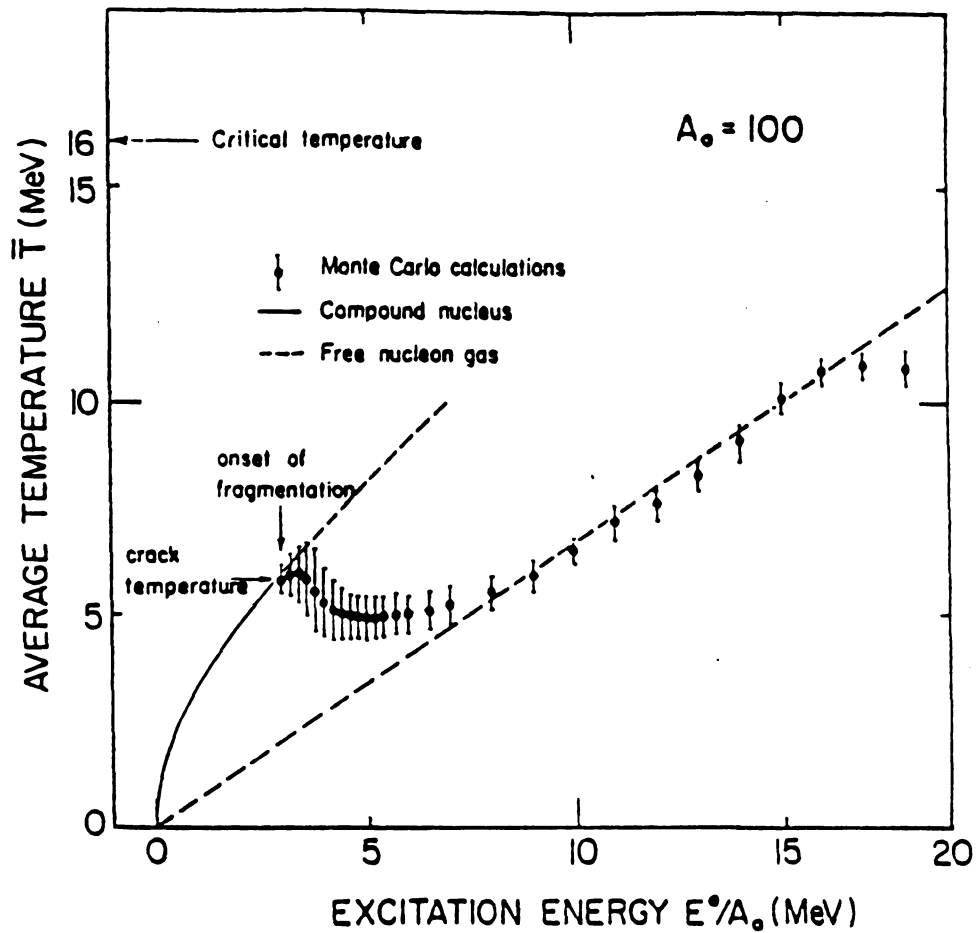


Figure III.3: The average temperature  $\bar{T}$  as a function of the excitation energy  $E^*/A_0$ . The onset of fragmentation occurs when the energy fluctuations are large enough to break internal bonds (crack formation). The dashed line illustrates the temperature of a free nucleon gas [Bond85b].

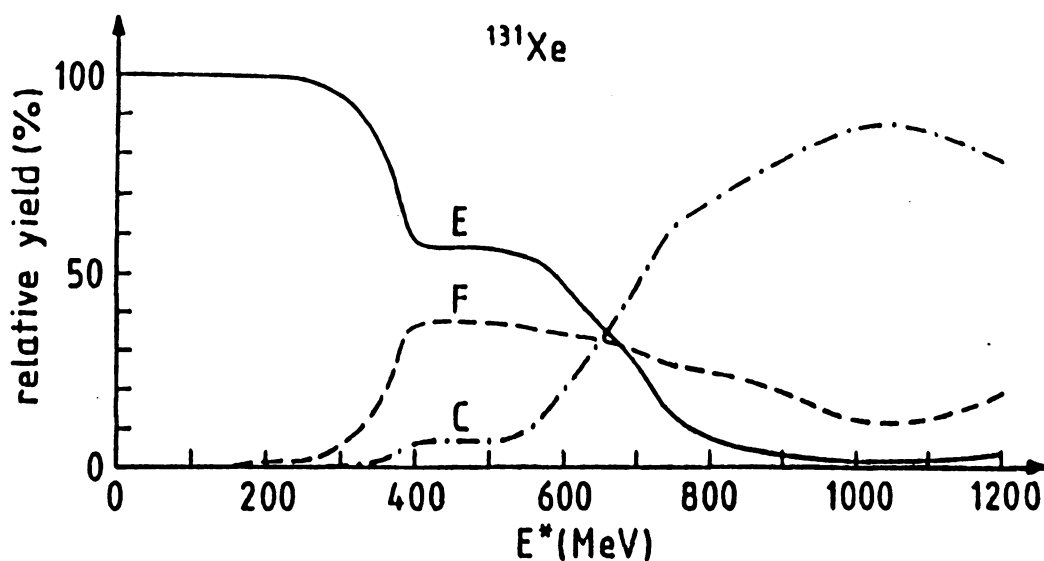


Figure III.4: Predictions from a micro-canonical statistical multi-fragmentation model. The relative probabilities of evaporation (E, solid), fission (F, dashed), and cracking (C, dot-dash) like events for  $^{131}\text{Xe}$  are shown [Gros87].

model first determines a relative potential between two pseudo-nuclei as a function of the relative separation. The potential is zero at zero relative separation, peaks at a separation comparable in size to the nuclear radius, and then falls at large separations. This potential creates a fission barrier that must be overcome in order for a decay to proceed. To determine the fission widths ( $\Gamma_{fission}$ ), one considers all possible states of relative momenta and separations. A determination is made as to whether each state decays or is stable.  $\Gamma_{fission}$  is then the ratio of the number of unstable states to the total number of states. In order to generalize this technique to multi-fragmentation, two new quantities are defined:

$$q_F^2 = \frac{1}{m_o} \sum_{n=1}^N m_n r_n^2 \quad (\text{III.1})$$

$$p_F = \frac{1}{q_F} \sum_{n=1}^N p_n r_n \quad (\text{III.2})$$

where the  $m_n$ ,  $p_n$  and the  $r_n$  are the mass, momenta and positions of the various fragments and  $m_o$  is the mass of a nucleon [Fai89]. As with the two-body model,

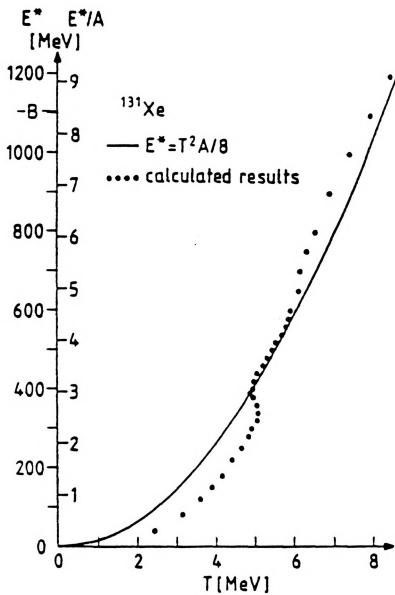


Figure III.5: The excitation energy as a function of the internal temperature calculated from a statistical multi-fragmentation [Gros87].

the potential is determined as a function of the relative co-ordinants. All possible states are considered to calculate the decay widths,  $\Gamma_N$ , for breakup into  $N$  large fragments. Figure III.6 displays the relative  $\Gamma_N$  as a function of the excitation energy of the nucleus. This figure demonstrates that for  $E^*$  above 3 MeV/nucleon the decay widths for multi-fragmentation channels are greater than widths for binary fission [López89b, López89c].

López and Randrup have analysed the results of their multi-fragmentation model in an effort to determine which observables could be used to distinguish a rapid fragmentation from a sequential binary decay [López89a]. Figure III.7 displays the predicted relative velocities of various types of fragments. The clearest separation between fission and fragmentation can be seen in the relative velocity spectrum between two heavy fragments. The events generated from a model simulating a sequential fission process display a larger relative velocity on average. The fission fragments experience a Coulomb repulsion which corresponds to the full size of the parent nucleus, while the heavy fragments produced in multi-fragmentation events have a reduced Coulomb effect because the field of the emitting system is strongly modified by the simultaneous emission of multiple charged-particles and of the fragment that is being studied. Figure III.8 shows the results of a shape analysis which compares predictions from a fission model to those from a multi-fragmentation model. The fission events appear elongated with respect to some primary axis while the fragmentation events display a more spherical shape. These two observables have been used in experimental studies that have attempted to demonstrate the existence of a multi-fragmentation process [Klot89, Trau89, Boug89b, Poul89, Harm90, Cebr90].

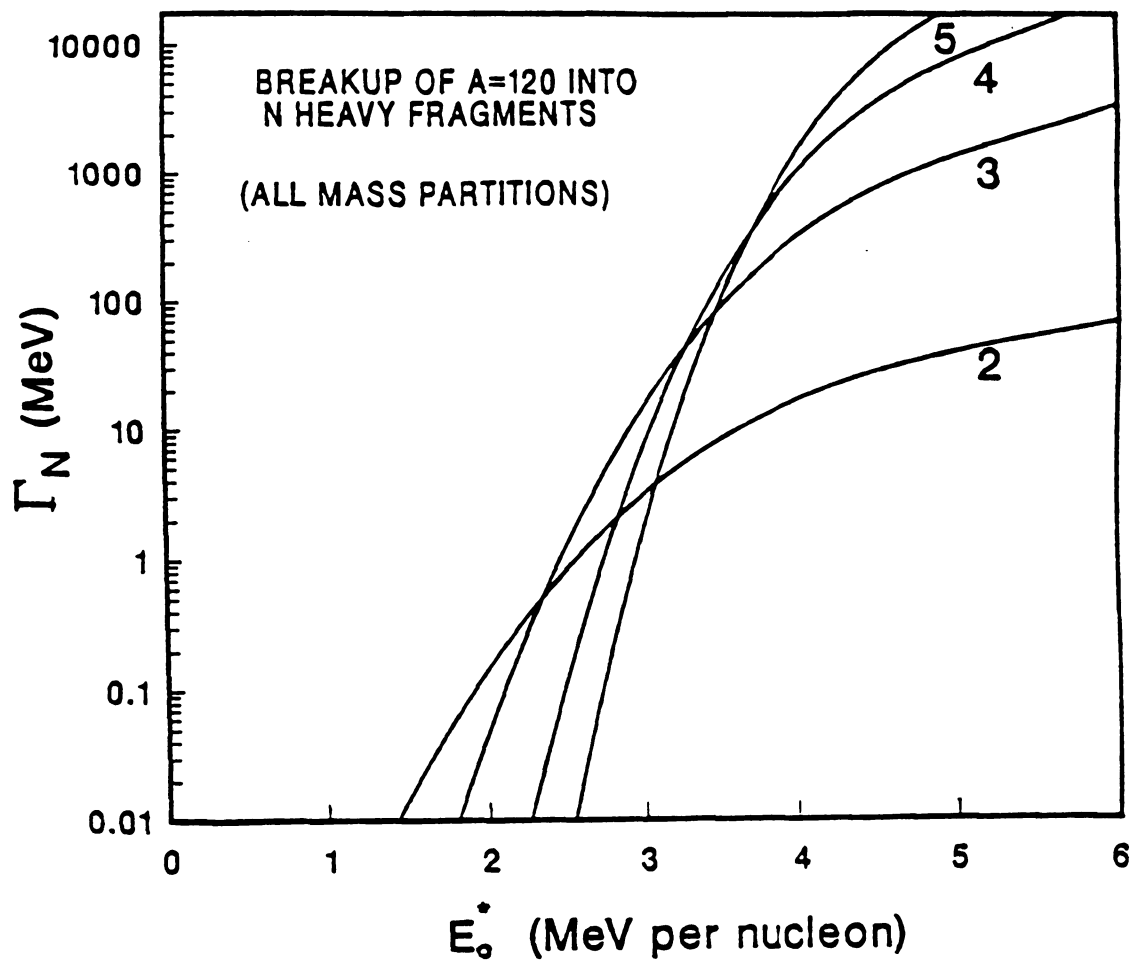


Figure III.6: The partial widths  $\Gamma_N$  for the breakup of  $^{120}\text{Sn}$  into  $N$  fragments with mass numbers  $A > 10$  as a function of the excitation energy of the source. The curves are labeled by the value of  $N$  [Lópe89b].

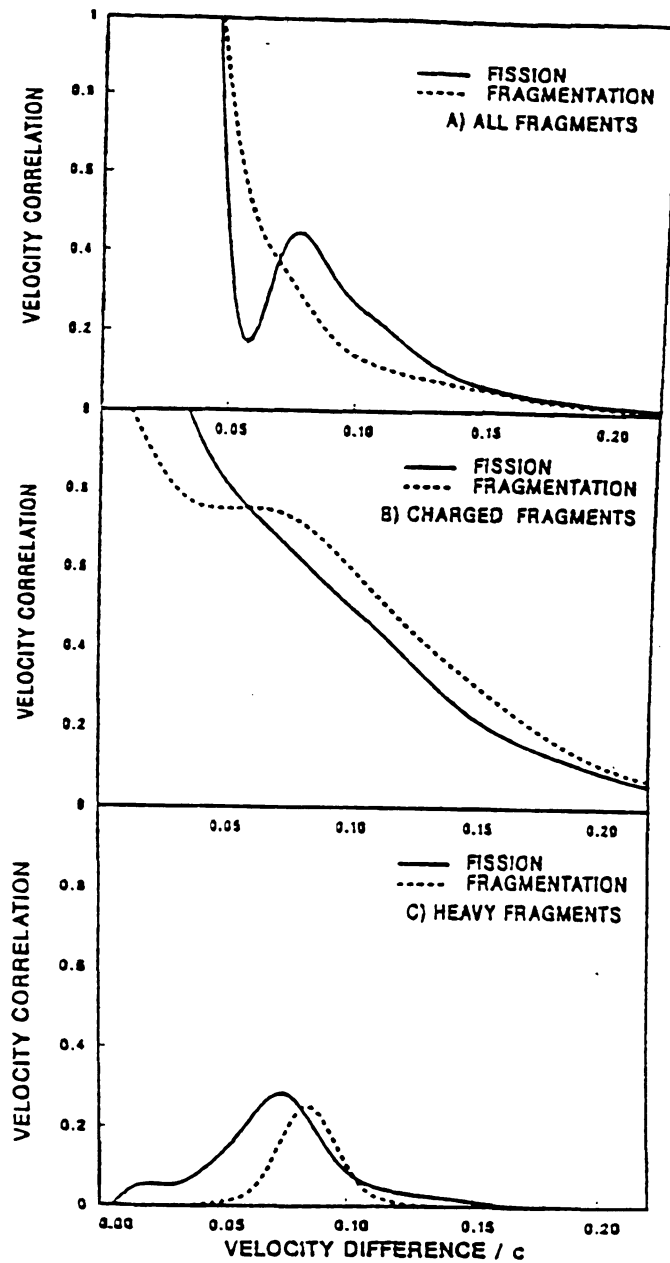


Figure III.7: Fragment velocity correlation functions for (a) all fragments (b) charged fragments only and (c) heavy fragments ( $A > 4$ ) only.  $A=150$ ,  $Z=62$ , and  $E^*=5$  MeV/nucleon [Lópe89a].



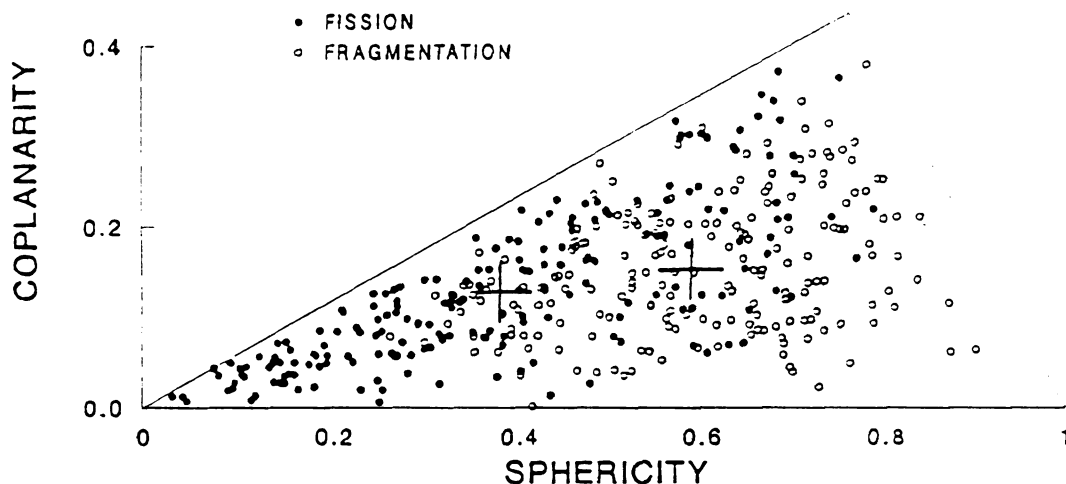


Figure III.8: Superposition of 200 events in the sphericity-coplanarity plane for  $A=150$ ,  $Z=62$ , and  $E^*=5$  MeV/nucleon [Lópe89a].

### 3 Geometrical Multi-fragmentation

This modeling technique attempts to describe the observed experimental features through purely geometrical arguments. The nucleus is abstractly considered as a lattice of nucleons with bonds between the nearest neighbors. The variables of interest for this analysis are the numbers of occupied or vacant lattice sites and the number of complete or broken bonds. In geometrical or percolation models, the excitation energy is modeled by a parameter corresponding to the probability that a given bond will break. An increase in excitation energy is modeled as an increase in this decomposition parameter. In order to determine the distribution of clusters that has been formed during the decay of an excited nucleus, the model considers which bonds have been broken. The aggregations of lattice sites (nucleons) that have been isolated are considered to form fragments without regard to how tenuous the interconnections may be. Though this analysis technique is simplistic, it can reproduce power-law shape of the production cross-section distribution and the value critical exponent observed in the Purdue data [Baue86]. Models of a similar nature can be made more sophisti-

cated through additions of post-breakup de-excitations and pre-breakup expansions [Néme89, Ngô89], but the general concept remains the same. These models provide a mechanism that will produce multi-fragment events through a purely statistical process.

## C Experimental Studies

The Plastic Ball group at LBL provided some of the first evidence that reaction channels consisting of multiple IMFs were populated during nuclear interactions. The evidence presented was in the form of simple multiplicity distributions from the reaction 200 MeV/nucleon Au+Au. The device used for these observations was the *Plastic Ball/wall* [Bade82], which consists of one thousand phoswich detectors covering almost all of  $4\pi$ . The beams were provided by the Bevalac accelerator facility. A high granularity device is appropriate for measuring the charged particle multiplicities, because the probability of non-detection due to multiple hits is reduced. Figure III.9 displays the observed IMF multiplicity,  $M_{IMF}$ , distributions for several different trigger requirements [Harr87, Doss87]. Though these studies conclusively demonstrated that reaction channels with  $M_{IMF}$  up to ten are populated and that in central collisions the maximum probability is a decay into several fragments, they did not isolate the decay mechanism. Proof of multi-fragment emission does not necessarily confirm *Multi-fragmentation*.

Another experimental group at LBL has been making an effort to determine the reaction process that leads to multi-fragment emission. This group works at both the 88-inch Cyclotron and at the Bevalac. They have carried out an exhaustive set of measurements employing reverse kinematics (heavy beams on light targets) [Sobo83, Sobo84, Char86, Char88a, Char88b, Han89, Plag89]. The energy of the beam par-

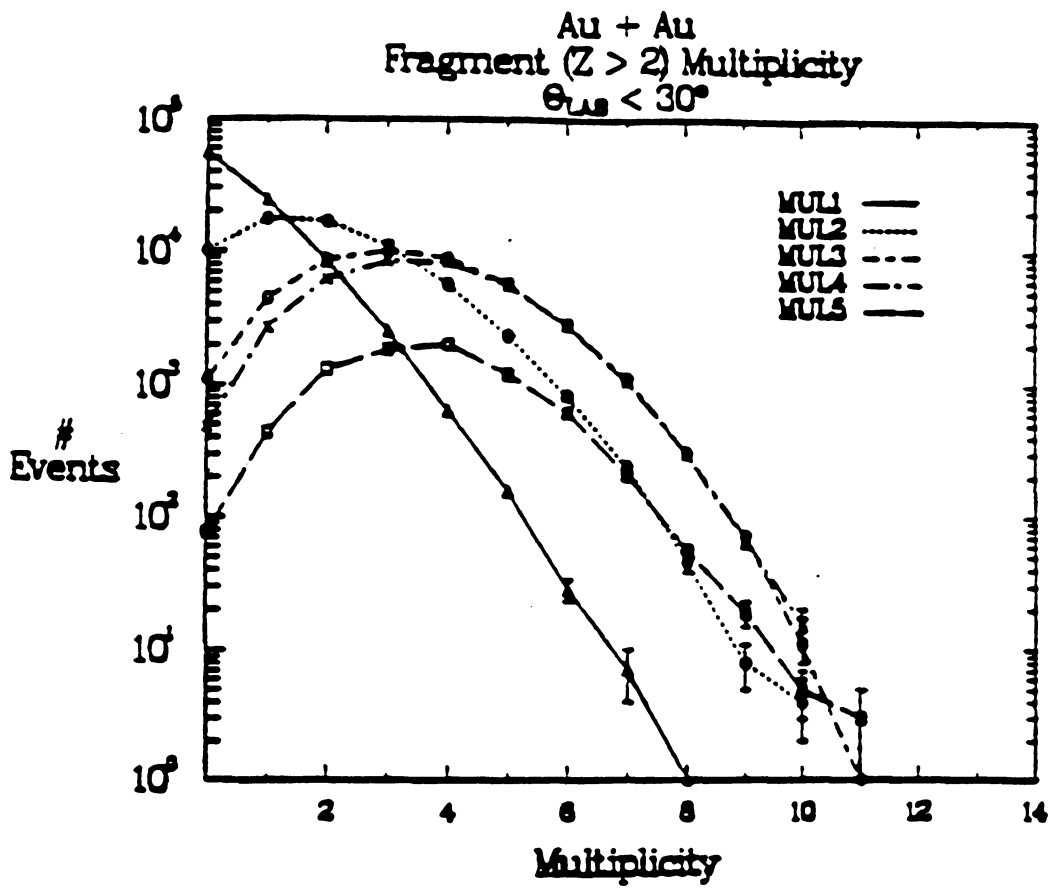


Figure III.9: The observed IMF ( $Z > 2$ ) multiplicity distributions from 200 MeV/nucleon Au+Au. The five curves represent five participant charge multiplicity bins [Doss87, Harr87].

ticles varied from 10 to 100 MeV/nucleon. To observe the reaction products, a set of silicon-silicon-plastic telescopes has been employed in a variety of configurations. The first data presented from this group were inclusive IMF production cross-sections [Sobo83, Char86]. Data of this sort were compared to predictions from a modified sequential binary decay code (GEMINI [Char88b]), and the agreement between the data and the calculations was taken as evidence against multi-fragmentation at this excitation energy. Figure III.10 displays an example of this sort of comparison [Wozn88]. A more exclusive analysis plotted the charge observed in one detector against the charge observed in another [Colo89]. Figure III.11 is an example of this analysis technique [Bowm87]. The strong clustering of events around the  $Z_1 + Z_2 = 60$  was taken as evidence that the dominant decay mode was a single fission. The conclusion was challenged by Gross. He maintained that his micro-canonical statistical multi-fragmentation code could reproduce the experimental results. Figure III.12 shows Gross's calculations [Gros88]. Though Gross may challenge the assignment of fission as the most probable decay mechanism, he can not rule it out.

A group from Darmstadt has performed a series of studies designed to address the question of multi-fragmentation. The detection system they employ consists of two detectors, a high resolution silicon/time-of-flight (TOF) detector at  $90^\circ$  and a large parallel-plate avalanche counter (PPAC) on the opposite side of the target. The experiments were carried out at the Saturne II facility at Saclay using 800 MeV/nucleon  $\alpha$  beams on a gold target. The trigger condition is an IMF/heavy fragment in each of the two detectors. The observable is the relative velocity between the two fragments. One expects an enhancement in the relative velocity between two back-to-back fragments produced by a sequential process as compared to the relative velocity expected from a simultaneous multi-fragmentation. Calculations by Gross suggest that the observed relative velocity spectrum was produced by a multi-fragmentation process

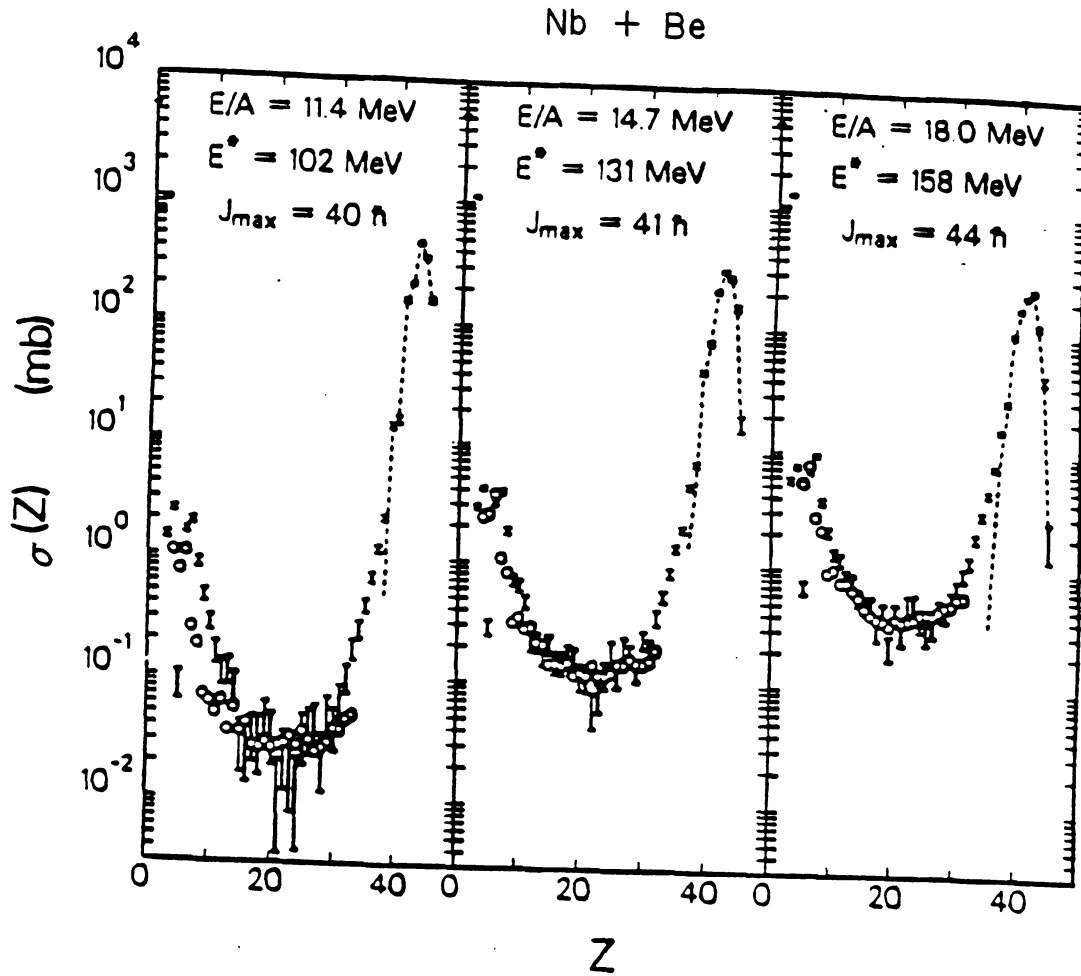


Figure III.10: Inclusive production cross-sections as a function of the fragment charge from the reaction Nb+Be at 11.4, 14.7, and 18.0 MeV/nucleon [Wozn88, Char88b].

## 50-Mev/u La + C

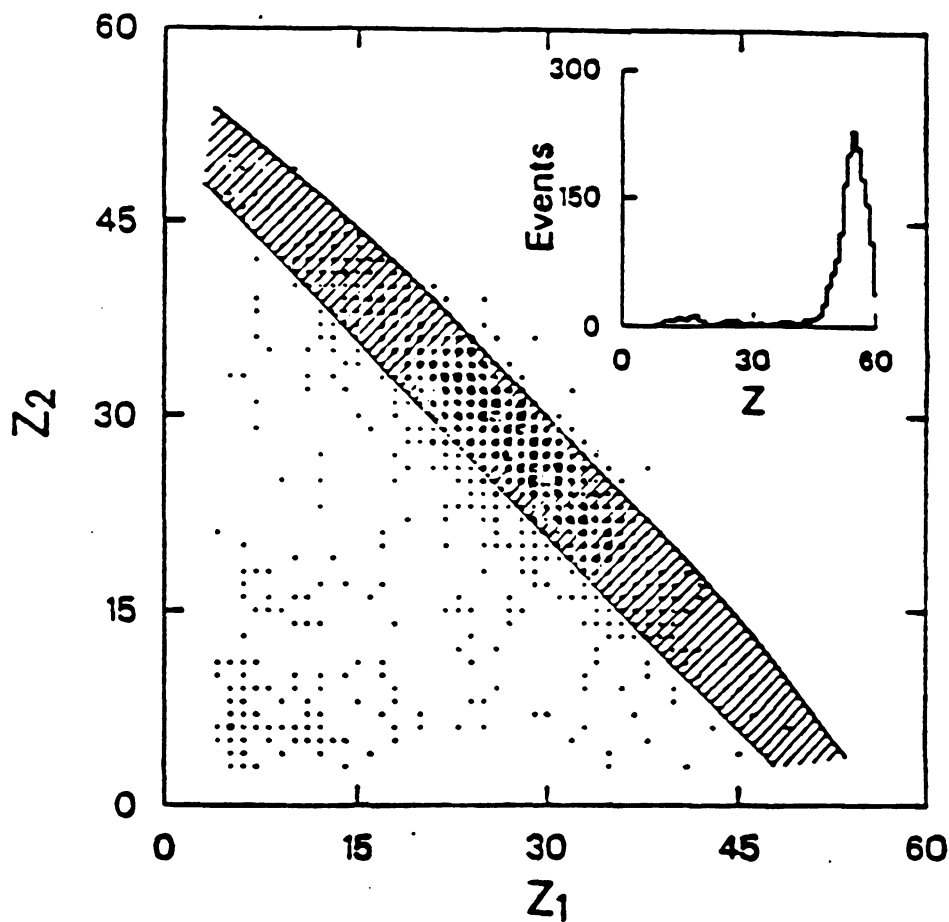


Figure III.11: A plot of the charge observed in the first detector against the charge observed in the second detector. The upper right corner shows a spectrum of  $Z_1 + Z_2$  [Bowm87].

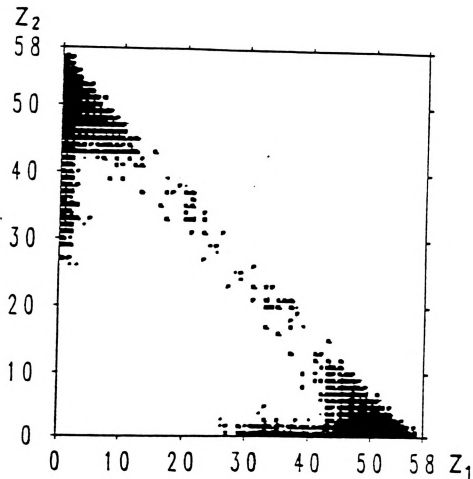


Figure III.12: A plot of  $Z_1$  against  $Z_2$ , where  $Z_1$  and  $Z_2$  are the charges of the two heaviest fragments produced by a microcanonical multi-fragmentation simulation of the decay of  $^{146}\text{Nd}^*$  [Gros88].

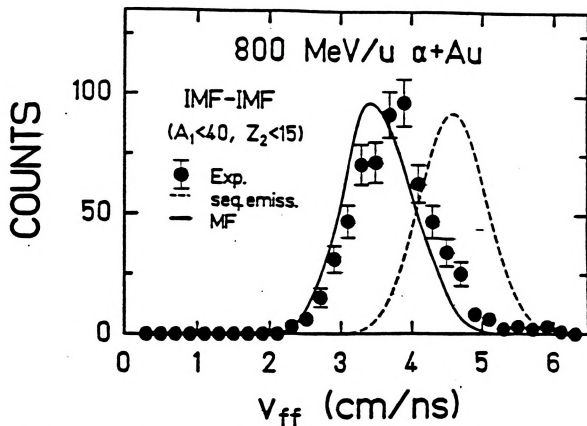


Figure III.13: Relative velocity distributions between IMFs. The solid dots are the experimental data with statistical errors [Klot89], the dashed line is the prediction from a sequential decay code, and the solid curve is the calculation from a simultaneous multi-fragmentation [Gros89].

[Gros89]. The observed spectrum and the predictions are displayed in Figure III.13 [Klot89, Cass89]. This analysis has been challenged by Pochodzalla [Poch89b]. He suggests that Gross's analysis failed to consider the pre-equilibrium evaporation of light particles. Pochodzalla's estimates of this early particle emission reduce the size of the fragmenting system from 184 to 156. This reduction in the mass (and charge) of the system, lowers the relative velocities of the outgoing fragments because the Coulomb repulsion has been reduced. Figure III.14 displays the predicted mass reduction as a function of excitation energy and the subsequent reduction in the centroid of the relative velocity distribution. Pochodzalla's calculations were based on the sequential decay code GEMINI and reproduced the experimental spectrum. Therefore,

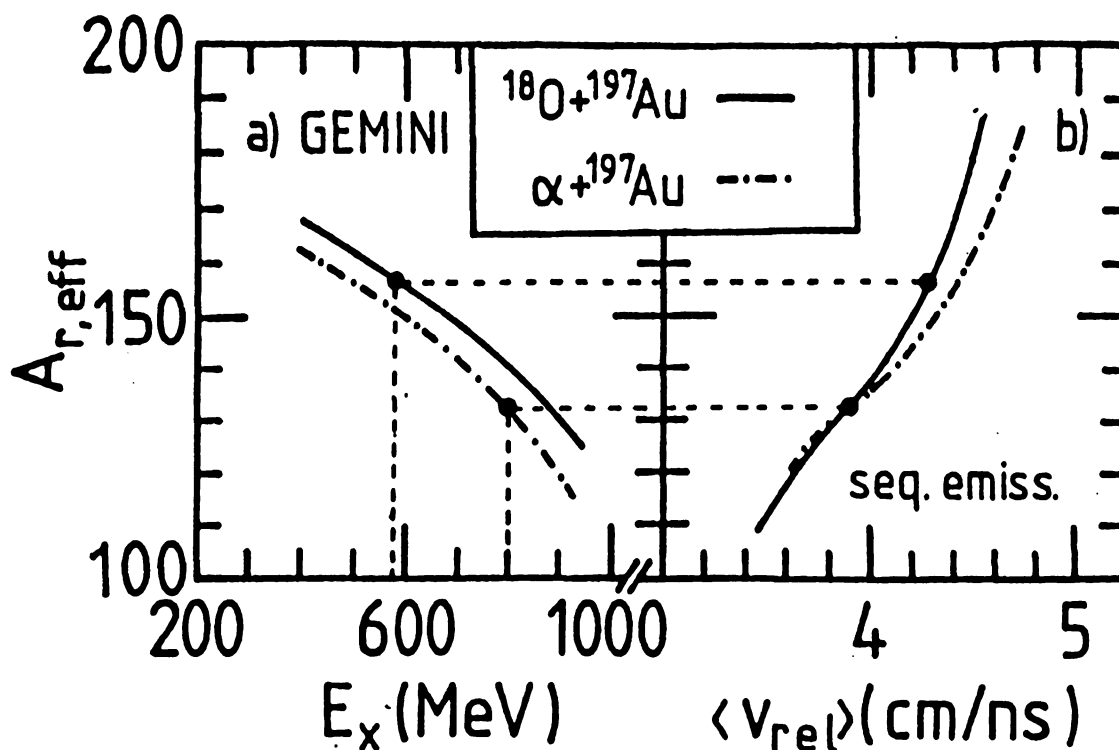


Figure III.14: Calculations for two systems ( $^{18}\text{O} + ^{197}\text{Au}$ , and  $\alpha + ^{197}\text{Au}$ ). The left side shows the effective mass ( $A_{eff}$ ) of the compound system as a function of the original excitation energy; the right side displays the centroid of the relative velocity distribution [Poch89b].

a sequential process can not be ruled out.

A group from GSI has been using a detection system consisting of twelve PPACs and seventy phoswichs and has been studying multi-fragmentation. Studies have been performed using oxygen and argon beams from the CERN synchrocyclotron and the SARA facility at Grenoble. The beam energies ranged from 30 to 84 MeV/nucleon. The targets were silver and gold. The original analysis of the data presented only IMF multiplicities as a function of excitation energy (Figure III.15) [Troc87, Poch88]. These data could not be used to resolve between a sequential and a multi-fragmentation process. The data were later analyzed in terms of the relative velocity at small relative angle. For this analysis, one expects that a simultaneous process will display a depletion at small relative velocity due to the Coulomb repulsion of particles produced



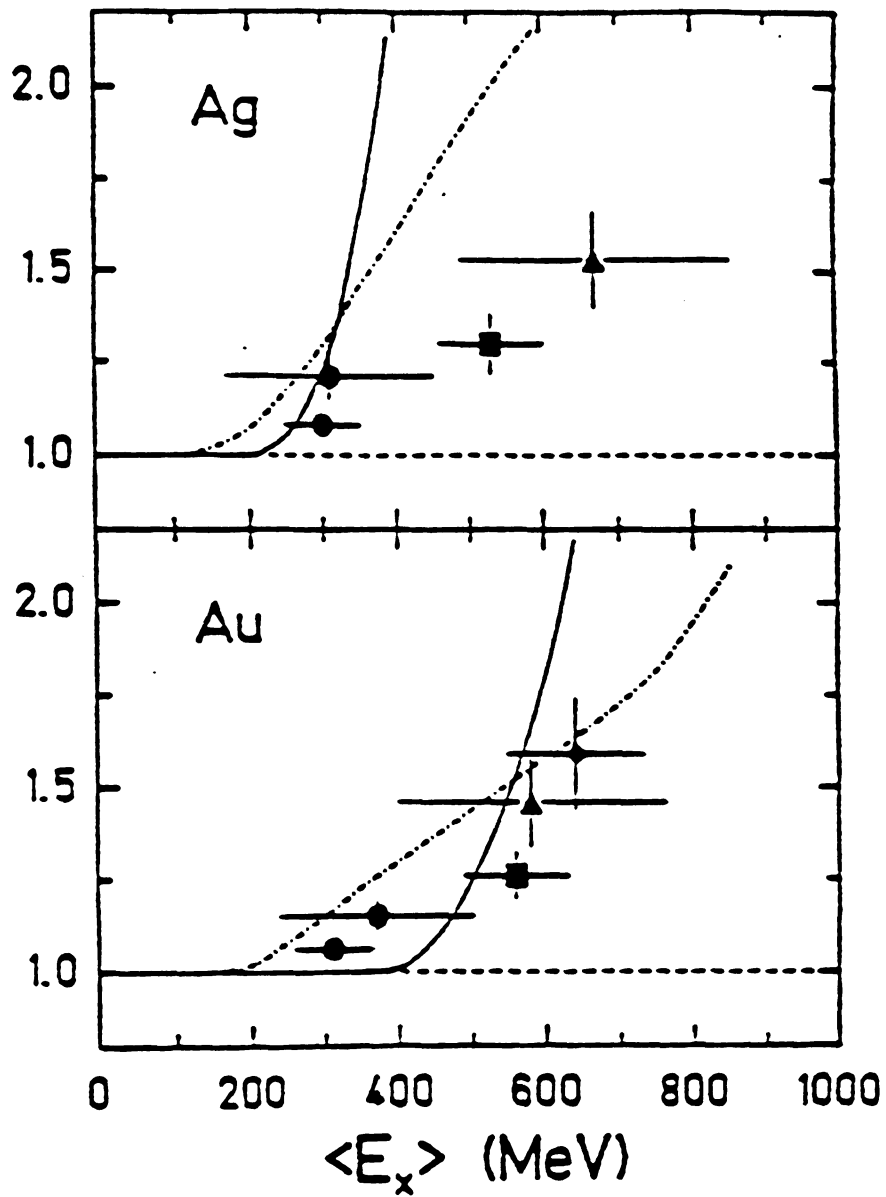


Figure III.15: A plot of the average IMF multiplicity as a function of excitation energy for various beams on silver (top) and gold (bottom) targets [Trau89].

close together in phase space. A model simulating a decay process with an adjustable decay time constant was fit to the data; Figure III.16 displays the results [Poch89a, Troc89, Trau89]. From this analysis one concludes that the decay process must have a time constant greater than 1000 Fm/c. An additional analysis of relative velocity of IMFs at large relative angle was conducted by the same authors. The conclusion from this study is that a sequential process dominates at excitation energies up to 6 MeV/nucleon.

A group from Caen has performed a set of experiments at GANIL [Rudo88, Hage89, Boug89a, Boug89b]. These experiments are similar in design to those of the GSI group. The detector apparatus consists of two arrays of PPACs, DELF [Boug87] and XYZt [Rudo86], and a wall of plastic scintillator, MUR [Biza86]. The system is sensitive to IMFs over 55% of  $4\pi$  and to light particles in the forward direction. A variety of beams and targets have been employed and the data has been analysed for evidence of compound nucleus formation [Hage89, Rudo88], collective motion, side-splash effects, event shape, and fragmentation time scale [Boug89a, Boug89b]. An example of their time scale studies is illustrated in Figure III.17. This figure displays the relative angles and velocities between three IMFs detected in events from the reaction 60 MeV/nucleon Ne+Au. The data are compared to predictions based on either a sequential, intermediate, or simultaneous decay process. The model considers an excited compound nucleus which decays into three fragments. The second decay occurs at a time delayed by either  $\infty$ , 300, or 0 Fm/c. From this analysis, the simultaneous process is ruled out, and a lower limit is set on the time scale for the disassembly process. Figure III.18 displays the results of an event shape analysis performed by the Caen group on data from the reaction 43 MeV/nucleon Kr + Au, Ag, Th. Though the event shape is analysed, it is not compared to simulations and therefore can not be used to determine the decay process.

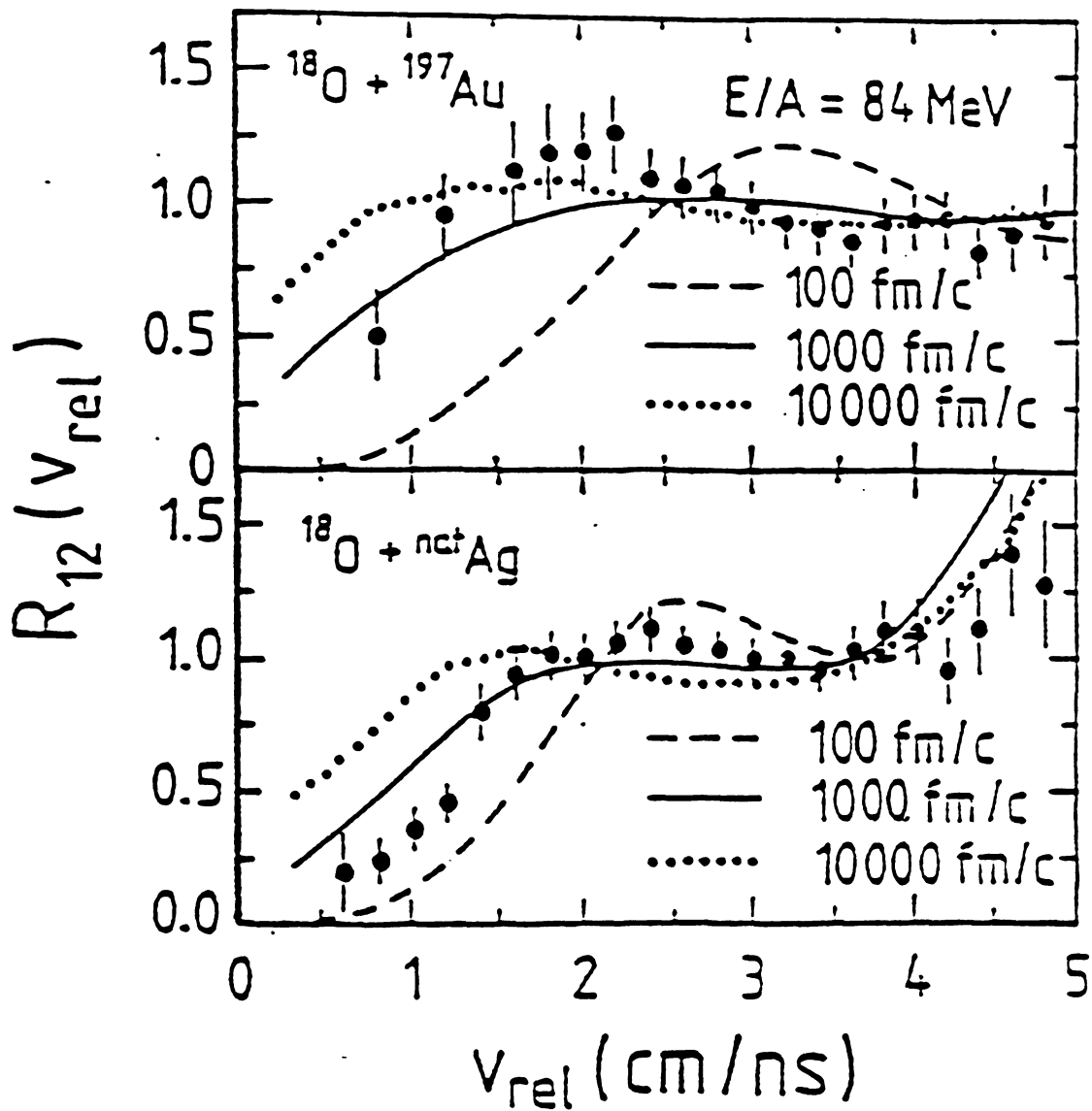


Figure III.16: The relative velocity correlation functions from 84 MeV/nucleon  $^{18}\text{O}$  on  $^{197}\text{Au}$  (top) and  $\text{natAg}$  (bottom). The three curves are calculations from a sequential decay code with an adjustable decay time scale [Trau89].

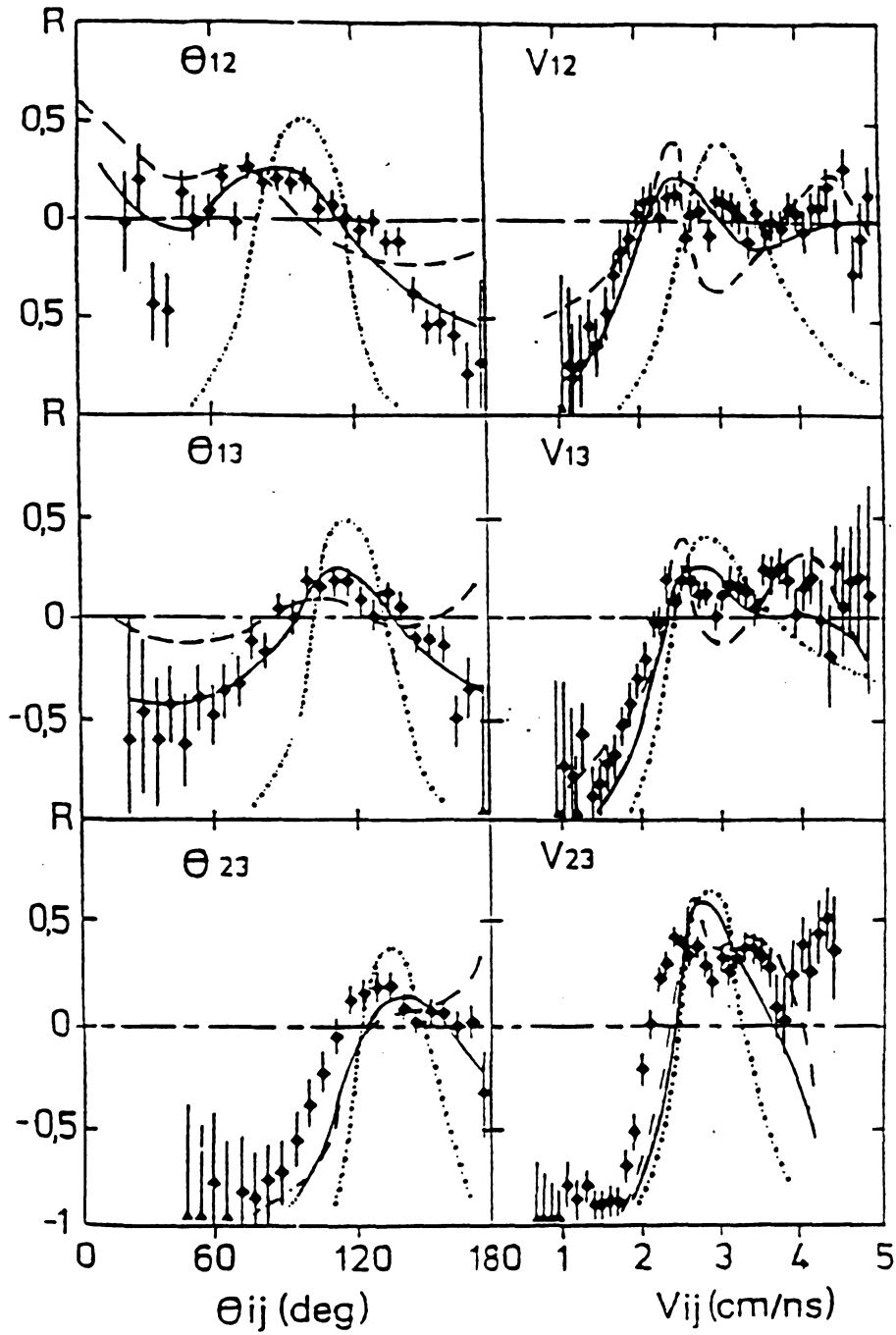


Figure III.17: The relative angles (left) and relative velocities (right) between pairs of IMFs from the reaction Ne + Au at 60 MeV/nucleon. The particles are ranked from heaviest to lightest [Boug89b].

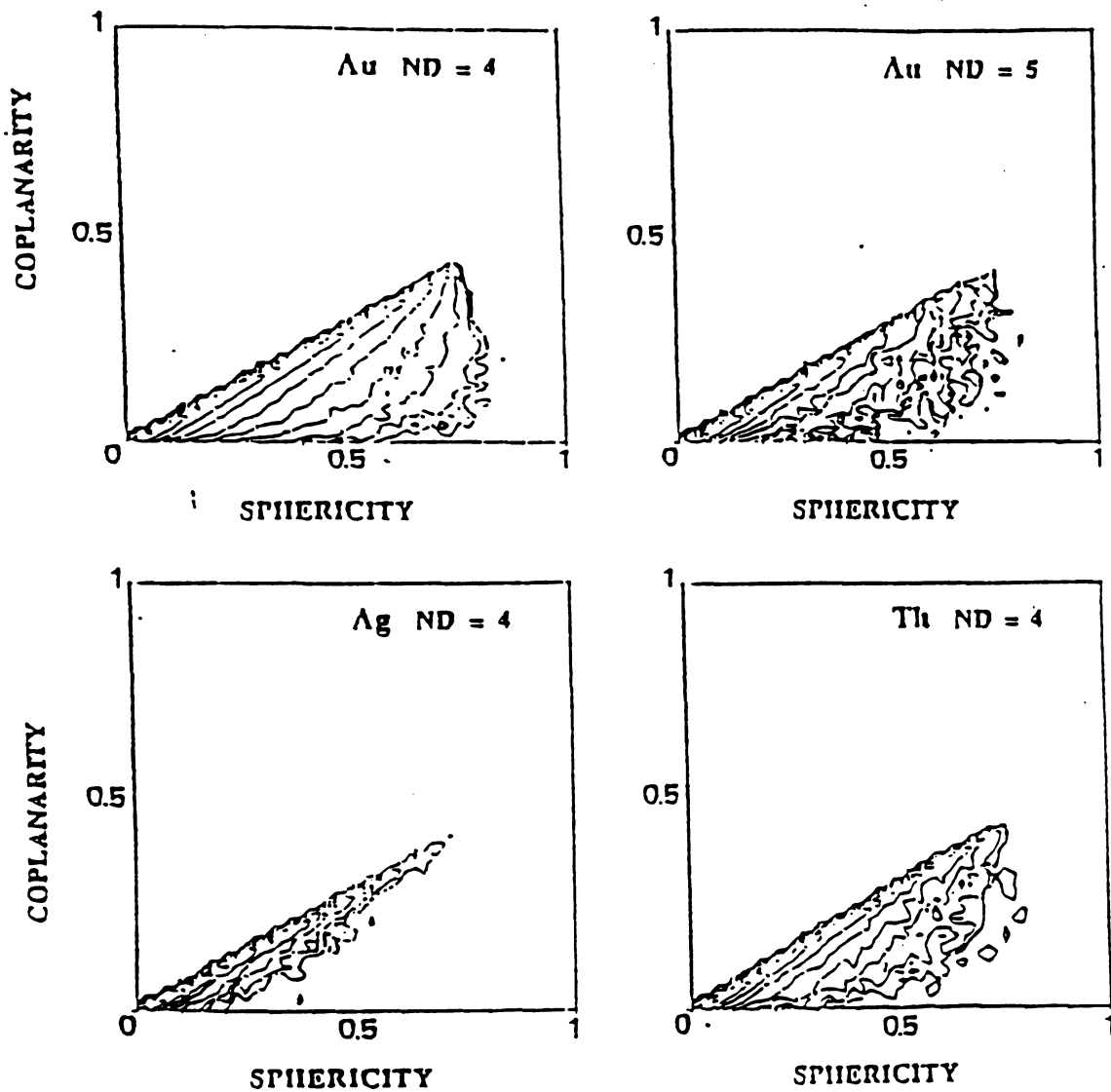


Figure III.18: Shape analysis for data from the reaction 43 MeV/nucleon Kr + Au, Ag, and Th. The  $ND$  value represents the number of IMFs detected [Boug89a].

The last group that is actively studying the question of the time scale of nuclear disassembly is another group from LBL. This group utilizes a forty-eight element phoswich array to study projectile fragmentation. The array is assembled in a seven-by-seven configuration with the center element removed to allow the beam to exit. The 88-inch cyclotron at LBL provides C, N, O, and Ne beams which are incident on Au targets at 32.5 MeV/nucleon. Only events in which the sum of the charges near beam velocity is equal to the charge of the projectile are analysed. These events are sorted by breakup channel and identified with an excitation energy, which is determined by the relative energy between the fragments. The researchers compared the production cross-sections for the various channels and the excitation energy as a function of the Q-value. From this analysis they suggest that the projectile and target each receive the same amount of excitation energy and do not reach a thermodynamic equilibrium. The excitation energy of the projectile varies from 1 to 4 MeV/nucleon and should span the regime where multi-fragmentation has been predicted to occur. The data are analysed using an event shape analysis in order to determine the decay process. Figure III.19 displays the data for a single breakup channel compared to predictions of both a sequential decay and a multi-fragmentation [Poul89]. The researchers find that the sequential decay more accurately reproduces all of the observed breakup channels.

## D Conclusions

Multi-fragmentation is expected to appear in reactions for which the internal excitation exceeds 4 MeV/nucleon. The theoretical calculations predict that at this excitation energy the nucleus should reach a region of instability. The fluctuations in energy and in density will cause bonds within the nucleus to be broken. The breaking of internal bonds leads to crack formation and then to fragmentation. The

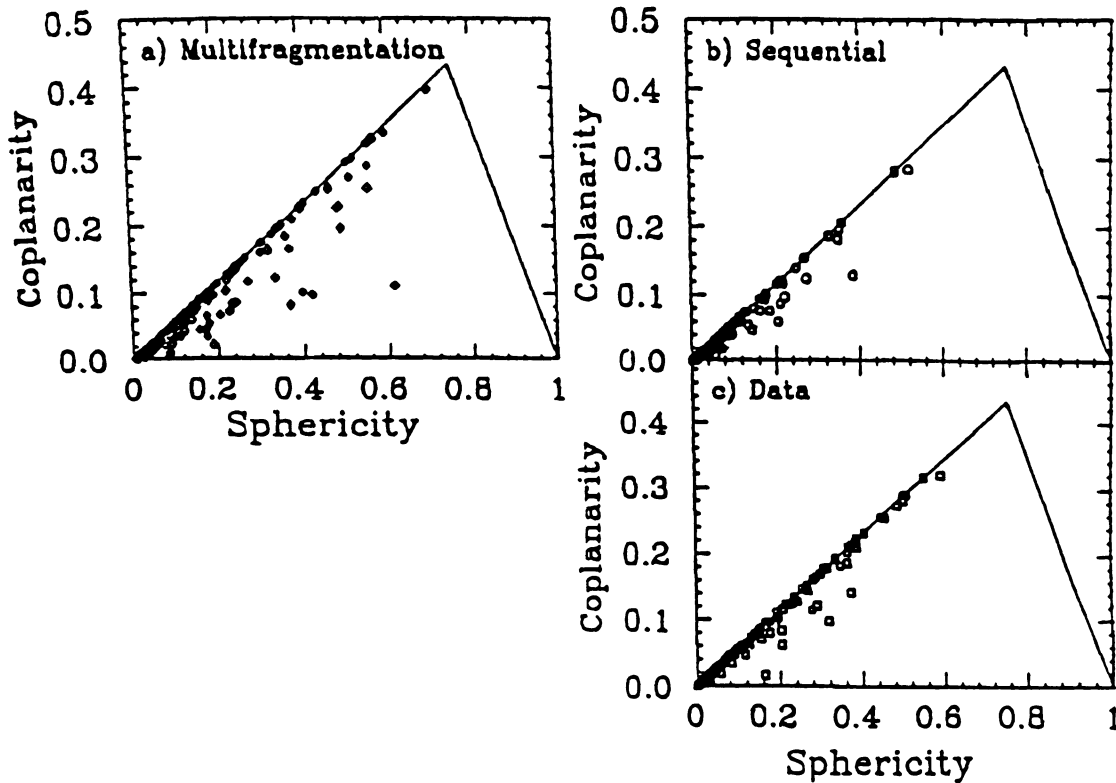


Figure III.19: Shape analysis plots for the breakup of  $^{16}\text{O}$  into four  $\alpha$ s (c). For comparison, the predictions from a multi-fragmentation (a) and a sequential decay (b) are shown [Poul89].

theories predict that there should be a dramatic rise in the IMF multiplicity as well as temperature anomalies associated with the onset of multi-fragmentation. These anomalies correspond to increases in the excitation energy of a system without apparent increases in the temperature. Since other processes may also lead to increased IMF multiplicities and nuclear temperatures can not be measured directly, the search for evidence for the existence of a multi-fragmentation process has concentrated on observables associated with the time scale of the disassembly process. These observables include relative velocity distributions for back-to-back fragments, small angle velocity correlations, and event shape distributions. The experimental studies have concentrated on the region of excitation energy from 1 to 6 MeV/nucleon, which encompasses all of the predicted threshold energies. Though a rise in IMF multiplicities is observed in this energy region, no experiment has yet been able to exclude the pos-

sibility that a sequential decay process is the preferred decay mechanism. Attempts to estimate the time scale of the decay process have ranged from 300 to 1000 Fm/c. A simultaneous process should show a lifetime of under 50 Fm/c. Therefore, the existence of a simultaneous multi-fragmentation decay mechanism at intermediate energies has not yet been confirmed.

# Chapter IV

## Multi-Particle Correlations

### A Introduction to Multi-particle Observables

The study of multi-particle observables in heavy ion nuclear physics was introduced by one of the early large detector array systems for nuclear physics, the *Plastic Ball/Wall* [Bade82]. The observables that have received the most attention are collective flow and ratios of production cross-sections for various particle types as a function of the observed multiplicity [Gutb89]. These observables probe questions concerning the equation of state of nuclear matter. A question that has received a great deal of theoretical attention recently has been the existence of a multi-fragmentation decay mechanism that occurs as the nuclear system enters a region of mechanical instability [Bert83]. This multi-fragment reaction mechanism is expected to become dominant at bombarding energies above the Fermi energy [Rand81, Fai83]. This process will be characterized by a simultaneous disassociation of the system into many fragments. Early attempts to identify this mechanism relied only on multiplicity distributions [Doss87, Klot87, Harr87]. It has, however, been demonstrated that information from such distributions or other inclusive observables (requiring the detection of only a single fragment) alone is insufficient to identify conclusively multi-fragmentation [More88, Lópe89a]. Models incorporating other processes also

can produce these inclusive results. A definitive identification of this process requires study of an observable which is sensitive to the time scale of the disassembly and not merely to the final distributions of fragments and their energies [Lópe89a, Jaca88]. Recently, experimental studies attempting to identify evidence of this process have been conducted [Boug88, Troc87, Klot89, Poch88, Poul89, Harm89]. Only one of these studies has claimed to see evidence of a multi-fragmentation process [Klot89], and even that result is disputed [Poch89a]. These studies have surveyed the range of excitation energies from 1 to 6 MeV/nucleon, which is where the theoretical analyses had predicted that the onset of multi-fragmentation would occur. The work that is presented in this chapter searches for evidence of multi-fragmentation on central collisions from the system  $Ar + V$  at bombarding energies of 35 to 85 MeV/nucleon. If one assumes complete fusion, the excitation energies attained during these collisions would be higher than those that have been previously examined. Evidence for the onset of multi-fragmentation is found within this bombarding energy range for 'symmetric systems'.

In this chapter we use an observable that has recently been proposed [Lópe89a] to be sensitive to the time scale of the fragmentation process. This observable is the spheroidal shape of the envelope of the energy flow from the reaction, which is defined as the event shape. This shape will be influenced by the dynamics of the break-up. The emission of fragments from a simultaneous multi-fragmentation process will be isotropic in the center-of-mass frame, and therefore the events should be spherical in shape in the limit of infinite multiplicity. Conversely, sequential emission should lead to an event shape that is elongated along one axis due to the kinematical constraints of the binary decays and the time ordered emission of the fragments. In the following analysis, I shall compare the average event shapes extracted from my experimental data to predictions from simulations of both a sequential decay and a simultaneous

multi-fragmentation.

## B Experimental Details

All the results described in this section were derived from experimental data acquired using the MSU  $4\pi$  Array [West85]. I have studied the  $^{40}\text{Ar} + ^{51}\text{V}$  system with beams provided by the K500 and K1200 cyclotrons. Incident energies of 35, 45, 55, 65, 75, and 85 MeV/nucleon were studied. For the experiments described in this work, the array was instrumented with 215 phoswich [Wilk52] detectors. The 170 main *ball* detectors covered an angular range from  $20^\circ$  to  $160^\circ$ , while the 45 detectors of the *forward array* extended the coverage in from  $20^\circ$  to  $7^\circ$ . The minimum energy required for a charged particle to be detected was determined by the pulse height necessary to fire the discriminators. This is related to the light generated by the stopping particle. In the ball detectors, this energy is approximately 4 MeV/Z, where Z is the charge of a given fragment (Appendix B describes in greater detail the nature of the light response of the scintillators). However, in order for a fragment to be identified it had to penetrate into the stopping scintillator, which required approximately 20 MeV/nucleon. For identified particles, we had isotopic resolution for  $Z=1$  fragments and charge resolution up to  $Z=6$ . Particles with energies from 4 MeV/Z to 20 MeV/nucleon were stopped in the  $\Delta E$  scintillator and were assigned an estimated charge and energy for this analysis. In the forward array detectors, the minimum energies required were 3 MeV/Z for detection and 12 MeV/nucleon for identification. For identified particles, we had isotopic resolution for  $Z=1$  fragments and charge resolution up to  $Z=18$ . Particles that were stopped in the  $\Delta E$  scintillator were assigned an estimated charge and energy. Further details of the detector specifications, the energy calibration of the scintillators, and the pre-analysis of the raw data are given in the appendices of this thesis.

The multi-particle analysis that was performed on the events from these data assumed only a single source for the emitted charged-particles. Therefore, an effort was made to minimize the contributions from both the target and the projectile remnants. The minimum energy thresholds effectively eliminated the target velocity data, however, a significant projectile component could be identified in the forward array detectors. Therefore, the data from the forward array were used only for the determination of the impact parameter and not in the event shape analysis. This suppressed the contribution of projectile-like spectator matter.

## 1 Exp 87008A

The first experiment using the MSU  $4\pi$  Array was performed in April of 1988. For this experiment, the K500 provided a 35 MeV/nucleon  $^{40}\text{Ar}$  beam of 70–100 electrical picoamps of current which was incident on targets of  $^{51}\text{V}$  ( $3.34 \text{ mg/cm}^2$ ) and  $^{197}\text{Au}$  ( $7.02 \text{ mg/cm}^2$ ). In addition, experimental runs were taken with a blank target frame and with no beam in order to measure the background due to beam halo hitting the aluminum target frame and due to cosmic rays induced events. The triggering requirement for these runs was an adjustable number of ball detectors ( $M_b$ ) firing in coincidence. The levels were set at  $M_b$  greater or equal to one, two, five, seven, and ten.

## 2 Exp 87008B

The second experiment using the MSU  $4\pi$  Array was performed in June of 1988. For this experiment, the K500 provided a 50 MeV/nucleon  $^{12}\text{C}$  of approximately 20–60 electrical picoamps of current. This beam was incident on targets of  $^{12}\text{C}$  ( $2.00 \text{ mg/cm}^2$ ), and  $^{197}\text{Au}$ . The triggering requirement for this run was either  $M_b$ , or an adjustable number of forward array detectors ( $M_{FA}$ ). The levels were set at  $M_b$

greater or equal to one, two, or five, and  $M_{FA}$  greater or equal to one or two.

### 3 Exp 88012

The third and fourth experiments using the MSU  $4\pi$  facility were collaborations with Hope College and Chalk River National Laboratory. The results from these experiments are not reported in this thesis. Following these experiments the detector array was moved to an interim vault location. The fifth experiment was performed in April of 1989. For this experiment, the K1200 provided beams of 45, 55, 65, 75, and 85 MeV/nucleon  $^{40}\text{Ar}$  of approximately 100 electrical picoamps of current. The energy systematics were extended in January of 1990 to include a 100 MeV/nucleon beam. These beams were incident upon a  $^{51}\text{V}$  target. For this experiment the trigger units had been improved so that  $M_b$  and  $M_{FA}$  could be added together to create an overall *system* multiplicity signal ( $M_S$ ). The triggering levels were set at  $M_S$  greater or equal to one, two, and five.

## C Event Characterization

One of the most powerful techniques available to an experimenter who is working with a semi-exclusive data set is the ability to characterize individual events and make selections based on the observed features. The MSU  $4\pi$  Array provides researchers with this type of data set. First, one must decide what parameters one wishes to use for categorizing the events and then determine which observables will provide information concerning those parameters.

The parameter that was chosen to characterize the events for this analysis was the magnitude of the impact parameter. This determines the degree of overlap between the target and the projectile nuclei and is related to the violence of the collisions

and the number of constituents that were exposed to the full force of the impact. The matter on the fringes of the colliding nuclei provides little information about the hottest and most dense phase of the interaction, because the regions that do not overlap do not interact strongly [West76]. The magnitude of the impact parameter is of great importance for separating effects which arise in the most violent collisions from effects that are common in the peripheral interactions.

The approach that we have taken for measuring the magnitude of the impact parameter on an event-by-event basis is to place cuts on the number of charges measured in the mid-rapidity region [Ogil89a]. We measure the total detected charge because our detector is sensitive to charge and not to mass, and we assume that the distribution of neutrons leaving the reaction will be similar to the measured distribution of protons. Only the charge detected in the mid-rapidity range ( $0.75 y_{target} < y_{fragment} < 0.75 y_{projectile}$ ) is counted, because it is assumed that the matter traveling at rapidities either higher or lower than those limits will be associated either with the disassembly of the projectile or the target remnant. This observable, therefore, is a measure of the size of the interaction region, which is determined by the impact parameter.

The reliability of this observable as a measure of the impact parameter has been studied using the *event simulator* **FRESCO** [Fai86]. This code uses statistical emission from three thermal moving sources of nuclear fragments. The *fireball geometry* [West76] is used to assign sizes and velocities for the different sources. The code conserves energy and momentum. We have used this code to produce events simulating the systems that we have studied experimentally. These events were then filtered through a software model of the MSU  $4\pi$  Array [Wils89]. This filter contains the minimum energy thresholds for detection and identification, the finite granularity, the regions which are not covered by detectors (either due to the finite thickness of the detector walls or due to gaps left to allow the beam to enter and exit the array),

the rejection of neutral particles, and the shadowing due to the target frame. We are therefore able to take a simulated event and determine exactly how it would have been seen by the  $4\pi$  Array. The mid-rapidity charge detected has been studied as a function of known impact parameter for these simulated events. Figure IV.1 displays a plot of the detected mid-rapidity charge versus the known impact parameter. The data are from a FREESCO simulation of Ca+Ca reactions at 40, 70, and 100 MeV/nucleon. The data points represent the average charge detected in the mid-rapidity region, while the error bars correspond to the width of the distributions. It should be noted that though the centroid of the mid-rapidity charge decreases as a function of impact parameter, the width of the distribution is quite large. Therefore, gating on the detected charge will yield a measure of the impact parameter ( $b$ ) that is accurate only to  $\pm 0.3 b_{max}$ , where  $b_{max}$  is defined as  $R_{target} + R_{projectile}$  (radii of the target and the projectile). We have chosen to identify four impact parameter bins. Details of these bins are given in table IV.1. Figure IV.2 displays the percentages that various impact parameters contribute to each bin (the data are from FREESCO simulations).

## D Event Shape Analysis

The data from these experiments have been studied using an event shape analysis technique. The event shape parameters allow the experimenter a quantitative measure of the general shape of the distribution of outgoing fragments from the reaction. The shape analysis is used to determine if the fragment distribution contains some amount of anisotropy. The analysis technique requires the observed event to be transformed into the center-of-mass reference frame. Figure IV.3a displays a typical event in the laboratory frame while Figure IV.3b shows the same event in the rest frame. Having transformed an event into the center-of-mass frame, one then constructs a kinetic flow

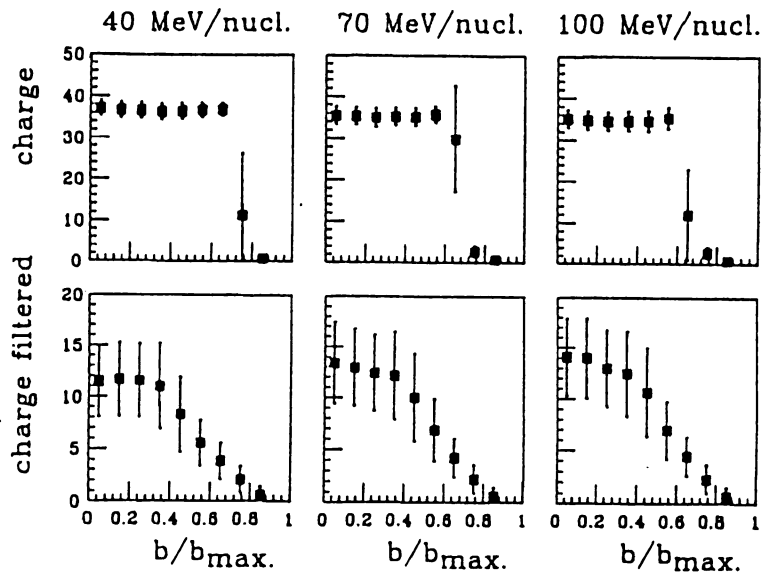


Figure IV.1: The mid-rapidity charge as a function of the known impact parameter. Both the total charge and the quantity that passed the filtering requirements are displayed [Ogil89a].

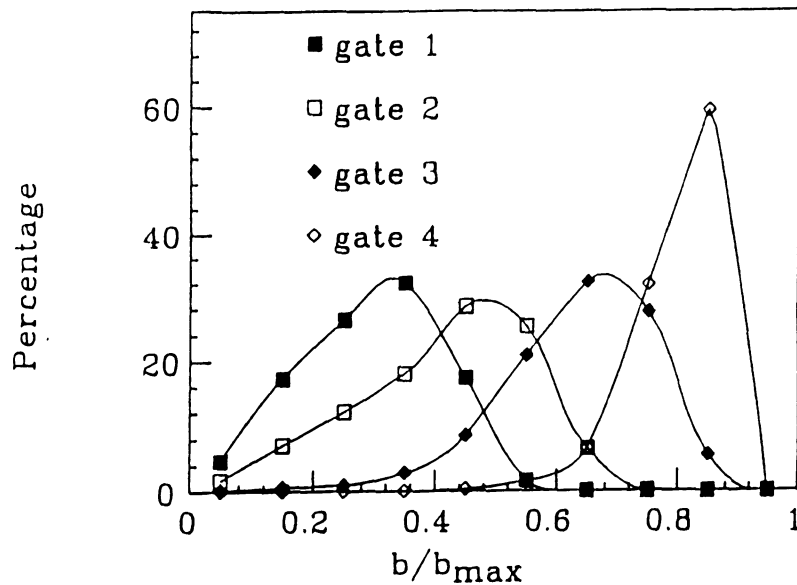


Figure IV.2: The relative contributions that different impact parameters make to each of the bins [Ogil89a].

Table IV.1: The mid-rapidity charge gates for the various impact parameter bins for the various systems that were studied.

System	Incident Energy	Bin 4 peripheral	Bin 3 mid- peripheral	Bin 2 mid- central	Bin 1 central
$^{40}\text{Ar} + ^{51}\text{V}$	35 MeV/n	0-2	3-6	7-11	>12
$^{40}\text{Ar} + ^{51}\text{V}$	45 MeV/n	0-2	3-6	7-11	>12
$^{40}\text{Ar} + ^{51}\text{V}$	55 MeV/n	0-2	3-7	8-12	>13
$^{40}\text{Ar} + ^{51}\text{V}$	65 MeV/n	0-2	3-7	8-12	>13
$^{40}\text{Ar} + ^{51}\text{V}$	75 MeV/n	0-2	3-7	8-12	>13
$^{40}\text{Ar} + ^{51}\text{V}$	85 MeV/n	0-2	3-7	8-12	>13
$^{40}\text{Ar} + ^{51}\text{V}$	100 MeV/n	0-2	3-7	8-12	>13
$^{40}\text{Ar} + ^{197}\text{Au}$	35 MeV/n	0-2	3-7	8-13	>14
$^{12}\text{C} + ^{12}\text{C}$	50 MeV/n	0-1	2-4	5-7	>8

tensor by summing over the fragments detected in a given event as follows:

$$\mathbf{F} = \sum_{i,j} F_{ij} \quad (\text{IV.1})$$

where

$$F_{ij} = \sum_{n=1}^M \frac{p_i^n p_j^n}{2m_n} \quad (\text{IV.2})$$

where  $p_i^n$  denotes the  $i$ th momentum component of the  $n$ th particle,  $m_n$  denotes the particle's rest mass, and  $M$  corresponds to the multiplicity of the event. Since this analysis is done over different fragment masses for each event, the  $\frac{1}{2m_n}$  weighting must be used to ensure that heavy fragments do not dominate the kinetic flow tensor.

In many physical problems involving tensors, it is desirable to carry out an orthogonal similarity transformation to reduce the matrix to a diagonal form, where all non-diagonal elements are equal to zero. For analysis of the kinetic flow tensor, the problem is to re-orient the co-ordinant axes in space such that the non-diagonal elements vanish. In the new co-ordinant system, the axes correspond to the *principal axes* of a 3-dimensional ellipsoid that approximates the kinetic flow distribution. The

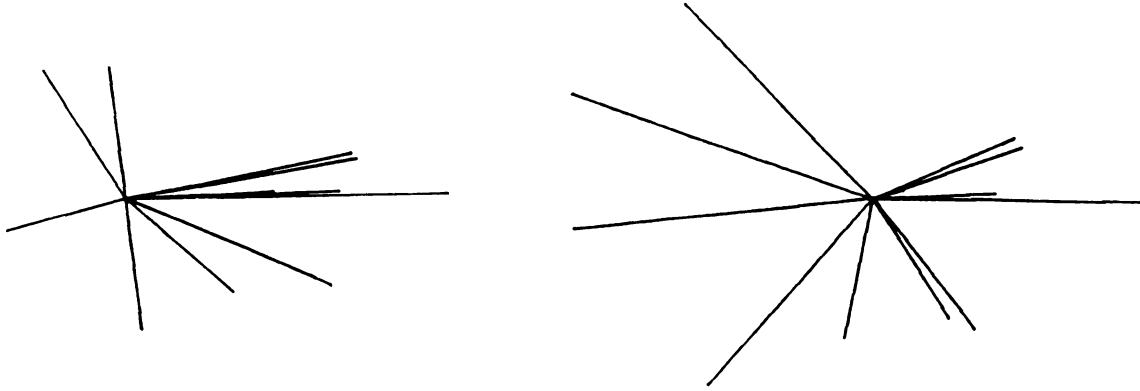


Figure IV.3: Illustration of a typical event. a) The lengths of the vectors corresponds to the velocity of the particles in the laboratory reference frame. b) The same event transformed to the center-of-mass reference frame.

directions and lengths of the principal axes is given by the orthonormal eigenvectors ( $\mathbf{u}_i$ ), and the eigenvalues ( $t_i$  of  $\mathbf{F}$  given by the equation:

$$\mathbf{F} = t_1 \mathbf{u}_1 \mathbf{u}_1^\dagger + t_2 \mathbf{u}_2 \mathbf{u}_2^\dagger + t_3 \mathbf{u}_3 \mathbf{u}_3^\dagger. \quad (\text{IV.3})$$

The eigenvalues, which correspond to the diagonal elements of the diagonalized tensor, satisfy the cubic equation:

$$t_i^3 + a_2 t_i^2 + a_1 t_i + a_0 = 0 \quad (\text{IV.4})$$

where

$$a_0 = F_{11}F_{23}^2 + F_{22}F_{13}^2 + F_{33}F_{12}^2 - F_{11}F_{22}F_{33} - 2F_{12}F_{13}F_{23} \quad (\text{IV.5})$$

$$a_1 = F_{11}F_{22} + F_{11}F_{33} + F_{22}F_{33} - F_{12}^2 - F_{13}^2 - F_{23}^2 \quad (\text{IV.6})$$

$$a_2 = -F_{11} - F_{22} - F_{33}. \quad (\text{IV.7})$$

Using auxiliary variables  $p$  and  $r$  as defined below, the three solutions to the cubic equation can be written as follows:

$$t_i = -\frac{1}{3}a_2 + 2p \cos\left[\frac{1}{3} \arccos(r/p^3) + (i-1)\frac{2}{3}\pi\right] \quad (\text{IV.8})$$

$$p = \frac{1}{3} \sqrt{a_2^2 - 3a_1} \quad (\text{IV.9})$$

$$r = \frac{1}{6}(a_1 a_2 - 3a_0) - \frac{a_2^3}{27} \quad (\text{IV.10})$$

Specifically, the three eigenvalues are:

$$t_1 = -a_2/3 + 2p \cos\left(\frac{1}{3} \arccos(r/p^3)\right) \quad (\text{IV.11})$$

$$t_2 = -a_2/3 + 2p \cos\left(\frac{1}{3} \arccos(r/p^3) + 2\pi/3\right) \quad (\text{IV.12})$$

$$t_3 = -a_2/3 + 2p \cos\left(\frac{1}{3} \arccos(r/p^3) + 4\pi/3\right) \quad (\text{IV.13})$$

The eigenvalues are then ordered by magnitude ( $t_1 < t_2 < t_3$ ) and used to define three reduced quantities [Gyul82]:

$$q_i = \frac{t_i^2}{\sum_{j=1}^3 t_j^2}. \quad (\text{IV.14})$$

In effect, the eigenvalues have been 'normalized' such that  $q_1 + q_2 + q_3 = 1$  for all distributions. From these reduced quantities, the sphericity,  $S = \frac{3}{2}(1 - q_3)$ , and the coplanarity,  $C = \frac{1}{2}\sqrt{3}(q_2 - q_1)$  parameters as defined by Fai and Randrup [Fai83] and applied to this problem by López and Randrup [Lópe89a] are determined.

The orthonormal eigenvectors of the tensor can be evaluated in spherical coordinates using the following calculations:

$$c_i = \frac{(F_{11} - t_i)(F_{33} - t_i) - F_{13}^2}{F_{12}F_{13} - F_{23}(F_{11} - t_i)} \quad (\text{IV.15})$$

$$\theta_i = \arccos(1/\sqrt{1 + c_i^2 + (t_i - F_{33} - F_{23}c_i)^2/F_{13}^2}) \quad (\text{IV.16})$$

$$\phi_i = \arctan(c_i F_{13}/(t_i - F_{33} - F_{23}c_i)) \quad (\text{IV.17})$$

The eigenvectors,  $\mathbf{u}_i = (1, \theta_i, \phi_i)$ , of the kinetic flow tensor represent the direction of the axes that best approximate a spheroidal envelope of the outgoing energy flow vectors of the fragments. The eigenvalues are related to the lengths of these principal

axes. The sphericity parameter represents the relative strength of the third or major axis with respect to the two other axes and is a measure of the amount of elongation. A spherical distribution would have three equal axes therefore,  $q_1 = q_2 = q_3 = \frac{1}{3}$ , which results in a sphericity equal to 1.0. The coplanarity parameter represents the asymmetry between the two minor axes, and is a measure of the degree of flattening of the spheroid. A spherical distribution would have a coplanarity of 0.0, while a flattened distribution would have an extremely small  $q_1$  axis, and therefore, the coplanarity parameter will be large. The data presented in this thesis are in the form of sphericity versus coplanarity (S-C) distributions and the centroids of these distributions, and conclusions will be based upon comparisons between experimental data and predictions from simulations.

The sphericity parameter can vary from 0 to 1 while the coplanarity can vary from 0 to  $\sqrt{3}/4$ . Figure IV.4 displays the S-C space. The triangular region formed by the lines connecting the points at (0,0), (0.75, 0.413), and (1,0) defines the limits of the space. The different regions of the space correspond to different distribution shapes. The origin (0,0) corresponds to a 1-dimensional object. The line from (0,0) to (.75, $\sqrt{3}/4$ ) contains the possible 2-dimensional ovals. The rest of the space is filled by 3-dimensional spheroids.

The importance of transforming the event into the reference frame of the emitting source is demonstrated by Figure IV.5. This figure displays the average sphericity parameter extracted from a set of La+La streamer chamber data [Krof89]. The velocity of the reference to which the data are boosted is varied. The maximum average sphericity value is extracted for a boost velocity of 0.18c ( $V_{CM} = 0.18 c$ ). The sphericity value is depressed when an incorrect transformation is performed because this induces a perceived motion of the entire system, which produces an artificial elongation in the direction of the transformation.

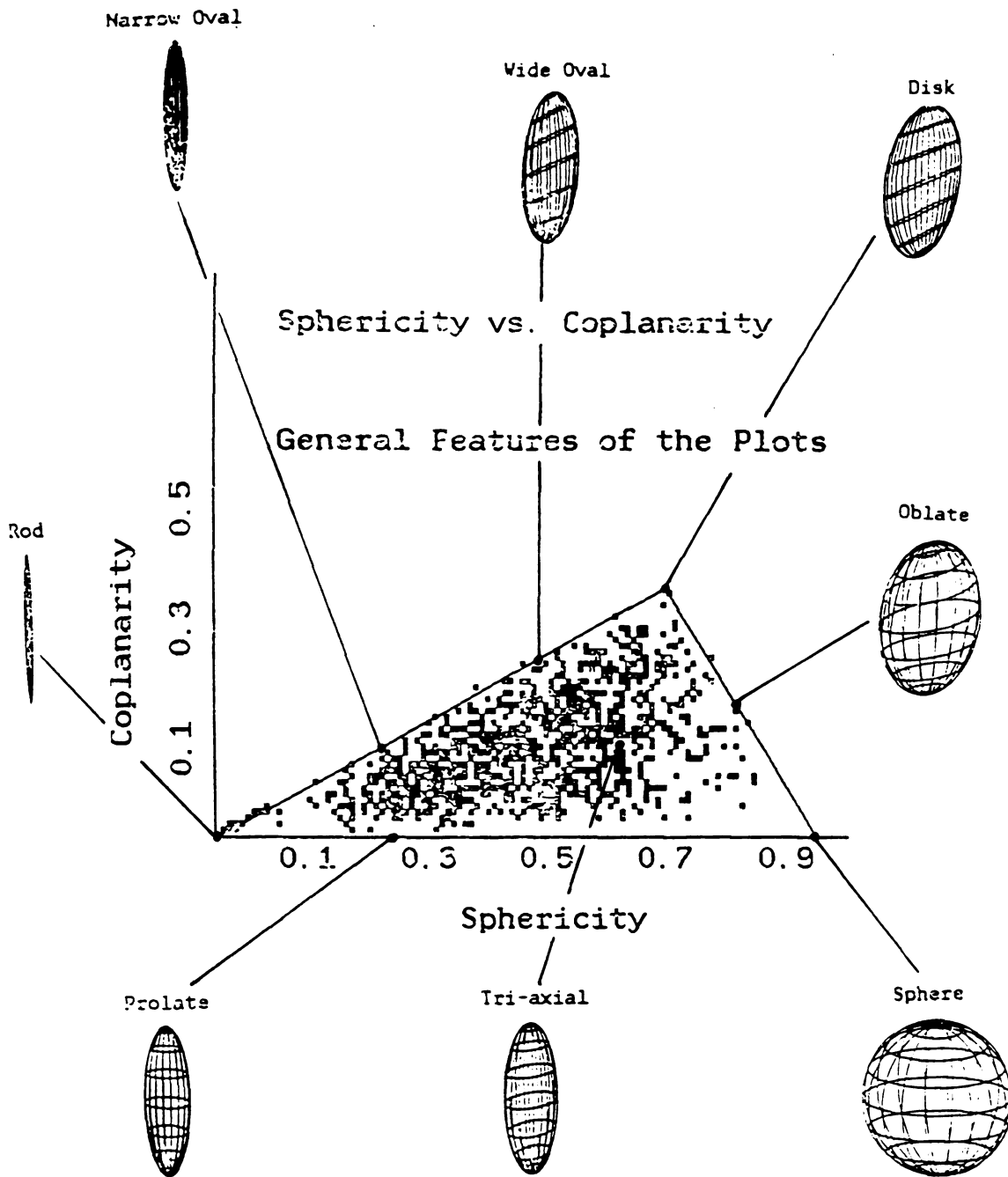


Figure IV.4: A display of which areas of the S-C space correspond to which spheroidal shapes.

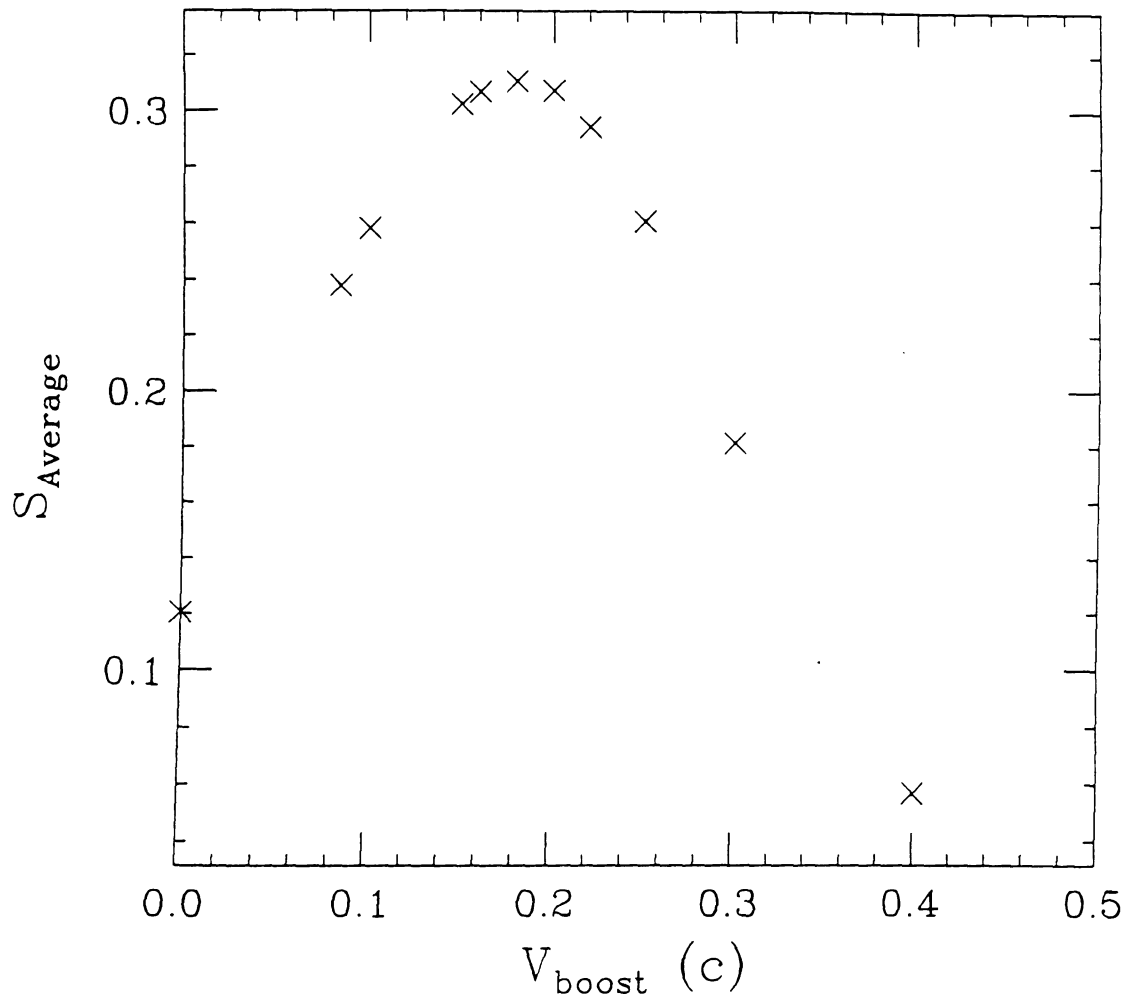


Figure IV.5: The average sphericity parameter extracted from a set of 70 MeV/nucleon La+La data as a function of the velocity with which the data were transformed.

## E Events Shape Distributions as a Function of Incident Energy

The Ar+V system was studied for a range of beam energies from 35 to 85 MeV/nucleon. We have studied the event shape for central events from these reactions and the distributions are displayed in Figures IV.6 to IV.11. For all of the beam energies the mid-rapidity charge cuts sampled events from similar impact parameters. The positions of the cuts changed because the detection efficiency of the array varies with the average energy of the exit fragments. The event shape distributions for all six of the beam energies are peaked along the 2-dimensional axis. The average event shape can be qualitatively categorized as a flattened prolate spheroid. The widths of the distributions get broader as the energy of the beam is increased. The centroids are listed in Table IV.2. Though the primary effect that causes this increase in the

Table IV.2: The average values for the sphericity and coplanarity parameters from the analysis of central collisions from the system  $^{40}\text{Ar} + ^{51}\text{V}$  at six different beam energies.

Incident Energy	$S_{ave}$	$C_{ave}$
35 MeV/n	$0.2826 \pm 0.0009$	$0.1264 \pm 0.0004$
45 MeV/n	$0.3025 \pm 0.0005$	$0.1338 \pm 0.0002$
55 MeV/n	$0.3211 \pm 0.0005$	$0.1384 \pm 0.0002$
65 MeV/n	$0.3452 \pm 0.0006$	$0.1433 \pm 0.0003$
75 MeV/n	$0.3496 \pm 0.0011$	$0.1439 \pm 0.0006$
85 MeV/n	$0.3826 \pm 0.0014$	$0.1492 \pm 0.0007$

average sphericity is the increase in the average multiplicity as a function of beam energy, it shall be demonstrated that the lower energies exhibit an anisotropic emission of fragments. This anisotropy in the average event shape can be attributed to the timescale of the decay mechanism.

These experimental distributions can be naively compared to those calculated by

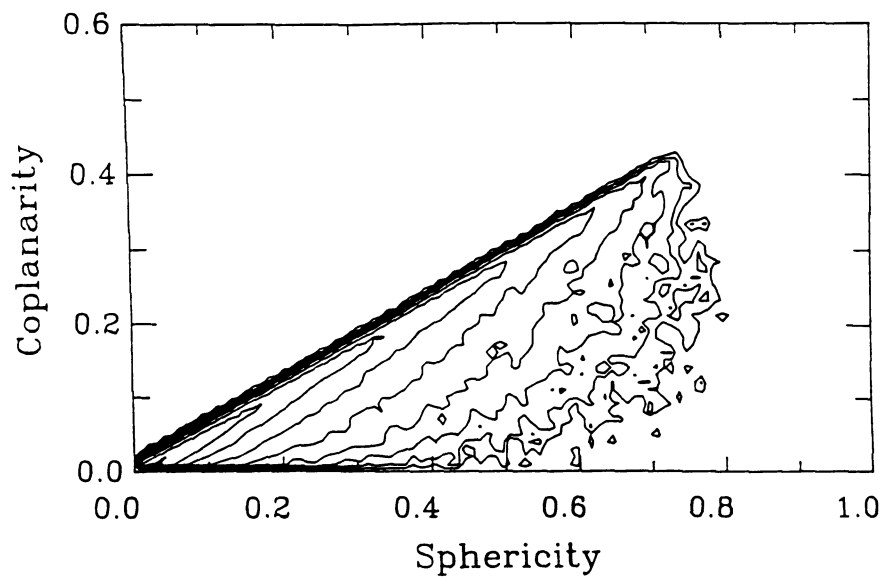


Figure IV.6: A contour plot of the event shape distribution gated on central events from the system 35 MeV/nucleon  $^{40}\text{Ar} + ^{51}\text{V}$ .

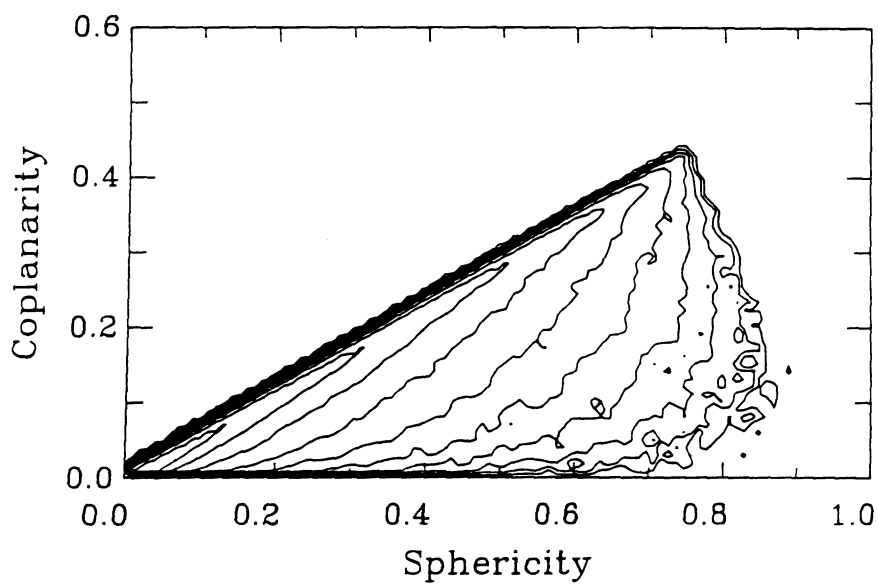


Figure IV.7: A contour plot of the event shape distribution gated on central events from the system 45 MeV/nucleon  $^{40}\text{Ar} + ^{51}\text{V}$ .

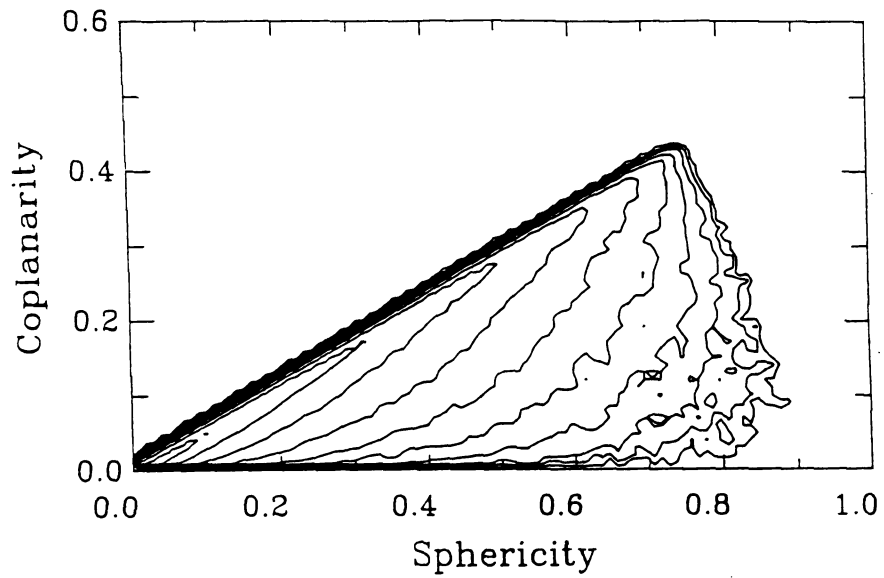


Figure IV.8: A contour plot of the event shape distribution gated on central events from the system 55 MeV/nucleon  $^{40}\text{Ar} + ^{51}\text{V}$ .

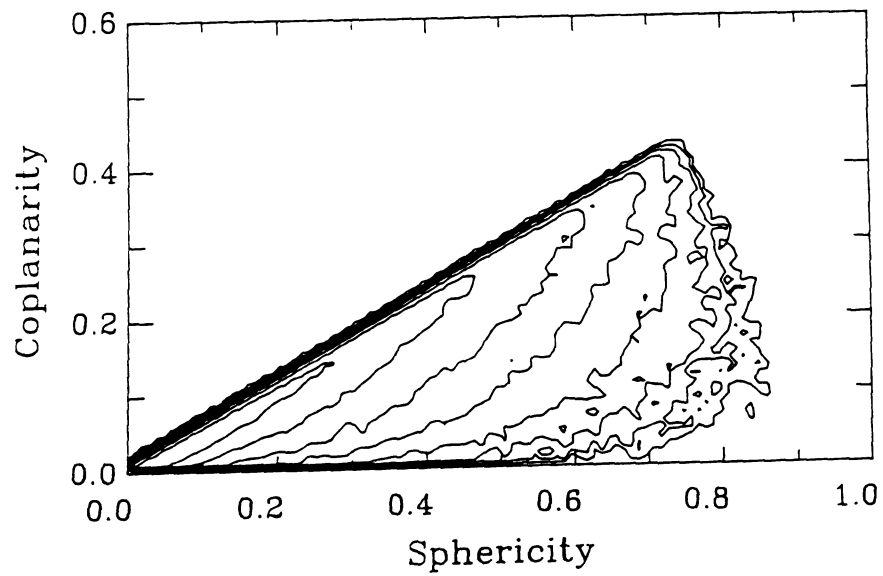


Figure IV.9: A contour plot of the event shape distribution gated on central events from the system 65 MeV/nucleon  $^{40}\text{Ar} + ^{51}\text{V}$ .

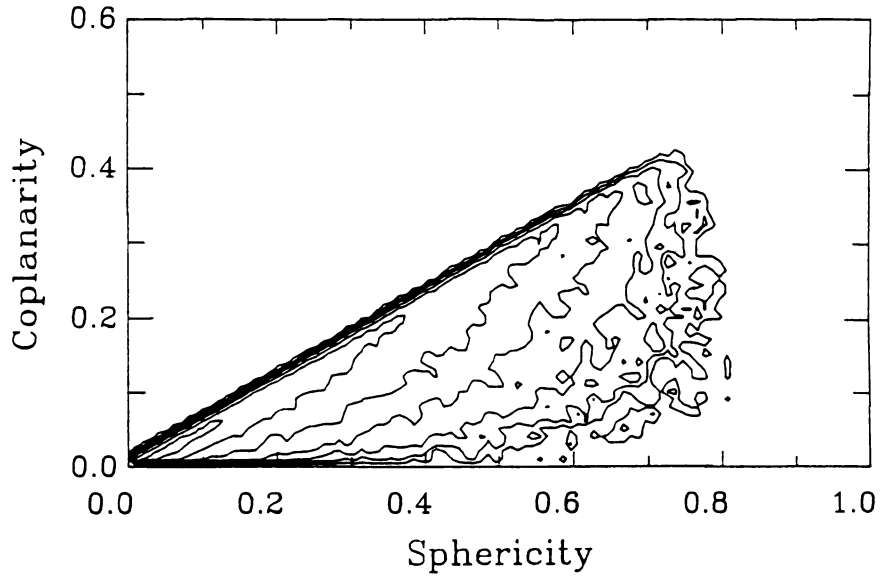


Figure IV.10: A contour plot of the event shape distribution gated on central events from the system 75 MeV/nucleon  $^{40}\text{Ar} + ^{51}\text{V}$ .

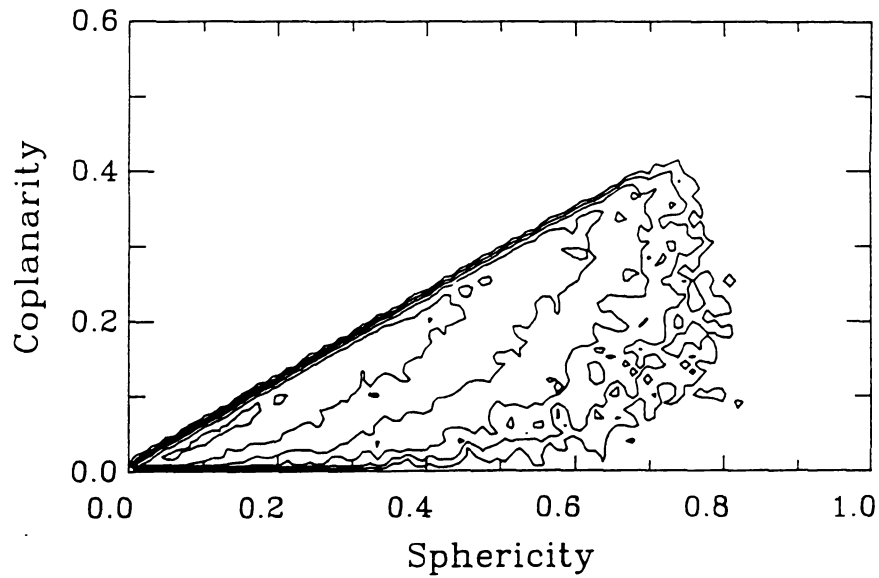


Figure IV.11: A contour plot of the event shape distribution gated on central events from the system 85 MeV/nucleon  $^{40}\text{Ar} + ^{51}\text{V}$ .

López and Randrup (refer to Figure III.8). One notes that the centroids for all six energies are below the prediction for the sequential decay. The theory has not been filtered, and therefore the average number of particles used in the event shape analysis is much greater than for the experimental data. It will be demonstrated that this multiplicity has a great effect on the extracted event shape. This comparison of the raw theory to the data highlights the importance of filtering the model predictions to account for the detection biases.

## F Comparison to Published Models

Though the event shape distributions may be interesting, it is not until a comparison to model predictions is made that one can begin to draw conclusions about the nature of the disassembly mechanism. The distributions shall be compared to models simulating a sequential emission of fragments and a simultaneous multi-fragmentation, which is defined as a purely isotropic form of disassembly.

### 1 First Order Observables

For the purpose of evaluating the overall performance of various models of nuclear disassembly a set of *first order observables* is introduced. These observables must be reproduced if one expects to be able to generate events that resemble those contained in the experimental data set. Discrepancies in these observables will cause differences in the multi-particle observables that are unrelated to the effect of interest. The observables that must be properly reproduced are the total detected multiplicity of charged particles (neutrons and gammas are excluded because the detector is insensitive to these particles), the multiplicity of fully identified charged particles (full identification requires the detected particle to have sufficient energy to penetrate into the slow scintillator), the mass distributions for hydrogen isotopes (the

only element for which isotopic resolution can be maintained after summing large numbers of detectors), the charge distribution of identified fragments, and the kinetic energy distributions for both protons and heliums. The total detected charged particle multiplicity of an event has an extremely strong effect on the event shape. It is essential to reproduce this quantity accurately. The identified multiplicity is a check on the accuracy of the energy distributions of a model. If the model is producing incorrect energy spectra at low energies, the ratio of the multiplicity of fully identified particles to total detected multiplicity will be incorrect. The tensor from which the sphericity and coplanarity are determined uses the momentum of each fragment, which is determined from the kinetic energy and mass of the fragment. It is therefore also important to identify accurately the mass of light fragments. For heavy fragments, isotopic resolution is less important, however one must reproduce the elemental distribution. The heavy fragments contribute the largest momentum vectors to the calculation and dominate the measured shape of an individual event. Though the ratio of the identified multiplicity to the total multiplicity tests the low end of the energy spectra, the top end must be checked as well. High energy light particles will dominate the event shape in the same manner as heavy fragments. The energy spectra define the apparent temperatures for the disassembling system. Models that assume thermal emission should reproduce the energy spectra.

Figure IV.12 displays the first order observables for the Ar + V reaction at 35 MeV/nucleon. Section a) of the figure displays the identified charged particle multiplicity. These particles must have more than the 20 MeV/nucleon energy which is necessary to penetrate into the stopping (slow) scintillator. Section b) displays the total charged particle multiplicity. This includes particles in the energy range from 4 MeV/nucleon to 20 MeV/nucleon that stop in the  $\Delta E$  (fast) scintillator. The mass distribution of light charged particles is shown in section c) and the charge distribu-

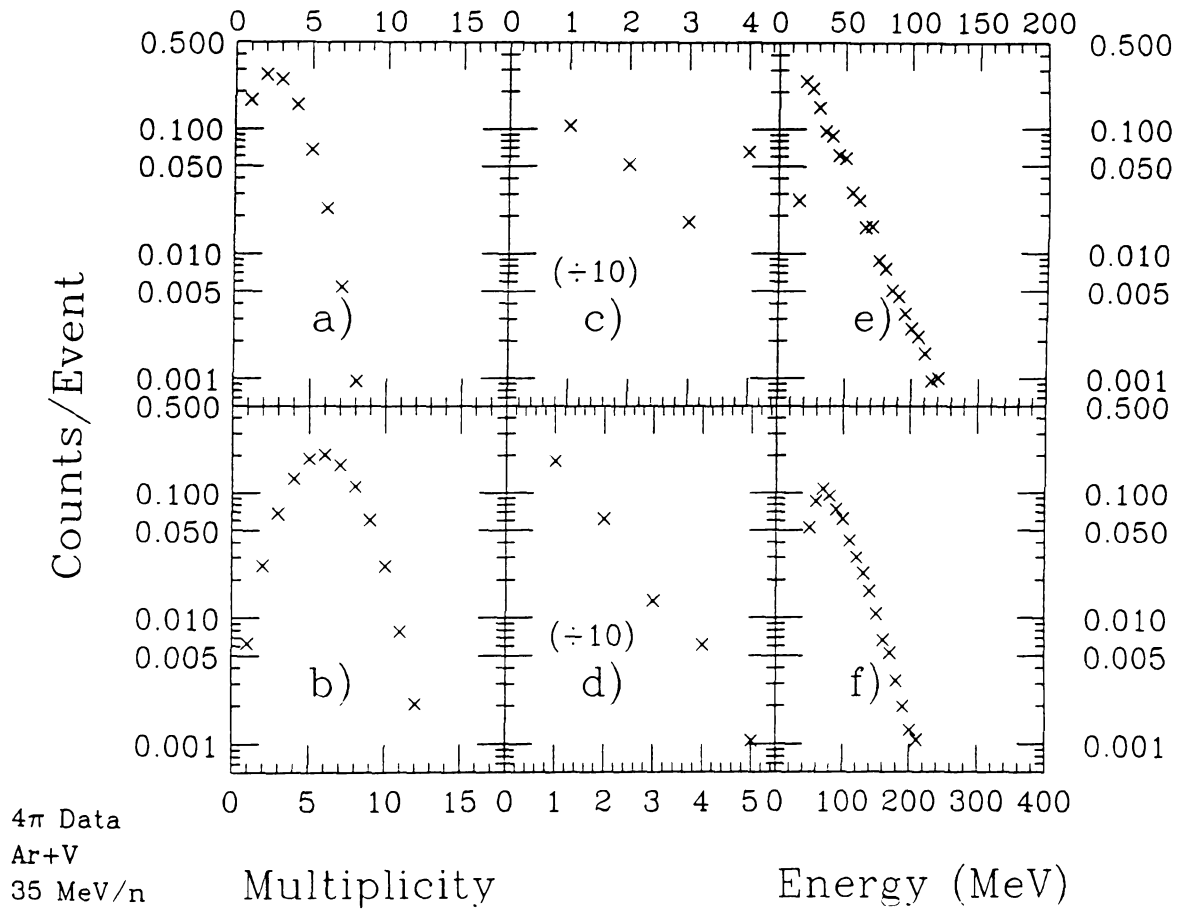


Figure IV.12: The first order observables for the system  $^{40}\text{Ar}+^{51}\text{V}$  at 35 meV/nucleon. a) The identified multiplicity, b) the total multiplicity, c) the mass distribution, d) the charge distribution, e) the proton kinetic energy spectrum, and f) the helium kinetic energy spectrum.

tion in section d). The proton and helium kinetic energy spectrum are displayed in sections e) and f) respectively. The energy has been transformed to the center-of-mass reference frame and summed over all angles. This figure represents the benchmark that a model must meet before the multi-particle observables can be compared.

## 2 GEMINI

*GEMINI* is a model for nuclear reactions that simulates a sequential binary fission process. It has been employed in several studies that have attempted to differentiate between sequential multi-fragment emission and simultaneous multi-fragmentation [Bowm87, Wozn88, Colo89, Poch89a, Poch89b, Trau89]. It is an extension of the Weizsacker model nuclear decay. The model was developed from the asymmetric fission work by Moretto. The details of the model are reviewed in a paper by Charity [Char88]. Since this model had received such wide scale use in similar analyses, it was the first simulation employed to describe this data set. Figure IV.13 demonstrates that this model is not satisfactory, because it fails to reproduce the first order observables. The model tends to produce too many protons, while failing to generate a sufficient number of IMFs.

## 3 López

López and Randrup have developed a simple model for sequential binary fission which they have employed as an alternative to multi-fragmentation in a paper that explored several possible analytical methods to differentiate experimentally the two processes [Lópe89a]. The model considers an excited nucleus in its rest frame. For a nucleus of mass  $A$ ,  $A/2$  possible exit channels are considered. For the channels with an odd number of nucleons, the extra nucleon is randomly determined to be either a neutron or a proton, therefore, the emitted fragments can never vary from the  $Z=N$  line

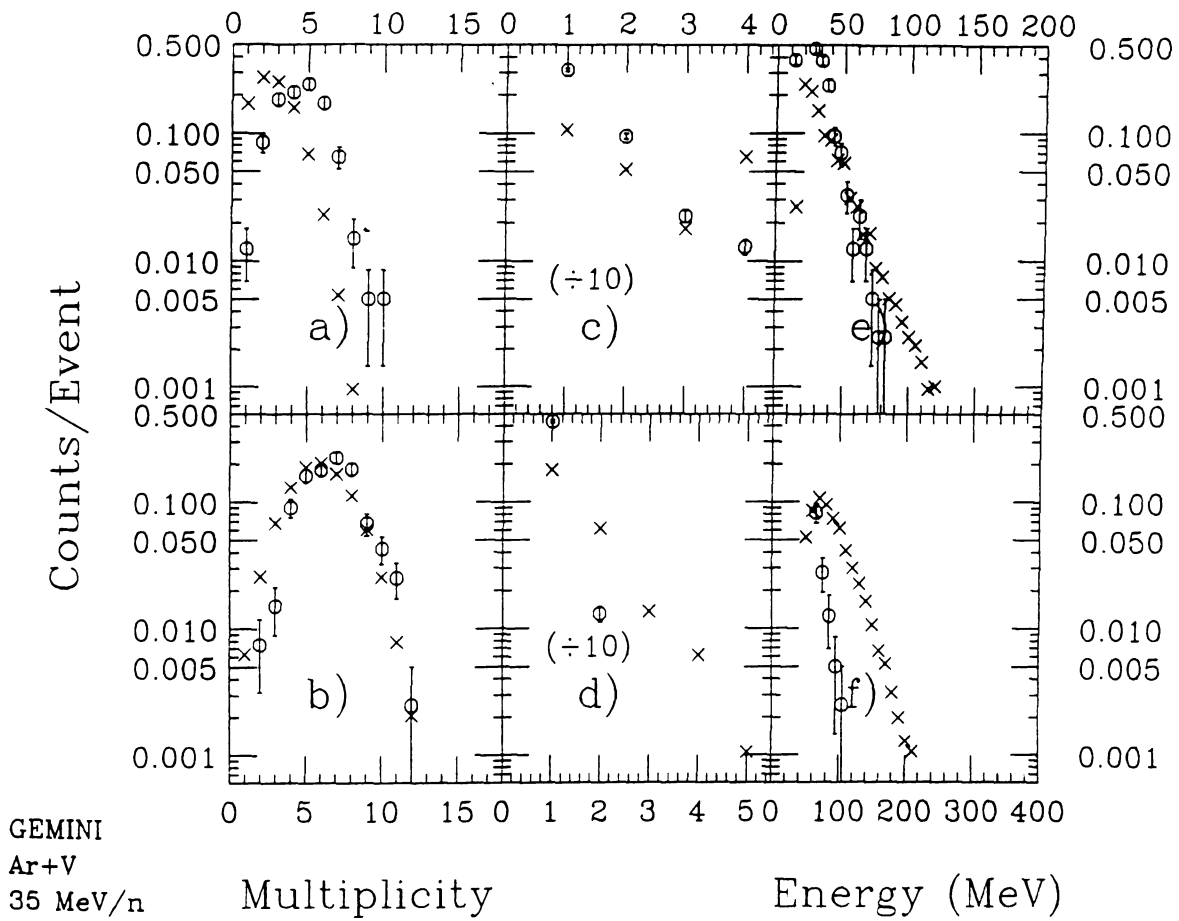


Figure IV.13: The results of the GEMINI simulation (circles) compared to the experimental data (crosses).

by more than a single unit. Additionally, emission of both neutrons and protons is considered for all decay decisions (except those for which emission of one of the two particles is forbidden - i.e.  ${}^2\text{He}$  decaying by neutron emission). The truncated list of exit channels is used to reduce the CPU time required by the simulation. For each exit channel considered, a fission barrier is calculated, and a relative probability determined for each channel based upon  $1/\text{lifetime}(\text{sec})$  for decay of the parent into a given exit channel. Having chosen a channel, an emission energy is determined. The directions are randomized, and the recoil determined to get the final momentum vectors for the two daughters. The daughters continue to decay until they either disassemble into their constituent nucleons or they no longer possess sufficient excitation energy to overcome the fission barriers. Using this routine, one is able to generate a set of events which can be compared to predictions from multi-fragmentation models.

Unfortunately, for the purposes of this analysis, the results from López's sequential binary fission model failed to reproduce the basic observables from the  $4\pi$  data set. Figure IV.14 displays the predictions from López's model against the experimental data at 35 MeV/nucleon. The main problem with López's model is that it tends to overproduce single low energy neutrons and protons. The model fails to produce the IMFs that are characteristic of the data at this energy. To be fair to López, the model was not designed to be used at these energies. The channel selection method may accurately describe a cold nuclear system, but when there is an abundance of excitation energy it does not reproduce the enhanced production of heavy clusters.

## G Other Effects That May Induce an Observed Elongation

López and Randrup suggested that a spherical average event shape could be used as a signature of multi-fragmentation [Lópe89a]. But this does not necessarily prove

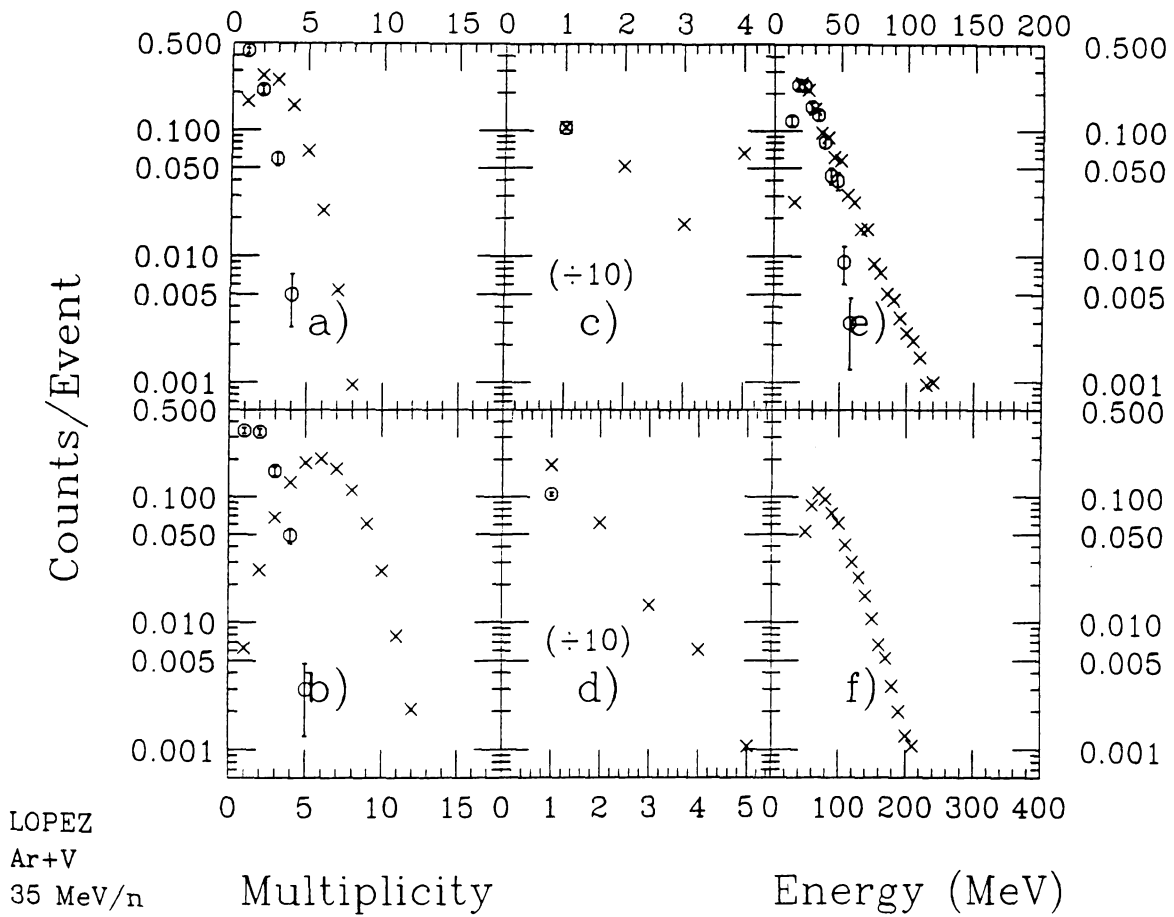


Figure IV.14: The results of López's simulation (circles) compared to the experimental data (crosses).

that an elongated event shape, as is observed in all of the systems that we have studied, can be used as evidence that a sequential disassembly process is at work. Several other effects that were not considered in López and Randrup's static analysis can also induce an elongation in the event shape distributions. Examples of such effects include finite multiplicity, rotation of the interaction region, collective flow, and spectator matter.

## 1 Finite Multiplicity Effect

The most trivial of these effects is an artifact of the limited multiplicity of the events used in this analysis. Since all of the available phase-space is not filled by an event with only a finite number of momenta vectors, a distortion is observed in the measured event shape. Only in the limit of infinite multiplicity will an event corresponding to isotropic emission have a purely spherical shape. Consider the case of only two fragments, the emission pattern may be isotropic, however the measured event shape must be two dimensional (the minor axis of the spheroid has to be zero). There is a substantial distortion of the measured event shape even for events with as many as 100 outgoing fragments.

This finite multiplicity effect was studied using some simple simulations. The first of these studies allowed only the emission directions to vary. All emitted particles were arbitrarily chosen to be 50 MeV protons. 1000 events were generated for each multiplicity up to 50. Figure IV.15 displays the trajectory of the average event shape from this simple model on Sphericity/Coplanarity space (S-C space) as a function of multiplicity. The multiplicity-one events all have a (0,0) event shape. The multiplicity-two events produce a distribution along the line from (0,0) to (0.750,0.413). The higher multiplicities begin to fill out the S-C space. As the multiplicity is increased, average event shape follows an arcing path towards the (1,0) limit.

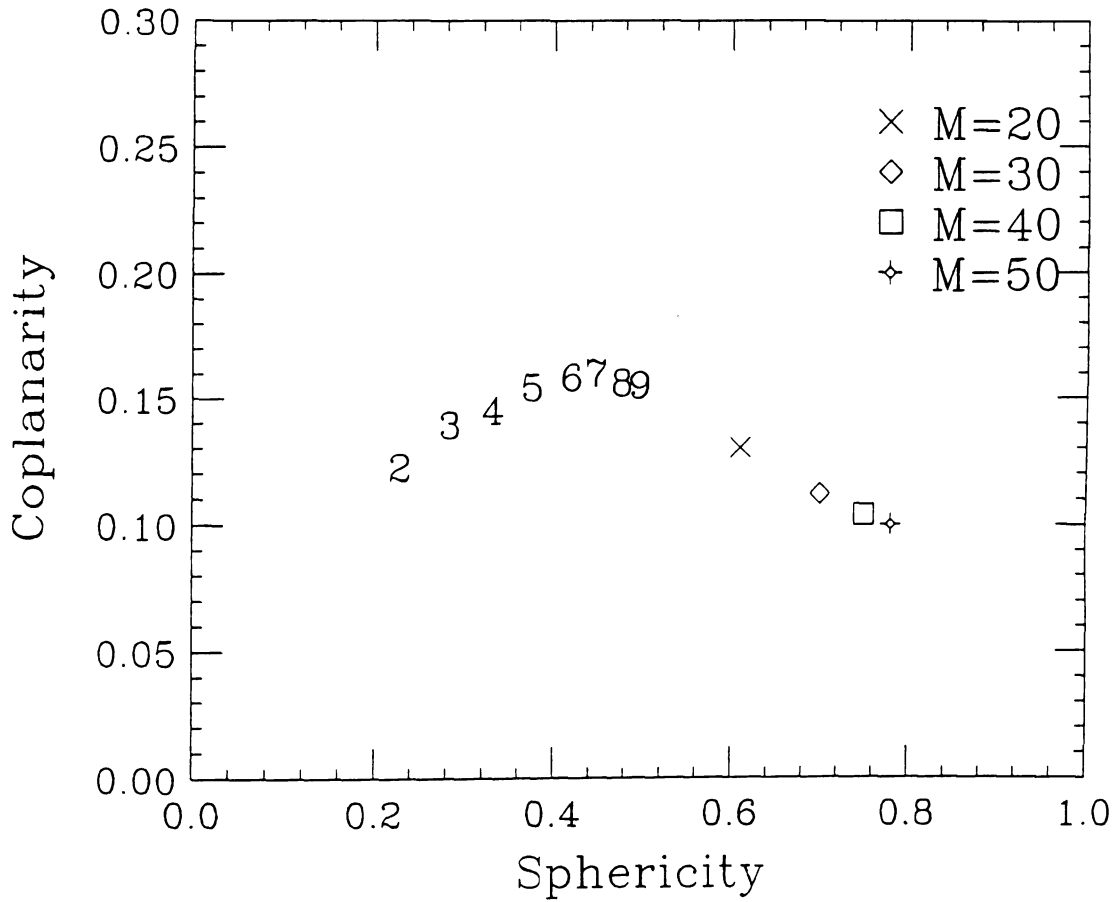


Figure IV.15: The trajectory of the S and C centroids as a function of multiplicity.

In order to make this simulation a little more interesting, the energy of the fragments was allowed to vary, and the detection biases were added. This version of the simulation was given a temperature, velocity, and multiplicity. The only allowed particles were again arbitrarily chosen to be protons. However, their energies were assigned based on a thermal model using the temperature. The directions of emitted particles were chosen randomly (isotropic in the rest frame of the source). Each fragment was then individually transformed into the laboratory reference frame and filtered by the detection acceptances. If a particle was rejected by the filter, another was chosen. Protons continued to be produced until the required event multiplicity was achieved, at which point, the event was analyzed. This moving thermal model contains most of the features of the real events. The multiplicity distributions and proton kinetic energy spectrum could be constrained to agree with the experimental data. The simple simulation lacks the variation in fragment charge and mass. The added energy variations and detection biases tend to depress the measured sphericity compared to that expected from the simpler model at the same multiplicity. For simulations constrained to multiplicities of 24, the simple finite multiplicity model yields an average sphericity of 0.65 while the filtered thermal version yields a value of 0.62.

## 2 Rotational Distortions

A rotating system will emit particles the momenta vectors of which are enhanced in the plane of rotation. This sort of emission pattern should produce observable distortions in the measured event shape. A simulation has been performed to test the nature of this effect [Li89]. The model considered a rotating spherical source which emitted thermal protons from its surface. The primordial emission spectrum was considered to be isotropic. A rotational component was added to the momentum of the emitted proton based upon where on the surface the particle was produced.

This effect has been studied as a function of multiplicity. Figure IV.16 displays the trajectories in sphericity/coplanarity space of the centroids of the event shape distributions predicted for four different rotational frequencies. An extrapolation of the multiplicity to infinity will produce centroids that lie on the line representing oblate spheroids (from (0.75,0.413) to (1.0,0.0)). Figure IV.17 provides a detailed view of the rotational effect for multiplicities around eight. These multiplicity values cover the range of the measured experimental multiplicity distributions at the six beam energies. The experimental rotational frequency is estimated to lie between  $r\omega=0.0$  and  $r\omega=0.1$  [Tsan86]. For events with an average multiplicity of eight, we expect a measured elongation of approximately -0.01 units of sphericity and +0.001 units of coplanarity. Additionally, the rotational effects should be strongest for collisions with large impact parameters. For central events, there is little initial angular momentum. In this analysis we select exclusively central events which should minimize the rotational distortions.

### 3 Collective Elongations

Reaction dynamics will also potentially add some collective effects. If the target nucleons and projectile nucleons retain some memory of their origin, their final trajectories may tend to form two jets. At low energies, the mean field attracts the projectile to the target and a partial orbit is carried out during the reaction. The fragments originating from the target will be scattered to negative angles with respect to the impact parameter. At high energies the collision occurs on a more rapid time scale. Before the participants are able to orbit, the nuclei interact and form a highly compressed region. The target and projectile remnants recoil from this collision and the target fragments are preferentially scattered to a positive angle. At some intermediate energy, one expects these two opposing effects to balance out to create a system which

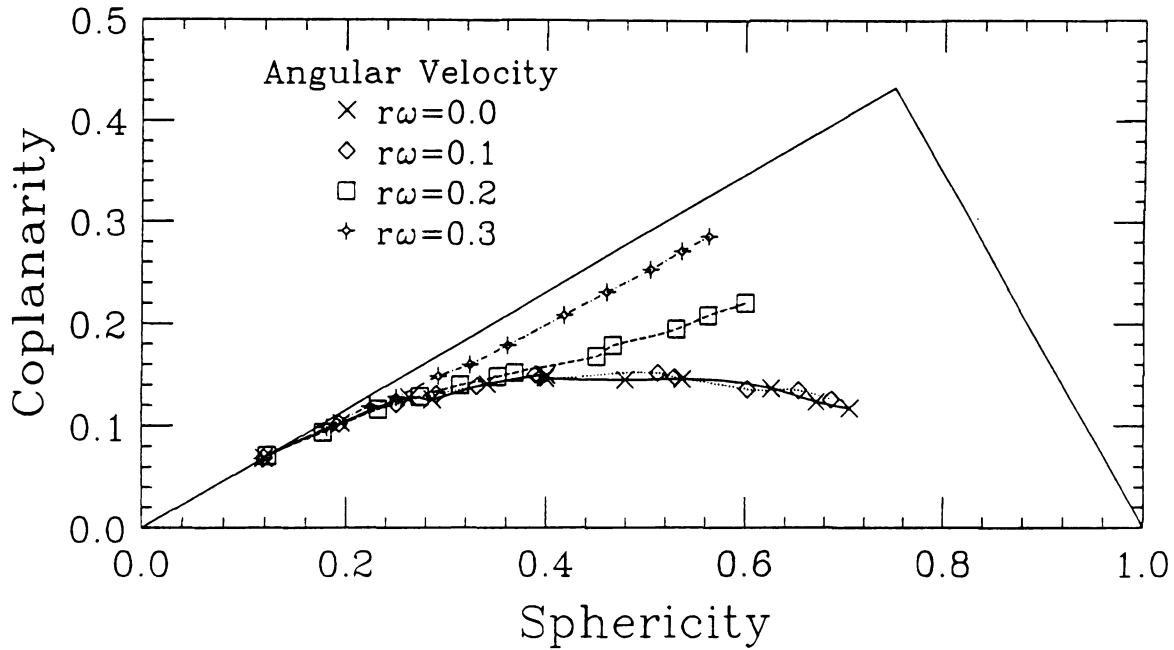


Figure IV.16: The trajectories of the S and C centroids as a function of multiplicity for emission from a rotating source.

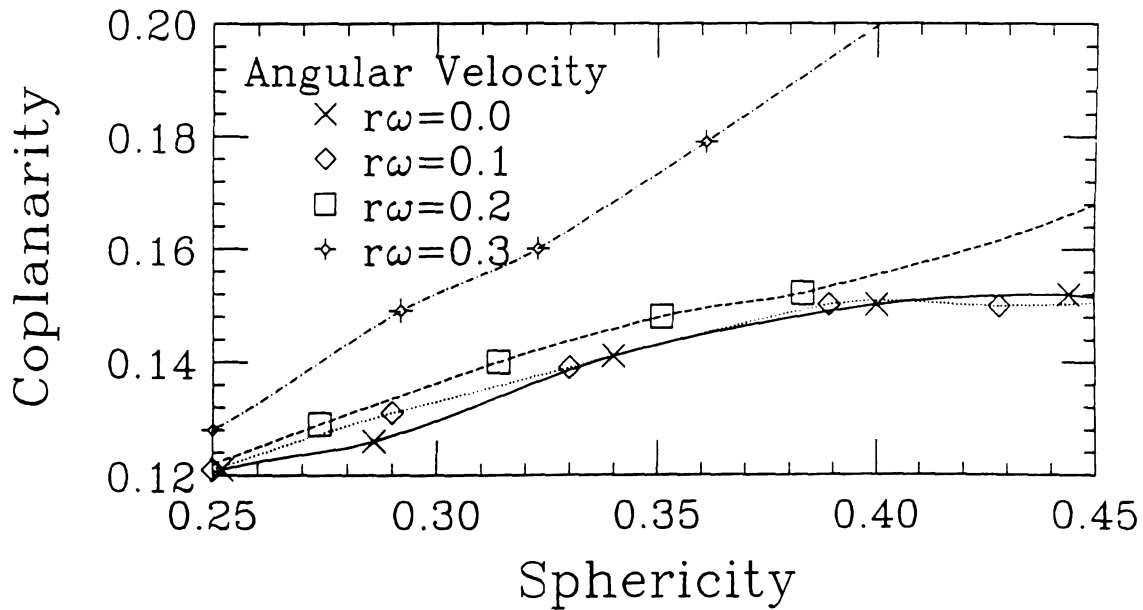


Figure IV.17: An expanded view of the trajectories from the rotational simulations in the region of the multiplicities that are measured for the experimental data.

is neutral with respect to preferential scattering angles.

The question of where this transition occurs has recently been probed by several groups [Krof89, Zhan89, Ogil90]. In addition, the magnitude of the collective motion has been measured for the Ar+V system at 35 through 85 MeV/nucleon [Ogil89b, Ogil89c, Ogil90]. Since the magnitude of this effect is known, the influence that it should have on the event shape analysis can be estimated. Figure IV.18 displays the predictions from various models. The simulations presented in this figure are all constrained to have a multiplicity of 24. Considered are rotational effects, collective motion effects, finite multiplicity effects, and the effect of the detector biases. The collective motion does not create a large elongation compared to that predicted by sequential decay. These calculations were not done for each of the beam energies, however, one can confidently say that the magnitude of the effect will diminish as a function of increased beam energy because it has been shown that the minimum collective motion is induced for reactions around 85 MeV/nucleon [Ogil90]. This is the energy at which the balance between the attractive scattering and the compression recoil occurs. As with the rotational effect, the collective motion should diminish for central events.

## H The Sequential Simulation

A new sequential simulation has been developed which is able to match accurately the first order observables from the  $4\pi$  data set. The simulations that had been developed by other groups had not been able to accomplish this feat, and as has been demonstrated, failure to reproduce the basic observables invalidates the comparison between the multi-particle observables from the experimental data and the predictions from a simulation. By developing a new model, we were able to control the algorithms

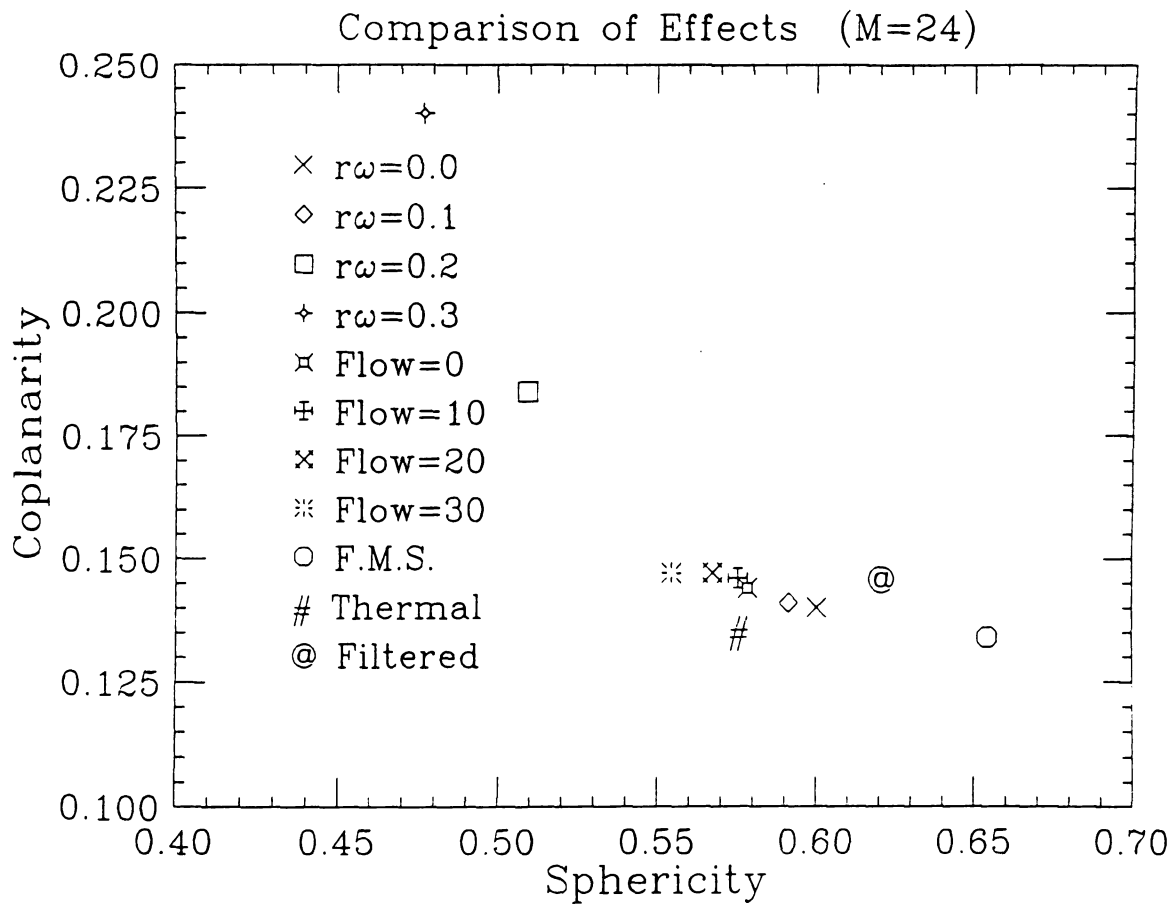


Figure IV.18: An overview of the relative magnitudes of the various effects that induce elongations.

which determine how the simulated nucleus decayed.

The simulation considers a nucleus at rest which has a given amount of internal excitation energy. The nucleus is allowed to dissipate this energy only through the emission of energetic fragments. These fragments were allowed to range from individual nucleons up to nuclei the masses of which corresponded to symmetric fission. For decaying nuclei with fewer than 12 nucleons, every possible exit channel was considered. To each channel, a barrier energy was assigned based on the rest masses of the two daughter fragments (reaction  $Q$  value). The binding energy per nucleon is highest for  $^{56}\text{Fe}$ . Since this simulation models decay from heavy nuclei into light and intermediate mass fragments, most channels will have a positive barrier energy. However, if the decay chain leads to a nucleus that is far from the valley of stability, it is possible to assign a negative barrier energy to an exit channel. A relative weight for each channel was determined based on the temperature of the excited nucleus.

Using the principles of thermodynamics and an estimate of the level density as a function of excitation energy, the temperature of the nuclear system can be determined. The entropy ( $S$ ) is related to the natural log of the level density ( $\Omega(E)$ ):

$$S = k \ln \Omega(E) \quad (\text{IV.18})$$

where  $k$  is Boltzmann's constant. The temperature is then related to the partial derivative of the entropy with respect to energy:

$$\frac{1}{T} = \frac{\partial S}{\partial E}, \quad (\text{IV.19})$$

which leads to:

$$\frac{1}{kT} = \frac{1}{\Omega(E)} \frac{\partial \Omega(E)}{\partial E}. \quad (\text{IV.20})$$

The density of nuclear energy levels increases rapidly as a function of energy. If the nucleons are considered to be a degenerate fermion gas contained within a box the

size of a nucleus, the level density is proportional to  $e^{-\sqrt{E}}$  [Beth61]. This density of states yields  $1/kT \propto 1/\sqrt{E}$ . Blatt and Weisskopf propose a level density of the form

$$\Omega(E) = C e^{2\sqrt{aE}} \quad (\text{IV.21})$$

where  $C$  and  $a$  are constants [Blat52]. Solving equation IV.20 yields  $1/kT = \sqrt{a/E}$ . Thus, the temperature of the parent nucleus can be calculated from the excitation energy ( $E^*$ ) using the formula  $T = \sqrt{E^*/a}$ . The constant  $a$  is the level density parameter, which is assigned values between  $A/12$  and  $A/8$ , where  $A$  is the mass number. Adjustments in  $a$  affected the calculated temperature and therefore influenced the kinetic energy distributions of the final fragments and the rate at which the thermalized system was able to dissipate its excitation energy.

From this temperature ( $T$ ), a probability was assigned to each channel using the formula  $P = e^{-b/T}$ , where  $b$  is the barrier energy. A relative probability is assigned to each channel, and a selection is made based on this probability using Monte Carlo techniques. For systems with greater than 12 nucleons, the total number of exit channels that were considered was truncated to reduce the amount of computational time required by the simulation. Only one combination of neutrons and protons was considered for each possible exit mass. For even mass channels, the emitted fragment was assigned the same number of neutrons and protons. For odd mass channels, the extra nucleon was randomly assigned as either a proton or a neutron. This method of choosing an exit fragment tends to lead to a single remnant which is neutron rich. The initial system started with a neutron excess, and the early decays (while the mass of the parent system is above 12) emitted fragments with approximately equal neutron and proton numbers, leaving the initial neutron excess with a single remnant. Once the mass of the remnant falls below 12 it was allowed to dissipate these extra neutrons. It is possible that this method of channel selection produces an

enhancement of neutron rich light fragments. The  $4\pi$  array does not have isotopic resolution for most elements, so this feature of the simulation can not be tested with a comparison to the experimental data.

Having selected a decay channel, a separation energy is picked from a thermal distribution using the mass of the emitted fragment and the temperature of the system. To this thermal energy, a Coulomb repulsion is added assuming a separation distance at emission of  $1.22(A_1^{1/3} + A_2^{1/3})$  Fm. The recoil momenta of the two daughter fragments are calculated from this separation energy assuming a random breakup direction. These recoil momenta are added to the momentum of the parent nucleus to get the total momenta of the daughters.

In order to determine the internal excitation energy of the two outgoing fragments, the separation energy and the reaction Q-value are subtracted from the excitation energy of the parent nucleus. If neither daughter is an individual nucleon, the remaining excitation energy is shared assuming equal temperatures of the two daughters ( $E_1^* = E^* \frac{A_1}{A_p}$ ,  $E_2^* = E^* \frac{A_2}{A_p}$  where  $E^*$  is the excitation energy remaining after subtraction of the barrier energy and the separation energy from the original excitation energy,  $A_1$  is the mass of the first daughter fragment,  $A_2$  is the mass of the second fragment, and  $A_p$  is the mass of the parent). If one of the outgoing fragments is a nucleon, then the other fragment keeps all of the remaining excitation energy. If both final fragments are nucleons, then the remaining excitation energy is added to the calculated separation energy. As the decay is followed through its stages, the average temperature of fragments falls, because internal excitation energy is being converted into kinetic energy and into a collection of less well bound nucleons.

This simulation differs from the others that had been developed in several ways. First, the method of assigning probabilities to the various possible exit channels uses the final state mass differences and not fission barrier heights. For systems with ex-

citation energies several times higher than the barriers, these barriers were no longer meaningful. Secondly, the method of assigning a thermal energy to the outgoing fragments differed from other models. And finally, the number of exit channels considered for light systems was more complete than other models that were examined.

In order to compare the results of the simulation to the experimental data it was necessary to run the simulated events through the  $4\pi$  filter. Since the simulation was carried out in the rest frame of the decaying system, it was necessary to boost the event into the laboratory frame prior to filtering. For analysis of the event, it was then boosted back into its original rest frame. Figures IV.19 to IV.24 display the results from the simulations (circles) compared to the experimental data (crosses) for the six beam energies. The input parameters for the simulation are given in table IV.3. The fit to the first order parameters is generally good. There are a few weak areas that should be noted. First, for 35 MeV/nucleon, the simulation underpredicts the number of deuterons. This is not a problem for the other beam energies. Second, for the low energies the simulation underpredicts the production cross-sections of heavy elements. Finally, for high energies the simulation overpredicts the low end of the helium energy spectrum, and consequently overpredicts the number of heliums. These are minor shortcomings. Overall the fit is far superior to that of the other models discussed earlier.

## I The Simultaneous Simulation

The event generator FREESCO [Fai86] creates events as if they were produced from a simultaneous break-up, however I chose to develop an original simultaneous simulation. This was necessary because it was essential that the simultaneous simulation and the sequential simulation agree with respect to the first order observables. The

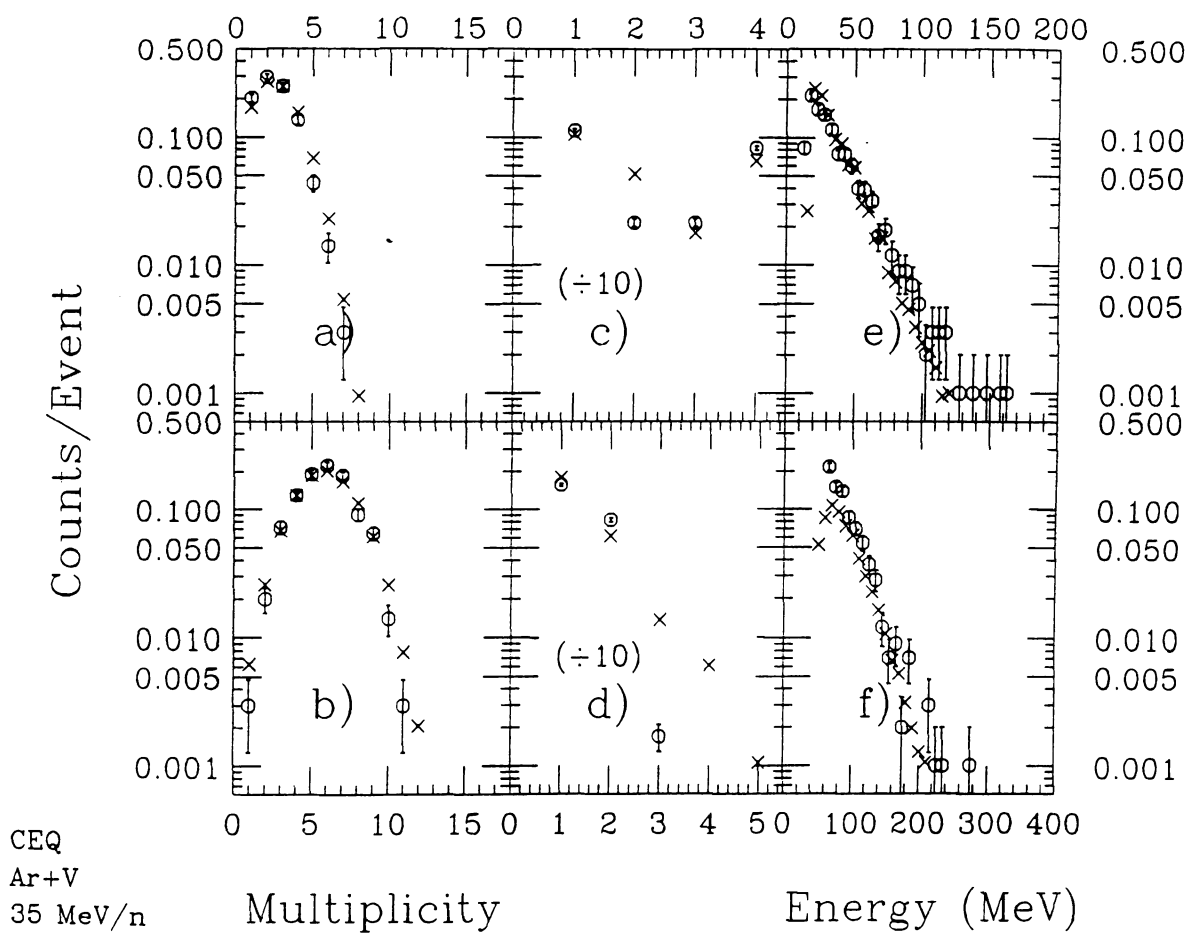


Figure IV.19: The results of the sequential simulation (circles) compared to the first order observables from the experimental data for the system Ar+V at 35 MeV/nucleon (crosses) .

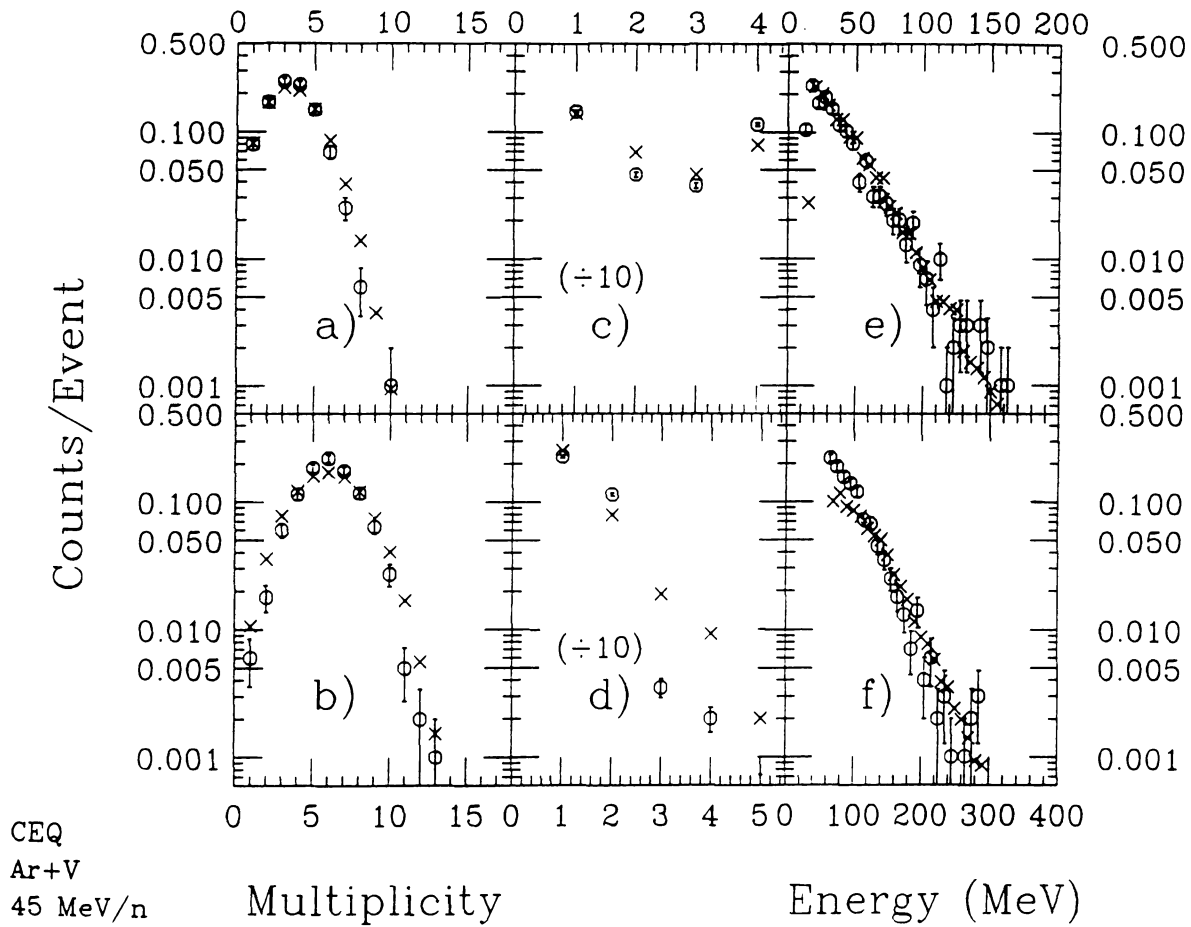
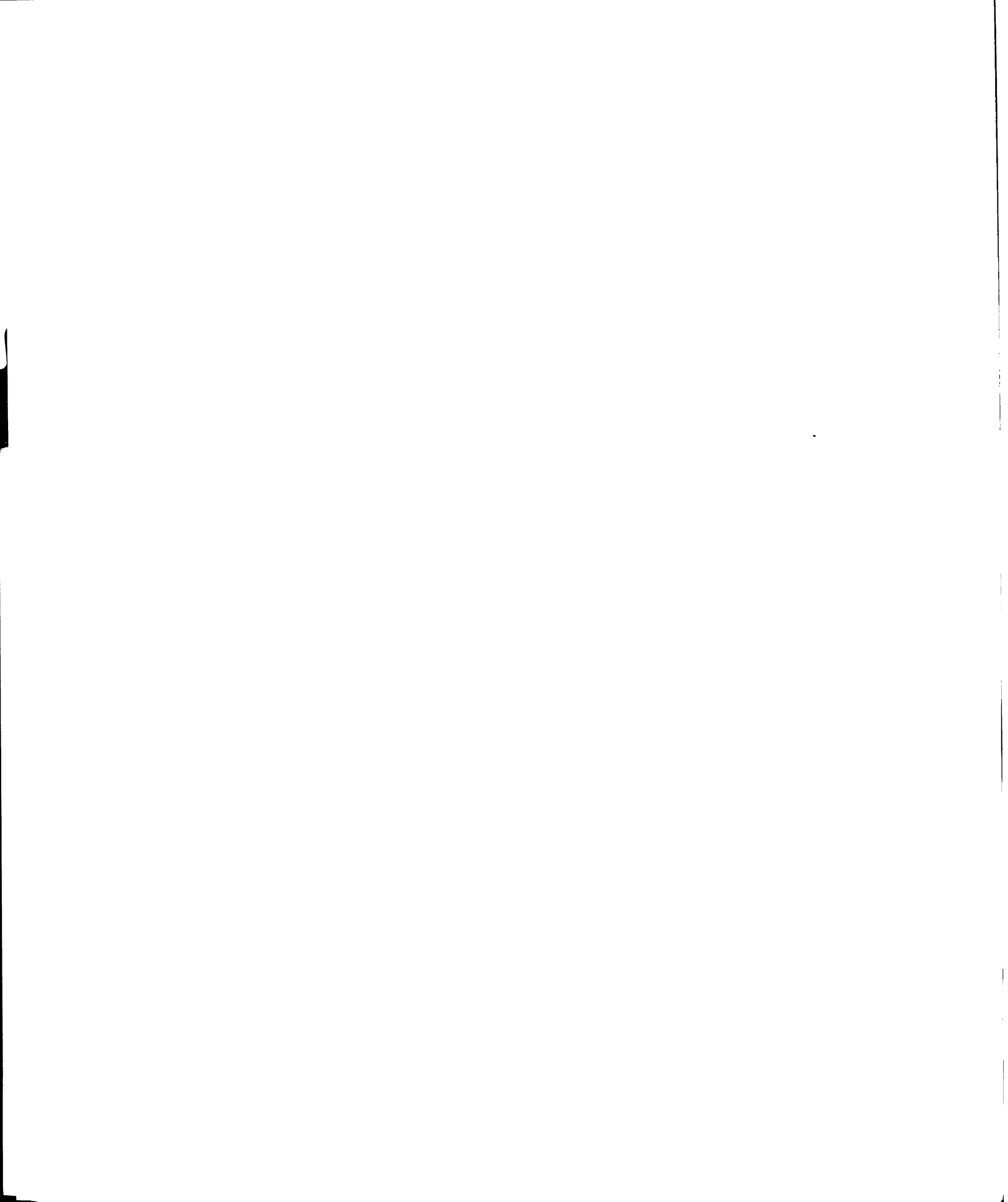


Figure IV.20: The results of the sequential simulation (circles) compared to the first order observables from the experimental data for the system Ar+V at 45 MeV/nucleon (crosses).



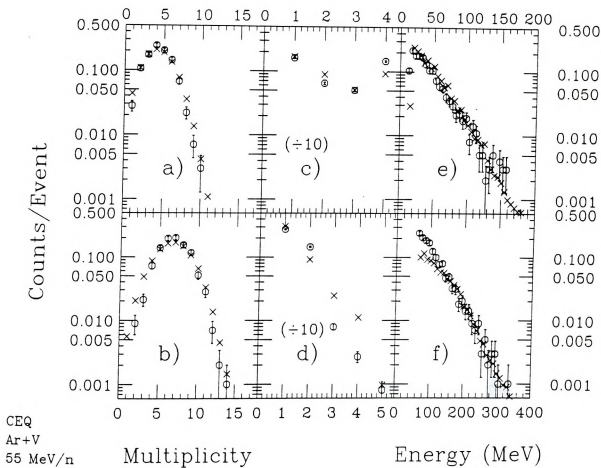


Figure IV.21: The results of the sequential simulation (circles) compared to the first order observables from the experimental data for the system Ar+V at 55 MeV/nucleon (crosses).

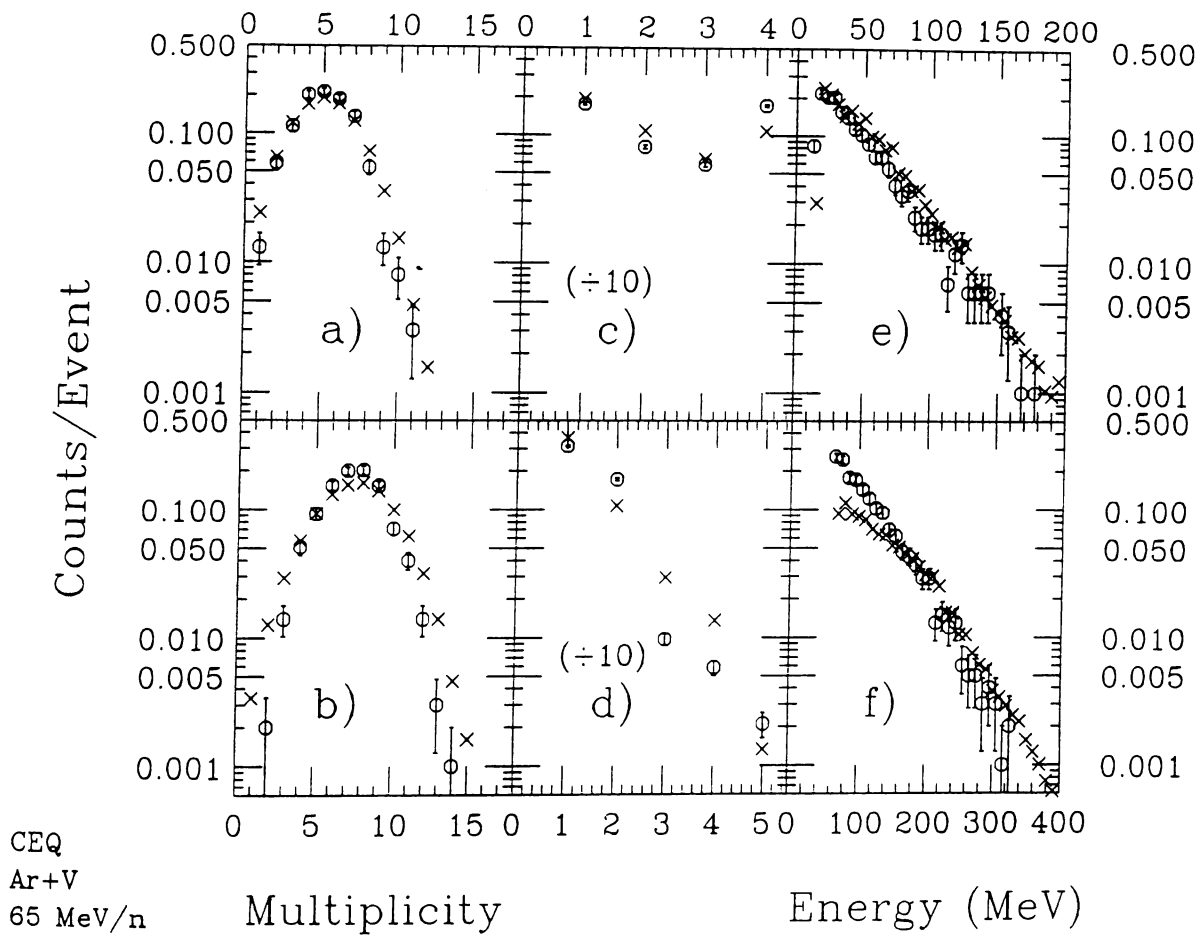


Figure IV.22: The results of the sequential simulation (circles) compared to the first order observables from the experimental data for the system Ar+V at 65 MeV/nucleon (crosses).

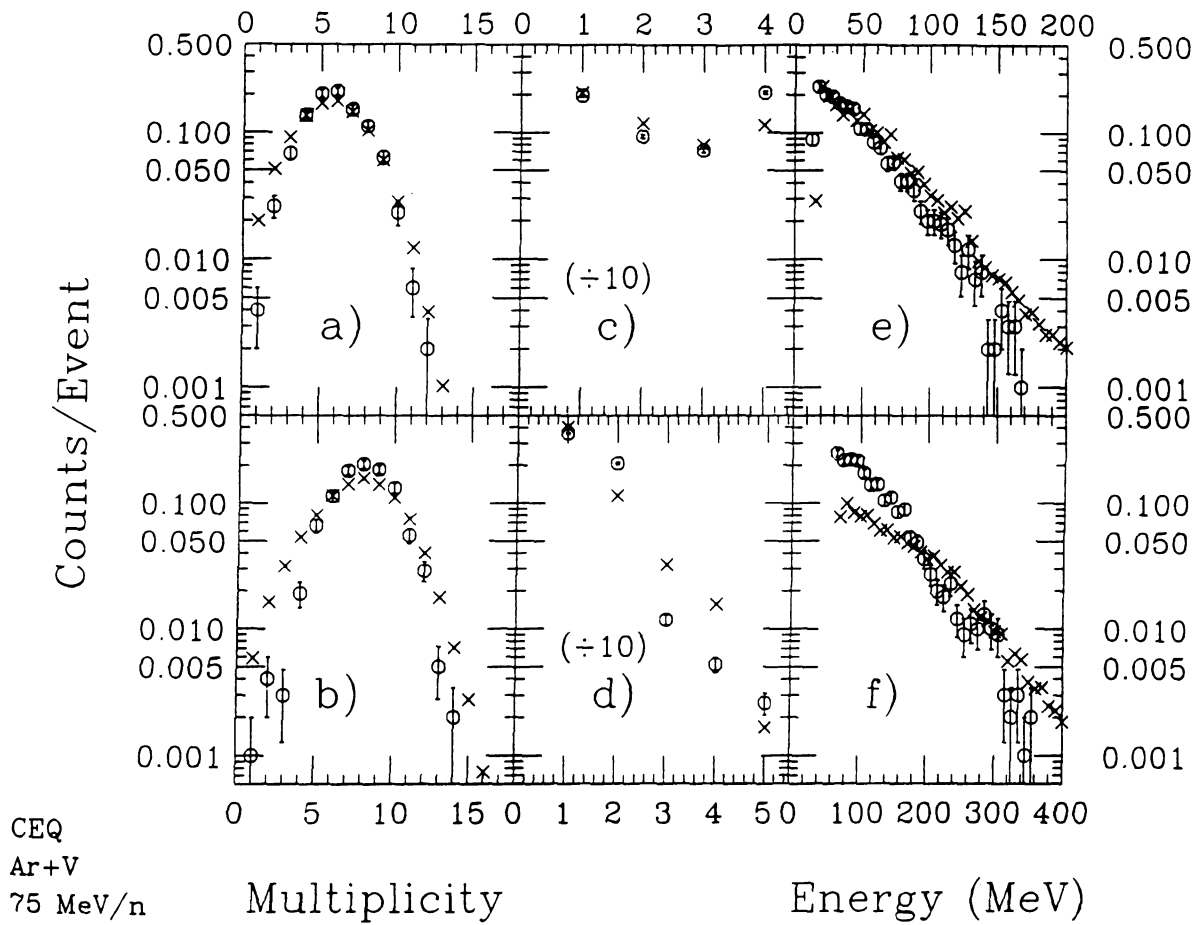


Figure IV.23: The results of the sequential simulation (circles) compared to the first order observables from the experimental data for the system Ar+V at 75 MeV/nucleon (crosses) .

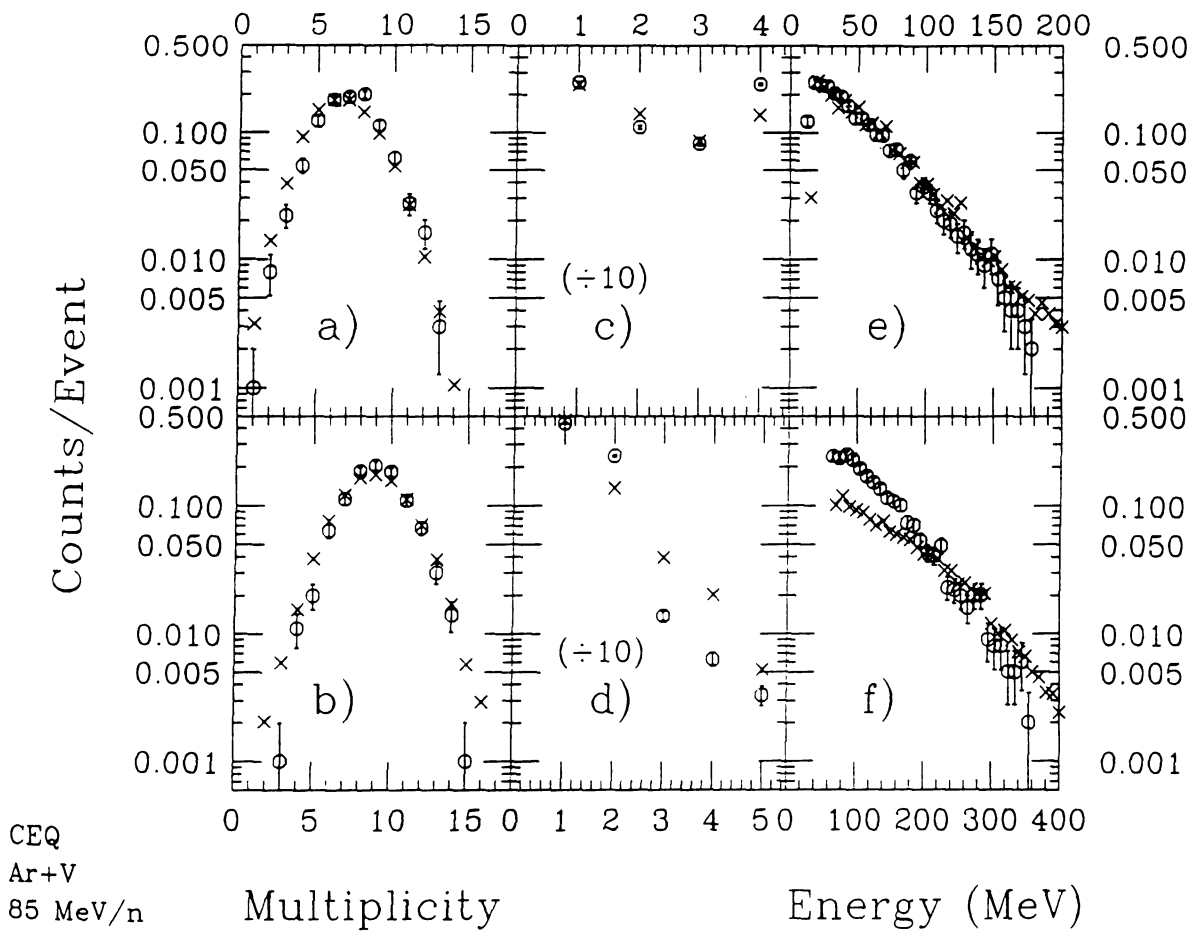


Figure IV.24: The results of the sequential simulation (circles) compared to the first order observables from the experimental data for the system Ar+V at 85 MeV/nucleon (crosses).

Table IV.3: The input parameters for the simulation for the six beam energies that were studied. The simulation attempted to reproduce central events from the reaction  $^{40}\text{Ar} + ^{51}\text{V}$ .

Incident Energy (MeV/nucleon)	$A_0$	$Z_0$	Excitation (MeV/nucleon)	$V_{CM}$ (c)
35	76	33	8.0	0.1200
45	76	33	10.3	0.1370
55	73	31	12.6	0.1516
65	70	29	14.8	0.1648
75	68	28	17.1	0.1771
85	70	29	19.4	0.1887

multi-particle observables have been demonstrated to be sensitive to variances in the basic observables. In order to ensure that the simultaneous simulation agrees with the predictions of the sequential model for the first order observables, events that had been generated from the sequential code were modified to create pseudo-simultaneous events as discussed below. The sequential simulation has already been shown to agree with the experimental data, and it was determined that it would be easier to create pseudo-simultaneous events from events from a sequential model than vice versa. It is easier to remove the kinetic correlations contained within the sequential events than to try to create some correlations in an event that had been generated with a simultaneous model. Several different methods of modifying the sequential events were considered with varying degrees of success.

## 1 Randomized Directions, Energy and Momentum Conserved

The first attempt to create simultaneous events used complete unfiltered events that had been generated from the sequential simulation. The final fragments were then all randomly assigned new emission directions. In order to ensure momentum conser-

vation, the recoil momentum of the entire new event was determined, and then the event was boosted into a frame where it was at rest. This affected the overall energy conservation, therefore kinetic energy values for all of the fragments were scaled so that the sum of the new kinetic energies equaled the sum of the original ones. This randomization of emission directions removed any correlations in the fragment distributions generating an isotropic event.

The new events were then transformed to the laboratory reference frame, filtered, transformed back to the rest frame of the decaying nucleus, and analysed with respect to the event shape. Unfortunately, though the technique seemed quite elegant because it conserved momentum and energy, the removal of the intrinsic correlations between the fragments resulted in larger average relative angles between fragments. There was no longer any primary axis with preferential emission to the poles. This resulted in fewer fragments being rejected by the filter code due to multiple hits on single detectors. The net effect was an increase in the average multiplicity of the events in this simulation as compared to the previous one. As has been demonstrated, the event shape parameters are extremely sensitive to multiplicity, therefore, another method of producing simultaneous events had to be developed.

## **2 Randomized Directions, Multiplicity Constrained**

I continued using the events which had been generated by the sequential simulation because that method introduced the fewest simulation dependent changes. However, the multiplicity had to be artificially constrained, otherwise the difference between the average event shapes from the two simulations would contain a significant multiplicity induced contribution. This second version of the simulation started with events from the sequential simulation, randomly chose fragments and redirected them one at a time. For each re-oriented particle, a check was made as to whether it was accepted

or rejected by the filter. The routine would continue to pick particles randomly and randomize their emission directions until the accepted number was equal to the number that had been accepted for the sequential event. Therefore, the multiplicities and particle make-up of the two events were identical, the only differences had to be related to the emission directions and resultant kinematic correlations.

### 3 Coulomb Trajectories

Selecting the emission directions completely randomly does not fill phase space properly, because it does not discriminate against production of pairs with low relative momentum. The Coulomb interaction between fragments causes pairs of particles which are emitted close in phase space to repel one another. This reduces the relative production of low relative momentum pairs. An approach that accounts for this process starts by distributing the final fragments in the sphere of a given radius, and then follows the Coulomb trajectories in order to get the final directions and energies of the particles. This technique reduces the probability of finding two particles emitted with a very small relative velocity and should therefore reduce the fraction of particles that are rejected due to multiple hits. This method suffers from the same problems as the simple directional randomization without multiplicity constraints; the accepted multiplicity is larger than that from the sequential simulation. This complicates the comparison between these two simulations, however, an informative comparison can be made between this simulation and the simple directional randomization. The similarity between those two cases suggests that the directional randomization technique is as valid as the more detailed trajectory calculations. Therefore, I did not use the Coulomb trajectory method in our analysis because it was not necessary and could not control the multiplicity.

## J Determination of the Reaction Mechanism

The goal of this study has been to differentiate between two possible descriptions of nuclear disassembly. The first mechanism is slow sequential binary decay. This process is an extrapolation of a model that has worked extremely well at lower energies. Though the constraints of the model must be relaxed in order for it to be able to reproduce the basic observables, it does not represent a new decay mode. The simultaneous multi-fragmentation is a rapid disassembly of the nucleus. It is an emission process that is qualitatively different from the emission processes at lower energies. The onset energy for multi-fragmentation can provide information about the equation of state of nuclear matter [Sura89].

In order to demonstrate that the event shape analysis technique is capable of resolving between the two alternate models for nuclear disassembly, the predicted shape distributions from the two simulations are plotted together in Figure IV.25. For clarity, the sphericity and coplanarity parameters for only one hundred events from each model are displayed. The large X's correspond to the centroids of the distributions. The uncertainties of the centroids are smaller than the width of the lines of the X's when calculated using the full 40,000 events generated at each energy by the simulations. There is a clear separation between the two centroids which indicates that this technique can resolve between these two models under experimental circumstances.

It has been suggested that correlations in velocity and emission angles can effectively be used to differentiate between these two possible decay mechanisms [Lópe89a, Gros89]. Several experimental groups have employed this type of analysis to study the question of the decay time-scale [Troc89, Boug89b, Poul89, Klot89]. Unfortunately, the velocity correlations are most sensitive when two heavy fragments are

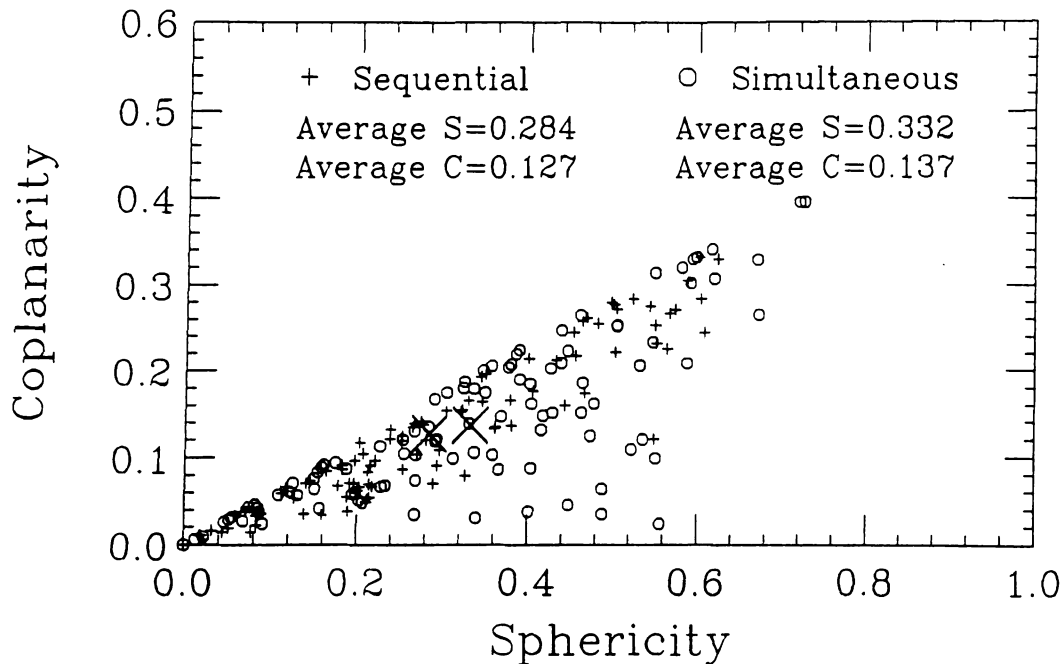


Figure IV.25: A scatter plot showing the sphericity and coplanarity values for 100 events generated from the sequential simulation (crosses) and for 100 events from the simultaneous simulation (circles).

compared, and the MSU  $4\pi$  array had high detection thresholds at the time of these experiments. Figure IV.26 displays the relative velocity and relative angle spectra for the experimental data and for the two simulations. The solid line corresponds to the experimental data, the circles correspond to the sequential simulation, and the x's correspond to the simultaneous simulation. There is little to distinguish the three curves in this data set. This technique works well for arrays designed for heavy fragments, but given the status of the MSU  $4\pi$  for these experiments, the event shape analysis was the best analysis technique for studying questions related to the time-scale of the disassembly.

Contour plots of the predicted shape distributions for the simulated sequential break-up process and the simultaneous multi-fragmentation are shown in Figures IV.27 through IV.32 for the six different beam energies. The shape distribution for the sequential events from the 35 MeV/nucleon case (Figure IV.27a) is that of a

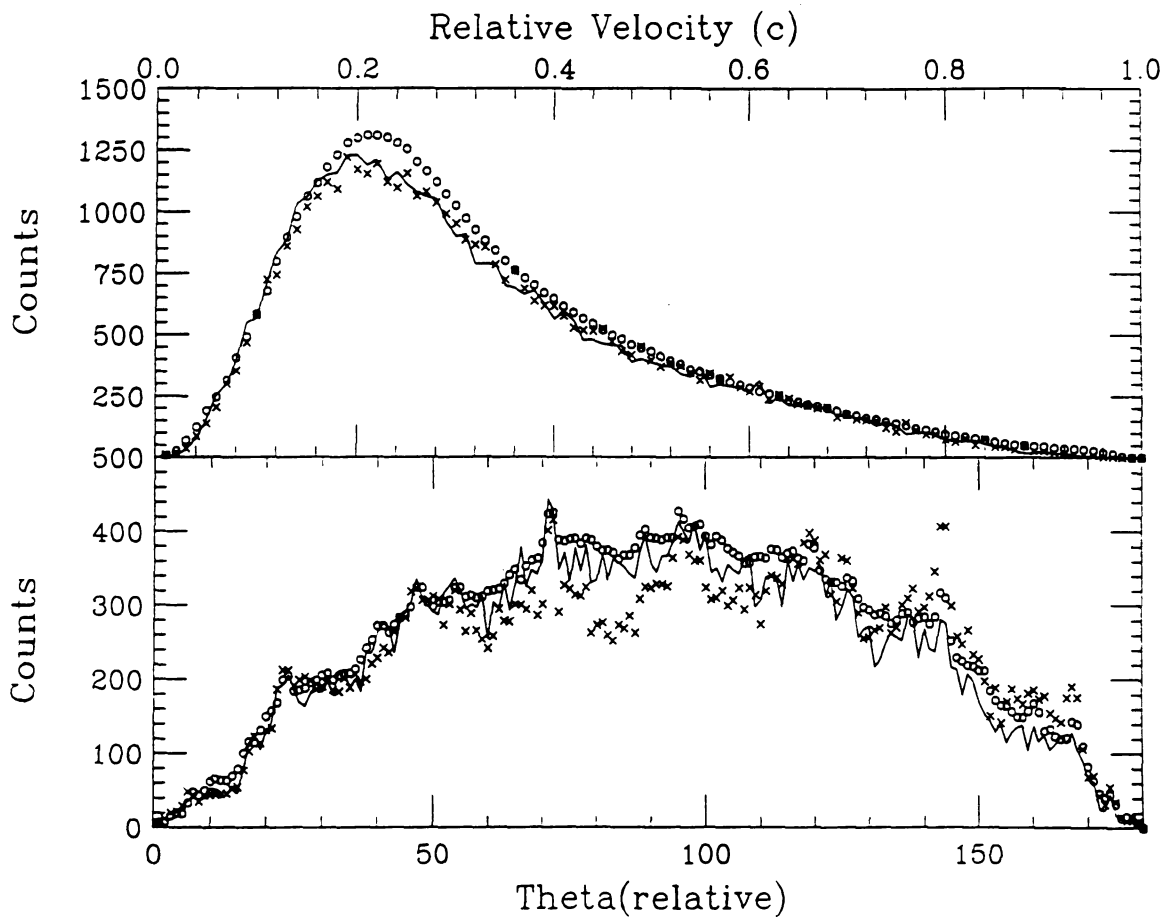


Figure IV.26: Distributions of the relative velocity and angle between any two particles from central events from the reaction 100 MeV/nucleon Ar+V.

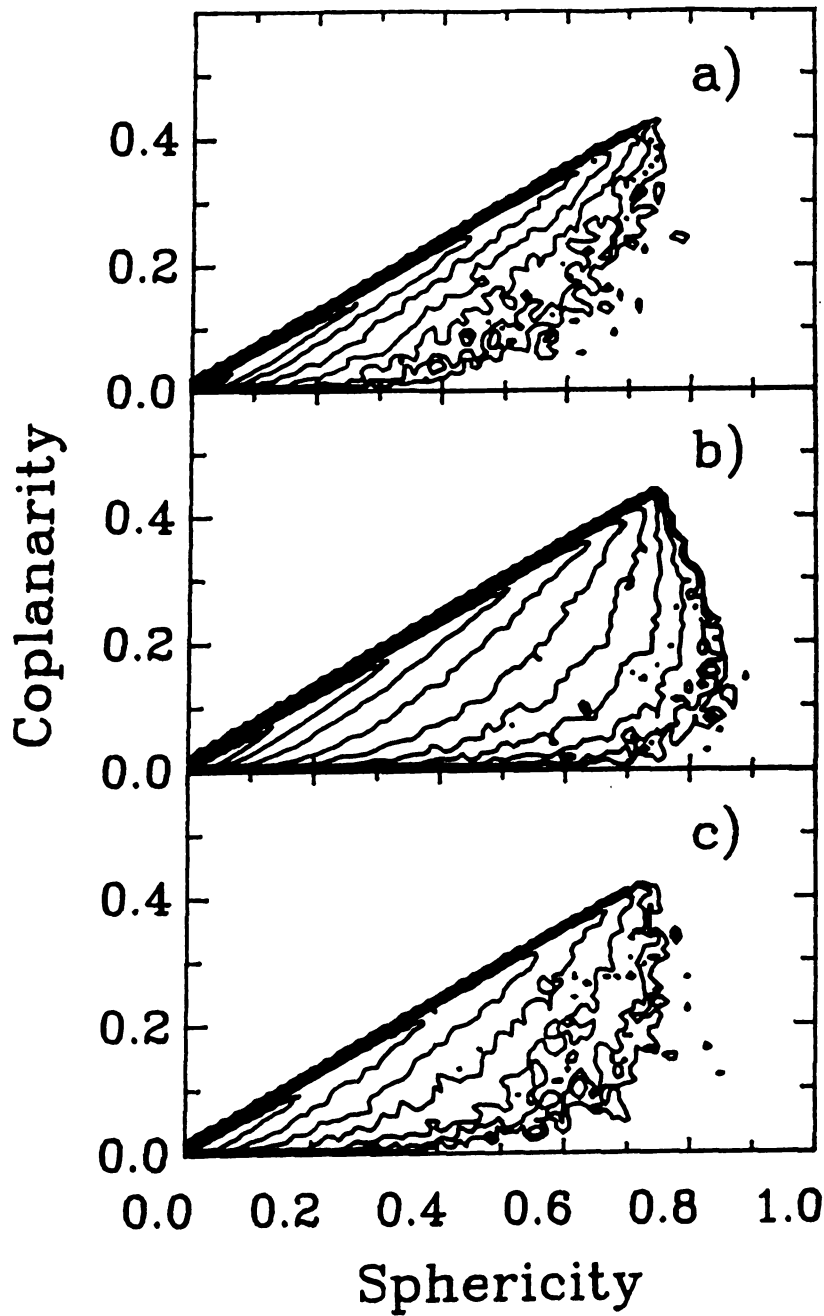


Figure IV.27: A comparison of the predicted event shape distributions from the a) sequential and c) simultaneous simulations to that measured for the b) experimental data for the reaction Ar+V at 35 MeV/nucleon.

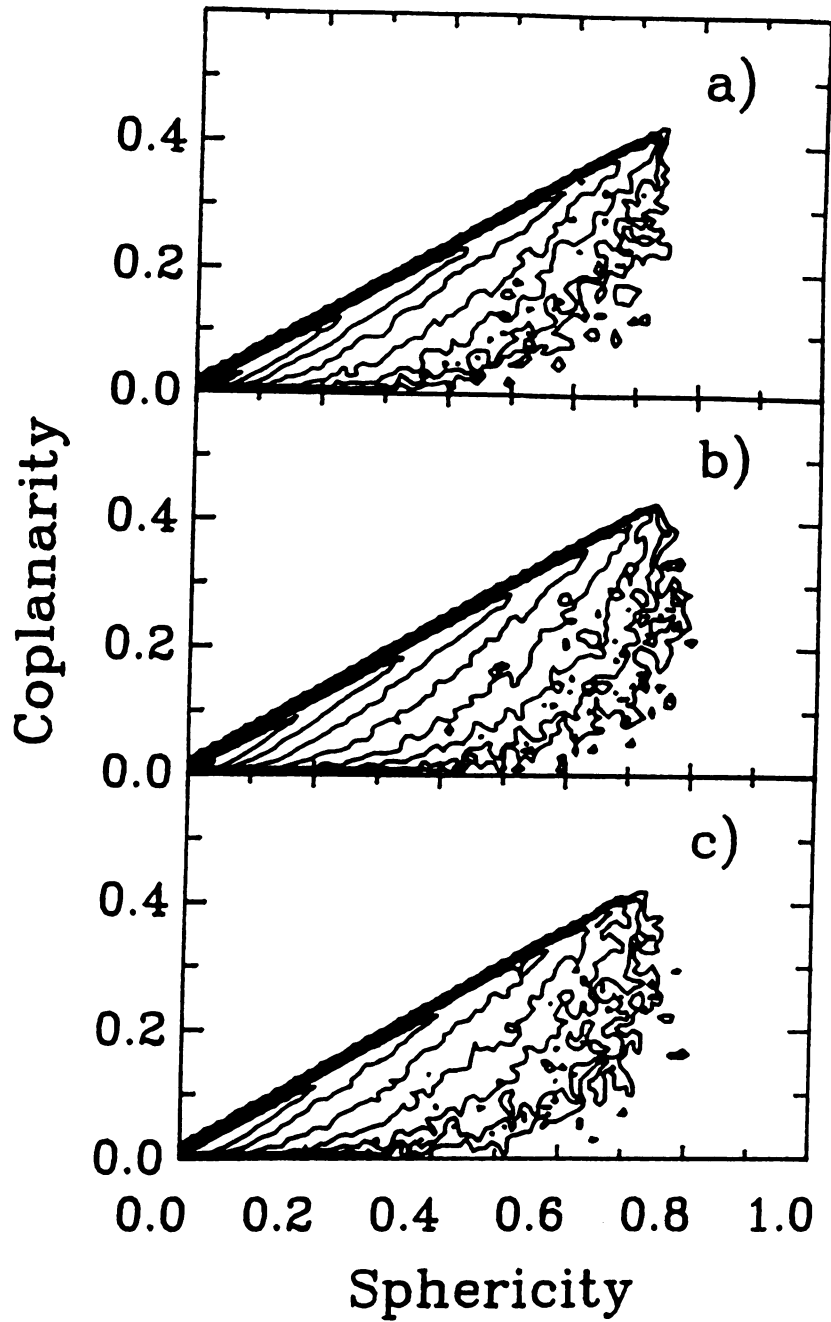


Figure IV.28: A comparison of the predicted event shape distributions from the a) sequential and c) simultaneous simulations to that measured for the b) experimental data for the reaction Ar+V at 45 MeV/nucleon.

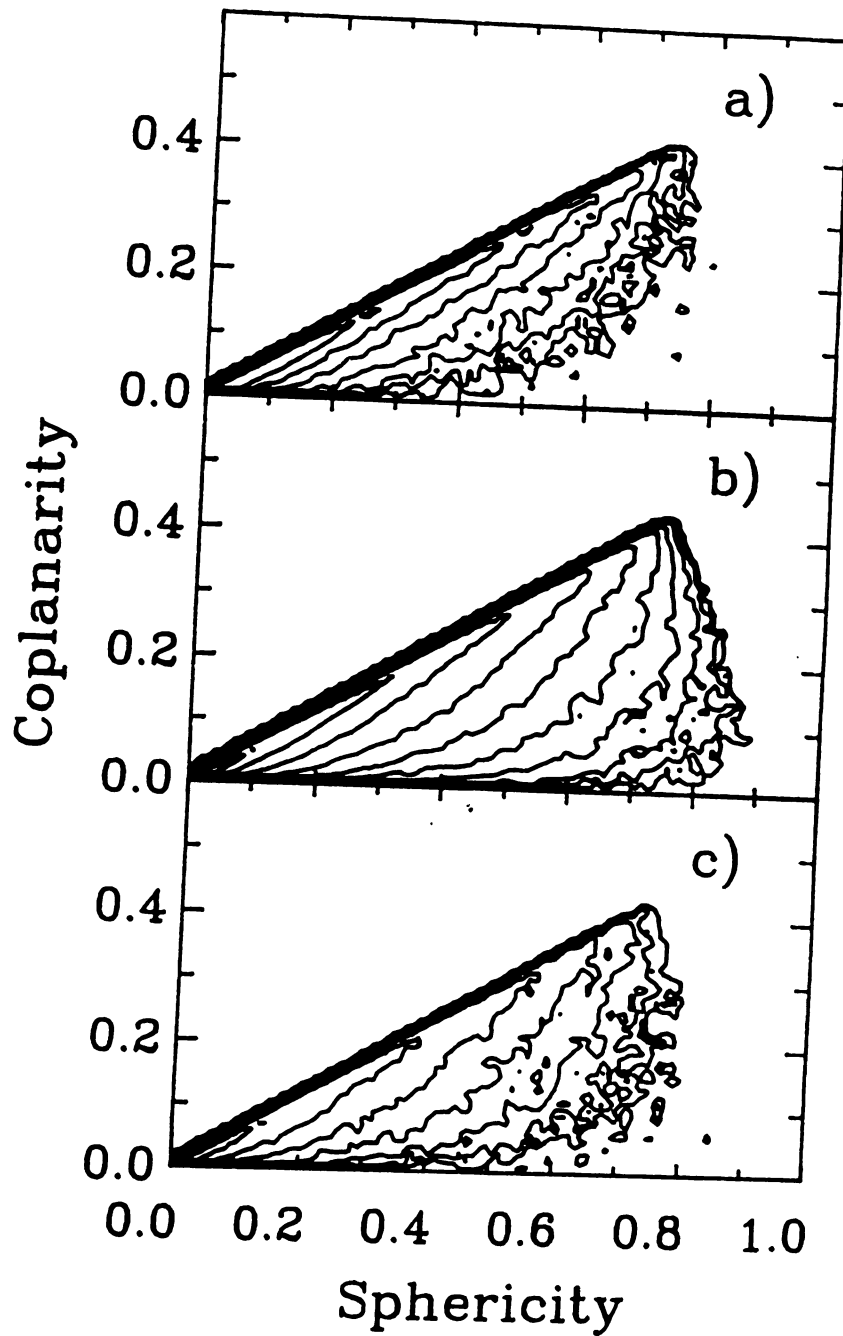


Figure IV.29: A comparison of the predicted event shape distributions from the a) sequential and c) simultaneous simulations to that measured for the b) experimental data for the reaction Ar+V at 55 MeV/nucleon.

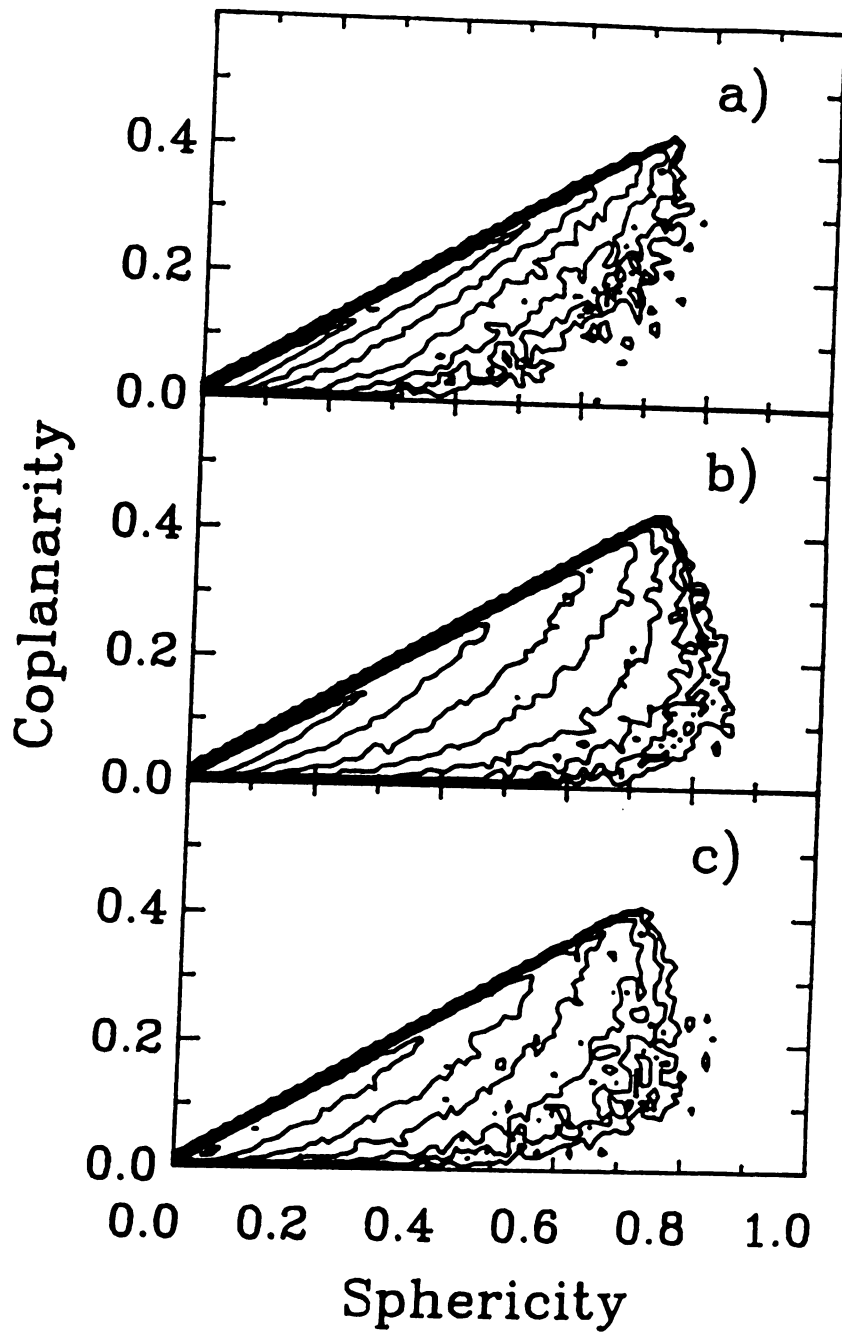


Figure IV.30: A comparison of the predicted event shape distributions from the a) sequential and c) simultaneous simulations to that measured for the b) experimental data for the reaction Ar+V at 65 MeV/nucleon.

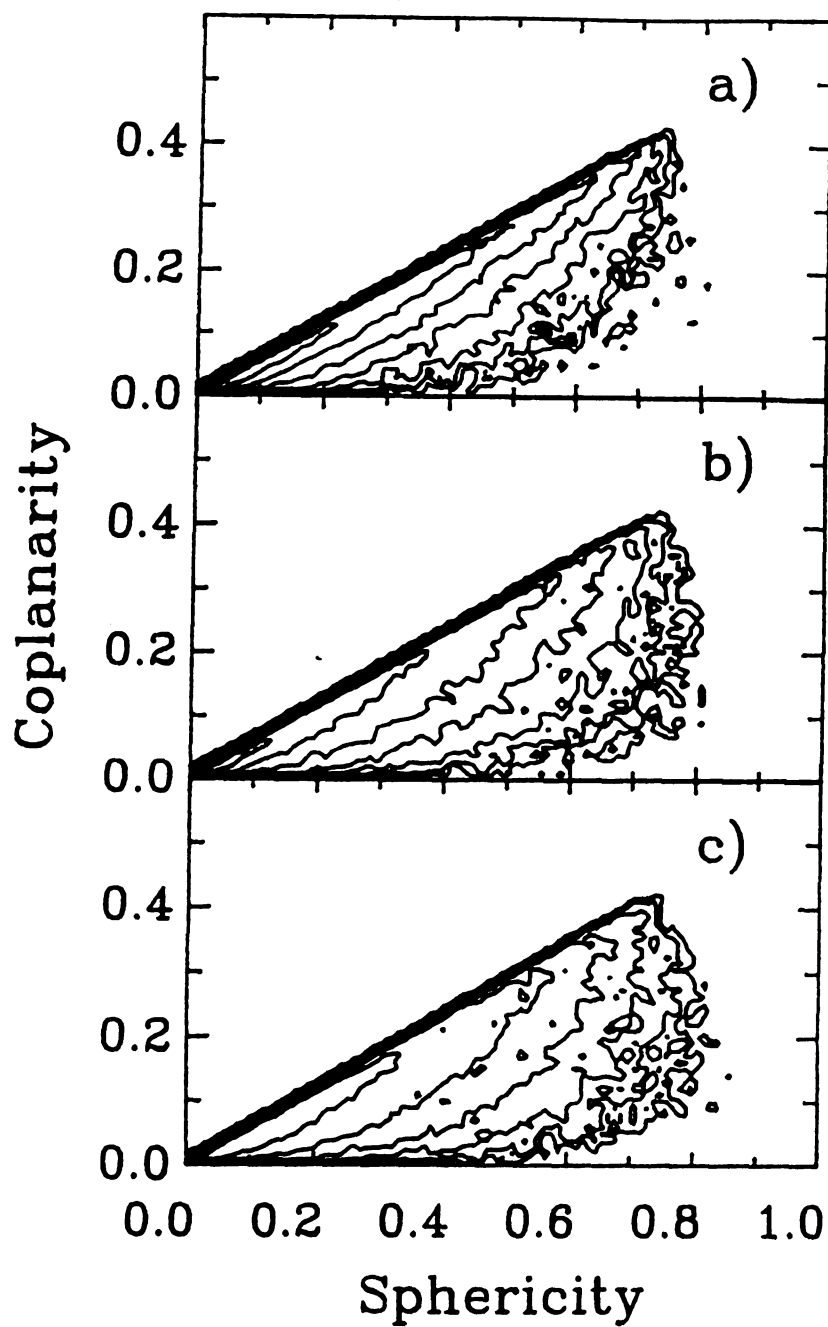


Figure IV.31: A comparison of the predicted event shape distributions from the a) sequential and c) simultaneous simulations to that measured for the b) experimental data for the reaction Ar+V at 75 MeV/nucleon.

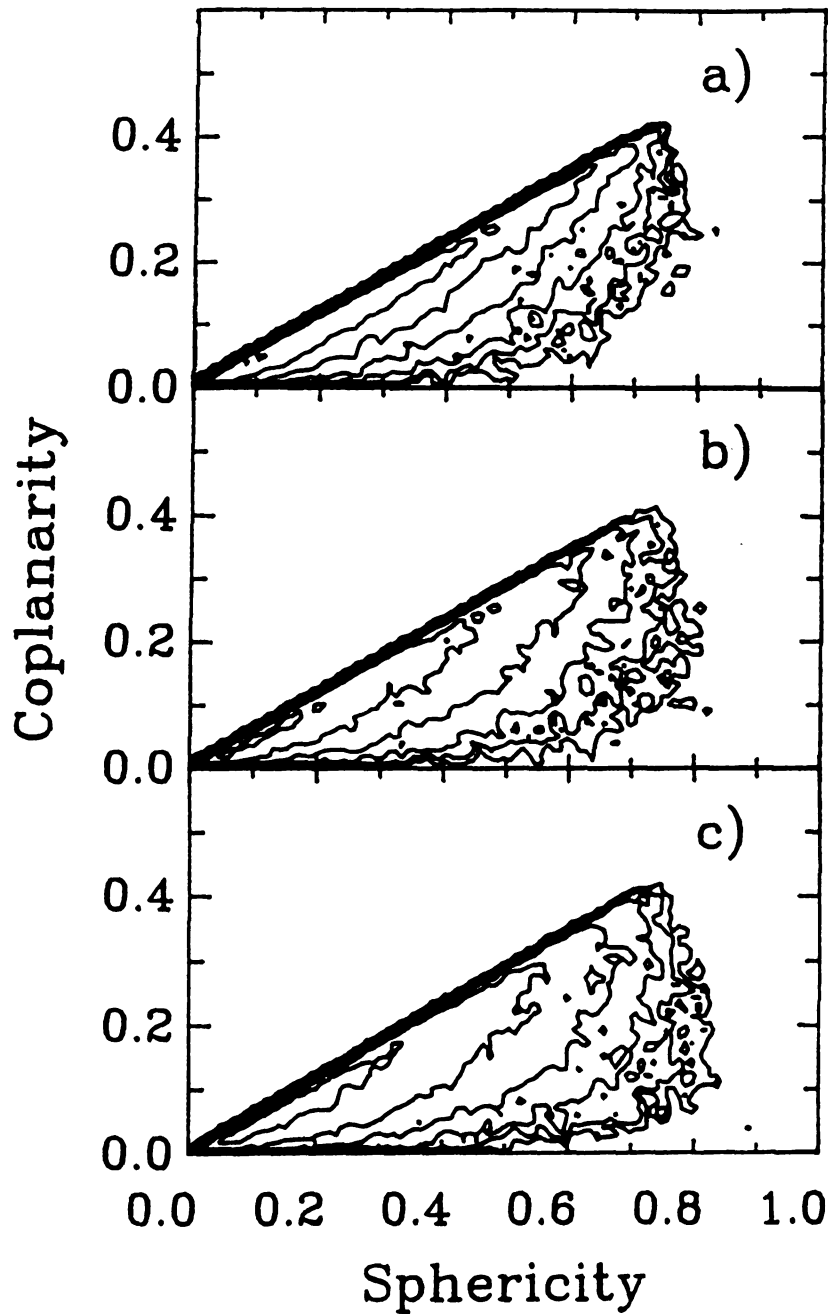


Figure IV.32: A comparison of the predicted event shape distributions from the a) sequential and c) simultaneous simulations to that measured for the b) experimental data for the reaction Ar+V at 85 MeV/nucleon.

flattened prolate spheroid (a long primary axis and an extremely short tertiary axis). This interpretation of the shape distribution is made by observing the steepness of the contours with respect to the line from  $(0,0)$  to  $(0.75,0.43)$ , which corresponds to two dimensional shapes. The elongation of the primary axis suggests a strong kinematic constraint caused by the initial decays of the system. These earliest decays occur when the system is maximally heated, thus these decays carry off the most energy and there is a large relative momentum between the two daughters. The later decays occur after the system has cooled and are less likely to define the principal axes. The simultaneous process does not contain the cooling through particle emission or the emission-by-emission momentum conservation that would lead to elongation in one or two principal axes. It should produce spherical event shapes in the limit of infinite multiplicity. The event shape distribution displayed in Figure IV.27c is on average less prolate (a larger sphericity) than the previous simulation. The same comparison can be made between the two distributions generated by the two simulations for each of the other five beam energies (Figures IV.28 to IV.32).

The contour plots provide qualitative information concerning the degree to which the two simulations are able to reproduce the event shape distributions of the experimental data. However, it is easier to quantify the results of these comparisons by studying the centroids of the distributions. Figures IV.33, IV.34, and IV.35 provide three alternate displays of the sphericity and coplanarity centroids as a function of beam energy for the experimental data and for the two simulations. For the 35 MeV/nucleon case, the experimental centroids are almost identical to those predicted for sequential decay. For energies greater than 35 MeV/nucleon the experimental centroids fall between the two predicted values indicating that the sequential model has failed for these energies. Figures IV.34 and IV.35 suggest that from 35 to 65 MeV/nucleon there is a progression from the sequential extreme to the simultaneous

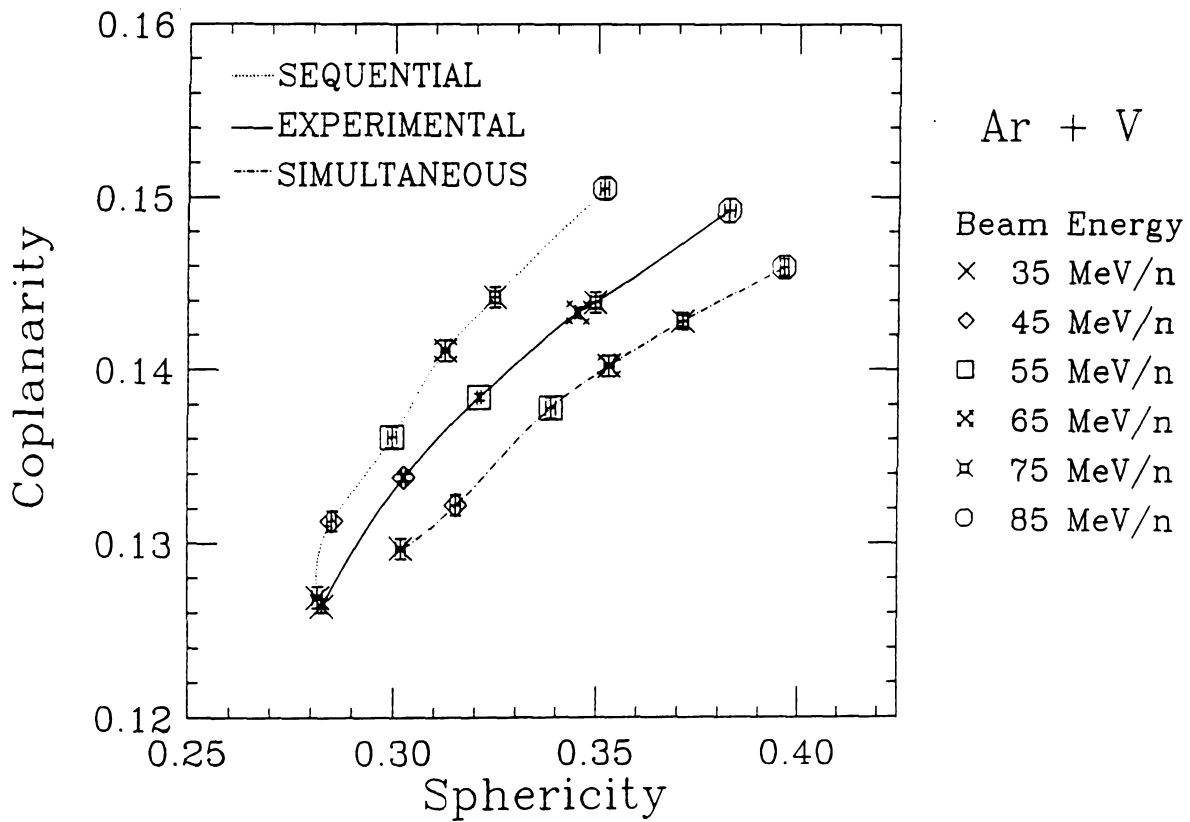


Figure IV.33: The trajectories of the sphericity and coplanarity centroids as the beam energy is increased from 35 to 85 MeV/nucleon.

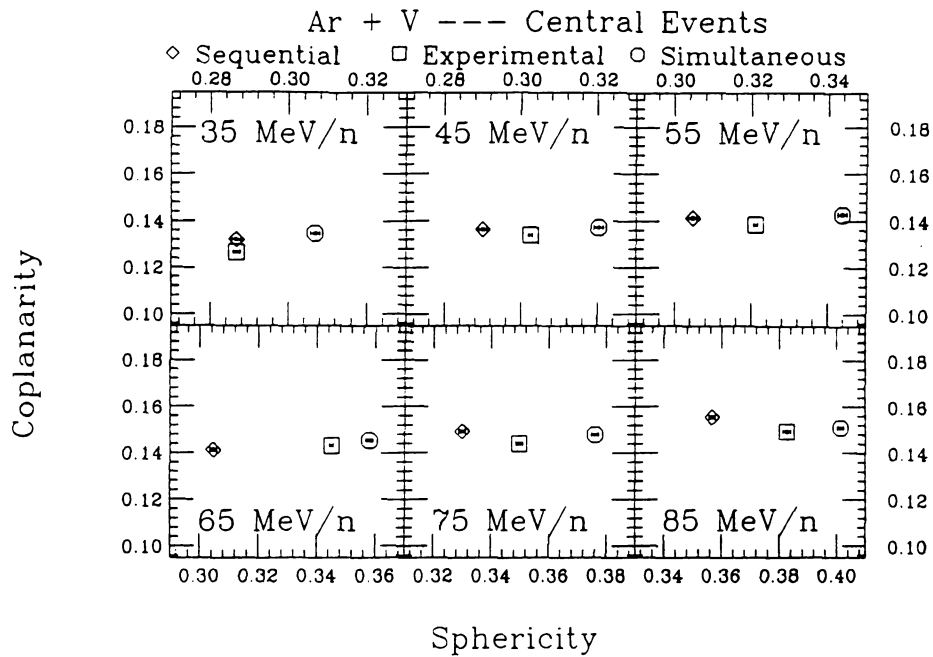


Figure IV.34:  $S_{Average}$  and  $C_{Average}$  for the two simulations and for the experimental data at each of the six beam energies.

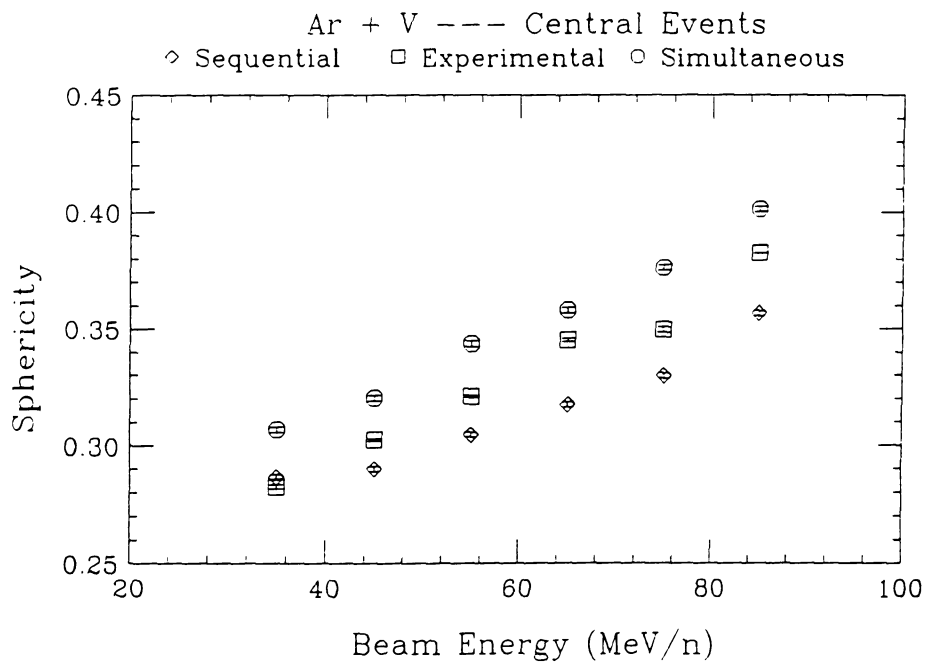


Figure IV.35: A plot of  $S_{Average}$  as a function of the incident energy for the two simulations and for the experimental data.

extreme. This progression is less clear when the data are plotted as in Figure IV.33. This figure plots the trajectories of the centroids in S-C space as the beam energy is increased. The average sphericity and coplanarity values increase with beam energy. This effect is due to the increased multiplicity of detected charged particles. The multiplicity increase is a function both of the increased energy available for particle production and the increased efficiency for detection. The trajectory of the simultaneous simulation closely follows the trajectory predicted by the simple finite multiplicity simulations as one would expect. Regardless of how the data are plotted, the experimental distributions never reach the predictions of the simultaneous simulation. This may be because the effects of other physical processes have not been considered (collective flow, rotation, spectator matter, etc.). Additionally, for the purposes of this analysis, simultaneous multi-fragmentation has been defined as isotropic emission, which may be an unrealistic requirement. This assumption was made to eliminate any spurious effects that may have arisen had the first order observables not been constrained to be identical between the two simulations and as similar as possible to the experimental data. It was decided to start with a model of sequential decay and then generate an approximation of multi-fragmentation. It would not have been possible to start with a reasonable model of multi-fragmentation and then try to insert the kinematic correlation that would have been manifested in a sequential decay. Therefore, the failure of the sequential model for beam energies above 35 MeV/nucleon is of greater significance than the failure of the isotropic simulation for the higher beam energies.

## K Conclusions

I conclude from this analysis that the kinematical constraints and the time ordered emission implicit in a sequential decay process create an observable elongation in

the predicted event shape. There is clear separation between the centroids of the event shape distributions predicted for a sequential decay and a simultaneous multi-fragmentation, indicating that this multi-particle observable is sensitive to the break-up dynamics. At 35 MeV/nucleon, the event shape distribution determined from our experimental data exhibits an elongation beyond that expected from an isotropic simultaneous simulation. The observed distribution agrees with that predicted for the simple sequential decay. This suggests that the decay dynamics of this system at excitation energies of approximately 8 MeV/nucleon are dominated by the same processes which have been observed at excitation energies below 5 MeV/nucleon. At 35 MeV/nucleon, the center-of-mass velocity is well below the Fermi velocity and mean field effects are expected to be strong. Sequential decay is expected to play an important role in the de-excitation process. At higher bombarding energies, the sequential model is no longer able to reproduce the observed distributions. This suggests that the expected change to a multi-fragmentation reaction mechanism may have occurred. The predictions of the simultaneous simulation never reach the experimental values even for the highest energies. This may suggest that the region above 35 MeV/nucleon, which corresponds to available excitation energies of 8 to 20 MeV/nucleon, is a transition region. There may be a mixing of the two processes, a mixing of events that could be individually characterized as one or the other process, or a separate transitory process. The failure of the simultaneous simulation may also be an artifact of the unrealistic requirement of isotropic emission, the sampling of impact parameters, the failure to account for rotation and collective flow, or the failure to exclude completely spectator matter for the cold target and projectile remnants. For the purposes of work, the onset of multi-fragmentation is defined as the point at which the sequential model fails, which is above 35 MeV/nucleon.

# Chapter V

## Conclusions

The studies described in this thesis attempt to address questions related to the equation of state of nuclear matter. The specific questions that were addressed included: at what density does a nuclear freeze-out occur, what is the temperature at which this freeze-out takes place, and at what excitation energy can the system be considered to go beyond the limits of the stability of normal nuclear matter and undergo a phase transition. All of these questions are concerned with the point during the evolution of a nuclear reaction that fragment formation occurs. In the expansion/freeze-out view of a reaction, the system initially converts excitation energy into mechanical work (expansion). This energy is later used to break nuclear bonds at the final stage of the reaction (freeze-out). The multi-fragmentation study was concerned with determining the amount of excitation energy necessary to allow the system to enter a region of mechanical instability. Upon entering this region, the system disassembles into fragments.

The nuclear density was estimated by observing the correlation between pairs of particles that were emitted independently from the thermalized source created during the interaction of a 500 MeV proton with a silver nucleus. The shape of the correlation functions were compared to model predictions which allowed the spatial dimensions (source radius) of the source to be determined. A rough estimate of the mass of

the source can be made by assuming that the target is completely thermalized and equilibrated prior to emission of fragments. This estimate does not allow for pre-equilibrium emission of particles or a separation of the thermalized zone and the target remnant. For the p+Ag reaction, one expects that the thermalized region would be completely contained within the target remnant. The excitation energy which was deposited by the incident proton as it passed through the target could then be dissipated through the entire target nucleus forming a single equilibrated source. The most reliable measurement of the source radius is extracted from the deuteron-deuteron correlation function. This particle pair does not contain peaks associated with resonant decays. These resonant decays distort the extracted radius. The radius of the thermalized source is measured to be approximately 9 Fm. This yields a freeze-out density of  $0.17^{+0.17}_{-0.08}\rho_0$ .

If one takes a system of a given number of nucleons and varies the input excitation energy, the resulting initial temperature will also vary. The system has two ways of dissipating this excitation energy: expansion and fragment formation. If the system does not emit any fragments, then the temperature of the system, when it reaches the freeze-out density, will depend on the initial excitation energy. Therefore, the measured temperature should depend upon the energy of the incident beam as this is the major factor which determines the excitation energy generated during the initial phase of the collision. The slope parameter of the kinetic energy spectra generated a measure of the temperature that exhibited this expected feature. An alternate method of measuring nuclear temperature, through the excited state populations, however, yielded a constant and low value for the temperature.

The study presented here was one of several studies that have attempted to analyze further the second method for determining nuclear temperatures. The populations of particle unstable excited states were measured through the detection of the daughter

fragments associated with the resonant decay. The individual states appear as peaks in the relative momentum spectra. An estimate of the populations can be made by integrating the peaks above a background for independent emission and correcting for the efficiency of the detection system. This analysis yields a temperature value  $4 \pm 1$  MeV. These values are consistent with those established in heavy-ion induced reactions.

A nuclear system should be able to reach a region of mechanical instability if the internal excitation energy exceeds a threshold value. At this point the disassembly will proceed simultaneously. A signature of this process can be found in the distribution of event shapes. If the reaction proceeds through a long-lived equilibrium process, the initial decays of the system will occur at the highest temperatures. These initial decays will define an axis along which the event shape will be elongated. If the reaction proceeds through a multi-fragmentation process, the event shape will be spherical in the limit of infinite multiplicity.

The shape distributions observed in a set of Ar+V data at bombarding energies from 35 to 85 MeV/nucleon are compared to predictions from simulations. Both a sequential decay and a simultaneous multi-fragmentation are simulated. The experimental distributions are evaluated to determine which of the two models more accurately describes the reaction dynamics at a given energy. It is observed that the sequential simulation reproduces the experimental distribution for the 35 MeV/nucleon case. For the higher five energies, the centroids of the experimental distributions fall between the two predictions. The failure of the sequential model above 35 MeV/nucleon is seen as an indication that the multi-fragmentation process is contributing to the disassembly of the system. Thus, the onset of multi-fragmentation is conclusively observed.

# APPENDICES

# Appendix A

## Technical Descriptions of the Detectors Systems

### A The 4-by-4 Close Packing Array

The 4-by-4 close packing array [Fox87] is a set of sixteen fast/slow plastic scintillator phoswichs [Wilk52]. These detectors were designed for a series of experiments which studied charged-particle correlations at small relative momenta (one of which is described in chapter II). A goal of these experiments was to measure the correlation function down to a relative momentum of less than 1 MeV/c, therefore it was essential that the detectors close-pack. In addition, it was necessary to determine the relative angle between two detected particles to within 1 degree. This angular resolution was achieved using a multi-wire proportional chamber (MWPC) [Hass84, Tick80, Tick81, Char70]. This placed a limitation upon the dimensions of the array, because it was necessary for the array to fit behind the MWPC (which had been constructed for a previous experiment) which had an active area that was 15 by 15 cm.

Each of the detectors in this array was a modified truncated square pyramid, refer to Figure A.1. Since perfect squares will not close-pack on the surface of a sphere, the detectors were skewed slightly. Ignoring the individual asymmetries in the lengths of each side, the front surfaces of the detectors were 1.5 inch squares. The front

Table A.1: Characteristics of the fast and slow scintillation material.

Constants	BC-412 (fast)	BC-444 (Slow)
Light Output % Anthracene	60	41
Rise Time (ns)	1.0	19.5
Decay Time (ns)	3.3	179.7
Pulse Width FWHM (ns)	4.2	171.9
Wavelength of Max Emission (nm)	434	428
No. of C Atoms per cm <sup>3</sup> (x10 <sup>22</sup> )	4.74	4.73
No. of H Atoms per cm <sup>3</sup> (x10 <sup>22</sup> )	5.23	5.25
Ratio H:C Atoms	1.104	1.109
No. of electrons per cm <sup>3</sup> (x10 <sup>23</sup> )	3.37	3.37

scintillator was a 1.588 mm thick wafer of BC412 plastic scintillator. The stopping scintillator is a 137 mm deep block of BC444 plastic scintillator. The characteristics of these scintillation materials are given in Table A.1. The back of the scintillators was approximately a 2.0 by 2.0 inch square. This gave the detectors a taper such that when placed 17 inches from the center of the target, each of the four edges pointed directly to the center. A two inch diameter Amperex photomultiplier tube (PMT) was directly coupled to the scintillator with an optical epoxy. The scintillators were painted with an opaque diffusive white paint to optimize light collection and minimize cross-talk between adjacent detectors. They were stacked in a four-by-four array, as illustrated in Figure A.2, when employed behind the MWPC. In this configuration, each detector covered a 5° range in polar angles and the entire array covered a total solid angle of 165 msr.

## B The Multi-Wire Proportional Chamber

The multi-wire proportional counter (MWPC) was designed to provide better than 1° of angular resolution between multiple simultaneous hits [Hass84 Tick80, Tick81, Char70]. It contained three wire planes, each of which contained 64 wires. The wires

MSU-87-027

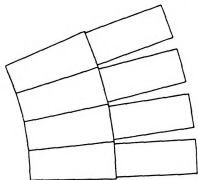


Figure A.1: A side view of four of the detectors.

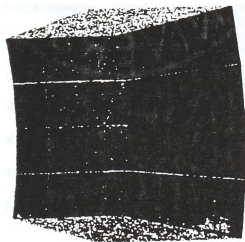


Figure A.2: Perspective view of the 4-by-4 array stacked for installation behind the MWPC.

on the X plane were arranged vertically, those on the Y plane were horizontal, and those on the Q plane were at  $45^\circ$ . Having three wire planes allowed correct position determination for multiple hits. Had only two wire planes been employed, there would have been ambiguities. The wires on each plane were spaced 2.5 mm apart. To minimize the fluctuations, the wires were clustered in sets of two. Therefore, each wire plane had 32 signals. The signal from each pair of wires was connected to a discriminator channel, which was read by the PCOS III system. Hit information was recorded. No record of the amplitude or the time was made for the individual wires. The MWPC was pressurized to 450 Torr of 50/50 Argon/Ethane. The X and Y planes were biased to 3127 V while the Q plane was biased to 2600 V.

Figure A.3 displays 16 scatter plots of the X and Y positions of the wires that were hit during a valid event for each of the telescopes. Each of the sixteen different plots requires a coincidence with a different one of the 16 phoswich detectors that were employed behind the array. For a valid event to be recorded, two phoswiches were required to fire in coincidence. Three wire planes were then needed to resolve the multiple hit ambiguities. The dark squares correspond to the wires in front of the given detector. Note that the 3rd and 14th wires in the X-plane were dead. The background counts that are plotted, but which are obviously not in front of the given detector, are generated because each valid event had two hits. Therefore, for each X-Y position in front of the selected detector there should also be a point elsewhere on the plot. The scales of the display have been adjusted to suppress many of the off-detector points.

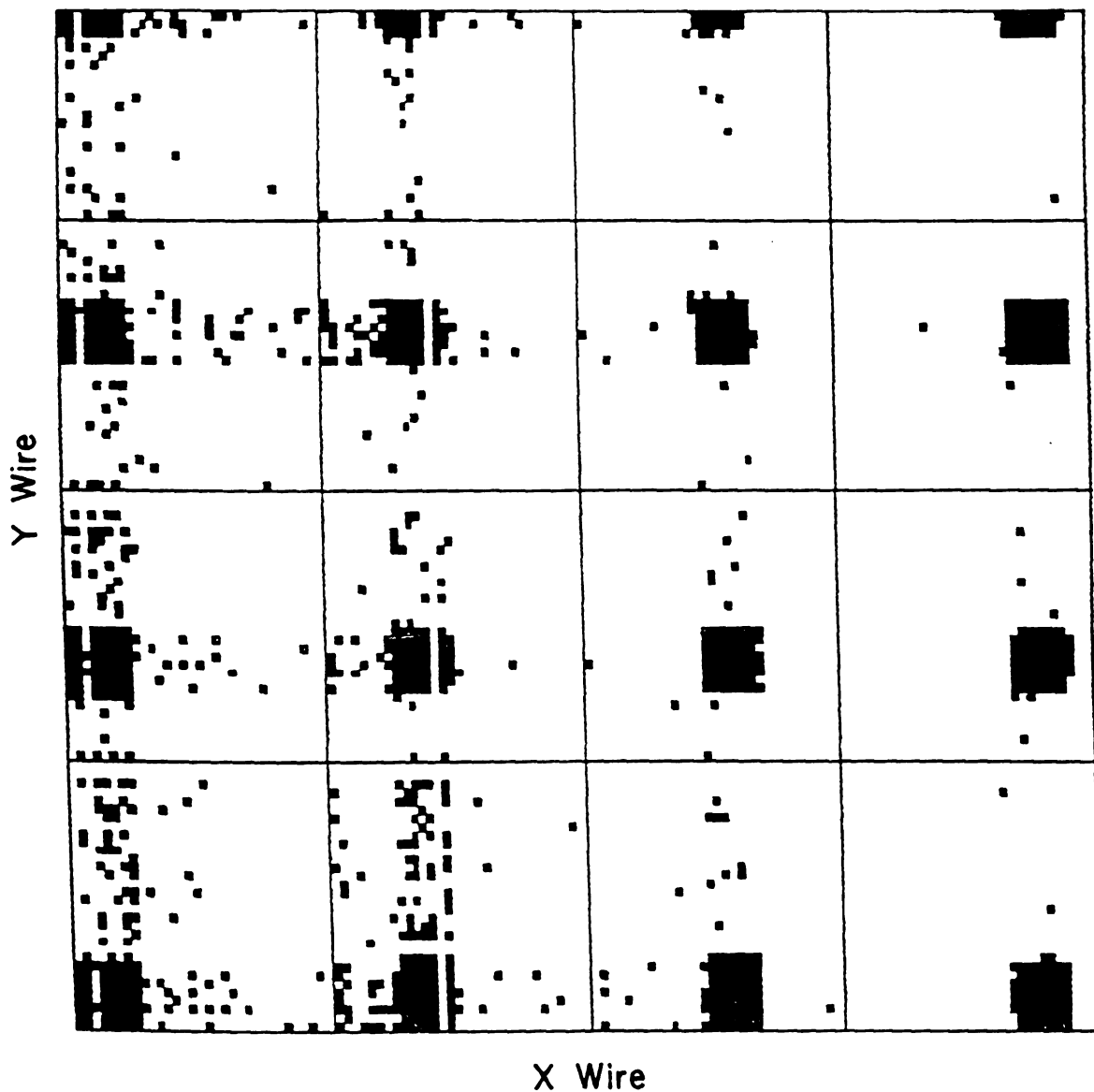


Figure A.3: Scatter plots of the X and Y positions determined by the MWPC when in coincidence with phoswichs 1-16

## C The Multiplicity Array Detectors

The multiplicity array detectors are a set of thirty fast/slow plastic scintillators. These detectors were elements of an array which was designed to detect the multiplicity of fragments emitted in the forward direction. At that time it was assumed that the charged-particle multiplicity was related to the impact parameter. Since the emitted fragments are forward focused, it seemed logical to design an array that covered angles forward of  $45^\circ$ . This would then allow the experimenter to tag an event with an observed multiplicity which could be used as a measure of the impact parameter. The major design goal of the project was to maximize the number of detector channels, therefore, the primary consideration of this array was cost per channel.

It was decided to make these detectors as simple as possible. The front scintillator is a disk of fast plastic (BC412). This disk is two inches in diameter and 1.588 mm thick. The stopping scintillator is a six inch deep cylinder of slow plastic (BC444). An Amperex PMT is coupled directly to the scintillator. The scintillator is painted with an opaque diffusive white paint and then wrapped with black tape.

## D The MSU $4\pi$ Array

The  $4\pi$  array was designed to study violent high multiplicity reactions. The apparatus completely surrounds the target with detectors. The geometric shape of the device is a truncated icosahedron. This is a solid with 32 facets, 20 of which are hexagons and 12 of which are pentagons. Figure A.4 displays a schematic diagram of the external support structure for the  $4\pi$ . Each facet comprises a single sub-array of the entire detection system. The subarrays will employ a logarithmic detection scheme [West85]. This enables the device to have a high dynamic range. This logarithmic detection system consists of three separate types of detector. These detector systems form

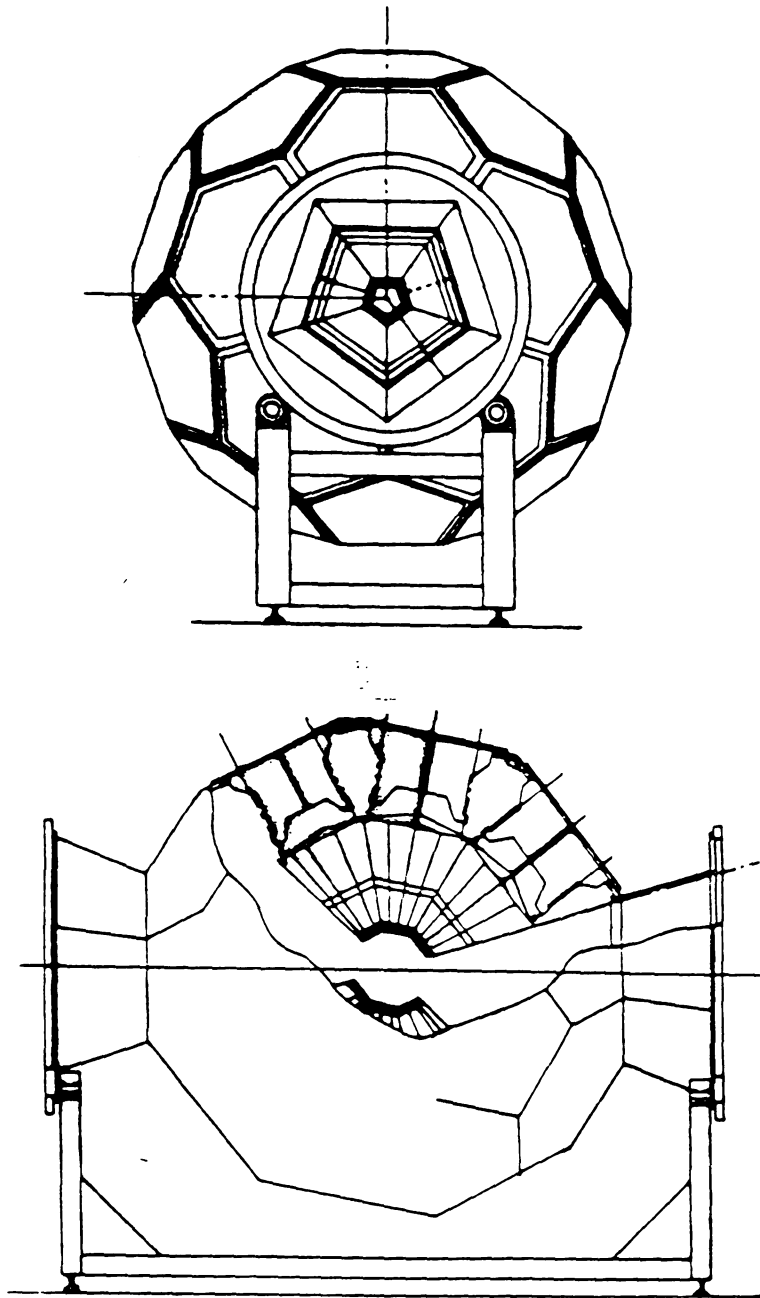


Figure A.4: A schematic diagram of the MSU  $4\pi$  Array.

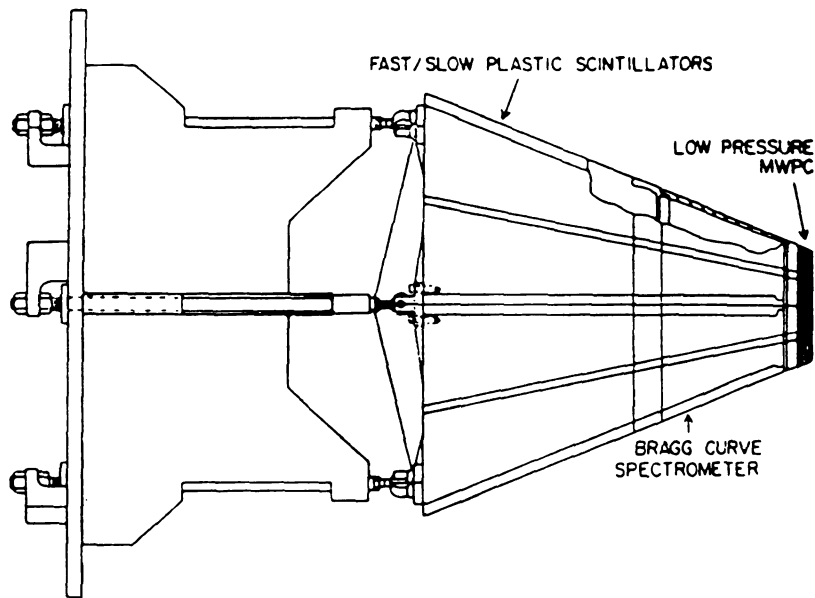


Figure A.5: A schematic diagram of a single module of the  $4\pi$  Array.

three shells, each with a higher stopping power than the one inside it. The innermost shell will be made up of low pressure gas counters. These will stop only the most highly ionizing fragments (mostly fission fragments). The second shell shall be made up of high pressure gas counters. These will stop the majority of the intermediate mass fragments. The outer shell is made up of phoswich scintillation counters. These detectors are optimized for light charged particles. A diagram of a single subarray is provided in Figure A.5.

For the experiments described in this thesis, the  $4\pi$  array was instrumented with only the outer shell of phoswich counters. For this shell only, each subarray is further divided into either five or six detectors (depending on whether it is a pentagonal or hexagonal module). This reduces the probability of multiple hits. The multiple hit problem is most severe for the light charged particles because they are produced in the largest abundance. The phoswich detectors in the  $4\pi$  array are similar to those described earlier in this appendix. Their dimensions, however, are larger. The  $\Delta E$

scintillator is 3.175 mm thick, the stopping scintillator is 30 cm thick, and they are shaped like truncated triangular pyramids.

One pentagonal facet had to be left open at both the entrance and exit of the array. This left a large uninstrumented region in the forward direction where the production cross-section is the highest. It was decided that the phoswich detectors described in sections A and C should be mounted in the empty forward wedge. These detectors now make up the *forward array* of the  $4\pi$ . As they were not designed for this purpose they do not close pack, but they provide substantial coverage in a very important angular range.

## Appendix B

# The Light Response of Plastic Scintillator

### A Scintillation Theory

Recently there has been an increase in the usage of organic scintillator as a detection material for nuclear physics. This has been brought about by an increase in the energy available from heavy ion accelerators and from the increased complexity of the experiments. As the energy of the projectile is increased, there is a comparable increase in the energy of the reaction products that must be detected. As the energy of the fragments is increased, the amount of detector material that is required to stop them must also be increased. It is a relatively simple and inexpensive task to make scintillation counters of greater and greater size. Solid state detectors, on the other hand, are limited to approximately  $5\text{mm}$  in thickness. Though an experimenter can employ a multiple element stack of silicon detectors, each of the elements will require an extra channel of electronics making the cost per telescope rise steeply with total stopping power. The increased complexity of experiments makes it necessary to employ arrays with large numbers of detectors. For such arrays, the cost per channel is a major consideration. Additionally, plastic scintillator is an ideal detection material for close-packed arrays, because it can be machined to arbitrary shapes and

requires an extremely small amount of packaging between the sensitive areas of the detectors. The fact that a large number of close packed arrays have been built using plastic scintillator [Bade82, West85, Schi85, Boug86, Lide87, Sara88, Poul88, Chap88, Lide88] demonstrates this point.

Plastic scintillator has some disadvantages compared to other types of detection material. For example, the intrinsic energy resolution is inferior to that of solid-state detectors and the light response is non-linear. The intrinsic energy resolution is a weakness that must be accepted, however, with a little work, the light response function can be determined and its complexity will not compromise the energy measurement.

The mechanism for light production in scintillation material is the de-excitation of electrons which have been perturbed from their ground state orbitals. As a charged-particle passes through matter, it interacts with the electrons throughout the lattice. These electrons are knocked out of their bound states into the conduction band of the material. As the electrons de-excite, they emit photons. If the band gap of the material is in the visible range, these photons will appear as scintillation light. The efficiency for conversion of the kinetic energy of the de-accelerating charged particle into photons with wavelengths in the visible range is reduced as the ionization density is increased, because the probability that multiple electrons will be excited at a single lattice site becomes non-negligible. This reduction in conversion efficiency occurs because only a single electron may occupy a given state at a given time, therefore, the additional electron must follow a different de-excitation route which may not involve emission of photons in the visible range. Additionally, an ion which is stopping quickly (high ionization density) may impart a greater kinetic energy to the electrons with which it interacts than an energetic light ion would impart. The additional energy of the electron will not be converted to light energy as the electron de-excites because

only the transition across the band gap will produce scintillation photons. These mechanisms account for the non-linearity observed in the light response of organic scintillation material.

Early work on the light response function was done by Birks [Birk64]. He derived the following formula that relates the fluorescence per unit path length ( $dL/dx$ ) to the specific energy loss for a charged particle ( $dE/dx$ ):

$$dL/dx = S(dE/dx)/(1 + kB(dE/dx)) \quad (\text{B.1})$$

where  $S$  is the scintillation efficiency and  $kB$  is a quenching parameter. This theory has been refined and the number of adjustable parameters has been increased [Chou52]. However, the basic  $dL/dx$  formula, which contains a saturation as a function of ionization density, is generally accepted. The total light produced by a particle stopping in a scintillator is then given by

$$L = \int_0^R S(dE(x)/dx)/(1 + kb(dE(x)/dx))dx \quad (\text{B.2})$$

where  $R$  is the range of the particle.  $dE(x)/dx$  is the function for the energy loss [Knol79]. For a particle that is stopped within the material, the energy loss function will be the Bragg curve. This theory has been supported by experimental results [Crau70].

One can not directly determine the scintillation efficiency or the quenching parameter as a function of ionization density. The experimenter would prefer to determine the light response as a function of quantities that can be easily measured, such as the incident particle's charge ( $Z$ ), mass ( $A$ ), and energy ( $E$ ). Attempts to determine functional forms for the light response in terms of these quantities have been relatively successful [Becc76, McMa88, Poul88].

In order to get a reliable energy calibration for a set of scintillation detectors, one

typically would have to calibrate each detector during each experiment. These calibration functions would be specific to an individual detector and an individual particle species. However, this task becomes prohibitive for large numbers of detectors and for experiments for which a large number of different particle types are required. We have completed an extensive study of the light response for a set of fast/slow phoswich [Wilk52] detectors which are elements of the MSU  $4\pi$  Array [West85]. Thirty detectors have been calibrated individually over the course of several experiments. The light response functions of all of the detectors were similar to one another and remained constant from experiment to experiment. We have generalized this function and applied it to the remaining 175 detectors in the array.

## **B The Calibration Experiments**

### **1 The Detectors**

The detectors that were used for these studies are elements of the MSU  $4\pi$  Array. This array contains phoswich detectors of four different geometries. The relevant characteristics of each detector type are listed in Table B.1. For all of the detectors, the front scintillator is BC412 (3.3 nsec decay time) and the stopping scintillator is BC444 (180 nsec decay time). Refer to Table A.1 for details about these two types of scintillator. The detectors were biased from 1000 to 1600 Volts depending on the maximum fragment charge desired for a particular application. The signal from the detector is passively split three ways. One signal determines the timing and the trigger logic, the other two signals are integrated in LeCroy FERA QDCs.

Table B.1: A listing of the specifications of each of the four types of phoswich detector that were employed in the studies of the light response.

Detector Type	Geometry	$\Delta E$ Thickness (mm)	$E$ Thickness (mm)	PMT Type
I	Truncated Square Pyramid	1.566	15.0	Amperex 2"
II	Right Cylinder	1.566	15.0	Amperex 2"
III	Truncated Triangular Pyramid	3.175	25.0	Amperex 3"
IV	Truncated Triangular Pyramid	3.175	25.0	Amperex 3"

## 2 Elastic Scattering

A calibration of the response of 16 type I detectors for protons and deuterons was performed using the SFU scattering chamber at the TRIUMF facility. The detectors were stacked in a four-by-four array behind a multi-wire proportional chamber (MWPC) which provided high resolution position information for the incident particles. A scintillator paddle was positioned in the forward direction on a movable arm. This configuration is displayed in Figure B.1 Proton beams of 200, 300, and 500 MeV were scattered off  $\text{CH}_2$  and  $\text{CD}_2$  targets. A coincidence was required between the paddle and the array for a valid event. Using the position information from the MWPC and assuming elastic scattering, the energy of the recoil particle could be calculated. Given the recoil energy one could determine the amount of energy which was deposited in each of the two scintillation elements. Figure B.2 displays scatter plots of relative light versus calculated energy from the slow scintillator for protons

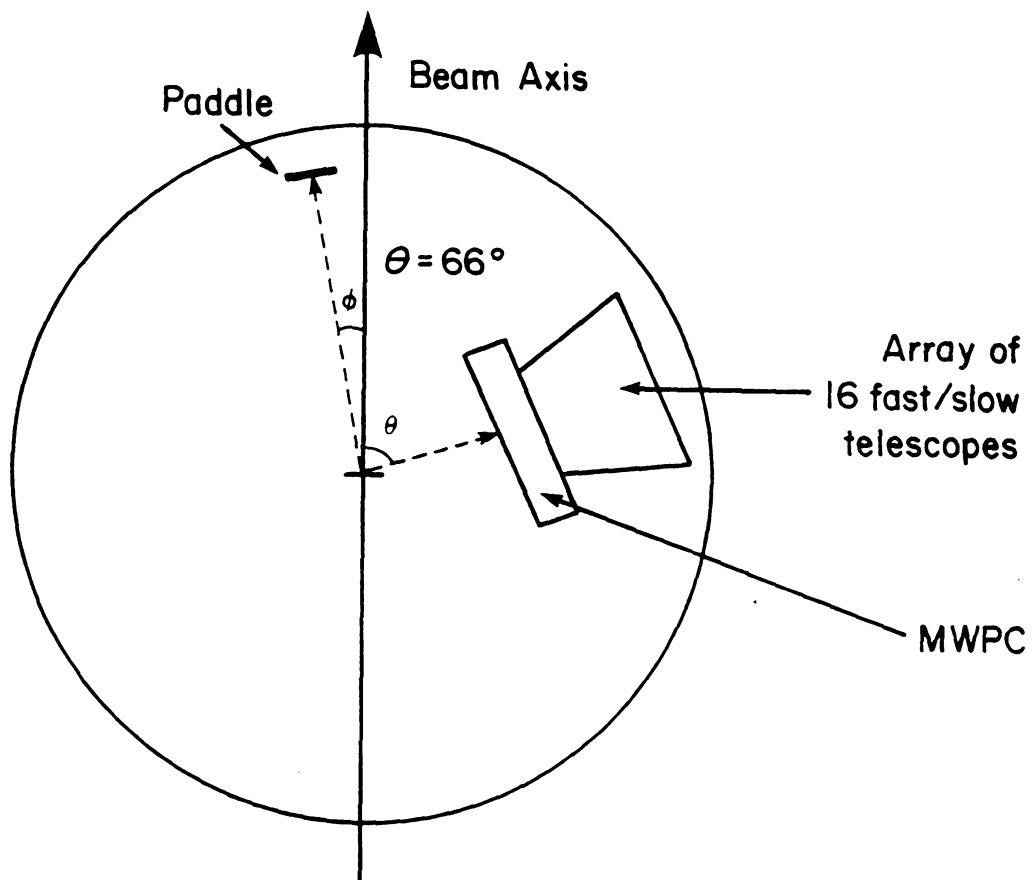


Figure B.1: The experimental configuration for a calibration of the response to protons and deuterons.

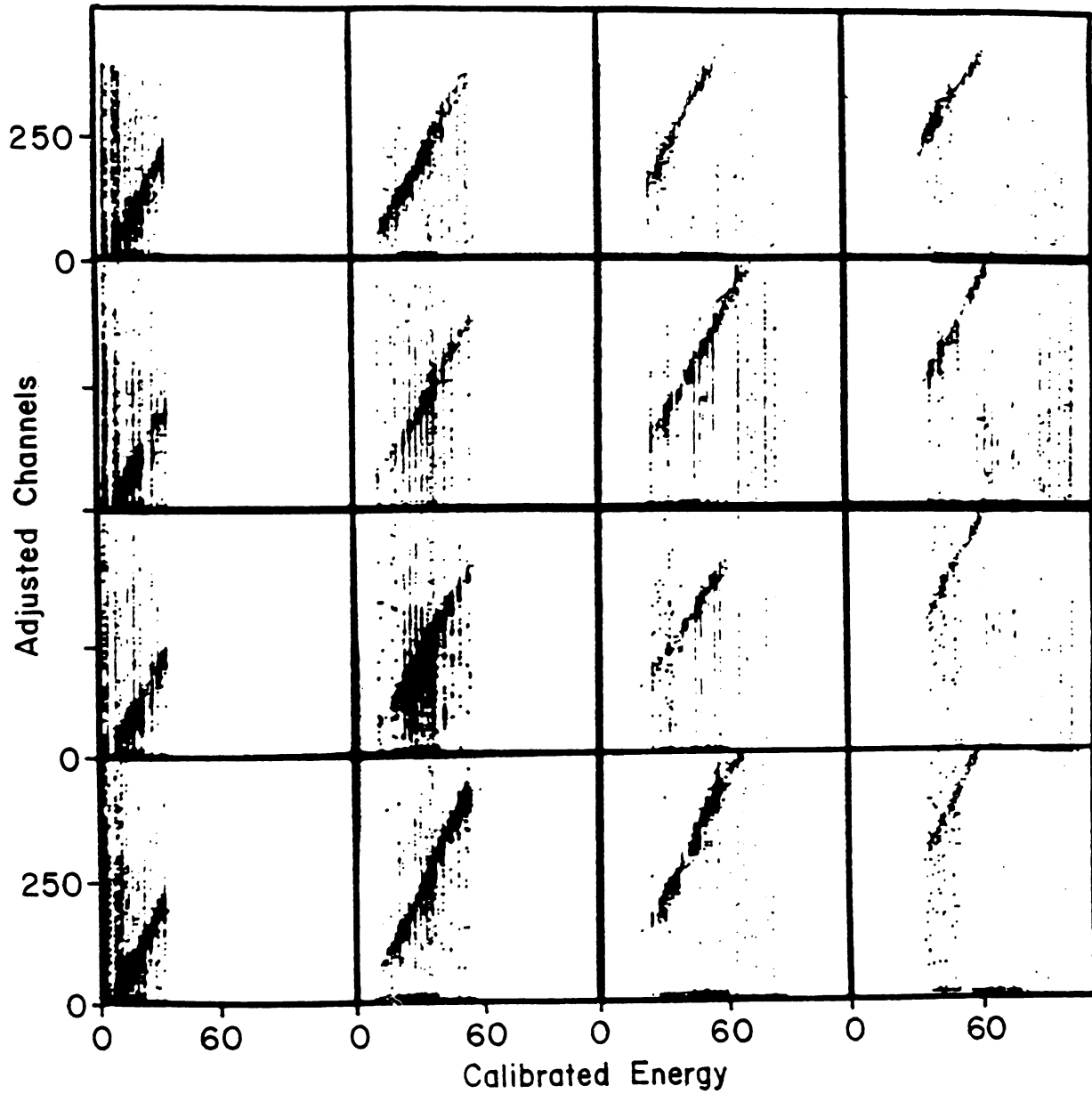


Figure B.2: A scatter plot of the magnitude of the signal from the slow scintillator against the calculated energy of the recoil proton from the reaction  $p[p,p]p$ .

Table B.2: The thicknesses of the aluminum degraders that were used in the calibration of the phoswich detectors and the energy deposited in each scintillator

Beam Energy	Particle Type	Degrader Thickness (mm)	$E_{(fast)}$ (MeV)	$E_{(slow)}$ (MeV)
212 MeV	$\alpha$	6.91	11.7	120
212 MeV	$\alpha$	9.45	16.7	74
212 MeV	$\alpha$	10.48	30.2	25
106 MeV	d	6.91	2.3	85
106 MeV	d	9.45	2.4	78
106 MeV	d	10.48	2.5	73
106 MeV	d	14.01	2.9	62
106 MeV	d	19.22	4.0	40
106 MeV	d	22.10	6.8	19

for each of the 16 detectors. Data from the three incident energies have been summed for these plots. All sixteen detectors were matched (refer to Appendix C) and the spectra were added. Figure B.3 displays a scatter plot of this summed data. The centroids of the light versus energy curve for each energy channel were determined. Figures B.4a and B.4b display the results for the calibration of the slow scintillator for protons and for deuterons.

### 3 Degraded Calibration Beams

Ten type I detectors were calibrated using degraded alpha and deuteron beams from the K500 cyclotron at MSU. The detectors were positioned on the rotating table in the 60 inch scattering chamber and were rotated to zero degrees one at a time. Degraders were positioned on the target ladder. The thicknesses of these degraders, the resulting energy of the calibration beams, and the energy deposited in each of the two scintillation elements are given in Table B.2. Figure B.5 displays the results of this calibration. The solid lines correspond to the fits to the experimental calibration data.

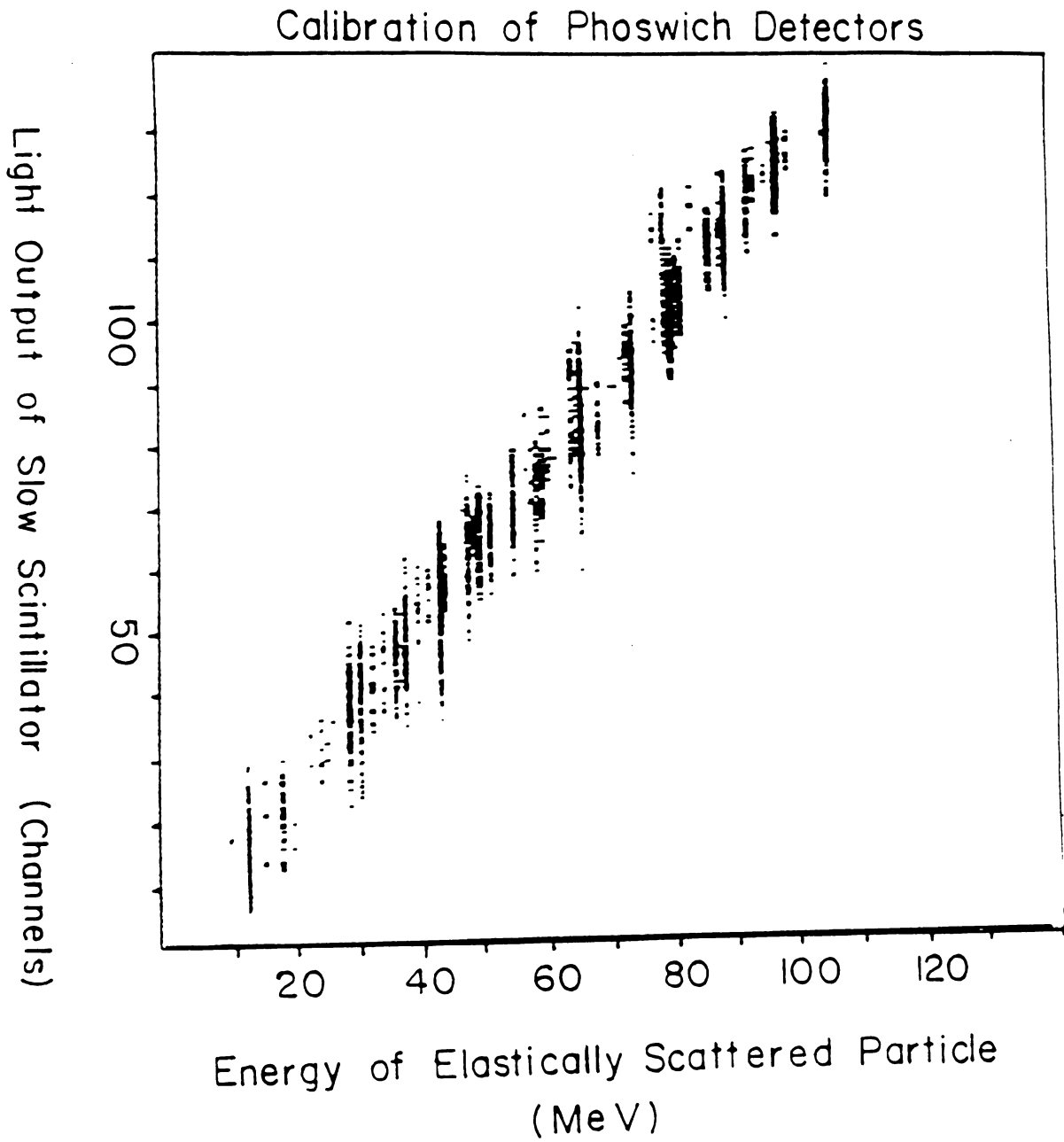


Figure B.3: A scatter plot of the magnitude of the signal from the slow scintillator against the recoil proton energy.

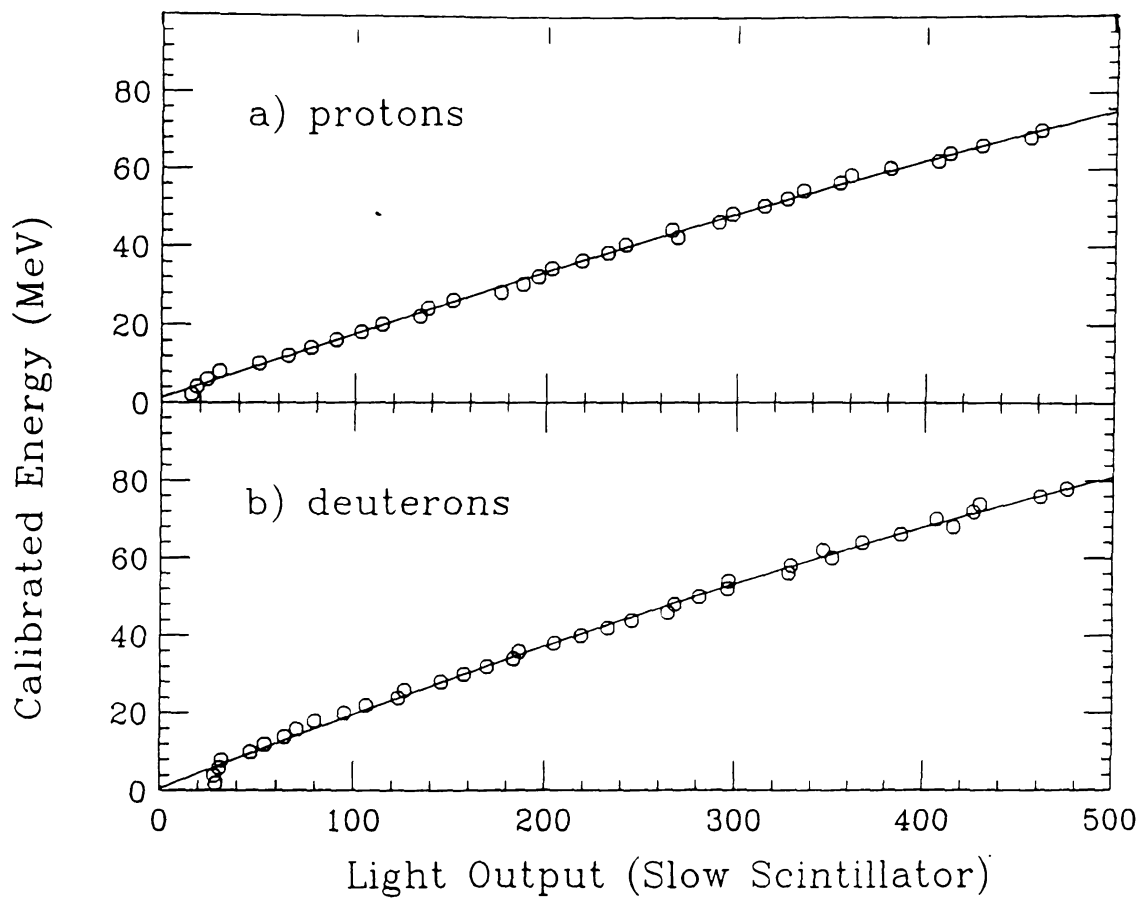


Figure B.4: The centroids of the light distribution were determined for each recoil energy. a) displays the proton response function, and b) displays the deuteron response function. The solid curves correspond to fits to the experimental calibration data.

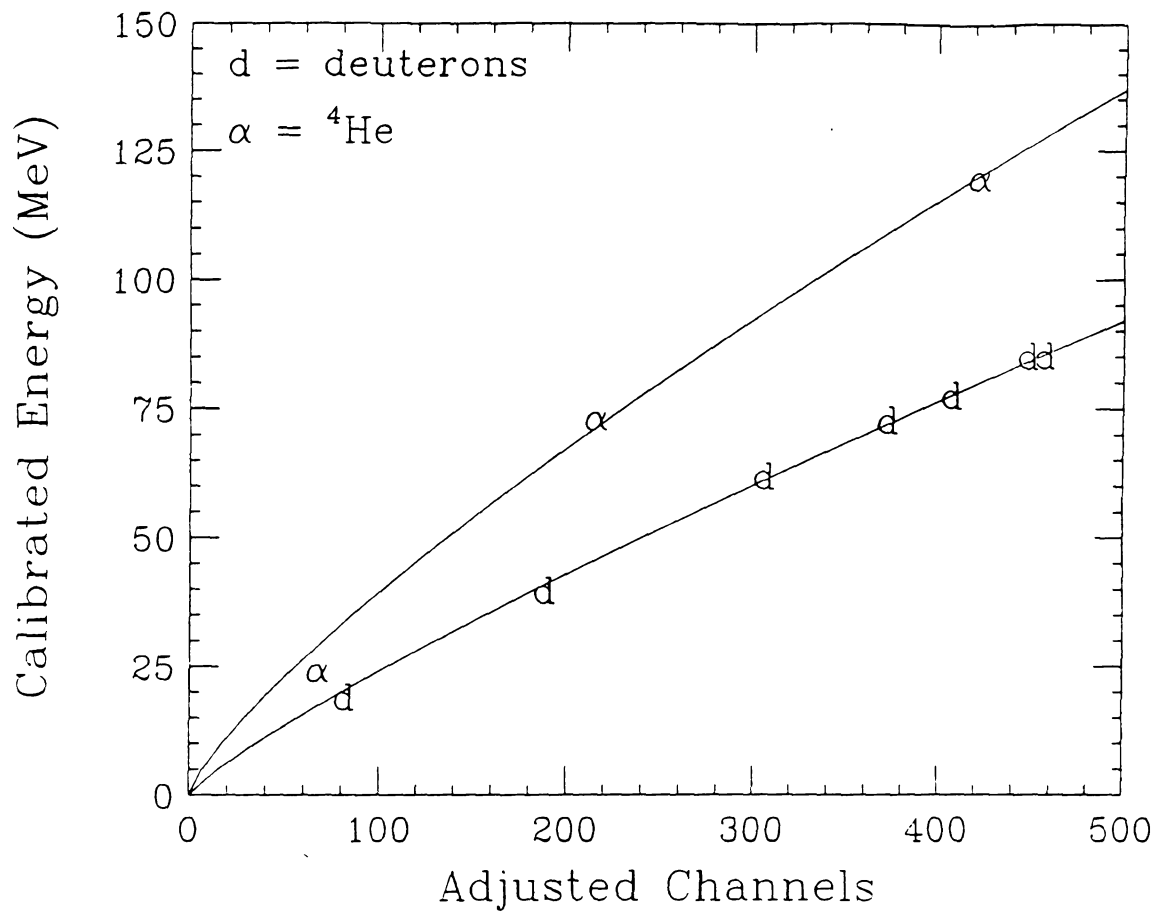


Figure B.5: The light response as a function of energy for the slow scintillator for deuterons and  $\alpha$  particles.

## 4 Fragmentation Beams

Ten type I, three type II, and 12 type III detectors have been calibrated using fragmentation beams at MSU. In our first application of fragmentation beams to provide calibration points for phoswichs, the K500 cyclotron provided a beam of 50 MeV/nucleon  $^{14}\text{N}^{6+}$  which was stopped in a 35 mil tantalum production target which was positioned in Beam Box 2. The detectors were positioned on the table of the 60 inch scattering chamber and were rotated one at a time into the beam of fragments. The strengths of the downstream beam line magnets (quadrupoles Q10, Q11, Q12, and Q14, dipole BM2, and quadrupoles Q14, Q15, Q16 and Q17) were varied to select the rigidity of the forward fragments produced in the target. The width of the accepted rigidity slice was determined by a one inch diameter collimator at the entrance to the scattering chamber. The beam line magnets, however, were not well calibrated (i.e. a 30% reduction in current did not correspond to a 30% reduction in field strength). Therefore, the exact energy of the outgoing fragments was measured with a silicon telescope and cross-checked with the estimated field strengths. In a later application of fragmentation beams, the six type III detectors were positioned in a test box behind the  $20^\circ$  exit port on the S320 spectrometer. The spectrometer was positioned at zero degrees with respect to the beam axis in order to receive the greatest flux of fragments. Once again, a beam of 50 MeV/nucleon  $^{14}\text{N}^{6+}$  was stopped in a tantalum target. The target was positioned in the target chamber of the S320. The field strengths of the magnets which make up the S320 (Quads Q20 and Q21, and dipole PM3) were set to select several different rigidities. An aperture at the entrance window limited the size of the accepted rigidity slice. This technique produced a beam which contained various isotopes of hydrogen, helium, lithium, beryllium, and boron. Given the charge, mass, and rigidity of each accepted particle type, the energy of the calibration points could be determined. The accepted particle types and energies are

listed in Table B.3. The energy in MeV is given for each particle type as a function of the rigidity settings of the S320 spectrograph. The rigidity values are presented in terms of the percentage of the original beam rigidity. The production beam was 50 MeV/n  $^{14}\text{N}^{6+}$ . The numbers presented in this table are the energy values that would have been accepted by the S320; the cross section for the production of some of these particles types at the quoted energy was too small to be observed.

This method produces a beam composed of many different species of fragments, and is only useful as a calibration technique if one is able to identify the different particle types in the detectors to be calibrated. The phoswichs that we were using were able to resolve all of the different calibration points. Figure B.6 displays a scatter plot of the fast signal against the slow signal for one detector at a single rigidity setting. The tails on the deuteron and alpha points are associated with particles which scattered out of the detectors. The detectors had not been collimated for these tests. These tails are noticeable only for the deuteron and alpha points because those points contain several orders of magnitude more counts than the others. The energy spread present in all of the points is a measure of the width of the accepted rigidity slice and not a measure of the resolution of the detectors.

A similar fragmentation calibration was performed using the Nautilus scattering chamber at GANIL.

## **C The Light Responses of the Scintillators**

### **1 Response Function of the Slow Scintillator**

The spectra from the different detectors and from different calibration runs have been matched [Appendix C], and the results are displayed in Figures B.7 to B.9. The

Table B.3: The energies of the observed fragment species during the fragmentation runs.

Particle Type	100%	90%	80%	70%	60%	50%
p	247	204	164	128	96	67
d	135	109	87	67	49	34
t	92	74	59	45	33	23
$^3\text{He}$	350	287	229	177	131	91
$^4\text{He}$	270	220	175	134	99	69
$^6\text{He}$	183	149	118	90	66	46
$^8\text{He}$	138	112	89	68	50	35
$^6\text{Li}$	404	330	262	202	149	103
$^7\text{Li}$	350	285	226	174	128	89
$^8\text{Li}$	308	250	198	152	112	78
$^9\text{Li}$	275	223	177	136	100	69
$^7\text{Be}$	610	498	397	306	226	158
$^9\text{Be}$	483	393	312	240	198	123
$^{10}\text{Be}$	437	355	282	216	159	111
$^{11}\text{Be}$	399	324	257	197	145	101
$^9\text{B}$	743	606	483	372	275	192
$^{10}\text{B}$	674	549	437	336	248	173
$^{11}\text{B}$	617	502	399	307	226	157
$^{12}\text{B}$	568	462	367	281	208	144
$^{10}\text{C}$	957	782	623	480	355	248
$^{11}\text{C}$	877	716	569	438	324	226
$^{12}\text{C}$	809	660	524	403	298	208
$^{13}\text{C}$	751	611	485	373	275	192
$^{14}\text{C}$	700	570	452	347	256	178

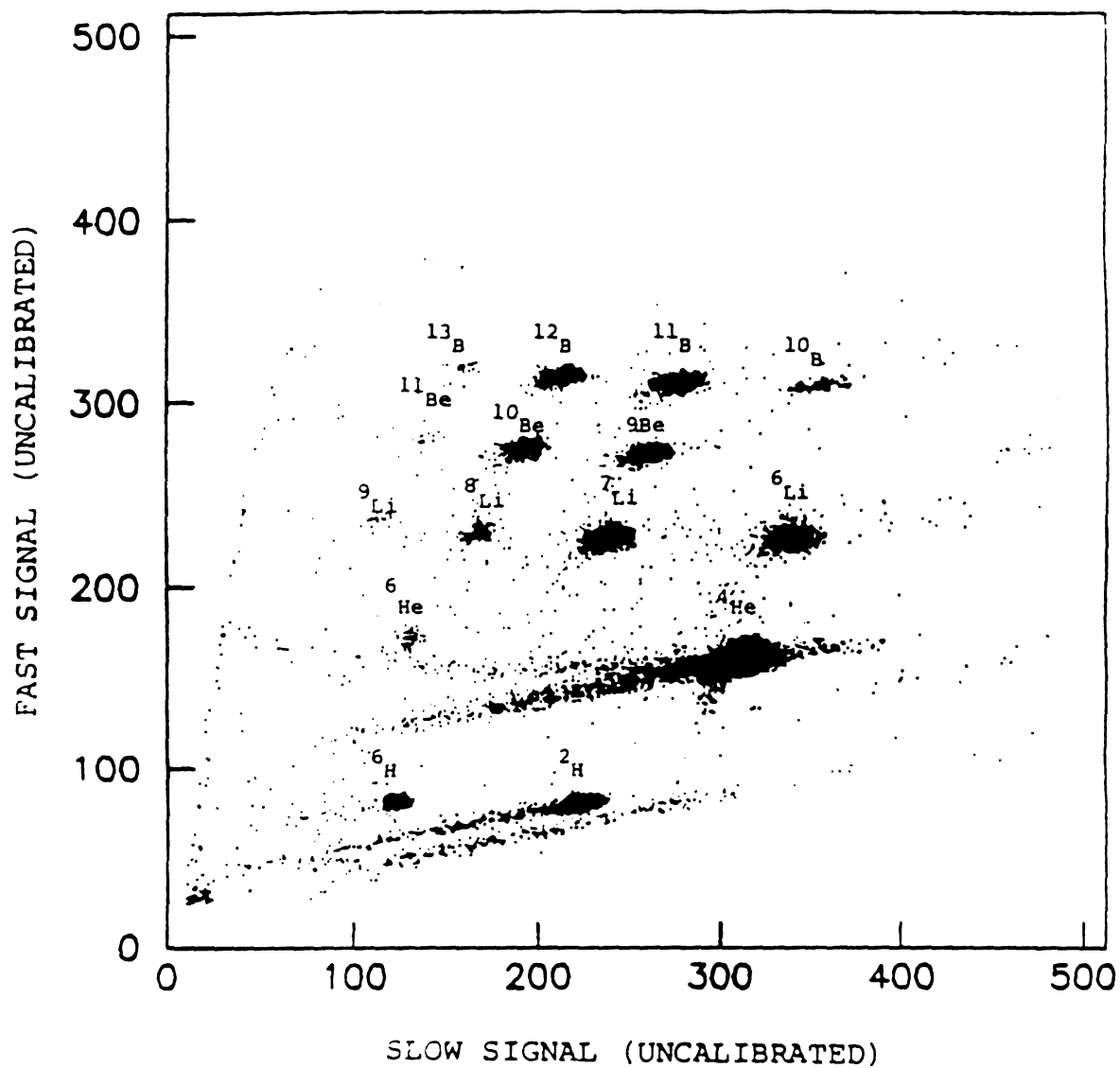


Figure B.6: A scatter plot displaying the raw data from a fragmentation calibration run. These data are from a single detector and a single rigidity setting. Several different isotopic species are simultaneously produced for each element.

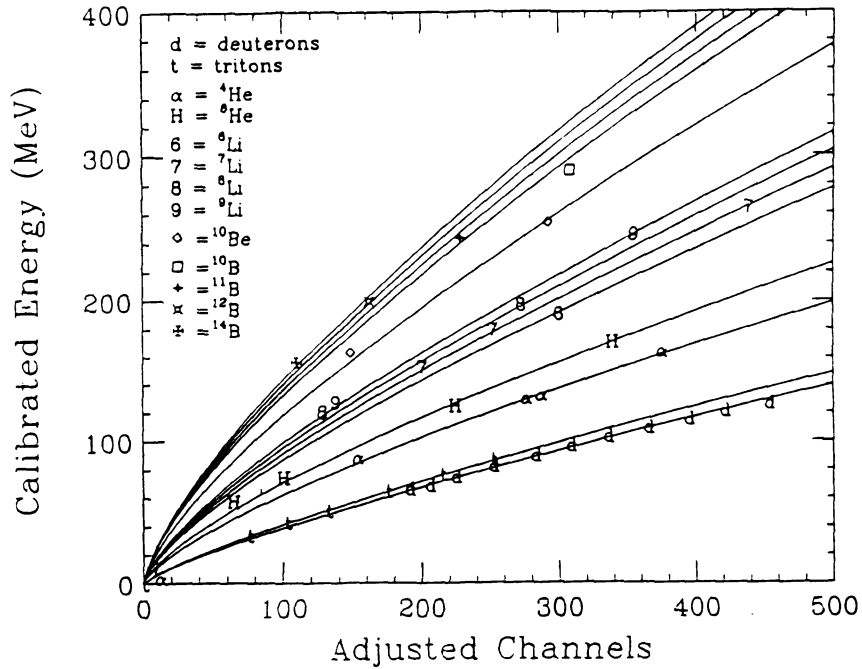


Figure B.7: This figure displays the light response of the slow scintillator as a function of energy for several different particle types. These data are from the fragmentation run in the 60 inch chamber using type I detectors.

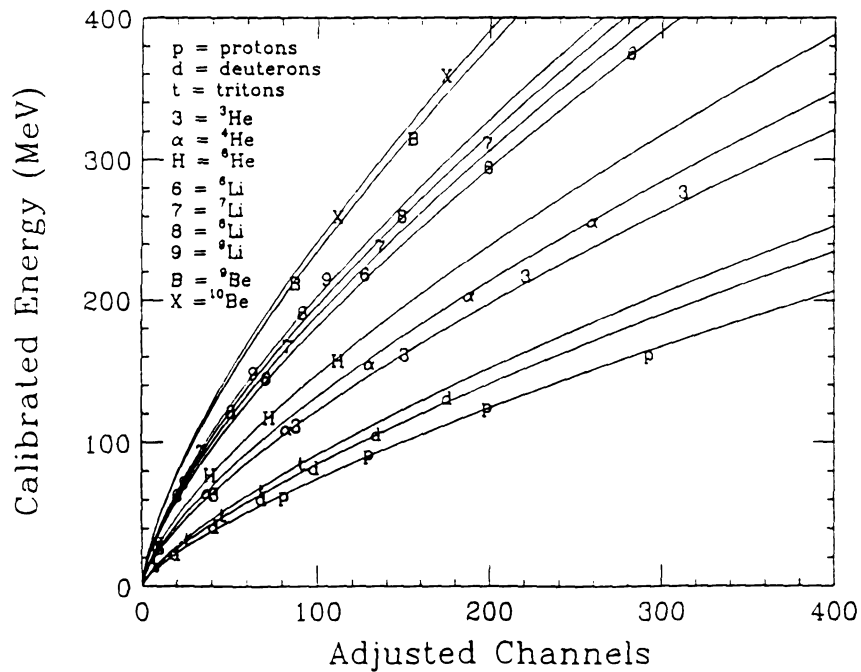


Figure B.8: This figure displays the light response of the slow scintillator as a function of energy for several different particle types. These data are from the fragmentation run using the S320 spectrometer and 6 type III detectors.

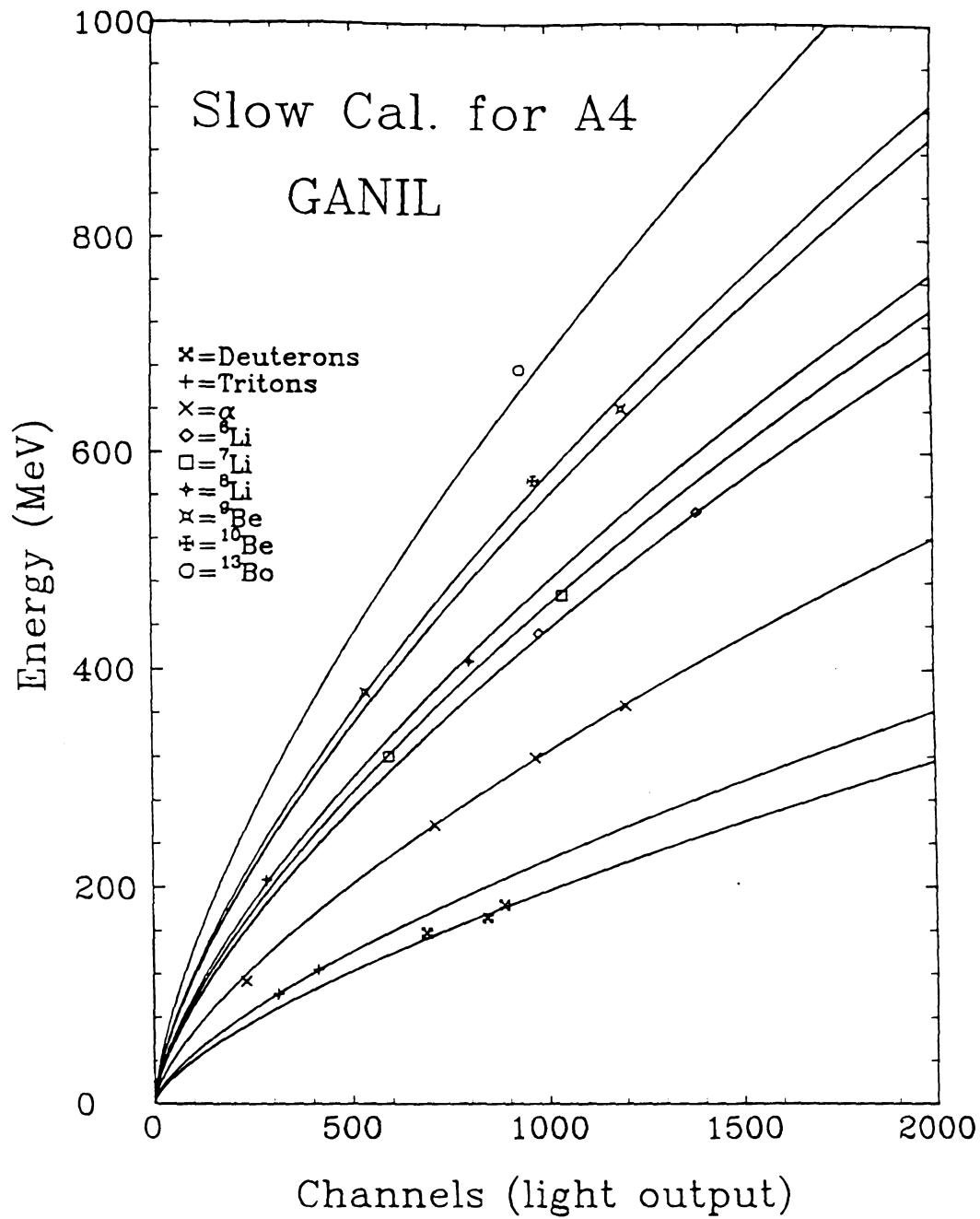


Figure B.9: This figure displays the light response of the slow scintillator as a function of energy for several different particle types. These data are from a fragmentation run at GANIL [Gont90].

solid curves are fits to the data using the formula

$$\text{Channel} = C E^{1.4} / Z^{0.8} A^{0.4} \quad (\text{B.3})$$

where  $C$  is a detector specific normalization constant,  $E$  is the energy of the fragment,  $Z$  is its charge, and  $A$  is its mass number. This formula for the light response agrees with the requirement that total light produced must decrease as a function of the average ionization density. The ionization density ( $dE/Dx$ ) increases with  $Z$  and  $A$ , therefore, the light response should vary inversely with respect to these quantities. The ionization density is a non-uniform function of energy, however, the average ionization density decreases with total energy. Therefore, the light production must increase with energy.

## 2 Response Function of the Fast Scintillator

The response function of the fast scintillator is more complicated than that of the slow scintillator. The energy ranges of greatest interest are those for which the particles stop in the slow scintillator. For these particles, the fast scintillator acts as a transmission detector. Particles which stop in the fast scintillator are of less interest because one can not identify the charge, mass or energy. The response function for transmission particles is different than for stopping particles because the region of highest ionization density, the Bragg Peak, does not occur within this scintillator material. Therefore, the ionization density is relatively uniform throughout the scintillator and is almost independent of  $Z$  and  $A$ . Figure B.10 illustrates this point. For a 1.5 mm  $\Delta E$  scintillator, the 100 MeV deuteron passes through depositing 3.75 MeV uniformly with distance. For reference, the  $\Delta E$  scintillators are 1.566 and 3.175 mm thick for the detectors used in these experiments. The generalization that the ionization density is independent of range, however, is not true for particles that deposit the majority of their total energy in the fast scintillator. The curve for the

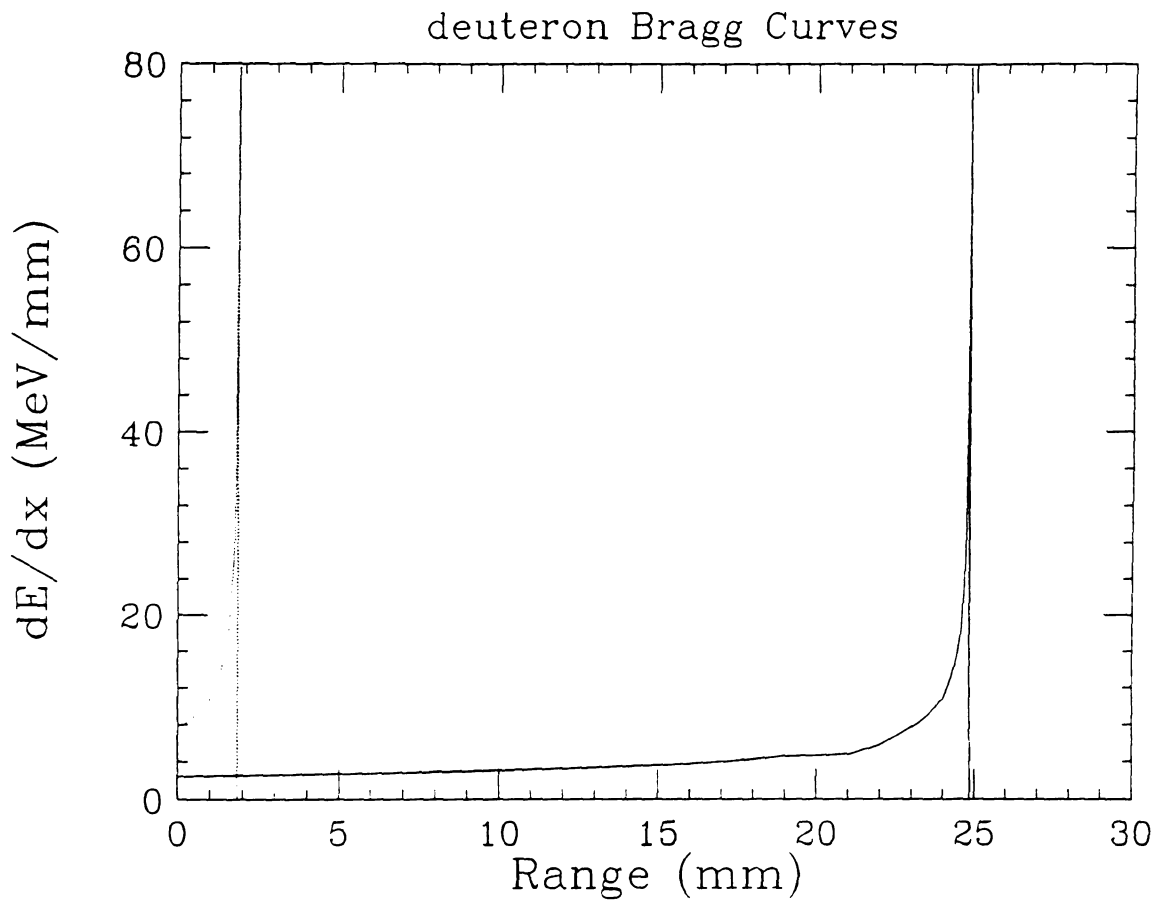


Figure B.10: An illustration of the ionization density as a function of depth in scintillation material for a 100 MeV deuteron (solid line) and a 25 MeV deuteron (dotted line).

25 MeV deuteron particle in Figure B.10 demonstrates the non-uniformities that are introduced when a major portion of the Bragg Peak is picked up in the fast scintillator. Figure B.11 displays a compilation of the results from the calibration studies for the fast scintillator. The solid curves come from fits to the data using the following formula:

$$Light(fast) = C E^{0.5} \quad (B.4)$$

For transmission particles, the ionization density is uniform and, therefore, depends only on the total energy deposited in the scintillator and not on the particle's charge or mass. Since light is a function of ionization density, the response of the  $\Delta E$  Scintillator for transmission particles is a function only of the energy deposited. This is demonstrated in Figure B.11. Most of the calibration points fall along a single calibration curve. The points that miss the curve are the highest energy points for a given particle species. The highest energy point corresponds to a particle that just barely has sufficient energy to punch out of the  $\Delta E$  scintillator. For those particles, a portion of the high ionization density region (the Bragg peak) will be picked up. These points will therefore produce less light than expected as is demonstrated in the figure.

Figure B.12 displays a set of data close to the punch-in region where the  $\Delta E$  response function is no longer independent of charge and mass. It is also possible for particle to stop within the  $\Delta E$  scintillator. For low energy particles that are stopped, the entire Bragg peak will be contained within the fast scintillator. The solid curves are fits to the data which include responses for the fast scintillator in both transmission and stopping mode. There are no data for this region because there is no identification for particles that stop in the fast scintillator. However, if one assumes that the light response will be similar in form to that determined for the slow scintillator, one can generate these complete response functions that span both the stopping and the

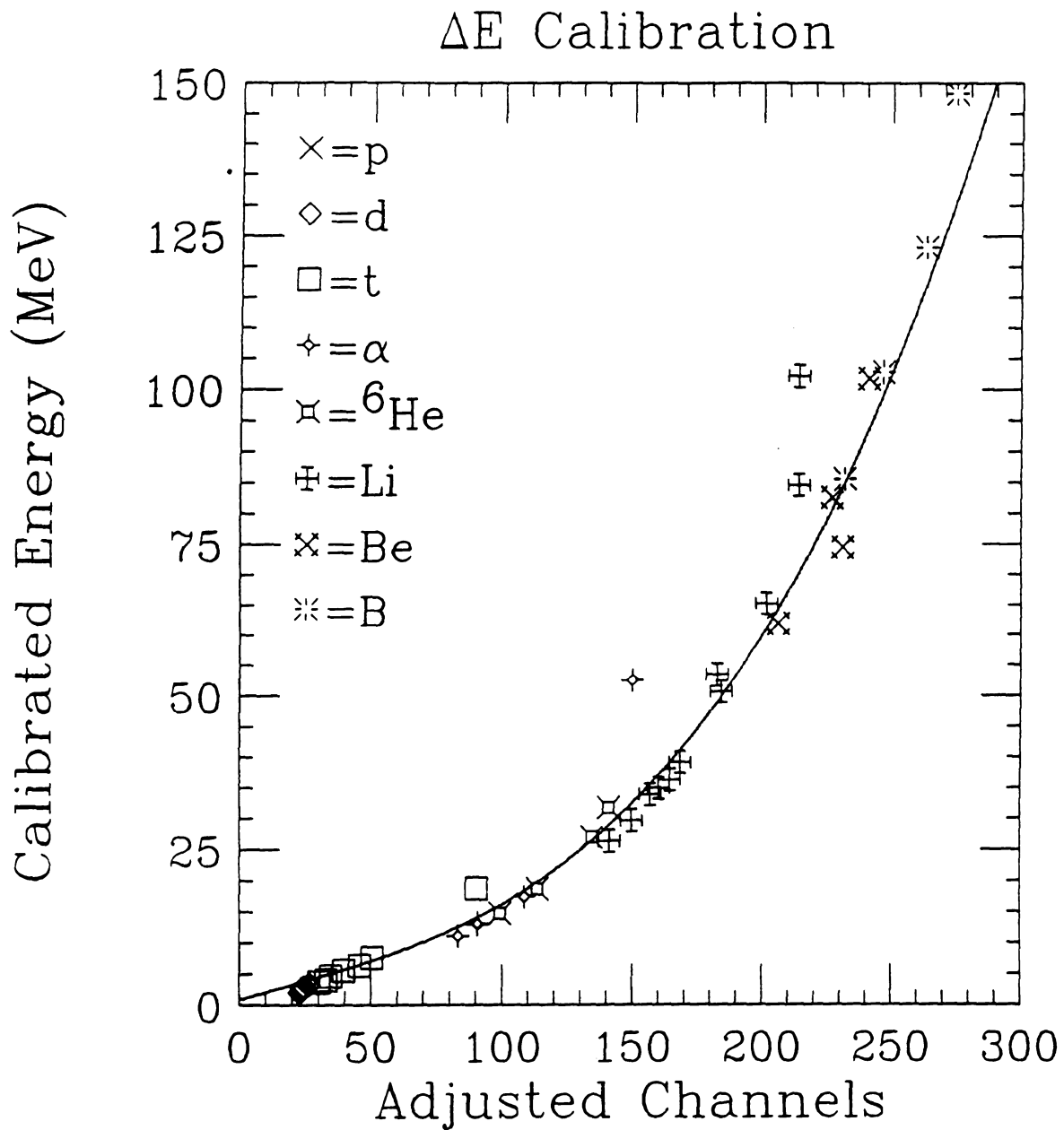


Figure B.11: A compilation of the data from the various calibration runs. This figure displays the light response of the fast scintillator as a function of energy for several different particle types.

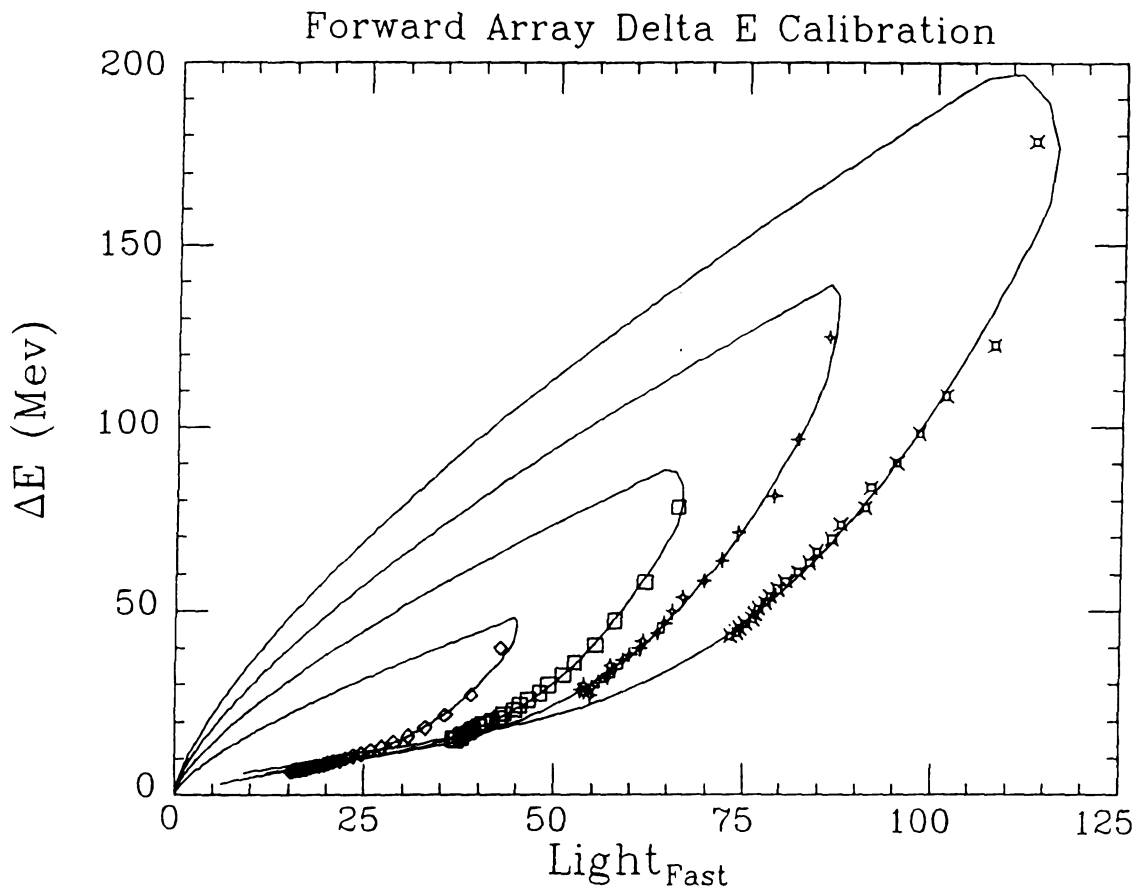


Figure B.12: A calibration of the  $\Delta E$  scintillator for energy near the punch-in region.

transmission regions.

## D Conclusions

This work presents functional forms for the light response of plastic scintillator. This is the first study to determine reliably the mass dependence of the functions, because it is the first to present data containing calibration points from multiple isotopes of more than one element. This work also examines the response function for organic scintillator operating as a transmission detector. The calibration functions presented here are general enough to be applied to other work using organic scintillator provided one has at least one calibration point in order to determine the calibration constant. (Appendix C describes how an experimenter using phoswich detectors can normalize to the forms using the shapes of the particle identification bands on a histogram of the fast versus slow signals. Using that technique one does not even need a single calibration point.)

/

# Appendix C

## Phoswich Analysis Routines

A phoswich detector is a device that utilizes two or more coupled scintillation elements (a phosphor sandwich) [Wilk52] for the detection and identification of charged particles. The light produced as a particle traverses these scintillators can be collected by a single photodetector, commonly a photomultiplier tube (PMT) or a photodiode. Typically the front scintillator is much thinner than the second. The light produced from this first scintillator which is related to the energy loss ( $\Delta E$ ) can be used as a measure of the rate of energy loss ( $dE/dx$ ) since the distance traversed ( $\Delta x$ ) by the particle is known to be the thickness of the scintillator. The light produced in the second scintillator ( $E$ ) is then a measure of the total energy of the particle. Since  $dE/dx$  is a function of the particle's energy, charge, and mass, a histogram of the signal from one scintillator versus the signal from the other will yield bands for the different elements and isotopes and can be used to identify the particle's charge ( $Z$ ) and mass ( $A$ ).

Figure C.1 displays the electronics setup for processing the signals from the phoswich detectors used in the MSU  $4\pi$  Array [West85]. The setup for any other experiment employing phoswichs would be similar. The important feature of the electronics diagram is the passive three-way signal splitter. One branch (Logic/Timing on the left) goes to a discriminator and then through a logic circuit which determines

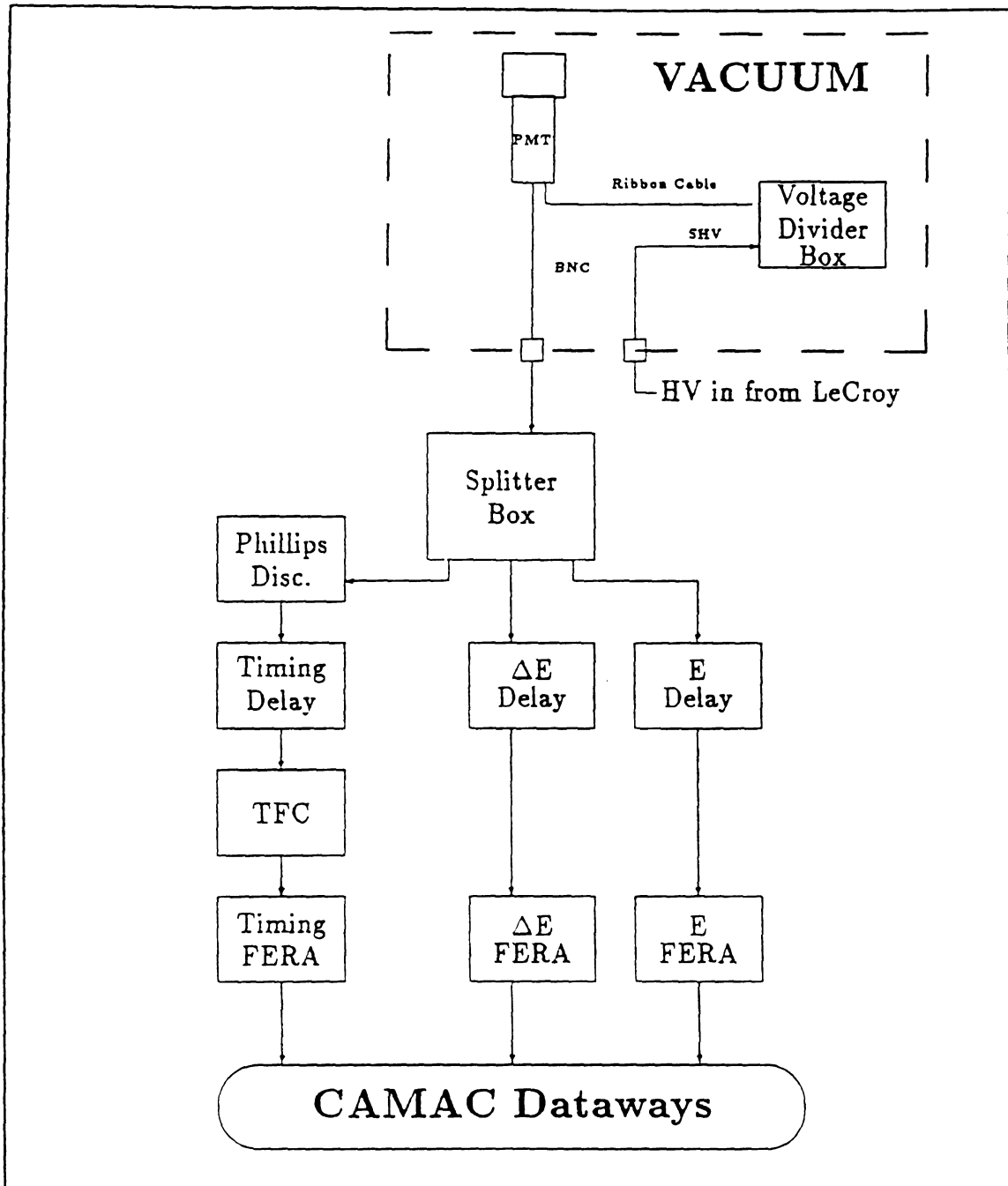


Figure C.1: The electronics diagram for the analysis of signals from the phoswich detectors used in the MSU  $4\pi$  Array.

if the event should be recorded. If the trigger requirements are satisfied, then gates are generated for the charge-to-digital converters (QDCs). The arrival time and the duration of these gates are important. The other two branches (Fast and Slow) are delayed, to allow the Logic/Timing circuit time to satisfy the trigger requirements and to generate the gates for the QDCs, and then integrated.

The gating of the signals on the Fast and Slow branches is important for optimal detector operation. The gates must arrive at the correct time, must be an appropriate length, and must not wander more than a few nanoseconds from event to event. The solid curve in Figure C.2 shows an idealized phoswich signal for a detector with a fast plastic (BC 412, 3.3 nsec decay time) front scintillator and a slow plastic (BC 444, 180 nsec decay time) stopping scintillator (refer to table A.1 for more details about the scintillators). The positions of the integration gates are indicated at the top of the figure. The fast gate should arrive before the signal starts and should end approximately at the inflection point where the contribution from the slow signal starts to dominate. The slow gate should start about 50 nsec after the the end of the fast gate, and it should be about 200 nsec in duration. There is a certain degree of latitude in the position and duration of the gates. Both the timing and the length of the gates affect the amplitudes of the integrated signals, however, they also affect the degree to which the light from one scintillator is picked up in the gate intended for the other. A decomposition of the signal into its fast (dotted) and slow (dot-dash) components is displayed beneath the curve for the total signal. This illustration demonstrates that there is some pick-up of slow component in the fast gate and vice-versa.

Figure C.3 displays a scatter plot of the signals from the fast versus slow gate. The ridge of high intensity which slopes away from the axis for the fast signal is populated by events from particles which were stopped in the fast scintillator. These

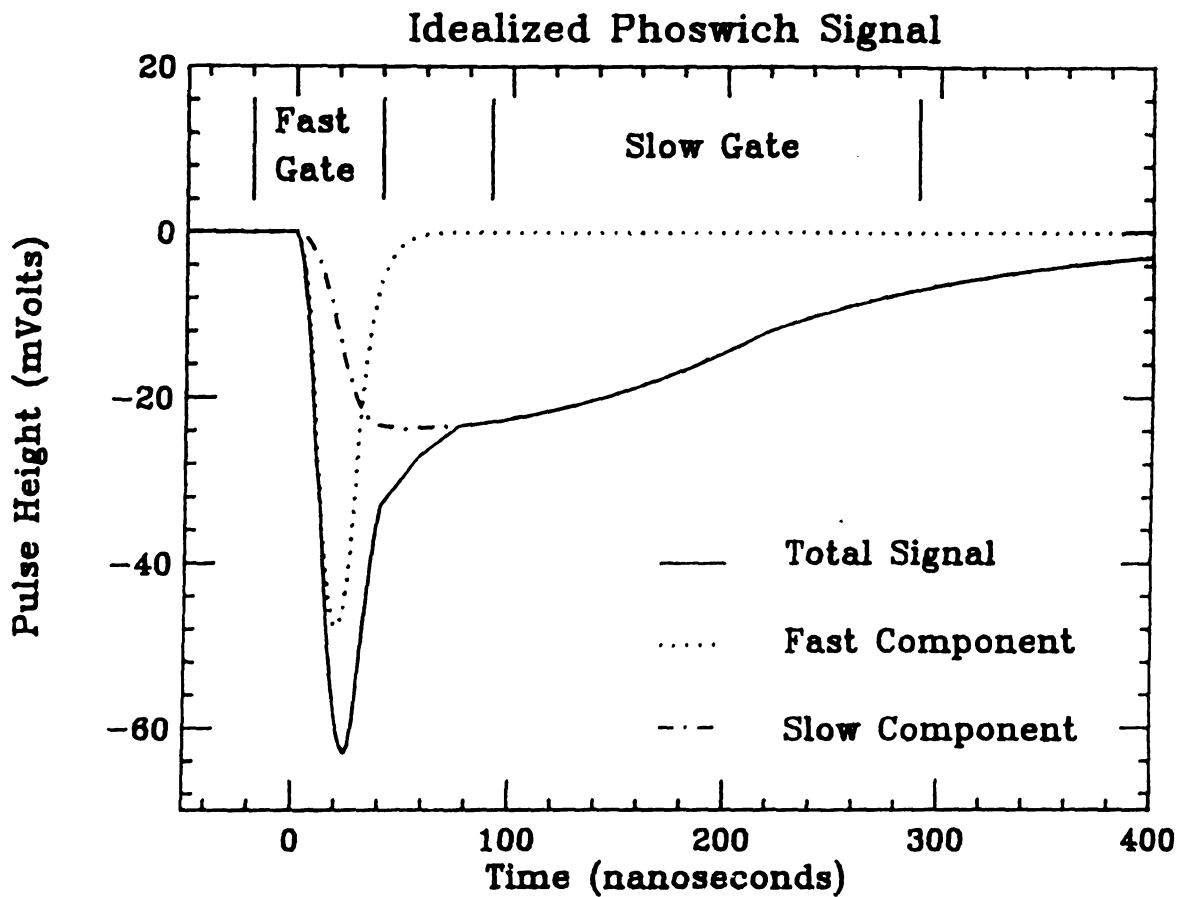


Figure C.2: An idealized phoswich signal for a charged particle incident on a detector with a fast plastic front scintillator and a slow plastic stopping scintillator.

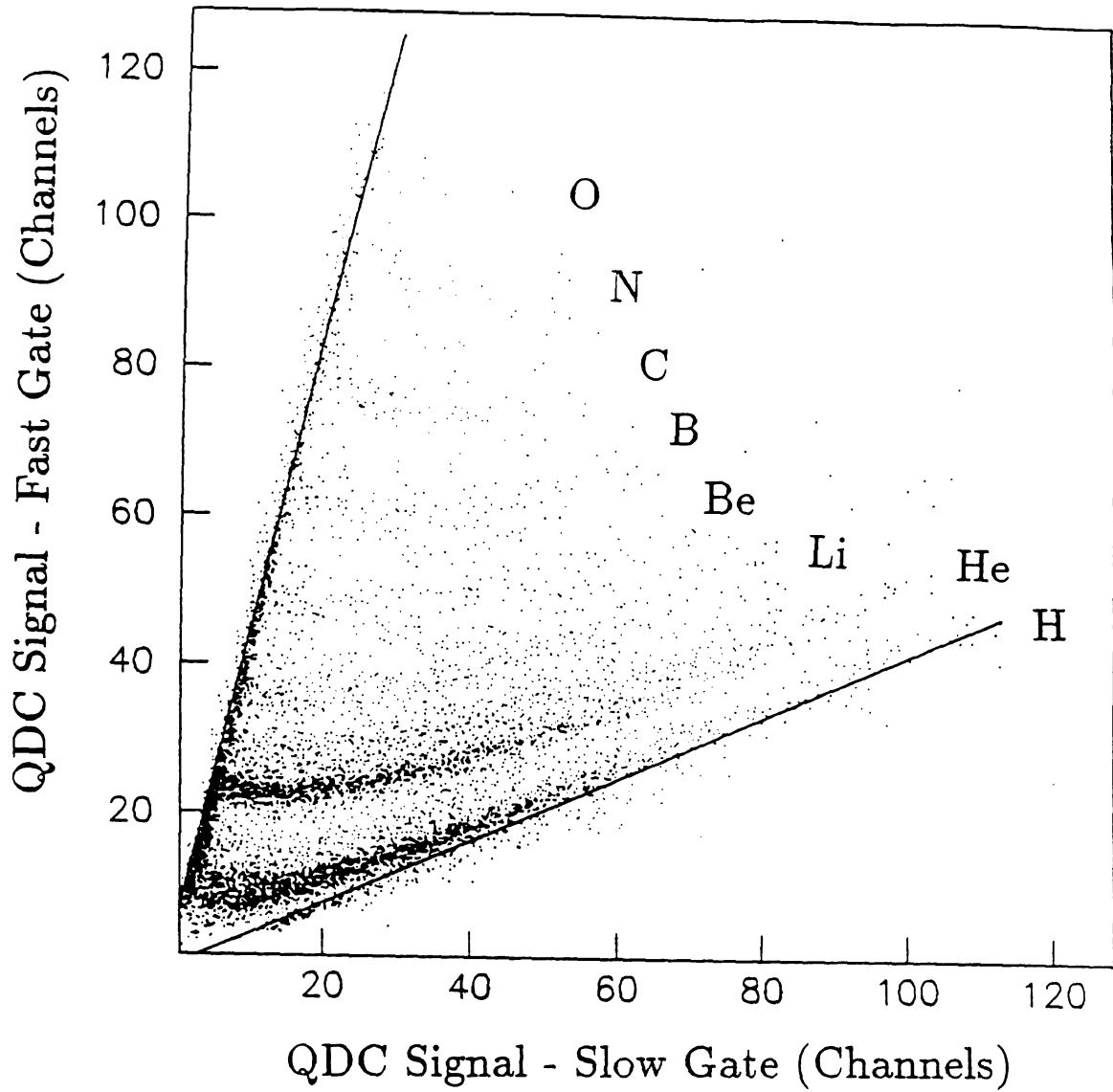


Figure C.3: A scatter plot of the signal in the fast gate versus the signal in the slow gate. The data are from a  $4\pi$  phoswich at  $23^\circ$ , the reaction is 35 MeV/nucleon Ar+V.

events produce signals with no slow component. The fact that the slope of the line ( $M_p$ ) is not infinite demonstrates the degree to which the fast signal is collected in the slow gate. The ridge of high intensity that rises above the axis for the slow signal is made up of events for which the triggering particle was either a gamma or a neutron. These particles interact with matter very differently than charged particles. Since slow scintillator makes up the bulk of the detector material, these events are most likely to produce signals with no fast component. The slope of this line ( $M_n$ ) is a measure of the fraction of the slow component recorded in the fast gate.

The intersection of the Punch-In and the Neutral lines corresponds to a signal with no fast or slow components. The location ( $X_0, Y_0$ ) of this intersection is a measure of the offsets in the QDCs. Adjustments in the pedestals of the fast encoding readout ADCs (FERAs) effect the position of this intersection.

Having determined the crosstalk between the two components of the signal and the offsets in the individual QDC channels, the fast versus slow scatter plot can be corrected to produce a plot of  $\Delta L$  versus  $L$ , where  $\Delta L$  is the light produced in the fast scintillator and  $L$  is the light from the slow scintillator. Each point in the raw plot is mapped using the following algorithm:

$$\Delta L = (Fast - Y_0) - (Slow - X_0) \times M_n \quad (C.1)$$

$$L = (Slow - X_0) - (Fast - Y_0)/M_p \quad (C.2)$$

Figure C.4 displays the corrected  $\Delta L$  versus  $L$  plots for 16 Fast/Slow telescopes.

The final stage of the analysis is the gain matching of the  $\Delta L$ - $L$  plots from individual detectors. This conformal mapping is done with two operations, a stretch in the  $\Delta L$  direction ( $G_{\Delta L}$ ) and another in the  $L$  direction ( $G_L$ ). The final mapping algorithms are:

$$\Delta L = G_{\Delta L} \times [(Fast - Y_0) - (Slow - X_0)M_n] \quad (C.3)$$

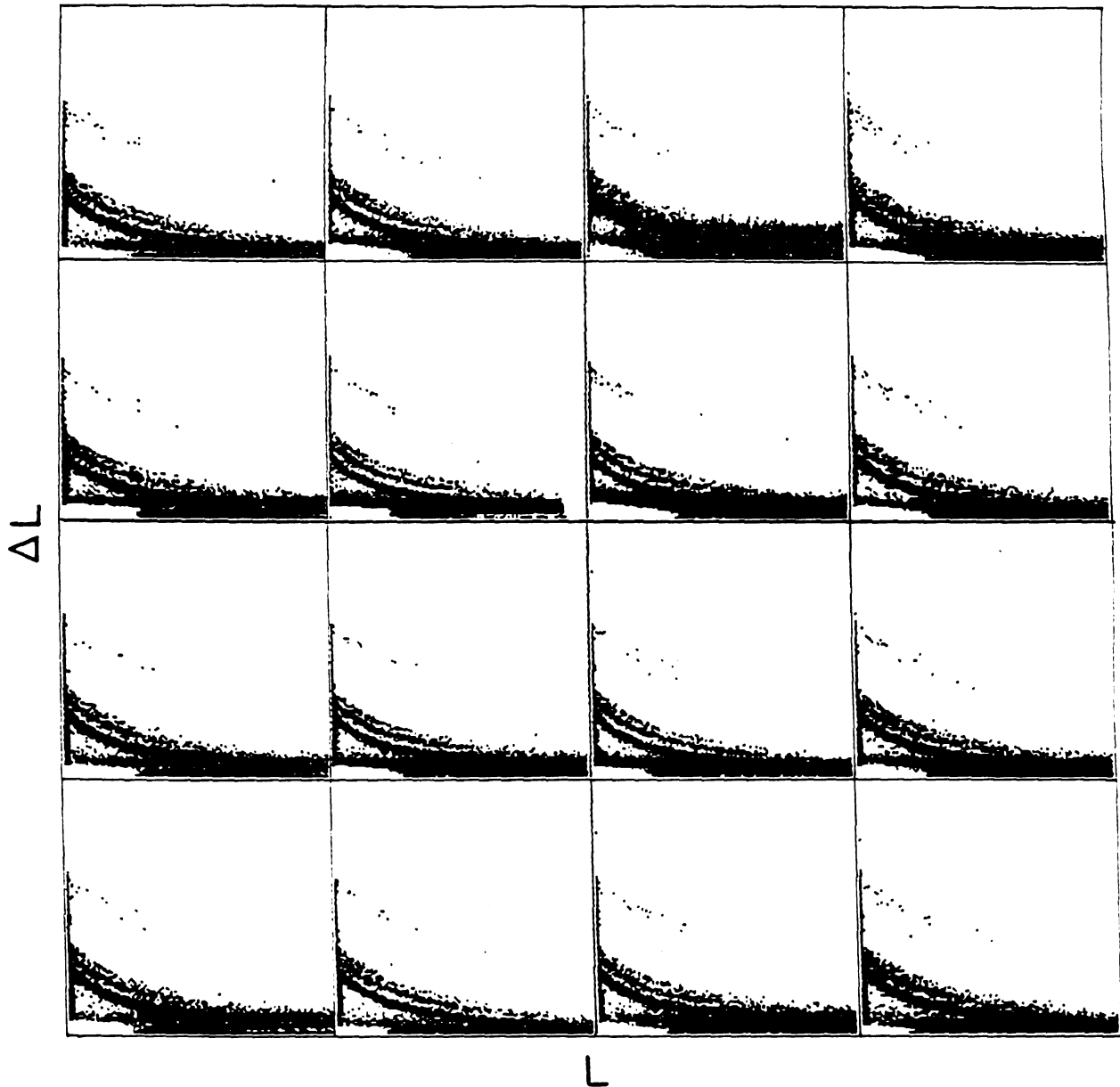


Figure C.4:  $\Delta L$ - $L$  plots for 16 phoswichs. The gains are set for  $\alpha s$ . The data are from the reaction 500 MeV p+Ag.

$$L = G_L \times [(Slow - X_0) - (Fast - Y_0)/M_p] \quad (C.4)$$

These stretch operations represent the gain of an individual photomultiplier tube relative to the average response of the other PMTs and the relative lengths of the fast and slow gates. Figure C.5 displays the summation of the same 16 spectra that have been presented in Figure C.4.

The light response of organic scintillator is non-linear with respect to a particle's charge, mass, and energy (details of the response function are given in Appendix B). We have made use of this response function to calculate the expected trajectories of the various particle bands in the  $\Delta L$ - $L$  space. These predictions are displayed in Figure C.6 and were used to create a map that contains the  $Z$ ,  $A$ , and energy (in MeV) for each pixel in the  $\Delta L$ - $L$  plot.

This technique for analysis of phoswich data allows the experimenter to easily handle large numbers of detectors. The master template provides the required particle identification gates and has the energy calibration built in. There is no need to individually calibrate each detector. One must, however, determine the six mapping parameters for each ( $X_0$ ,  $Y_0$ ,  $M_p$ ,  $M_n$ ,  $G_L$ , and  $G_{\Delta L}$ ). A software package has been developed to facilitate the extraction of these parameters. Starting from a raw data set, a trained operator can determine the mapping parameters for all 215 phoswiches used in the MSU  $4\pi$  Array in less than four hours.

## Particle Identification Map

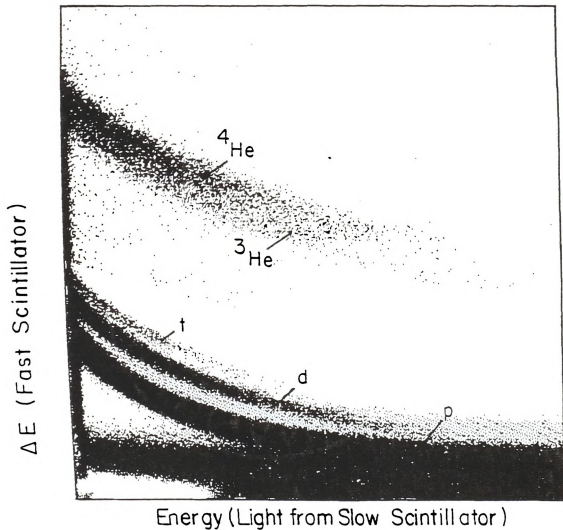


Figure C.5: A summation of  $\Delta L-L$  spectra from the same 16 phoswichs displayed in the previous figure.

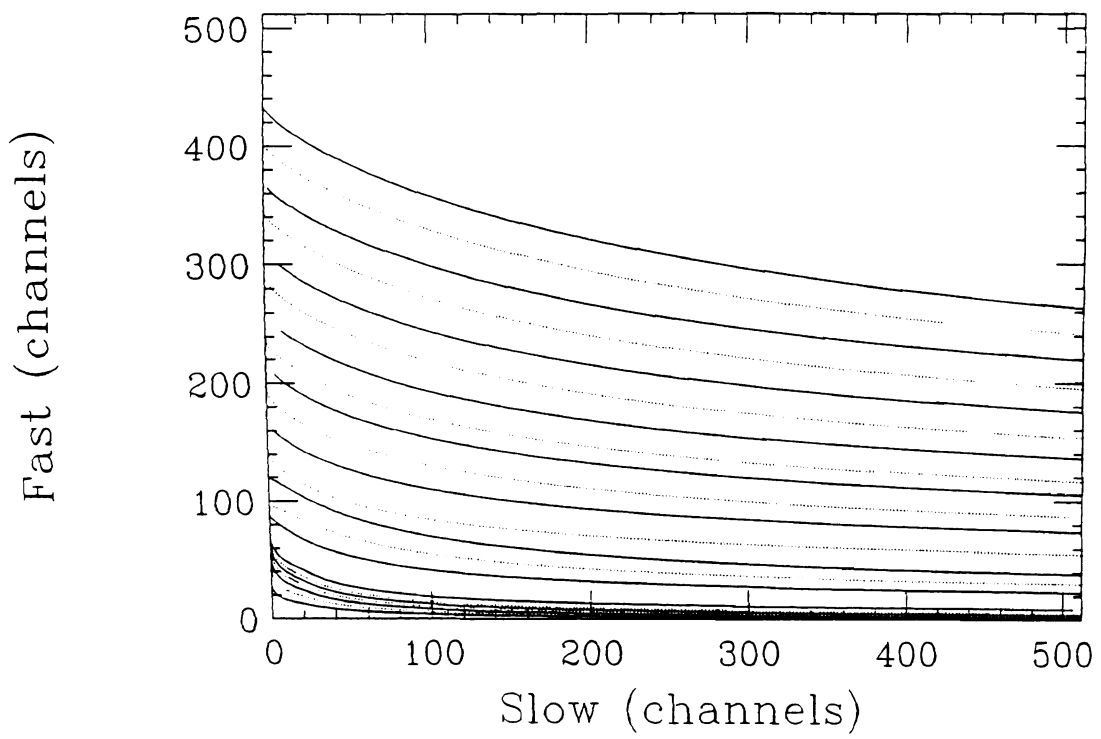


Figure C.6: The predicted particle bands (dotted) and the particle identification gates (solid).

## LIST OF REFERENCES

## LIST OF REFERENCES

- [Ajze88] F. Ajzenberg-Selove, Nucl. Phys. **A490** 1 (1988).
- [Bade82] A. Baden, H.H. Gutbrod, H. Löhner, M.R. Maier, A.M. Poskanzer, T. Renner, H. Riedesel, H.G. Ritter, H. Spieler, A. Warwick, F. Weik, and H. Wieman, Nucl. Inst. Meth. **A203** 189 (1982).
- [Barr80] M. Barranco and J. Buchler, Phys. Rev. **C22** 1729 (1980).
- [Baue86] W. Bauer, U. Post, D.R. Dean, and U. Mosel, Nucl. Phys. **A452** 699 (1986).
- [Baym71] G. Baym, H.A. Bethe, and C.J. Pethick, Nucl. Phys. **A175** 225 (1971).
- [Becc76] F.D. Becchetti, C.E. Thorn, and M.J. Levine, Nucl. Inst. Meth. **138** 93 (1976).
- [Bert83] G. Bertsch and P.J. Siemens, Phys. Lett. **B126** 9 (1983).
- [Beth61] H.A. Bethe and P. Morrison, *Elementary Nuclear Theory* (John Wiley & Sons, New York) 200 (1961).
- [Birk64] J.B. Birks, *The Theory and Practice of Scintillation Counting* (Pergamon Press, Oxford) 60 (1964).
- [Biza86] G. Bizard, A. Drouet, F. Lefebvres, J.P. Patry, B. Tamain, F. Guilbault, and C. LeBrun, Nucl. Inst. Meth. **A244** 483 (1986).
- [Blat52] J.M. Blatt and V.F. Weisskopf, *Theoretical Nuclear Physics*, (John Wiley & Sons, New York) 371 (1952).
- [Blat79] J.M. Blatt and V.F. Weisskopf, *Theoretical Nuclear Physics*, (Springer, Berlin, 1979).
- [Bloc86] C. Bloch, W. Benenson, E. Kashy, R. Blue, R.M. Ronnigen, and H. Utsunomiya, Phys. Rev. **C34** 850 (1986).
- [Bloc87] C. Bloch, W. Benenson, A.I. Galonsky, E. Kashy, J. Heltsley, L. Heilbronn, M. Lowe, B. Remington, D.J. Morrissey, and J. Kasagi, Phys. Rev. **C34** 917 (1986).
- [Bloc88] C. Bloch, W. Benenson, A.I. Galonsky, E. Kashy, J. Heltsley, L. Heilbronn, M. Lowe, R.J. Radtke, B. Remington, J. Kasagi, and D.J. Morrissey, Phys. Rev. **C37** 2469 (1988).
- [Boal84] D.H. Boal, Phys. Rev. **C30** 749 (1984).
- [Boal86] D.H. Boal and J.C. Shillcock, Phys. Rev. **C33** 549 (1986).
- [Boal89] D.H. Boal, J.N. Glosli, and C. Wicentowich, Phys. Rev. Lett. **62** 737 (1989)
- [Bohr39] N. Bohr and J.A. Wheeler, Phys. Rev. **56** 426 (1939).
- [Bond85a] J.P. Bondorf, R. Donangelo, I.N. Mishustin, C.J. Pethick, H. Schulz, and K. Sneppen, Nucl. Phys. **A443** 321 (1985).

- [Bond85b] J. Bondorf, R. Donangelo, I.N. Mishustin, and H. Schulz, Nucl. Phys. **A444** 460 (1985).
- [Boug86] R. Bougault, D. Horn, G.C. Ball, M.G. Steer, and L. Potvin, Nucl. Inst. Meth. **A203** 189 (1986).
- [Boug87] R. Bougault, J. Duchon, J.M. Gautier, A. Genoux-Lubain, C. LeBrun, J.F. Lecolley, F. Lefebvres, M. Louvel, P. Mosrin, and R. Regimbart, Nucl. Inst. Meth. **A259** 473 (1987).
- [Boug88] R. Bougault, F. Delaunay, A. Genoux-Lubain, C. LeBrun, J.F. Lecolley, F. Lefebvres, M. Louvel, J.C. Steckmeyer, J.C. Adloff, B. Bilwes, R. Bilwes, M. Gleser, G. Rudolf, F. Scheibling, L. Stuttge, and J.L. Ferrero, Nucl. Phys. **A488** 255c (1988).
- [Boug89a] R. Bougault, F. Delaunay, A. Genoux-Lubain, C. LeBrun, J.F. Lecolley, F. Lefebvres, M. Louvel, J. Steckmeyer, J.C. Adloff, B. Bilwes, R. Bilwes, M. Glaser, G. Rudolf, F. Scheibling, L. Stuttge, and J.L. Ferrero, Preprint LPCC 89-03 (1989).
- [Boug89b] R. Bougault, J. Colin, F. Delaunay, A. Genoux-Lubain, A. Hajfani, C. LeBrun, J.F. Lecolley, M. Louvel, J.C. Steckmeyer, Phys. Lett. **B232** 291 (1989).
- [Bowm87] D.R. Bowman, W.L. Kehoe, R.J. Charity, M.A. McMahan, A. Moroni, A. Bracco, S. Bradley, I. Iori, R.J. McDonald, A.C. Mignerey, L.G. Moretto, M.N. Namboodiri, and G.J. Wozniak, Phys. Lett. **B189** 282 (1987).
- [Bowm89] D. Bowman, PhD. Thesis 43 (1989).
- [Cass89] Y. Cassagnou, M. Conjeaud, R. Dayras, S. Harar, G. Klotz-Engmann, R. Legrain, V. Lips, H. Oeschler, E.C. Pollaco, C. Volant, Symposium on Nuclear Dynamics and Nuclear Disassembly, ACS Meeting, Dallas, Texas, April 10-14 (1989).
- [Cebr90] D.A. Cebra, S. Howden, J. Karn, A. Nadasen, C.A. Ogilvie, A. Vander Molen, G.D. Westfall, W.K. Wilson, J.S. Winfield, and E. Norbeck, Phys. Rev. Lett. **64** 2246 (1990).
- [Chap88] T. Chapuran, D.P. Balamuth, J.W. Arrison, and J. Gorres, Nucl. Inst. Meth. **A272** 767 (1988).
- [Char86] R.J. Charity, M.A. McMahan, D.R. Bowman, Z.H. Liu, R.J. McDonald, G.J. Wozniak, L.G. Moretto, S. Bradley, W.L. Kehoe, A.C. Mignerey, and M.N. Namboodiri, Phys. Rev. Lett. **56** 1354 (1986).
- [Char88a] R.J. Charity, D.R. Bowman, Z.H. Liu, R.J. McDonald, M.A. McMahan, G.J. Wozniak, L.G. Moretto, S. Bradley, W.L. Kehoe, and A.C. Mignerey, Nucl. Phys. **A476** 516 (1988).
- [Char88b] R.J. Charity, M.A. McMahan, G.J. Wozniak, R.J. McDonald, L.G. Moretto, D.G. Sarantides, L.G. Sobotka, G. Guarino, A. Pantaleo, L. Fiore, A. Gobbi, and K.D. Hildenbrand, Nucl. Phys. **A483** 371 (1988).

- [Char70] Charpak, *Ann. Rev. Nucl. Sci.* **20**, 195 (1970).
- [Chen87a] Z. Chen, C.K. Gelbke, J. Pochodzalla, C.B. Chitwood, D.J. Fields, W.G. Lynch, and M.B. Tsang, *Phys. Lett.* **B186** 280 (1987).
- [Chen87b] Z. Chen, C.K. Gelbke, J. Pochodzalla, C.B. Chitwood, D.J. Fields, W.G. Gong, W.G. Lynch, and M.B. Tsang, *Nucl. Phys.* **A473** 564 (1987).
- [Chen87c] Z. Chen, C.K. Gelbke, W.G. Gong, Y.D. Kim, W.G. Lynch, M.R. Maier, J. Pochodzalla, M.B. Tsang, F. Saint-Laurent, D. Ardouin, H. Delagrange, H. Doubre, J. Kasagi, A. Kyanowski, A. Péghaire, J. Péter, E. Rosato, G. Bizard, F. Lefèbvres, B. Tamain, J. Québert, and Y.P. Viyogi, *Phys. Lett* **171** (1987).
- [Chen87d] Z. Chen, C.K. Gelbke, W.G. Gong, Y.D. Kim, W.G. Lynch, M.R. Maier, J. Pochodzalla, M.B. Tsang, F. Saint-Laurent, D. Ardouin, H. Delagrange, H. Doubre, J. Kasagi, A. Kyanowski, A. Péghaire, J. Péter, E. Rosato, G. Bizard, F. Lefèbvres, B. Tamain, J. Québert, and Y.P. Viyogi, *Phys. Rev.* **C36** 2297 (1987).
- [Chit85] C.B. Chitwood, J. Aichelin, D.H. Boal, G. Bertsch, D.J. Fields, C.K. Gelbke, W.G. Lynch, M.B. Tsang, J.C. Shillcock, T.C. Awes, R.L. Ferguson, F.E. Obenshain, F. Plasil, R.L. Robinson, and G.R. Young, *Phys. Rev. Lett.* **54** 302 (1985).
- [Chit86] C.B. Chitwood, C.K. Gelbke, J. Pochodzalla, Z. Chen, D.J. Fields, W.G. Lynch, R. Morse, M.B. Tsang, B.H. Boal, and J.C. Shillcock, *Phys. Lett.* **B172** 27 (1986).
- [Chou52] C.N. Chou, *Phys. Rev.* **87** 904 (1952).
- [Colo89] N. Colonna, R.J. Charity, D.R. Bowman, M.A. McMahan, G.J. Wozniak, L.G. Moretto, G. Guarino, A. Pantaleo, L. Fiore, A. Gobbi, and K.D. Hildenbrand, *Phys. Rev. Lett.* **62** 1833 (1989).
- [Crau70] R.L. Craun and D.L. Smith, *Nucl. Inst. Meth.* **80** 239 (1970).
- [Curt83] M.W. Curtin, H. Toki, and D.K. Scott, *Phys. Lett.* **B123** 289 (1983).
- [Dani79] P. Danielewicz, *Nucl. Phys.* **A314** 465 (1979).
- [Deák87] F. Deák, A. Kiss, Z. Seres, G. Caskey, A. Galonsky, and B. Remington, *Nucl. Inst. Meth.* **A258** 67 (1987).
- [Deák89] F. Deák, A. Kiss, Z. Seres, A. Galonsky, C.K. Gelbke, L. Heilbronn, W. Lynch, T. Murakami, H. Schelin, M.B. Tsang, B.A. Remington, and J. Kasagi, *Phys. Rev.* **C39** 733 (1989).
- [DeAn89] A.R. DeAngelis and A.Z. Mekjian, *Phys. Rev.* **C40** 105 (1989).
- [deSh74] A. deShalit and H. Feshbach, *Theoretical Nuclear Physics Volume I: Nuclear Structure*, John Wiley & Sons, New York, p. 17, (1974).

- [DeYo88] P.A. DeYoung, M.S. Gordon, Xiu Qin Lu, R.L. McGrath, J.M. Alexander, D.M. de Castro Rizzo, and L.C. Vaz, *Phys. Rev.* **C39** 128 (1988).
- [Doss87] K.G.R. Doss, H.A. Gustafsson, H. Gutbrod, J.W. Harris, B.V. Jacak, K.H. Kampert, B. Kolb, A.M. Poskanzer, H.G. Ritter, H.R. Schmidt, L. Teitelbaum, M. Tincknell, S. Weiss, and H. Wieman, *Phys. Rev. Lett.* **59** 2720 (1987).
- [Fai83] G. Fai and J. Randrup, *Nucl. Phys.* **A404** 551 (1983).
- [Fai86] G. Fai and J. Randrup, *Comp. Phys. Comm.* **42** 385 (1986).
- [Fai89] G. Fai, Preprint KSUPHY-005 (1989).
- [Fiar73] S. Fiarman and W.E. Meyerhof, *Nucl. Phys.* **A206** 1 (1973).
- [Finn82] J.E. Finn, S. Agarwal, A. Bujak, J. Chuang, L.J. Gutay, A.S. Hirsch, R.W. Minich, N.T. Porile, R.P. Scharenberg, B.C. Stringfellow, and F. Turkot, *Phys. Rev. Lett.* **49** 1321 (1982).
- [Fish61] M.E. Fisher and J.W. Essam, *J. Math. Phys.* **2** 609 (1961).
- [Fox87] D. Fox, PhD. Thesis 12 (1987).
- [Fox88] D. Fox, D.A. Cebra, J. Karn, C. Parks, A. Pradhan, A. Vander Molen, J. van der Plicht, G.D. Westfall, W.K. Wilson, and R.S. Tickle, *Phys. Rev.* **C38** 146 (1988).
- [Frie81] W.A. Friedman and V.R. Pandharipande, *Nucl. Phys.* **A361** 502 (1981).
- [Frie88] W.A. Friedman, *Phys. Rev. Lett.* **60** 2125 (1988).
- [Galo87] A. Galonsky, G. Caskey, L. Heilbronn, B. Remington, H. Schelin, F. Deak, A. Kiss, Z. Seres, and J. Kasagi, *Phys. Lett.* **B197** 511 (1987).
- [Gold60] G. Goldhaber, S. Goldhaber, W. Lee, and A. Pais, *Phys. Rev.* **120** 300 (1960).
- [Gont90] P. Gonthier, private communication (1990).
- [Gree80] R.E.L. Green and R.G. Korteling, *Phys. Rev.* **C22** 1594 (1980).
- [Gros86] D.H.E. Gross, Zhang X., and Xu S., *Phys. Rev. Lett.* **56** 1544 (1986).
- [Gros87] D.H.E. Gross and H. Massman, *Nucl. Phys.* **471** 339c (1987).
- [Gros88] D.H.E. Gross, *Phys. Lett.* **B203** 26 (1988).
- [Gros89] D.H.E. Gross, G. Klotz-Engmann, and H. Oeschler, *Phys. Lett.* **B224** 29 (1989).
- [Gutb89] H.H. Gutbrod, A.M. Poskanzer, H.G. Ritter, Review article for *Reports on Progress in Physics* (1989).
- [Gyul82] M. Gyulassy, K.A. Frankel, and H. Stöcker, *Phys. Lett.* **110B** 185 (1982).

- [Hage89] K. Hagel, A. Péghaire, G.M. Jin, D. Cussol, H. Doubre, J. Péter, F. Saint-Laurent, G. Bizard, R. Brou, M. Louvel, J.P. Patry, R. Regimbart, J.C. Steckmeyer, B. Tamain, Y. Cassagnou, R. Legrain, C. LeBrun, E. Rosato, R. MacGrath, S.C. Jeong, S.M. Lee, Y. Nagashima, T. Nakagawa, M. Ogi-hara, J. Kasagi, and T. Motobayashi, *Phys. Lett.* **B229** 20 (1989).
- [Hahn87] D. Hahn and H. Stöcker, *Phys. Rev.* **C35** 1311 (1987).
- [Hanb54] R. Hanbury-Brown and R.Q. Twiss, *Nature* **178** 1046 (1954).
- [Han89] H.Y. Han, K.X. Jing, E. Plagnol, D.R. Bowman, R.J. Charity, L. Vinet, G.J. Wozniak, and L.G. Moretto, *Nucl. Phys.* **A492** 138 (1989).
- [Harm89] B.A. Harmon, J. Pouliot, J.A. López, J. Suro, R. Knop, Y. Chan, D.E. DiGregorio, and R.G. Stokstad, *Phys. Lett* **B** (1989).
- [Harr87] J.W. Harris, B.V. Jacak, K.H. Kanpert, G. Claesson, K.G.R. Doss, R. Fergusson, A.I. Gavron, H.A. Gustafsson, H. Gutbrod, B. Kolb, F. Lefebvres, A.M. Poskanzer, H.G. Ritter, H.R. Schmidt, L. Teitelbaum, M. Tincknell, S. Weiss, H. Wieman, and J. Wilhelmy, *Nucl. Phys.* **A471** 241c (1987).
- [Hass84] B.E. Hasselquist, Ph.D. Dissertation, 28 (1984).
- [Heil89] L. Heilbronn, A. Galonsky, X. Yang, F. Deák, A. Kiss, and Z. Seres, *Phys. Rev.* **C40** 2576 (1989).
- [Heis88] H. Heiselberg, C.J. Pethick, and D.G. Ravenhall, *Phys. Rev. Lett.* **61** 818 (1988).
- [Jaca83] B.V. Jacak, G.D. Westfall, C.K. Gelbke, L.H. Harwood, W.G. Lynch, D.K. Scott, H. Stöcker, M.B. Tsang, and T.J.M. Symons, *Phys. Rev. Lett.* **51** 1846 (1983).
- [Jaca87] B.V. Jacak, G.D. Westfall, G.M. Crawley, D. Fox, C.K. Gelbke, L.H. Harwood, B. Hasselquist, W.G. Lynch, D.K. Scott, H. Stöcker, M.B. Tsang, G. Buchwald, and T.J.M. Symons, *Phys. Rev.* **C35** 1751 (1987).
- [Jaca88] B.V. Jacak, *Nucl. Phys.* **A488** 325c (1988).
- [Jaqa83] H. Jaqaman, A.Z. Mekjian, and L. Zamick, *Phys. Rev.* **C27** 2782 (1983).
- [Kiss87] A. Kiss, F. Deak, Z. Seres, G. Caskey, A. Galonsky, L. Heilbronn, and B.A. Remington, *Phys. Lett.* **B184** 149 (1987).
- [Klot87] G. Klotz-Engmann, H. Oeschler, E. Kankeleit, Y. Cassagnou, M. Conjeaud, R. Dayras, S. Harar, M. Mostefai, R. Legrain, E.C. Pollacco, and C. Volant, *Phys. Lett.* **B187** 245 (1987).
- [Klot89] G. Klotz-Engmann, H. Oeschler, J. Stroth, E. Kankeleit, Y. Cassagnou, M. Conjeaud, R. Dayras, S. Harar, R. Legrain, E.C. Pollacco, and C. Volant, *Nucl. Phys.* **A499** 392 (1989).
- [Knol79] G.F. Knoll, *Radiation Detection and Measurement* John Wiley & Sons, New York 249 (1979).

- [Koon77] S. Koonin, Phys. Lett. **B70** 43 (1977).
- [Kopy74] G.I. Kopylov and M.I. Podgoretskii, Soviet J. Nucl. Phys. **18** 336 (1974).
- [Krof89] D. Krofcheck, W. Bauer, G.M. Crawley, C. Djalali, S. Howden, C.A. Ogilvie, A. Vander Molen, G.D. Westfall, W.K. Wilson, R.S. Tickle, and C. Gale, Phys. Rev. Lett. **63** 2028 (1989).
- [Kyan86] A. Kyanowski, F. Saint-Laurent, D. Ardouin, H. Delagrangé, H. Doubre, C. Gregoire, W. Mittig, A. Peghaire, J. Peter, Y.P. Viyogi, B. Zwieglinski, J. Quebert, G. Bizard, F. Lefebvres, B. Tamain, J. Pochodzalla, C.K. Gelbke, W. Lynch, and M. Maier, Phys. Lett. **B181** 43 (1986).
- [Lamb78] D.Q. Lamb, J.M. Lattimer, C.J. Pethick, and D.G. Ravenhall, Phys. Rev. Lett. **41** 1623 (1978).
- [Land59] L.D. Landau and E.M. Lifschitz, *Statistical Physics* Pergamon Press, London (1959).
- [Lee90a] J.H. Lee, W. Benenson, and D.J. Morrissey, Phys. Rev. **C41** 1562 (1990).
- [Lee90b] J.H. Lee, W. Benenson, C. Bloch, Y. Chen, R.J. Radtke, E. Kashy, M.F. Mohar, D.J. Morrissey, R. Blue, and R.M. Ronningen, Phys. Rev. **C41** 2406 (1990).
- [Li89] T. Li, private communication (1989).
- [Lide87] F. Liden, J. Nyberg, and A. Johnson, Nucl. Inst. Meth. **A253** 305 (1987).
- [Lide88] F. Liden, A. Johnson, A. Kerek, E. Dafni, and M. Sidi, Nucl. Inst. Meth. **A273** 240 (1988).
- [Lópe89a] J.A. López and J. Randrup, Nucl. Phys. **A491** 477 (1989).
- [Lópe89b] J.A. López and J. Randrup, Nucl. Phys. **A503** 183 (1989).
- [Lópe89c] J.A. López and J. Randrup, Preprint LBL-27039 (1989).
- [McMa88] M.A. McMahon, IEEE Trans. Nucl. Sci. **35**, 42 (1988).
- [Metr53] N. Metropolis, A. Rosenbluth, M. Rosenbluth, A. Teller, B. Teller, J. Chem. Phys. **21**, 1087 (1953).
- [Mign88] A.C. Mignerey, Workshop on Nuclear Dynamics, Sun Valley, Idaho (1988).
- [More88] L.G. Moretto and G.J. Wozniak, Nucl. Phys. **A488** 337c (1988).
- [Morr84] D.J. Morrissey, W. Benenson, E. Kashy, B. Sherrill, A.D. Pantagiotou, R.A. Blue, R.M. Ronningen, J. van der Plicht, and H. Utsunomiya, Phys. Lett. **B148** 423 (1984).
- [Morr85] D.J. Morrissey, W. Benenson, E. Kashy, C. Bloch, M. Lowe, R.A. Blue, R.M. Ronningen, B. Sherrill, H. Utsunomiya, and I. Kelson, Phys. Rev. **C32** 877 (1985).

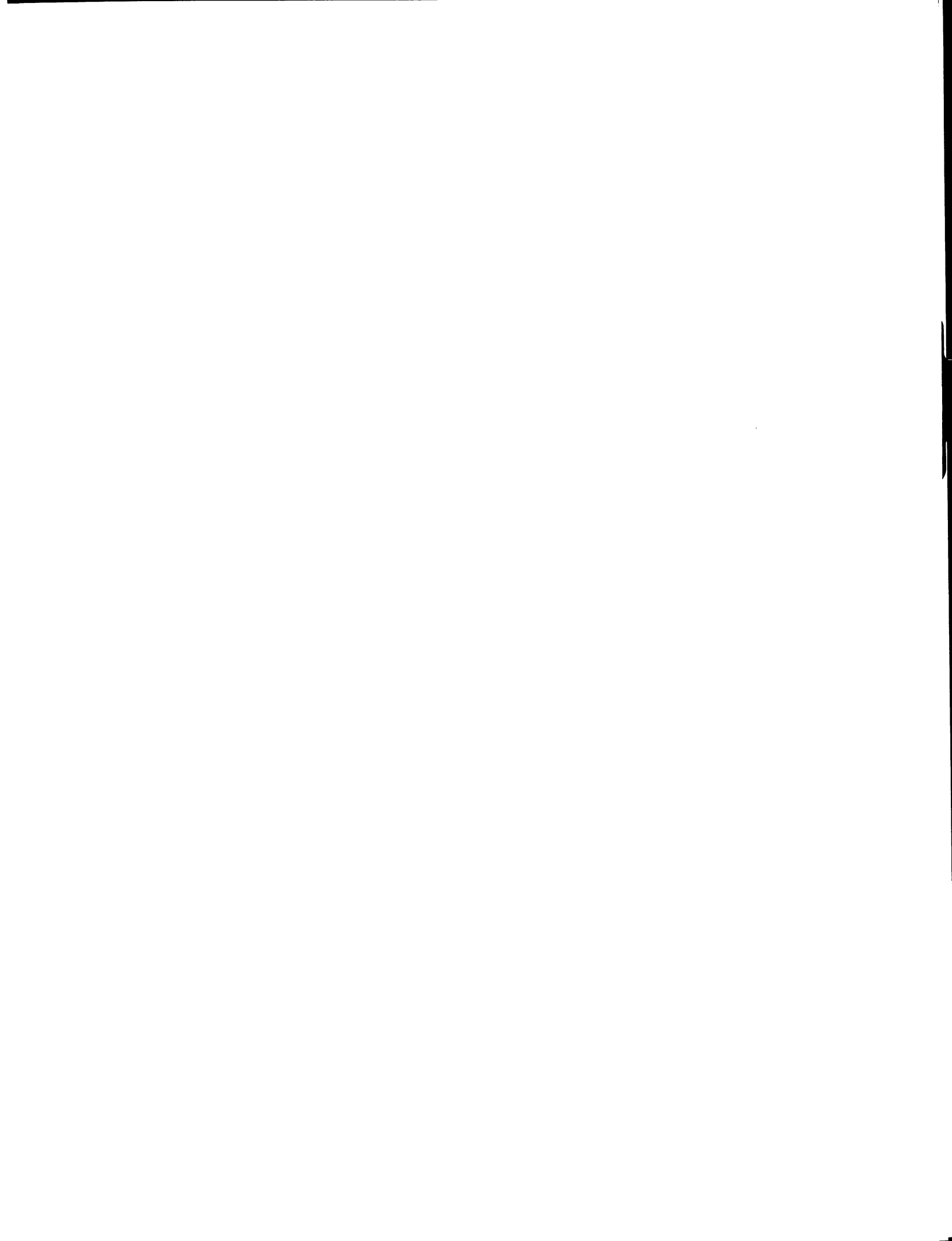
- [Morr86] D.J. Morrissey, C. Bloch, W. Benenson, E. Kashy, R.A. Blue, R.M. Ronningen, and R. Aryaeinajad, *Phys. Rev.* **C34** 761 (1986).
- [Naya89] T.K. Nayak, T. Murakami, W.G. Lynch, K. Swartz, D.J. Fields, C.K. Gelbke, Y.D. Kim, J. Pochodzalla, M.B. Tsang, H.M. Xu, F. Zhu, and K. Kwiatkowski, *Phys. Rev. Lett.* **62** 1021 (1989).
- [Néme89] J. Németh, G. Papp, C. Ngô, and M. Barranco, Preprint (1989).
- [Ngô89] C. Ngô, S. Leray, M.E. Spina, H. Ngô, B. Remaud, and F. Sébille, XII Oaxtepec Nuclear Physics Symposium, Mexico, January (1989).
- [Ogil89a] C.A. Ogilvie, D.A. Cebra, J. Clayton, S. Howden, J. Karn, A. Vander Molen, G.D. Westfall, W.K. Wilson, and J.S. Winfield, *Phys. Rev.* **C40**, 654 (1989).
- [Ogil89b] C.A. Ogilvie, D.A. Cebra, J. Clayton, P. Danielewicz, S. Howden, J. Karn, A. Vander Molen, G.D. Westfall, W.K. Wilson, and J.S. Winfield, *Phys. Rev.* **C40**, 2592 (1989).
- [Ogil89c] C.A. Ogilvie, D.A. Cebra, J. Clayton, P. Danielewicz, S. Howden, J. Karn, A. Nadasen, A. Vander Molen, G.D. Westfall, W.K. Wilson, and J.S. Winfield, *Phys. Lett.* **231B**, 35 (1989).
- [Ogil90] C.A. Ogilvie, W.K. Wilson, W. Benenson, D.A. Cebra, J. Clayton, S. Howden, J. Karn, T. Li, A. Vander Molen, G.D. Westfall, J.S. Winfield, B. Young, and A. Nadasen, To be printed *Phys. Rev. C* (1990).
- [Peth87] C.J. Pethick and D.G. Ravenhall, *Nucl. Phys.* **A471** 19c (1987).
- [Plag89] E. Plagnol, L. Vinet, D.R. Bowman, Y.D. Chan, R.J. Charity, E. Chavez, S.B. Gazes, H. Han, W.L. Kehoe, M.A. McMahan, L.G. Moretto, R.G. Stokstad, G.J. Wozniak, and G. Auger, *Phys. Lett.* **B221** 11 (1989).
- [Poch85a] J. Pochodzalla, W.A. Friedman, C.K. Gelbke, W.G. Lynch, M. Maier, D. Ardouin, H. Delagrange, H. Doubre, C. Grégoire, A. Kyanowski, W. Mittig, A. Péghaire, J. Péter, F. Saint-Laurent, Y.P. Viyogi, B. Zwieglinski, G. Bizard, F. Lefèbvres, B. Tamain, and J. Québert, *Phys. Rev. Lett.* **55** 177 (1985).
- [Poch85b] J. Pochodzalla, W.A. Friedman, C.K. Gelbke, W.G. Lynch, M. Maier, D. Ardouin, H. Delagrange, H. Doubre, C. Grégoire, A. Kyanowski, W. Mittig, A. Péghaire, J. Péter, F. Saint-Laurent, Y.P. Viyogi, B. Zwieglinski, G. Bizard, F. Lefèbvres, B. Tamain, and J. Québert, *Phys. Lett.* **B161** 256 (1985).
- [Poch85c] J. Pochodzalla, W.A. Friedman, C.K. Gelbke, W.G. Lynch, M. Maier, D. Ardouin, H. Delagrange, H. Doubre, C. Grégoire, A. Kyanowski, W. Mittig, A. Péghaire, J. Péter, F. Saint-Laurent, Y.P. Viyogi, B. Zwieglinski, G. Bizard, F. Lefèbvres, B. Tamain, and J. Québert, *Phys. Lett.* **B161** 275 (1985).
- [Poch86a] J. Pochodzalla, C.B. Chitwood, D.J. Fields, C.K. Gelbke, W.G. Lynch, M.B. Tsang, D.H. Boal, and J.C. Shillcock, *Phys. Lett.* **B174** 36 (1986).

- [Poch86b] J. Pochodzalla, C.K. Gelbke, C.B. Chitwood, D.J. Fields, W.G. Lynch, M.B. Tsang, and W.A. Friedman, *Phys. Lett.* **B175** 275 (1986).
- [Poch87] J. Pochodzalla, W.A. Friedman, C.K. Gelbke, W.G. Lynch, M. Maier, D. Ardouin, H. Delagrangé, H. Doubre, C. Grégoire, A. Kyanowski, W. Mittig, A. Péghaire, J. Péter, F. Saint-Laurent, Y.P. Viyogi, B. Zwieglinski, G. Bizard, F. Lefebvres, B. Tamain, and J. Québert, *Phys. Rev.* **C35** 1695 (1987).
- [Poch88] J. Pochodzalla, *Nucl. Phys.* **A488** 353c (1988).
- [Poch89a] J. Pochodzalla, W. Trautman, and U. Lynen, *Phys. Lett.* **B232** 41 (1989).
- [Poch89b] J. Pochodzalla, R.J. Charity, U. Lynen, H.Sann, W. Trautmann, and R. Trockel, *Phys. Rev.* **C40** 2918 (1989).
- [Poul88] J. Pouliot, Y. Chan, A. Dacal, A. Harmon, R. Knop, M.E. Oritz, E. Plagnol, and R.G. Stokstad, *Nucl. Inst. Meth.* **A270** 69 (1988).
- [Poul89] J. Pouliot, Y. Chan, A. Dacal, D.E. DiGregorio, B.A. Harmon, R. Knop, M.E. Oritz, E. Plagnol, R.G. Stokstad, C. Moisan, L. Potvin, C. Rioux, and R. Roy, *Phys. Lett.* **223** 16 (1989).
- [Rand81] J. Randrup and S.E. Koonin, *Nucl. Phys.* **A356** 223 (1981).
- [Rudo86] G. Rudolf, J.C. Adloff, A. Kamili, F. Scheibling, B. Boishu, A. Genoux-Lubain, C. LeBrun, J.F. Lecolley, F. Lefebvres, M. Louvel, R. Regimbart, O. Granier, S. Leray, R. Lucas, C. Mazur, C. Ngo, M. Ribrag, and E. Tomasi, *Phys. Rev. Lett.* **57** 2905 (1986).
- [Rudo88] G. Rudolf, J.C. Adloff, B. Bilwes, R. Bilwes, M. Glaser, F. Scheibling, L. Stütge, G. Bizard, R. Bougault, R. Brou, F. Delaunay, A. Genoux-Lubain, C. LeBrun, J.F. Lecolley, F. Lefebvres, M. Louvel, J.C. Steckmeyer, J.C. Ferrero, Y. Cassagnou, R. Legrain, F. Guilbault, C. LeBrun, B. Rastegar, G.M. Jin, A. Péghaire, J. Peter, and E. Rosato, Preprint (1988).
- [Sain88] F. Saint-Laurent, A. Kyanowski, D. Ardouin, H. Delagrangé, H. Doubre, C. Grégoire, W. Mittig, A. Péghaire, J. Péter, G. Bizard, F. Lefebvres, B. Tamain, J. Québert, Y.P. Viyogi, J. Pochodzalla, C.K. Gelbke, W. Lynch, M. Maier, *Phys. Lett.* **B202** 190 (1988).
- [Sara88] D.G. Sarantides, L.G. Sobotka, T.M. Semkow, V. Abeante, J. Elson, J.T. Hood, Z. Li, N.G. Nicolis, D.W. Stracener, and J. Valdes, *Nucl. Inst. Meth.* **A264** 319 (1988).
- [Schi85] H.R. Schimdt, M. Bantel, Y. Chan, S.B. Gazes, S. Wald, and R.G. Stokstad, *Nucl. Inst. Meth.* **A242** 111 (1985).
- [Schu82] H. Schulz, L. Münchow, G. Rópké, and M. Schmidt, *Phys. Lett.* **B119** 12 (1982).
- [Sobo83] L.G. Sobotka, M.L. Padgett, G.J. Wozniak, G. Guarino, A.J. Pacheco, L.G. Moretto, Y. Chan, R.G. Stokstad, I. Tserruya, and S. Wald, *Phys. Rev. Lett.* **51** 2187 (1983).

- [Sobo84] L.G. Sobotka, M.A. McMahan, R.J. McDonald, C. Signarbieux, G.J. Wozniak, M.L. Padgett, J.H. Gu, Z.H. Liu, Z.Q. Yao, and L.G. Moretto, *Phys. Rev. Lett.* **53** 2004 (1984).
- [Stau79] D. Stauffer, *Phys. Rep.* **54** 1 (1979).
- [Stöc83] H. Stöcker, G. Buchwald, G. Graebner, P. Subramanian, J.A. Maruhn, W. Greiner, B.V. Jacak, G.D. Westfall, *Nucl. Phys.* **400** 63c (1983).
- [Sura89] E. Suraud, Preprint (1989).
- [Tick80] R.S. Tickle, G.M. Crawley, W.G. Lynch, M.B. Tsang, and J. Yurkon, MSU Cyclotron Laboratory Annual Report, 86 (1980-81).
- [Tick81] R.S. Tickle, B.E. Hasselquist, G.M. Crawley, and J. Yurkon, MSU Cyclotron Laboratory Annual Report, 77 (1981-82).
- [Trau89] W. Trautmann, K.D. Hildenbrand, U. Lynen, W.F.J. Müller, H.J. Rabe, H. Sann, H. Stelzer, R. Trockel, R. Wada, E. Eckert, P. Kreutz, A. Kühmichel, and J. Pochodzalla, Symposium on Nuclear Dynamics and Nuclear Disassembly, ACS Meeting, Dallas, Texas, April 10-14 (1989).
- [Troc87] R. Trockel, U. Lynen, J. Pochodzalla, W. Trautmann, N. Brummund, E. Eckert, R. Glasow, K.D. Hildenbrand, K.H. Kampert, W.F.J. Müller, D. Pelte, H.J. Rabe, H. Sann, R. Santo, H. Stelzer, and R. Wada, *Phys. Rev. Lett.* **59** 2844 (1987).
- [Troc89] R. Trockel, K.D. Hildenbrand, U. Lynen, W.F.J. Müller, H.J. Rabe, H. Sann, W. Trautmann, R. Wada, E. Eckert, P. Kreutz, A. Kühmichel, and J. Pochodzalla, *Phys. Rev.* **C39** 729 (1989).
- [Tsan86] M.B. Tsang, R.M. Ronningen, G. Bertsch, Z. Chen, C.B. Chitwood, D.J. Fields, C.K. Gelbke, W.G. Lynch, T. Nayak, J. Pochodzalla, T. Shea, and W. Trautmann, *Phys. Rev. Lett.* **57** 559 (1986).
- [Wada89] R. Wada, D. Fabis, K. Hagel, G. Nebbia, Y. Lou, M. Gonin, J.B. Natowitz, R. Billerey, B. Cheynis, A. Demeyer, D. Drain, D. Guinet, C. Pastor, L. Vagneron, K. Zaid, J. Alarja, A. Giorni, D. Heuer, C. Morand, B. Viano, C. Mazur, C. Ngö, S. Leray, R. Lucas, M. Ribrag, and E. Tomasi, *Phys. Rev.* **C39** 497 (1989).
- [West76] G.D. Westfall, J. Gosset, P.J. Johansen, A.M. Poskanzer, W.G. Meyer, H.H. Gutbrod, A. Sandoval, R. Stock, *Phys. Rev. Lett.* **37** 1202 (1976).
- [West85] G.D. Westfall, J.E. Yurkon, J. van der Plicht, Z.M. Koenig, B.V. Jacak, R. Fox, G.M. Crawley, M.R. Maier, B.E. Hasselquist, R.S. Tickle, and D. Horn, *Nucl. Inst. Meth.* **A238** 347 (1985).
- [Wilk52] D.H. Wilkinson, *Rev. Sci. Instr.* **23** 414 (1952).
- [Wils89] W.K. Wilson, private communication (1989).
- [Wozn88] G.J. Wozniak and L.G. Moretto, *Nucl. Phys.* **A488** 337c (1988).

- [Xu86] H. Xu, D.J. Fields, W.G. Lynch, M.B. Tsang, C.K. Gelbke, M.R. Maier, D.J. Morrissey, J. Pochodzalla, D.G. Sarantides, L.G. Sobotka, M.L. Halbert, D.C. Hensley, D. Hahn, and H. Stöcker, *Phys. Lett.* **B182** 155 (1986).
- [Xu89] H. Xu, W.G. Lynch, C.K. Gelbke, M.B. Tsang, D.J. Fields, M.R. Maier, D.J. Morrissey, T.K. Nayak, J. Pochodzalla, D.G. Sarantides, L.G. Sobotka, M.L. Halbert, and D.C. Hensley, *Phys. Rev.* **C40** 186 (1989).
- [Zhan87] Zhang X., D.H.E. Gross, Xu S., and Zheng Y., *Nucl. Phys.* **A461** 668 (1987).
- [Zhan89] W.M. Zhang, R. Madey, M. Elaasar, J. Schambach, D. Keane, B.D. Anderson, A.R. Baldwin, J. Cogar, J.W. Watson, G.D. Westfall, G. Krebs, and H. Wieman, submitted to *Phys. Rev. Lett.* (1989).





MICHIGAN STATE UNIV. LIBRARIES



31293009108584